Hybrid and Vapor Deposition Processes for Perovskite Thin-Film Photovoltaics

Zur Erlangung des akademischen Grades eines

DOKTORS DER INGENIEURWISSENSCHAFTEN
(Dr.-Ing.)

von der KIT-Fakultät für
Elektrotechnik und Informationstechnik des
Karlsruher Instituts für Technologie (KIT)

angenommene

DISSERTATION

von

M.Sc. Julian Petry
geboren in: Wiesbaden, Deutschland

Tag der mündlichen Prüfung:	12.05.2026
Hauptreferent:	Prof. Dr. Ulrich W. Paetzold
Korreferent:	Prof. Dr. Steve Albrecht

Kurzfassung

Perowskit-Photovoltaik hat inzwischen Wirkungsgrade erreicht, welche den Übergang von der Verarbeitung im Labormaßstab zur industriellen Fertigung motivieren, insbesondere bei Perowskit-Silizium-Tandem-Solarzellen. Die skalierbare Umsetzung wird jedoch weiterhin durch enge stöchiometrische und grenzflächenbezogene Prozessfenster, Durchsatzbeschränkungen sowie starke, von Anlagen und Substraten abhängige Schwankungen eingeschränkt, die häufig eine erneute Prozessoptimierung erfordern. Diese Arbeit befasst sich mit diesen Herausforderungen aus einer fertigungsorientierten Perspektive, indem sie die Thermochemie der Ausgangsstoffe, das Quellendesign, die Grenzflächenchemie und die Wahl der Prozessroute mit robusten Prozessfenstern für die skalierbare Herstellung von Perowskit-Dünnschichten verknüpft.

Bei der Gasphasenabscheidung wird der Fertigungsdurchsatz in erster Linie durch flüchtige organische Materialien begrenzt. Formamidiniumiodid (FAI) zersetzt sich oberhalb von etwa 220–240 °C erheblich, während PbI_2 und CsI thermisch stabil bleiben und daher nicht geschwindigkeitsbestimmend sind. Eine Durchsatzanalyse für ein Ziel von 1000 M10-Wafern pro Stunde zeigt, dass Prozesswege, welche die Gasphasenabscheidung organischer und anorganischer Materialien entkoppeln, für die industrielle Umsetzung attraktiv sind.

Eine vollständig sequenzielle Gasphasenabscheidung minimiert den Bedarf an Quellen und die Komplexität der Anlage, während die teilsequenzielle Prozesse und Kodeposition den Quellenbedarf im Vergleich zu dem vollständig sequenziellen Referenzprozess um etwa 5% bzw. 157% erhöhen. Darüber hinaus werden die Partikelgrößenverteilung der Materialien und die Tiegelgeometrie als wichtige Parameter für eine wiederholbare FAI-Abscheidung identifiziert, wodurch das Quellendesign als entscheidender Faktor für die Reproduzierbarkeit des Dampfflusses und die Übertragbarkeit zwischen verschiedenen Anlagen etabliert wird.

Im Hinblick auf die gasphasenbasierte Kodeposition untersucht die Dissertation, wie die Grenzflächenchemie die Phasenselektivität und die effektive Einlagerung von FAI beeinflusst. Freiliegende Phosphonsäuregruppen in selbstorganisierten Monolagen der Lochtransportschichten stabilisieren die photoaktive α-Phase während der frühen Kristallisation und unterdrücken die Bildung der δ-Phase. Untersuchung mittels Dichtefunktionaltheorie stützt einen kinetischen Einfangmechanismus, bei dem Wasserstoffbrückenbindungen zwischen Phosphonsäuregruppen und Oberflächeniodiden die Aktivierungsbarriere für die $\alpha \rightarrow \delta$-Umwandlung erhöhen. Darüber hinaus ist die effektive FAI-Einlagerungsrate stark substratabhängig, sodass Änderungen der Oberflächenterminierung das stöchiometrische Prozessfenster verschieben und eine Anpassung der FAI-Zufuhr erfordern, um einen optimalen Bauteilwirkungsgrad zu erzielen. Diese Empfindlichkeiten lassen sich durch gemischte selbstorganisierte Monolagen gezielt einstellen, wodurch sich die rationale Grenzflächenanpassung als steuerbare Strategie für phasenselektives Wachstum etabliert.

Um die durch die Abscheidung organischer Ausgangsstoffe bedingten Durchsatzbeschränkungen zu überwinden und gleichzeitig eine konforme Beschichtung strukturierter Substrate zu gewährleisten, wurde eine vollständig sequenzielle hybride Zweistufen-Plattform entwickelt und mit dem herkömmlichen Verfahren der Kodeposition der abgeschiedenen anorganischen Dünnschicht verglichen. Die sequenzielle Abscheidung eines CsCl/PbI_2-Gerüsts erzeugt eine porösere und strukturiertere Dünnschicht mit überwiegend vertikalen oder geneigten PbI_2-Plättchen, während die Kodeposition dichtere Gerüste mit überwiegend horizontalen Plättchen ergibt, wodurch das Infiltrations- und Umwandlungsverhalten der organischen Kationen verändert wird. Trotz dieser Unterschiede zeigt das sequenzielle Verfahren bei einer angestrebten Bandlücke von etwa 1,70 eV eine vergleichbare Leistung wie das als Laborstandard geltende Co-Depositionsverfahren und erreicht einen Wirkungsgrad von 20,3% bei verbesserter Wiederholbarkeit von Charge zu Charge. Die Abscheidungszeit für anorganische Gerüste wird im Vergleich zum Referenzprozess um weitere 80% auf unter 20 Minuten reduziert, ohne dass dabei Leistungseinbußen auftreten. Die Kompatibilität mit tandemrelevantem texturiertem Silizium wird durch einen ersten Perowskit/Silizium Tandem Prototyp mit einem Wirkungsgrad von 24,1% demonstriert. Schließlich ermöglicht die modulare sequenzielle Plattform eine systematische Bandlückenoptimierung in Richtung Dreifachsolarzellen, was zu Bauteilwirkungsgraden von 20,0% bei 1,52 eV und 15,3 % bei 1,84 eV führt.

Diese auf die Fertigung ausgerichtete Perspektive zeigt, dass die industrielle Umsetzung der Perowskit-Photovoltaik durch Einschränkungen hinsichtlich Durchsatz, Übertragbarkeit und Reproduzierbarkeit der Umwandlung begrenzt ist. Die Entkopplung der Prozessabläufe, das Quellendesign und die Grenzflächeneigenschaften sind entscheidende Faktoren für die Realisierung reproduzierbarer und tandemkompatibler Fertigungsprozesse mit einem hohen Produktionsdurchsatz.

Abstract

Perovskite photovoltaics has achieved efficiencies that motivate transfer from laboratory-scale processing to industrial manufacturing, particularly in perovskite/silicon tandem architectures. However, scalable implementation *via* vapor phase deposition remains limited by narrow stoichiometric process windows, throughput constraints, and strong tool- and substrate-dependent variability that frequently requires re-optimization. This thesis addresses these challenges from a manufacturing-oriented perspective by linking precursor thermochemistry, source design, interface chemistry, and process route choice to robust operating windows for scalable perovskite thin-film fabrication.

For vapor-phase deposition, fabrication throughput is primarily constrained by volatile organic precursors. Formamidinium iodide (FAI) undergoes significant decomposition above about 220–240 °C, whereas PbI_2 and CsI remain thermally stable and are therefore not rate-limiting. A bottom-up throughput analysis for a target of 1000 M10-sized wafers h^{-1} demonstrates that process routes which decouple organic and inorganic precursor vapor deposition are attractive for industrial implementation. Fully sequential vapor deposition minimizes source demand and equipment complexity, whereas partial sequential and co-deposition increase equipment demand by about 5% and 157%, respectively, relative to the fully sequential baseline. Furthermore, precursor particle-size distribution and crucible geometry are identified as decisive parameters for repeatable FAI deposition, establishing source design as a key determinant for vapor-flux reproducibility and tool-to-tool transferability.

For vapor-based co-deposition, the thesis resolves how interface chemistry influences phase selectivity and effective FAI incorporation. Exposed phosphonic acid functional groups in self-assembled monolayer hole-transport layers stabilize the photoactive α-phase during early crystallization and suppress δ-phase formation. Density-functional theory supports a kinetic trapping mechanism in which hydrogen bonding between phosphonic-acid groups and surface iodides increases the activation barrier for the $\alpha \rightarrow \delta$ transformation. In addition, the effective FAI incorporation rate is strongly substrate-dependent, such that changes in surface termination shift the stoichiometric process window and necessitate adjustment of the FAI supply to achieve optimal device performance. These sensitivities can be deliberately tuned through mixed self-assembled monolayers, establishing rational interface engineering as a controllable strategy for phase-selective growth.

To overcome throughput limitations imposed by organic precursor deposition while retaining conformal coating on textured substrates, a fully sequential hybrid two-step platform is established and benchmarked against the conventional co-deposited inorganic scaffold route. Sequential $CsCl/PbI_2$ scaffold deposition produces a more porous and textured scaffold with predominantly vertical or tilted PbI_2 platelets, whereas co-deposition yields denser scaffolds with predominantly horizontal platelets, thereby modifying organic-cation infiltration and conversion behavior. Despite these differences, the sequential route demonstrates comparable device performances to the laboratory-standard co-deposition route at a target bandgap of

about 1.70 eV, achieving a champion efficiency of 20.3% with improved batch-to-batch repeatability. Inorganic scaffold deposition time is further reduced by 80% relative to the baseline process to below 20 min without loss in performance. Compatibility with tandem-relevant textured silicon is demonstrated by a first perovskite/silicon tandem prototype with an efficiency of 24.1%. Finally, the modular sequential platform enables systematic bandgap engineering toward multi-junction architectures, yielding device efficiencies of 20.0% at 1.52 eV and 15.3% at 1.84 eV.

This manufacturing-oriented perspective reveals that industrial translation of vapor-based perovskite photovoltaics is constrained by limitations in throughput, transferability, and conversion repeatability. Process route decoupling, source design, and interface engineering emerge as key parameters for enabling repeatable, high-throughput, and tandem-compatible manufacturing processes.

Contents

List of Abbreviations

2PACz	(2-(9H-carbazol-9-yl)ethyl)phosphonic acid
4dPA	1,4-butylenediphosphonic acid
4PADBCz	(4-(7H-dibenzo[c,g]carbazol-7-yl)butyl)phosphonic acid
AAA	Triple-A (solar simulator class)
AFM	Atomic Force Microscopy
ALD	Atomic Layer Deposition
AM1.5G	Air Mass 1.5 Global
BAI	Butylammonium iodide
BB	Blackbody
BCP	Bathocuproine
C_{60}	Fullerene C_{60}
CA	Contact Angle
CapEx	Capital Expenditure
CBM	Conduction Band Minimum
CIGS	Copper indium gallium selenide
CRediT	Contributor Roles Taxonomy
CSM	Confocal Scanning Microscopy
CSS	Close-space sublimation
CVD	Chemical Vapor Deposition
DB	Detailed balance
DFT	Density Functional Theory
DMSO	Dimethyl sulfoxide
DSC	Differential Scanning Calorimetry
DTS	Duran Tube Sublimation

EDTA Ethylenediaminetetraacetic acid

EQE External Quantum Efficiency

ETL Electron-transport layer

FA Formamidinium

FABr Formamidinium bromide

FAI Formamidinium iodide

FAPI Formamidinium lead iodide ($FAPbI_3$)

FF Fill Factor

FWHM Full Width at Half Maximum

GHG Greenhouse Gas

GIWAXS Grazing-Incidence Wide-Angle X-ray Scattering

HTL Hole-transport layer

ICP-OES Inductively Coupled Plasma Optical Emission Spectroscopy

IEA International Energy Agency

IPCC Intergovernmental Panel on Climate Change

IRENA International Renewable Energy Agency

ISOS International Summit on Organic Photovoltaics Stability

I_{SC} Short-circuit current

ITO Indium tin oxide

IZO Indium zinc oxide

J_{SC} Short-circuit current density

KEMS Knudsen Effusion Mass Spectrometry

LCOE Levelized Cost of Electricity

LUMO Lowest unoccupied molecular orbital

MA Methylammonium

MACl Methylammonium chloride

MAI Methylammonium iodide

$MAPbI_3$ Methylammonium lead iodide

MBG Mid-bandgap

MeO2PACz
(2-(3,6-dimethoxy-9H-carbazol-9-yl)ethyl)phosphonic acid

Me4PACz
(4-(3,6-dimethyl-9H-carbazol-9-yl)butyl)phosphonic acid

MPP Maximum Power Point

MWp Megawatt-peak

NBG Narrow bandgap

NCI Non-covalent interaction

NK N K-edge (Nitrogen K edge)

NMR Nuclear Magnetic Resonance

NREL National Renewable Energy Laboratory

OLED Organic light-emitting diode

PCE Power Conversion Efficiency

$PDAI_2$ Propane-1,3-diammonium iodide

PL Photoluminescence

PLQY Photoluminescence Quantum Yield

PSC Perovskite Solar Cell

PTAA Poly[bis(4-phenyl)(2,4,6-trimethylphenyl)]amine

PV Photovoltaics

PVD Physical Vapor Deposition

QCM Quartz Crystal Microbalance

QFLS Quasi-Fermi Level Splitting

RH Relative Humidity

RJ Recombination Junction

RMS Root Mean Square

RSD Relative Standard Deviation

SAM Self-Assembled Monolayer

SEM Scanning Electron Microscopy

Seq Sequential deposition route

Spiro – OMeTAD
2,2',7,7'-Tetrakis[N,N-di(4-methoxyphenyl)amino]-9,9'-spirobifluorene

SSD Source-to-substrate distance

TCO Transparent Conducting Oxide

TCSPC Time-Correlated Single Photon Counting

TDMASn Tetrakis(dimethylamino)tin

TEA Triethanolamine

TGA Thermogravimetric Analysis

TSC Tandem Solar Cell

TW Terawatt

UHV Ultra-high vacuum

UWBG Ultra-wide-bandgap

VBM Valence Band Maximum

V_{OC} Open-circuit voltage

VTD Vapor-Transport Deposition

WBG Wide bandgap

WLI White Light Interferometry

XES X-ray Emission Spectroscopy

XRD X-ray Diffraction

1 Introduction

Motivation and Contextualization

Human-made climate change represents the most consequential challenge of our time, mandating rapid greenhouse-gas (GHG) mitigation across all sectors.[1] This urgency of climate change effects is reflected both in the continued rise of global mean temperature (**Figure 1.1 A**) and in the dominant contribution of the energy sector to global net anthropogenic GHG emissions, accounting for approximately three-quarters of the total emissions in 2022.[2–4] The energy sector is of central importance because of increasing demand of decarbonized electricity to enable the large-scale low-carbon electrification of transport, heat and industry, thereby exerting a cross-sector influence on economy-wide emissions reductions.[3,5] A sectoral comparison of emissions intensities highlights that low-carbon electricity generation options such as wind, hydro and photovoltaics (PV) exhibit orders-of-magnitude lower life-cycle GHG emissions than fossil-based generation (**Figure 1.1 B**), underscoring that abundant, clean, and affordable electricity is a prerequisite for economy-wide decarbonization.[3,6] Beyond climate targets, expanding domestic clean power also contributes to energy security by diversifying energy sources and reducing reliance on imported fossil fuels, thereby lowering exposure to international fuel price volatility and enhancing the resilience of electricity systems, a factor that has gained renewed relevance in recent years.[7–9]

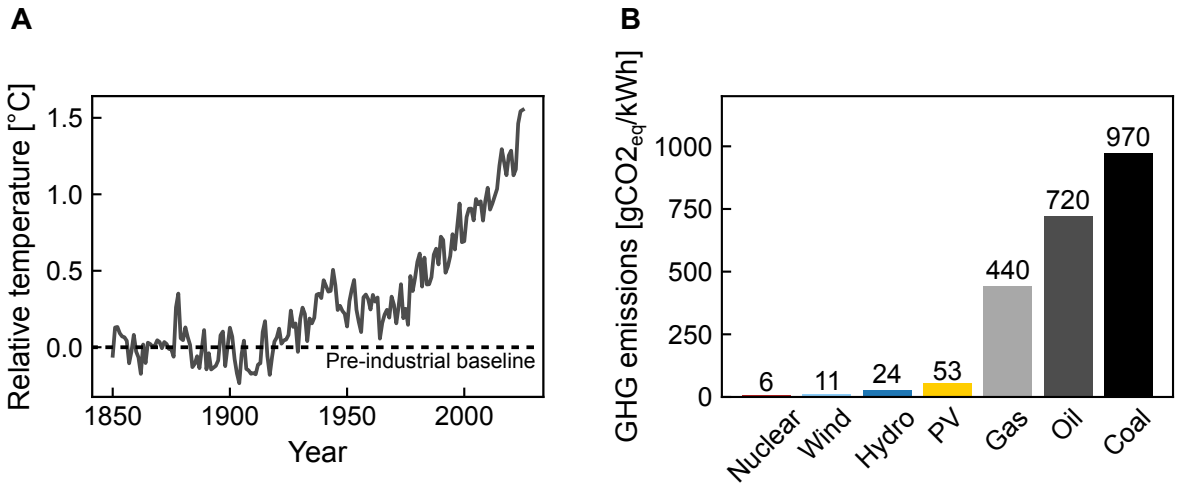

Figure 1.1: Climate motivation for decarbonizing electricity. **A** Increase in relative global mean temperature, illustrating the ongoing global warming trend.[10] **B** Life-cycle GHG emissions intensities for different electricity generation technologies, highlighting the mitigation potential of low-carbon power.[11] GHG: greenhouse-gas

Among the options for low-carbon electricity, solar PV is a key technology due to high scalability, rapid deployability, and increasing cost-competitiveness with a low levelized cost of electricity (LCOE).[12–14] The economic basis for this scale-up is the sustained decline in PV module spot prices (**Figure 1.2 A**), with learning rates on the order of 34% per doubling at mass-production scale.[13,15] In parallel, deployment trends demonstrate rapid growth in PV capacity (**Figure 1.2 B**). In 2024, global cumulative PV capacity surpassed 2.2 TW,[16,17] with annual global installations approaching 1 TW.[17–19] Together, these trends indicate that PV is transitioning from a fast-growing technology to a dominant driver of clean electricity supply.

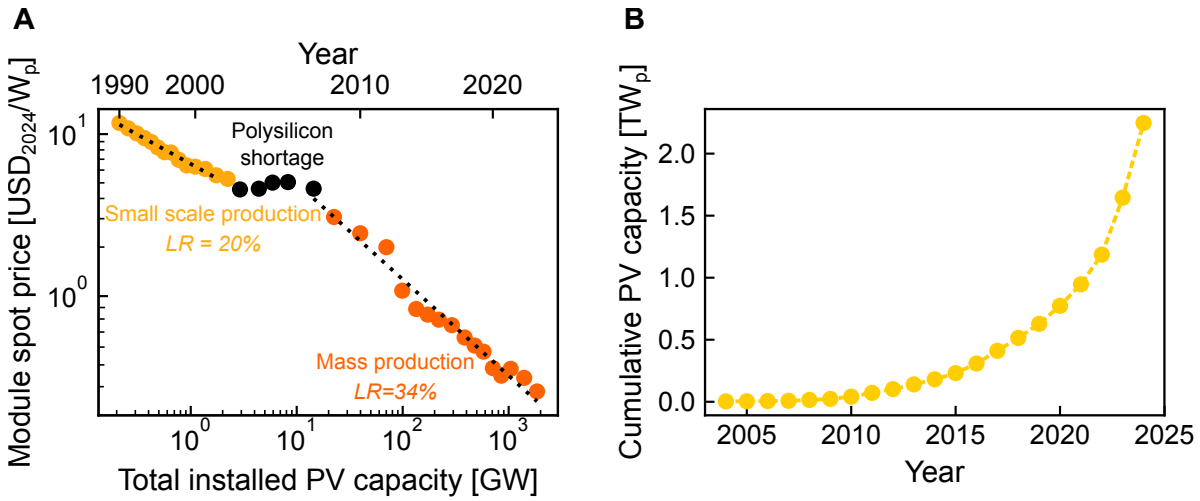

Figure 1.2: PV as a scalable low-carbon electricity technology. **A** Historical decline in PV module cost, reflecting learning effects and economies of scale.[15] **B** Growth in PV deployment, indicating rapid expansion toward multi-terawatt cumulative capacity.[16,17] PV: Photovoltaic, W_p: Watt peak, TW_p: Terrawatt peak

As PV scales toward multi-terawatt deployment, further gains in module efficiency become increasingly valuable because they reduce the LCOE together with land and material use per unit of electricity generated.[20] However, silicon solar cells are approaching practical single-junction efficiency limits,[21] motivating tandem solar cell concepts that more effectively utilize the solar spectrum.[22–25] Tandem architectures (**Figure 1.3 A**) combine absorbers with complementary bandgaps to reduce thermalization and transmission losses, enabling efficiencies beyond the single-junction limit. In particular, perovskite/silicon (PVK/Si) tandem solar cells combine the mature silicon platform with a tunable, wide bandgap perovskite top cell. An unprecendented increase in efficiency was demonstrated for the PVK/Si tandem technology in recent years as summarized in **Figure 1.3 B**.[23,26–31] Growing interest in PVK/Si tandem technology is manifested in steadily increasing capital investments already exceeding 100 million US$/a and first products to begin commercial distribution, indicating a transition from laboratory demonstrations toward early commercialization.[32–35] Accordingly, the key question is shifting from whether tandems can reach record efficiencies to whether they can be produced with high yield, long-term stability, and at industrial-scale fabrication throughput.[19,32]

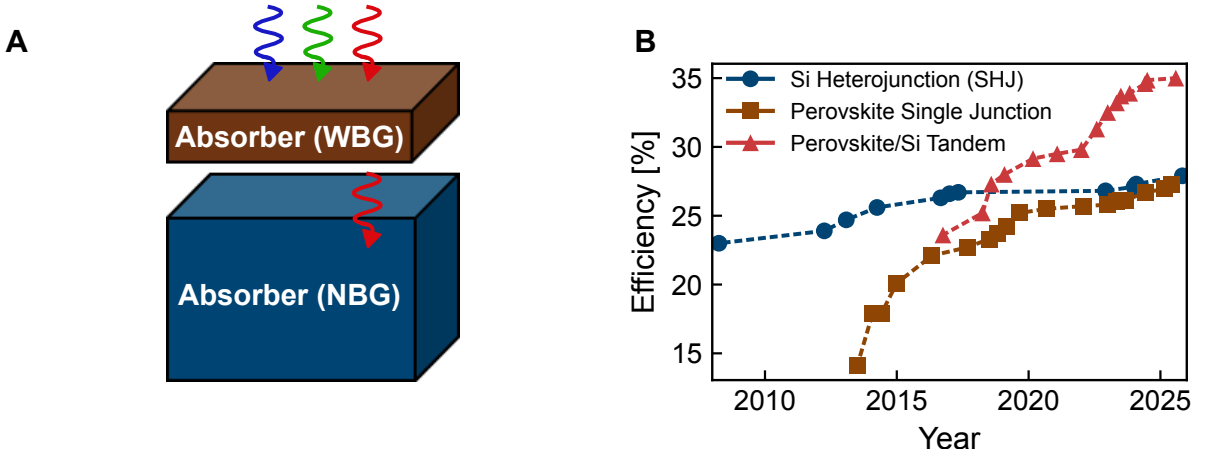

Figure 1.3: A Schematic illustration of a tandem solar cell combining absorbers with complementary bandgaps (WBG and NBG) for improved spectral utilization. **B** Best research-cell efficiency chart documenting the rapid efficiency progress of perovskite single-junction- and perovskite/silicon tandem solar cells in comparison to established Si solar cells.[23] WBG: wide bandgap, NBG: narrow bandgap

The unprecedented rate of improvement in record perovskite-based solar cell performance underscores their strong potential as a disruptive technology in the PV sector.[22,23,32] However, beyond record efficiencies, the decisive challenge is the reliable transfer of laboratory processes into industrially viable, high-yield manufacturing.[32,36] In this context, vapor-phase deposition is particularly attractive because it offers a mature industrial tool chain and a scalable manufacturing approach that enables uniform large-area coating, high process control, and precise compositional tuning.[36–40] Compared to solution processing, vapor deposition is solvent-free and thus avoids solvent-handling, drying/wetting sensitivities, and solvent-orthogonality constraints that can complicate multilayer fabrication and monolithic tandem integration due to fabrication incompatibilities.[37] Under high-vacuum conditions, film formation is driven by a small parameter set of primarily deposition rates, substrate temperature, and pressure, which facilitates monitoring and repeatable deposition over large areas, for example through real-time rate feedback using quartz-crystal microbalances.[38] Vapor deposition further supports homogeneous, pinhole-free films and conformal coverage on micron-textured silicon substrates relevant for tandem integration, while enabling cluster-tool concepts in which multiple layers can be deposited sequentially without ambient exposure. At the same time, reproducible absorber formation can remain challenging because process windows may be narrow and the deposition outcome can be affected by interfaces, precursor thermochemistry, source utilization, and reactor design, with these factors also potentially affecting fabrication throughput.[36–38,40–44] Addressing these throughput- and process integration-related bottlenecks is therefore central to translating the advantages of vapor-deposited perovskites into robust large-area production for both single-junction and tandem photovoltaic technologies.[36,37]

Research Objectives

This thesis addresses the translation challenge of transferring laboratory-scale insights to industrially relevant fabrication from a manufacturing-oriented perspective by treating perovskite absorbers both as high-efficiency semiconductors and process-limited components that must be deposited reproducibly, rapidly, and with efficient source utilization under realistic equipment constraints. For this, the work systematically examines how the choice of process route, deposition-source design, precursor thermochemistry and interfacial interactions jointly determine stable operating windows for vapor-phase perovskite fabrication. It aims to bridge the gap between laboratory deposition recipes and industrially relevant processes, where throughput, yield, and robustness are as decisive as peak efficiency.

With the overarching aim of facilitating the industrialization of perovskite photovoltaics, this thesis is structured around the following strategic research objectives:

1. **Derive guidelines for industrial scale-up**
   Identify dominant throughput bottlenecks and trade-offs between process route and capital expenditure that govern the feasibility of high-throughput vapor-phase perovskite deposition, including limitations imposed by achievable deposition rates, source design, and production-line layout.

2. **Elucidate interface- and process-induced layer growth mechanisms**
   Investigate how interfacial surface chemistry and deposition-route choice govern early-stage crystallization, phase selectivity, and the effective stoichiometric process window through their impact on organic precursor incorporation and infiltration kinetics.

3. **Assess industrially relevant vapor-deposition process routes**
   Evaluate deposition routes with respect to their compatibility with industrial manufacturing requirements, including throughput, process acceleration, bandgap tunability, repeatability, and equipment complexity.

4. **Identify factors limiting process transferability and repeatability**
   Determine how reactor design, substrate-dependent growth effects, and material properties drive process re-optimization and performance variability across different deposition routes and device architectures. Formulate general approaches that reduce sensitivity to narrow stoichiometric tolerances and enable stable, repeatable phase formation by interface engineering and deposition-route design.

Outline

A brief introduction is provided in Chapter 1, which motivates perovskite photovoltaics in the context of scalable low-carbon electricity generation and frames the manufacturing-oriented research objectives of this thesis. Chapter 2 introduces the theoretical background required to interpret the device results, covering photovoltaic operation in *p–i–n* architectures, key performance metrics and efficiency limits, structure-property relations of hybrid metal halide perovskites, and fundamentals of vapor-phase deposition and two-step conversion. Chapter 3 summarizes the experimental methods used for device fabrication and characterization, including vacuum and hybrid deposition routes as well as optoelectronic, structural, and chemical analysis techniques. Chapter 4 investigates industrialization strategies for vapor-deposited perovskite absorbers, focusing on throughput bottlenecks, precursor thermochemistry, source design, and scale-up considerations. Chapter 5 examines interface-driven growth effects in co-deposited perovskites on phosphonic-acid SAM hole-transport layers and elucidates how interfacial interactions affect incorporation kinetics and phase selectivity. Chapter 6 establishes and benchmarks a hybrid two-step process framework based on sequential inorganic scaffold deposition, evaluates process acceleration, and demonstrates transfer to tandem architectures and bandgap engineering. Finally, Chapter 7 concludes the thesis by summarizing the main findings and outlining perspectives for robust, scalable perovskite PV manufacturing. Additional supporting data and author contributions are provided in the Appendix.

2 Fundamentals

This chapter introduces the physical principles required to interpret the device results in this thesis, starting from the photovoltaic effect and inverted p–i–n perovskite architectures relevant for tandem integration. It explains charge generation, separation, and selective extraction in p–i–n stacks through energy-band alignment and quasi-Fermi level splitting, and connects microscopic drift-diffusion transport to macroscopic performance metrics through the one-diode equivalent-circuit model. The chapter further summarizes thermodynamic efficiency limits via the Shockley-Queisser detailed-balance framework and motivates tandem concepts, before reviewing key structure-property relations of hybrid metal halide perovskites, including crystal polymorphism, optoelectronic properties, and compositional bandgap engineering. Finally, it provides fundamentals of vapor-phase perovskite deposition, covering vapor transport in vacuum, thin-film nucleation and growth modes, and practical factors that govern co-deposition and two-step conversion such as stoichiometry control, substrate dependence, diffusion-limited conversion of inorganic scaffolds, and the role of moisture in the conversion process during the two-step deposition route.

2.1 Photovoltaics

The term "photovoltaic" is derived from the Greek word $\phi\omega\varsigma$ ("phōs") which translates to light and "volt", the unit of electrical voltage,[a] and describes the conversion of photon energy into electrical power. Solar cells exploit the photovoltaic effect in a semiconducting material to convert incident sunlight into electrical power. Thin-film solar cells such as perovskite devices often use a *p–i–n* architecture, which is described in the following.

2.1.1 Working Principle of *p–i–n* Perovskite Solar Cells

Inverted *p–i–n* perovskite solar cells (PSCs) are particularly attractive for two-terminal (2T) tandem integration due to their low-temperature processing, reduced hysteresis, and compatibility with silicon bottom cells.[45,46] The architecture enables deposition of the perovskite top cell on temperature- and process-sensitive substrates while offering improved interfacial stability and simplified recombination junction design. In contrast, conventional *n–i–p* architectures typically rely on organic hole-selective contacts such as spiro-OMeTAD[b] or PTAA[c], which can introduce parasitic absorption, require additional oxidation or doping steps, and exhibit limited environmental stability when exposed to illumination.[47–53] These drawbacks become particularly critical in tandem configurations where the hole transport layer is located on the illuminated side of the device. As a result, *p–i–n* PSC architectures have emerged as a leading platform for high-efficiency and scalable tandem photovoltaic technologies.

The working principle of a *p–i–n* solar cell is based on a vertically stacked device architecture consisting of a transparent front electrode, a hole-selective contact (hole transport layer (HTL), *p*-type), an intrinsic light-absorbing layer (*i*-layer), an electron-selective contact (electron transport layer (ETL), *n*-type), and a rear electrode. In perovskite solar cells, the intrinsic absorber is typically a weakly doped or nominally intrinsic hybrid metal halide perovskite, while the transport layers provide selective charge extraction and define the internal electric fields through their work functions and energy-level alignment.[45] This architecture decouples light absorption from charge transport and enables efficient carrier collection even for relatively thick absorber layers. Since the space-charge region in *p–i–n* perovskite solar cells is often small compared to the thickness of the intrinsic absorber, only a limited fraction of the perovskite layer experiences a built-in electric field. As a result, these devices can often be approximated as flatband solar cells.[54,55]

[a] Named in honor of the Italian physicist Alessandro Volta, the inventor of the electric battery.
[b] spiro-OMeTAD: 2,2',7,7'-tetrakis[N,N-di(4-methoxyphenyl)amino]-9,9'-spirobifluorene
[c] PTAA: poly[bis(4-phenyl)(2,4,6-trimethylphenyl)amine]

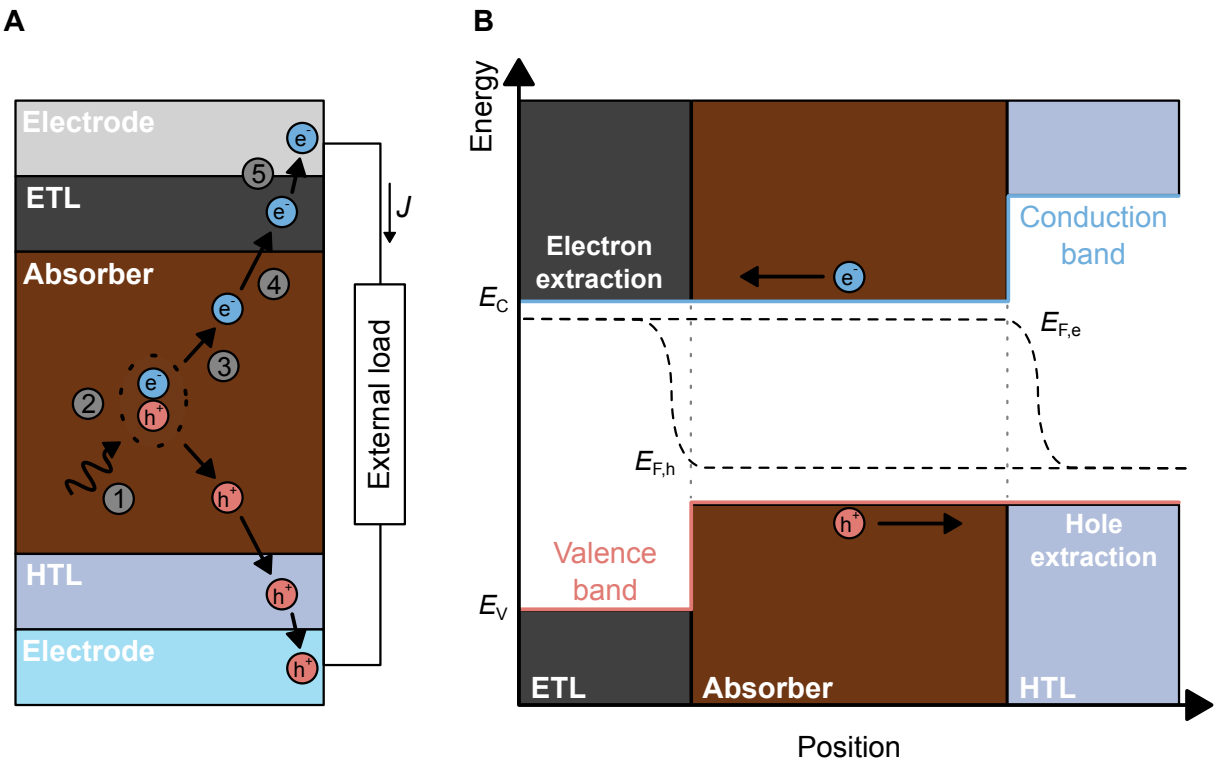

Figure 2.1: **A** Schematic illustration of the working principle of a *p–i–n* solar cell architecture. Incident photons are absorbed in the intrinsic perovskite layer (1), generating electron–hole pairs (2) that rapidly dissociate into free charge carriers (3). Electrons and holes diffuse toward the ETL and HTL, respectively (4). Selective extraction at the contacts enables current flow through the external circuit under load (5). Steps (3)-(5) are equivalent for the hole extraction process. **B** Corresponding energy-band diagram under illumination, showing band alignment between ETL, absorber, and HTL. The splitting of the electron and hole quasi-Fermi levels ($E_{\mathrm{F,n}}$ and $E_{\mathrm{F,p}}$) within the absorber determines the maximum achievable open-circuit voltage, while spatial gradients of the quasi-Fermi levels drive charge extraction. Favorable conduction- and valence-band alignment enables efficient electron and hole extraction while suppressing interfacial recombination. ETL: electron transport layer, HTL: hole transport layer

The corresponding device architecture and the processes from absorption of an incident photon to charge extraction at the electrodes are depicted in **Figure 2.1 A**. Upon illumination (1), photons with energies exceeding the semiconductor bandgap are absorbed in the intrinsic absorber layer, generating electron–hole pairs (2). Photons with energies below the bandgap are transmitted, while photons with energies higher than the bandgap dissipate the excess energy through thermalization. The photogenerated charge carriers rapidly dissociate into free electrons and holes (3) at room temperature.[d] Charge carrier separation is governed by diffusion and local electric fields arising from the asymmetric energy-level alignment at the *p*-

[d] It is noted that the existence of excitons in perovskite solar cells and their contribution to charge carrier dynamics is a highly debated topic. Exciton contribution cannot be generalized as it depends on the perovskite composition and structure (*e.g.* 2D perovskites *vs.* 3D perovskites).[56–58]

and *n*-type contacts. Photogenerated electrons are transported toward the ETL, while holes are transported toward the HTL due to charge carrier diffusion, resulting in spatial charge separation across the absorber thickness. Efficient separation requires sufficiently long carrier lifetimes and diffusion lengths.

Charge extraction occurs at the selective contacts, where transport layers block the minority charge carriers and suppress interfacial recombination. Electrons are extracted through the ETL into the rear electrode, while holes are extracted through the HTL into the front electrode (5), enabling current flow through the external circuit under load. The selectivity of the transport layers for the respective charge carriers is crucial for minimizing non-radiative recombination losses and maintaining a high open-circuit voltage (V_{OC}). In the ideal case, the interfaces exhibit favorable band alignment and a low density of defect states, enabling efficient carrier extraction without additional recombination losses.

In an energy-band picture depicted in **Figure 2.1 B**, electron extraction in a *p–i–n* device is determined by the relative alignment between the absorber conduction band (CB; with energy E_{C}) minimum and the CB or lowest unoccupied molecular orbital (LUMO) of the ETL. Under illumination, the electron and hole quasi-Fermi levels split within the absorber, with the electron quasi-Fermi level ($E_{\mathrm{F,n}}$) shifting toward the CB and the hole quasi-Fermi level ($E_{\mathrm{F,p}}$) toward the valence band (VB; with energy E_{V}). Here, the absorber is driven out of equilibrium by the continuous generation of excess electrons and holes, which leads to the formation of separate quasi-Fermi levels for the two carrier populations which are then extracted at different potentials. The maximum achievable open-circuit voltage (V_{OC}) is given by the difference between these quasi-Fermi levels at the selective contacts. At short circuit (I_{SC}), photogenerated charge carriers are extracted efficiently, resulting in maximum current and only small quasi-Fermi level splitting (QFLS). At V_{OC}, carrier extraction is blocked in the external circuit, so carriers accumulate until recombination balances generation, giving the maximum QFLS. Between these two limits, the device operates with both finite current and finite voltage, reflecting the balance between carrier extraction and recombination. Efficient electron extraction requires that the ETL conduction band lies energetically below or close to the perovskite conduction band, enabling efficient interfacial electron transfer, which can be described within the framework of Marcus theory according to Lee *et al.*[59] Analogously, the HTL valence band must align favorably with the perovskite valence band to enable efficient hole extraction (equivalent to electron injection). The magnitude of the QFLS, which is limited by radiative and non-radiative recombination processes, directly determines the maximum achievable device voltage and thus links microscopic carrier energetics to macroscopic photovoltaic performance.

2.1.2 Electrical Representation and Photovoltaic Metrics

The electrical behavior of a *p–i–n* solar cell under illumination can be described on two complementary levels. First, on a macroscopic level, by an equivalent-circuit model that reproduces the measured current–voltage (*I–V*) characteristics, and second, on a microscopic level in terms of charge-carrier transport and recombination within the device stack. The derivation and interpretation below follow the physical picture laid out by P. Würfel and U. Würfel *et al.*[60,61]

Factors driving charge carrier dynamics

In steady state, electrical current originates from the directed motion of electrons and holes under the action of two forces which are an electrical force associated with the electrostatic potential $\phi(\mathbf{r})$ and a chemical force associated with spatial gradients in the carrier concentration. The electric field is defined as

$$\mathbf{E}(\mathbf{r}) = -\nabla\phi(\mathbf{r}).$$

For each carrier species $k \in \{n, p\}$ (electrons n and holes p), the total current density $\mathbf{J}_k$ is decomposed into a field-driven (drift) contribution $\mathbf{j}_{f,k}$ and a concentration-driven (diffusion) contribution $\mathbf{j}_{d,k}$,

$$\mathbf{J}_k = \mathbf{j}_{f,k} + \mathbf{j}_{d,k}. \tag{2.1}$$

Electrical force (field-driven drift current). The electrical potential energy of a carrier is $z_k q\phi$, where q is the elementary charge ($q > 0$) and z_k is the carrier charge number ($z_n = -1$ for electrons and $z_p = +1$ for holes). The corresponding driving force is proportional to $-\nabla(z_k q\phi)$. In linear response, the drift current density can be written as

$$\mathbf{j}_{f,k} = \sigma_k \mathbf{E} = -\frac{\sigma_k}{z_k q}\nabla(z_k q\phi)\,, \tag{2.2}$$

where σ_k is the conductivity of carrier type k. In the drift–diffusion model,

$$\sigma_n = qn\mu_n, \qquad \sigma_p = qp\mu_p,$$

with n and p the electron and hole concentrations (number densities), and μ_n and μ_p the electron and hole mobilities.

Chemical force (concentration-driven diffusion current). Carrier diffusion arises because random thermal motion leads to a net particle flux from regions of high to low concentration. The particle flux $\mathbf{\Phi}_k$ follows Fick's law,

$$\mathbf{\Phi}_k = -D_k \nabla n_k,$$

where n_k denotes the carrier concentration of species k ($n_n \equiv n$, $n_p \equiv p$) and D_k is the diffusion coefficient. Multiplying by the carrier charge $z_k q$ yields the diffusion current density

$$\mathbf{j}_{d,k} = z_k q\, \mathbf{\Phi}_k = z_k q\,(-D_k \nabla n_k)\,. \tag{2.3}$$

Equivalently, diffusion can be written as a response to the gradient of the carrier chemical potential $\Phi_{\mathrm{chem},k}$,

$$\mathbf{j}_{d,k} = -\frac{\sigma_k}{z_k q}\nabla\Phi_{\mathrm{chem},k}. \tag{2.4}$$

For non-degenerate (Maxwell-Boltzmann) statistics at temperature T, one may write

$$\Phi_{\mathrm{chem},n} \approx k_{\mathrm{B}}T \ln\!\left(\frac{n}{N_C}\right), \qquad \Phi_{\mathrm{chem},p} \approx k_{\mathrm{B}}T \ln\!\left(\frac{p}{N_V}\right),$$

where k_{B} is the Boltzmann constant, and N_C and N_V are the effective densities of states of the conduction and valence band, respectively. Hence, $\nabla\Phi_{\mathrm{chem},k}$ is directly linked (for constant N_C, N_V) to ∇n or ∇p. The diffusion coefficient and mobility are described by Einstein's relation,

$$D_k = \mu_k \frac{k_{\mathrm{B}}T}{q} \qquad (k \in \{n, p\}). \tag{2.5}$$

Electrochemical potential and quasi-Fermi levels. Since charge carriers are exposed to both electrical and chemical forces simultaneously, it is useful to combine both driving potentials into a single quantity, the electrochemical potential

$$\eta_k \;=\; z_k q\phi + \Phi_{\mathrm{chem},k}. \tag{2.6}$$

Adding Eqs. (2.2) and (2.4) and using Eq. (2.6) yields a compact expression for the total current density,

$$\mathbf{J}_k = -\frac{\sigma_k}{z_k q}\,\nabla\eta_k. \tag{2.7}$$

Under steady-state illumination, electrons and holes are generally not in mutual equilibrium and are therefore described by two quasi-Fermi levels $E_{\mathrm{F,n}}$ and $E_{\mathrm{F,p}}$. In this case, the electrochemical potentials are

$$\eta_{\mathrm{n}} = E_{\mathrm{F,n}}, \tag{2.8}$$

$$\eta_{\mathrm{p}} = -E_{\mathrm{F,p}}, \tag{2.9}$$

so that Eq. (2.7) becomes

$$\mathbf{J}_{\mathrm{n}} = \frac{\sigma_{\mathrm{n}}}{q}\,\nabla E_{\mathrm{F,n}}, \tag{2.10}$$

$$\mathbf{J}_{\mathrm{p}} = \frac{\sigma_{\mathrm{p}}}{q}\,\nabla E_{\mathrm{F,p}}. \tag{2.11}$$

Equations (2.10)–(2.11) emphasize that carrier transport is fundamentally governed by gradients of the quasi-Fermi levels (electrochemical potentials), rather than by the electric field alone. Selective extraction in a *p–i–n* heterojunction therefore requires strongly asymmetric conductivities for the two carrier types in the contact regions: near the ETL, σ_{n} must be large while σ_{p} must be small, and *vice versa* near the HTL.

Connection to the drift-diffusion expressions. Inserting $\sigma_{\mathrm{n}} = qn\mu_{\mathrm{n}}$, $\sigma_{\mathrm{p}} = qp\mu_{\mathrm{p}}$, $\mathbf{E} = -\nabla\phi$, and using Einstein's relation (Eq. (2.5)) yields the drift–diffusion form of the carrier current densities,

$$\mathbf{J}_{\mathrm{n}} = qn\mu_{\mathrm{n}}\mathbf{E} + qD_{\mathrm{n}}\nabla \mathrm{n}, \tag{2.12}$$

$$\mathbf{J}_{\mathrm{p}} = qp\mu_{\mathrm{p}}\mathbf{E} - qD_{\mathrm{p}}\nabla \mathrm{p}. \tag{2.13}$$

Role of diffusion and collection. Diffusion is particularly relevant in weakly doped (nominally intrinsic) absorbers because illumination generates spatial gradients in $n(x)$ and $p(x)$, which drive diffusion currents toward both contacts. Whether this diffusive flux contributes to useful photocurrent or to parasitic recombination depends on contact selectivity. If minority-carrier transport is not sufficiently suppressed at a contact, carriers can diffuse to the "wrong" electrode and recombine, resulting in non-radiative recombination, reducing V_{OC}. The diffusion length

$$L_k = \sqrt{D_k \tau_k} \qquad (k \in \{\mathrm{n}, \mathrm{p}\}), \tag{2.14}$$

describes the distance a charge carrier diffuses before recombination, where τ_k is the effective carrier lifetime. If L_k exceeds the absorber thickness, diffusion-assisted collection remains efficient even for modest internal electric fields. If L_k is reduced (*e.g.*, by enhanced non-radiative recombination), collection losses increase and both I_{SC} and V_{OC} can degrade.

One-diode model and photovoltaic metrics

Equivalent circuits provide a compact macroscopic description of the *I–V* characteristics of a solar cell and can be directly connected to the microscopic picture of generation and recombination in the absorber. For better comparability between devices with different active area A, the current density $J = I/A$ is often used. In the following, expressions are written for the terminal current I. The steady-state current i in the absorber of thickness d can be written as the spatial integral of the net generation rate,

$$i \;=\; \int_0^d q\,[G(x) - R(x)]\,\mathrm{d}x, \tag{2.15}$$

where $G(x)$ is the local generation rate of electron–hole pairs, and $R(x)$ is the local recombination rate. Under illumination, recombination increases compared to equilibrium (dark) due to the enhanced carrier concentrations. In the quasi-equilibrium description this increase is governed by the quasi-Fermi level splitting. The recombination rate can be written as $R(x) = R_{\mathrm{dark}}\,\exp[(E_{\mathrm{F,n}}(x) - E_{\mathrm{F,p}}(x))/(k_{\mathrm{B}}T)]$. With the equilibrium condition $G_{\mathrm{dark}} = R_{\mathrm{dark}}$ and by identifying the quasi-Fermi level splitting between the selective contacts with the terminal voltage ($E_{\mathrm{F,n}} - E_{\mathrm{F,p}} = qV$), this leads to the characteristic illuminated current–voltage relation of an ideal solar cell,

$$I(V) \;=\; I_0\left[\exp\left(\frac{qV}{k_{\mathrm{B}}T}\right) - 1\right] \;-\; I_{\mathrm{SC}}, \tag{2.16}$$

where I_{SC} is the short-circuit current and I_0 is the dark saturation current. Equation (2.16) is formally identical to the Shockley diode equation with an additional photocurrent term. This motivates the equivalent-circuit representation of an ideal solar cell as a current source in parallel with a diode.

Single-diode equivalent circuit

Real devices exhibit non-ideal properties for which the ideal circuit is extended by a series resistance R_{s} and a shunt resistance R_{sh}, resulting in the single-diode model as depicted in **Figure 2.2 A**.

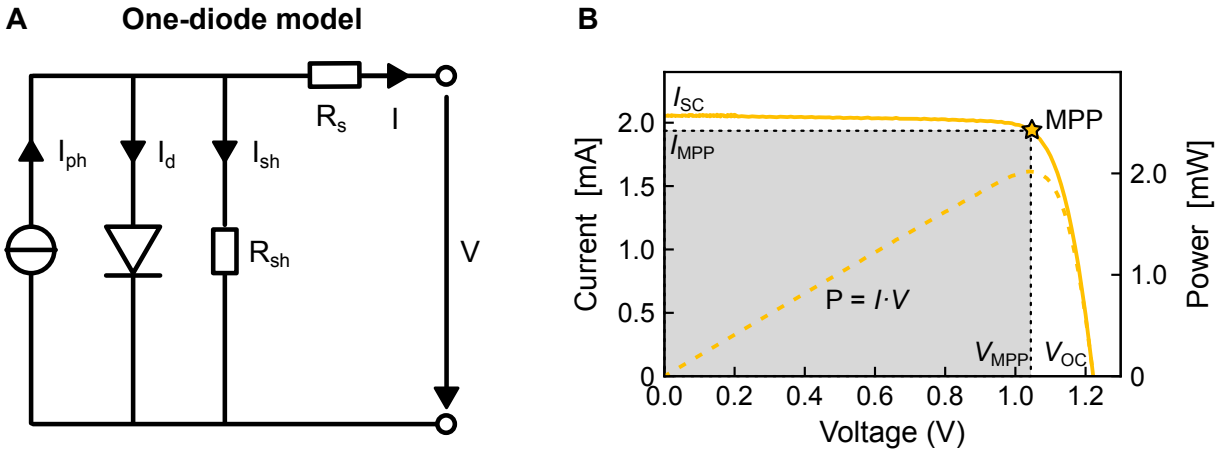

Figure 2.2: A Equivalent one-diode circuit model of a solar cell, consisting of a photogenerated current source (I_{ph}), a diode representing recombination losses, a series resistance (R_{s}), and a shunt resistance (R_{sh}). **B** Representative current–voltage (I–V) curve under illumination, illustrating the definitions of the short-circuit current I_{SC}, open-circuit voltage V_{OC}, maximum power point (MPP), fill factor (FF), and the extracted electrical power $P = I \cdot V$.

The current source represents the photogenerated current I_{ph} (proportional to the absorbed photon flux and collection efficiency), the diode current (I_{d}) represents recombination losses (radiative in the ideal case), R_{s} summarizes ohmic losses along the current path (finite conductivities of absorber, transport layers, electrodes, and contact resistances), and R_{sh} accounts for parasitic leakage paths that bypass the diode (*e.g.*, pinholes, imperfect interfaces, edge shunts). The output current can be written as

$$I \;=\; I_{\mathrm{ph}} - I_{\mathrm{d}} - I_{\mathrm{sh}}, \tag{2.17}$$

where I_{sh} is the shunt current.

Using the diode equation and including the voltage drop across the series resistance (note that the exact sign convention depends on the definitions of positive current and voltage), the single-diode equation can be written as

$$I(V) \;=\; I_{\mathrm{ph}} - I_0\left[\exp\!\left(\frac{q\,(V - IR_{\mathrm{s}})}{n_{\mathrm{id}}\,k_{\mathrm{B}}T}\right) - 1\right] - \frac{V + IR_{\mathrm{s}}}{R_{\mathrm{sh}}}, \tag{2.18}$$

where I_0 is the dark saturation current, n_{id} is the diode ideality factor and V is the applied terminal voltage.

Physical interpretation of I_0, n_{id}, R_{s}, and R_{sh} Microscopically, the parameter I_0 quantifies how strongly recombination increases under forward bias. A larger I_0 corresponds to stronger recombination (bulk and/or interfacial), which reduces the attainable quasi-Fermi level splitting and therefore lowers V_{OC}. In the ideal radiative case, the diode current represents radiative recombination losses. In real devices, additional non-radiative pathways can be represented by extending the circuit (*e.g.*, an additional diode term in parallel) or, in a simplified treatment, by an effective ideality factor n_{id}. The series resistance R_{s} captures ohmic voltage losses. At finite current, part of the externally measured voltage drops across R_{s}, reducing the voltage available across the recombination diode and thus lowering the fill factor. The shunt resistance R_{sh} introduces a leakage channel that becomes particularly detrimental near short-circuit, where it reduces the extracted current.

Short-circuit current and open-circuit voltage

A representative *I–V* curve is depicted in **Figure 2.2 B** and the corresponding figures of merit are discussed in the following. The short-circuit current is defined at $V = 0$,

$$I_{\mathrm{SC}} = I(V = 0), \tag{2.19}$$

and for $R_{\mathrm{s}} \to 0$ and $R_{\mathrm{sh}} \to \infty$ one obtains $I_{\mathrm{SC}} \approx I_{\mathrm{ph}}$. The open-circuit voltage is defined by $I(V_{\mathrm{OC}}) = 0$. In the ideal limit ($R_{\mathrm{s}} \to 0$, $R_{\mathrm{sh}} \to \infty$), Eq. (2.18) reduces to

$$I(V) = I_{\mathrm{ph}} - I_0 \left[\exp\left(\frac{qV}{n_{\mathrm{id}} k_{\mathrm{B}} T} \right) - 1 \right], \tag{2.20}$$

and the open-circuit voltage is obtained as

$$V_{\mathrm{OC}} \;=\; \frac{n_{\mathrm{id}} k_{\mathrm{B}} T}{q} \, \ln\left(\frac{I_{\mathrm{ph}}}{I_0} + 1 \right). \tag{2.21}$$

In the quasi-Fermi level picture, the externally measured voltage corresponds to the difference in electrochemical potentials between the selective contacts,

$$qV \;=\; E_{\mathrm{F,n}}\big|_{\text{electron contact}} \;-\; E_{\mathrm{F,p}}\big|_{\text{hole contact}}, \tag{2.22}$$

and at open circuit this quasi-Fermi level splitting is maximal.

Maximum power point, fill factor, and efficiency The electrical output power is

$$P(V) \;=\; I(V)\, V. \tag{2.23}$$

The maximum power point (MPP) is defined by the operating point $(V_{\mathrm{MPP}}, I_{\mathrm{MPP}})$ that maximizes P, such that

$$P_{\mathrm{MPP}} \;=\; I_{\mathrm{MPP}} V_{\mathrm{MPP}}. \tag{2.24}$$

The fill factor (FF) is defined as the ratio between the maximum extractable power and the product $I_{\mathrm{SC}}V_{\mathrm{OC}}$,

$$\mathrm{FF} \;=\; \frac{I_{\mathrm{MPP}}V_{\mathrm{MPP}}}{I_{\mathrm{SC}}V_{\mathrm{OC}}} \;=\; \frac{J_{\mathrm{MPP}}V_{\mathrm{MPP}}}{J_{\mathrm{SC}}V_{\mathrm{OC}}}, \tag{2.25}$$

where $J_{\mathrm{SC}} = I_{\mathrm{SC}}/A$ and $J_{\mathrm{MPP}} = I_{\mathrm{MPP}}/A$. High R_{s} reduces FF by limiting current at high voltages (ohmic voltage losses), while low R_{sh} reduces FF by introducing leakage currents that distort the curve near short circuit. In *p–i–n* devices, insufficient contact selectivity can further reduce FF by enabling minority-carrier leakage and enhanced recombination under forward bias.

The power conversion efficiency (PCE) is defined as the maximum electrical power output divided by the incident optical power on the active area,

$$\mathrm{PCE} \;=\; \frac{P_{\mathrm{MPP}}}{P_{\mathrm{in}}} \;=\; \frac{J_{\mathrm{SC}}\,V_{\mathrm{OC}}\,\mathrm{FF}}{P_{\mathrm{in}}}, \tag{2.26}$$

where P_{in} is the incident optical power density. Under standard test conditions, the AM1.5G spectrum is used with an integrated power density of $P_{\mathrm{in}} = 1000\ \mathrm{W\,m^{-2}}$ (equivalently $100\ \mathrm{mW\,cm^{-2}}$). Together, J_{SC}, V_{OC}, and FF fully determine the PCE and therefore serve as the primary figures of merit for benchmarking perovskite solar cells.

2.1.3 Efficiency Limits and Recombination Mechanisms

The maximum achievable power conversion efficiency of a solar cell is fundamentally constrained by thermodynamic considerations, which are formalized in the detailed balance (DB) limit introduced by Shockley and Queisser[62] and later extended by Tiedje *et al.*[63] This limit defines a theoretical upper bound for an idealized single-junction photovoltaic device. It is derived by considering detailed balance between photon absorption from the solar spectrum and spontaneous photon emission from the solar cell under steady-state operation.

Within this framework, not all incident photon power can be converted into electrical power because a substantial fraction of the solar spectrum is either not absorbed or is irreversibly lost through fundamental loss mechanisms which are summarized in **Figure 2.3 A**. Photons with energies below the absorber bandgap are transmitted without contributing to photocurrent, while photons with energies exceeding the bandgap generate charge carriers that rapidly relax to the band edges, dissipating excess energy as heat through carrier thermalization. In addition, radiative recombination is unavoidable at open-circuit conditions and imposes a fundamental upper bound on the achievable open-circuit voltage, such that qV_{OC} is always smaller than the bandgap energy at finite temperature.

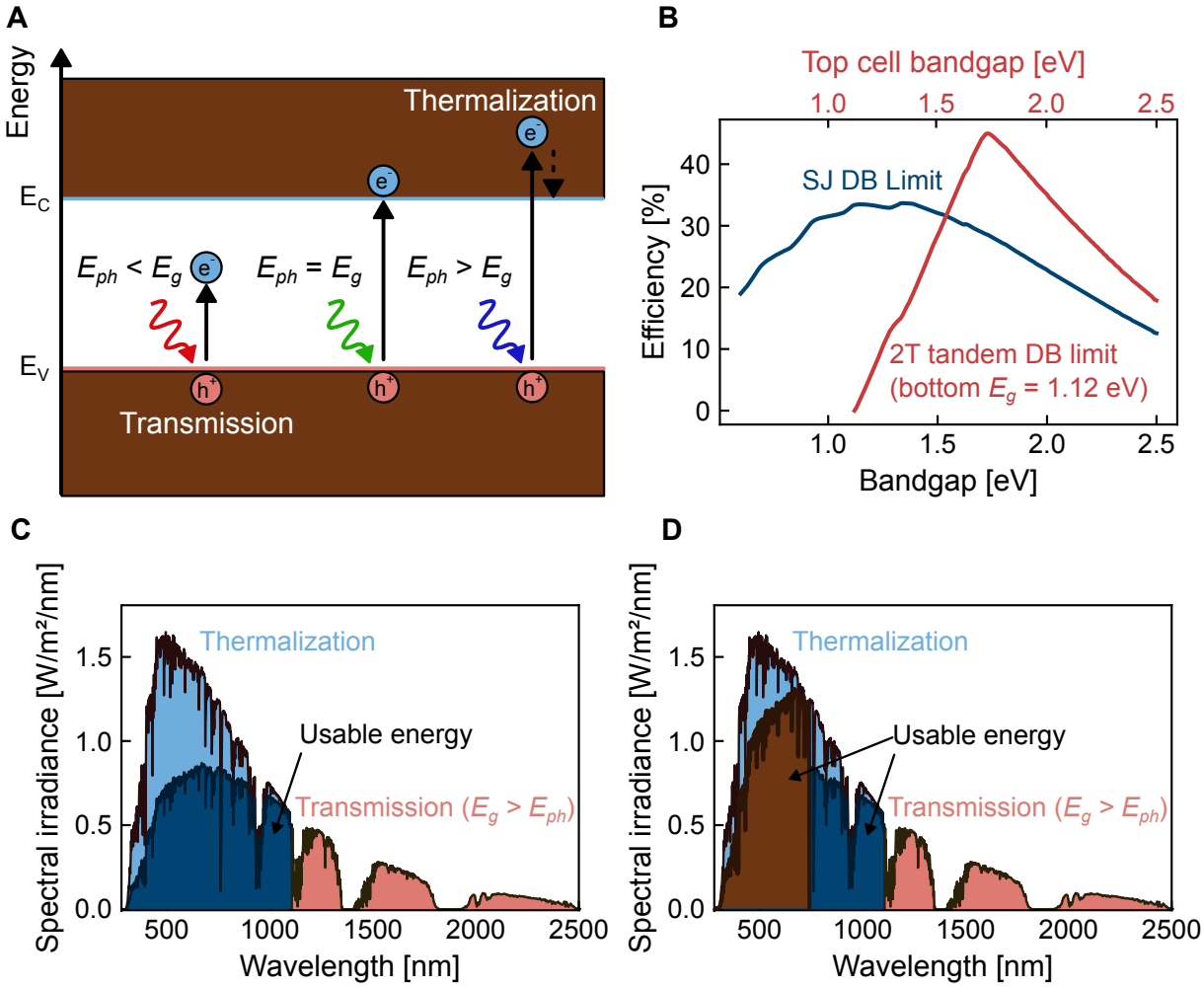

Figure 2.3: Illustration of the detailed-balance limit and the fundamental loss mechanisms that limit the efficiency of single-junction and tandem solar cells. (**A**) Schematic representation of spectral loss channels in an absorber with bandgap E_g: photons with energy $E_{\mathrm{ph}} < E_g$ are not absorbed and are transmitted, whereas photons with $E_{\mathrm{ph}} > E_g$ generate charge carriers that rapidly relax to the band edges, dissipating the excess energy as heat (thermalization). **B** Efficiency limit of single-junction (blue) and 2T tandem solar cells (red) – for a fixed bottom-cell bandgap of 1.12 eV – according to the detailed balance limit. **C/D** Illustration of usable energy from the AM1.5G spectrum[64] including thermalization and transmission losses for single-junction and tandem solar cells.

The detailed balance limit is derived under a set of idealized assumptions: First, the absorber is assumed to exhibit step-function absorption. Second, all photons with energies above the bandgap are absorbed with unit probability, while photons with energies below the bandgap are not absorbed at all, with no reflection or parasitic optical losses. Third, each absorbed photon is assumed to generate exactly one electron–hole pair, implying unity internal quantum efficiency and the absence of non-radiative recombination pathways. Fourth, all recombination is assumed to be purely radiative and in thermal

equilibrium with the surroundings, such that spontaneous emission follows blackbody radiation at the cell temperature. Lastly, charge-carrier extraction is assumed to be lossless, with no resistive losses, no transport limitations, and ideal selective contacts. In addition, the device is assumed to operate under non-concentrated sunlight at a fixed temperature, typically 300 K.

An important consequence of the detailed balance formalism is that voltage losses arise from both recombination and from entropy generation associated with photon emission into a much larger solid angle than that from which sunlight is absorbed. This entropic contribution ensures that even in the purely radiative limit, the open-circuit voltage remains below the bandgap energy. Any additional non-radiative recombination channels increase the dark saturation current and further reduce V_{OC} below the detailed balance limit, highlighting the critical role of material quality and defect suppression for high-efficiency devices.

In perovskite absorbers, recombination can proceed through three mechanisms: band-to-band (radiative) recombination, Shockley-Read-Hall (SRH) recombination, and Auger recombination.[65–67] Band-to-band recombination corresponds to the direct radiative recombination of electrons and holes and represents the fundamental loss channel already included in the detailed-balance limit. In contrast, SRH recombination is a non-radiative trap-assisted process mediated by defect states and is typically the dominant recombination pathway limiting the achievable efficiency of perovskite solar cells under 1-sun operation, because it reduces the QFLS and thereby lowers V_{OC}. Surface and interface recombination is a particularly critical origin of SRH recombination, because defects and undercoordinated atoms at the perovskite/contact interfaces often introduce trap states that accelerate non-radiative carrier loss and can therefore dominate the voltage deficit in practical devices.[67] Auger recombination involves a three-particle interaction in which the recombination energy of an electron-hole pair is transferred to a third carrier rather than emitted as a photon. This process becomes relevant mainly at high carrier densities, for example under concentrated illumination or in highly excited regions, and is therefore less important than SRH recombination for standard photovoltaic operating conditions. Consequently, the efficiency of practical perovskite solar cells is limited by the competition between radiative recombination and parasitic SRH recombination, while Auger recombination generally represents a secondary loss channel under normal device operation.

Balancing spectral transmission losses, thermalization losses, and radiative recombination leads to a maximum efficiency of approximately 33% for an ideal single-junction solar cell with an optimal bandgap of around 1.1 eV under standard solar illumination (**Figure 2.3 B**).[62,63] Transmission and thermalization losses within the detailed balance framework further clarify why multi-junction solar cells provide a viable route to surpass the efficiency limit of single-junction devices (**Figure 2.3 C/D**). By combining absorbers with different bandgaps in a stacked architecture (as depicted in **Figure 2.4**), sub-bandgap transmission losses and above-bandgap thermalization losses can be substantially reduced, allowing more efficient use of the solar power and higher overall PCEs. Achieving this requires material systems with precisely adjustable bandgaps and high radiative efficiency across a wide compositional range. In this context, metal halide perovskites have emerged as a particularly promising material class, as their bandgaps can be continuously tuned over a broad energy range while retaining favorable optoelectronic properties.[68]

The structural, electronic, and compositional versatility of perovskite materials, which underscore their suitability for tandem and multi-junction photovoltaics, is discussed in detail in the following section.

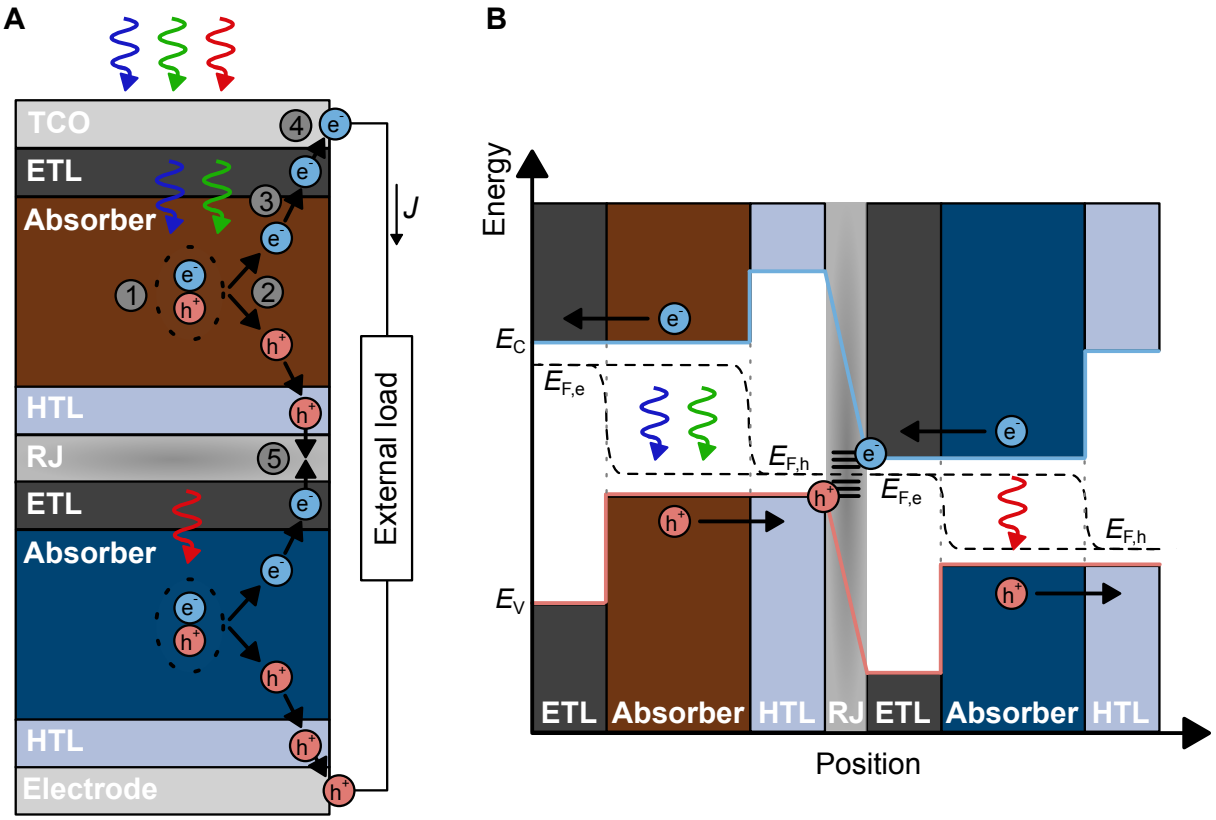

Figure 2.4: Working principle of a monolithic two-terminal perovskite tandem solar cell with an interconnecting RJ. **A** Schematic device stack (TCO/ETL/WBG absorber/HTL/RJ/ETL/NBG absorber/HTL/electrode) illustrating the sequence from photon absorption to current extraction. Incident photons of higher energy are absorbed in the top and bottom absorbers, generating electron-hole pairs (1), carriers separate (2) and are transported toward the selective contacts (3-4). Holes from the top sub-cell and electrons from the bottom sub-cell recombine in the RJ (5), enabling series connection of both sub-cells. **B** Corresponding simplified energy-band diagram (conduction band edge E_C, valence band edge E_V) showing selective energy-level alignment for electron and hole extraction at ETL/absorber and absorber/HTL interfaces, the quasi-Fermi levels for electrons ($E_{F,n}$) and holes ($E_{F,p}$) in each absorber under illumination, and their connection across the RJ. The tandem output voltage is given by the sum of the quasi-Fermi level splittings of the two sub-cells, while the current is limited by the series-connected photocurrent. Modified from Ko *et al.*[69] RJ: Recombination junction, WBG: wide-bandgap, NBG: narrow-bandgap, TCO: transparent conductive oxide, ETL: electron transport layer, HTL: hole transport layer, QFLS: quasi-Fermi level splitting

2.2 Hybrid Organic-Inorganic Metal Halide Perovskites

Hybrid organic-inorganic metal halide perovskites constitute a versatile class of semiconductors that have emerged as leading absorber materials for next-generation thin-film photovoltaics. Their unprecedented rise in PCE has been enabled by a unique combination of strong optical absorption, long charge-carrier diffusion lengths, and broad compositional tunability even as a polycrystalline thin film.[23,70] Structurally, these materials adopt the general ABX_3 perovskite composition.[e] The optoelectronic properties and operational stability of perovskite solar cells are interlinked with the crystal structure and phase stability of the perovskite absorber which are discussed in the following section.

2.2.1 Crystal Structure and Polymorphism

Hybrid metal halide perovskites crystallize in the ABX_3 structure, where the A-site is occupied by a monovalent organic or inorganic cation (*e.g.*, formamidinium (FA^+), methylammonium (MA^+), Cs^+), the B-site by a divalent metal cation (typically Pb^{2+} or Sn^{2+}), and the X-site by halide anions (*e.g.* I^-, Br^-, Cl^-).

A widely used geometric descriptor to assess the structural stability of the cubic perovskite lattice is the Goldschmidt tolerance factor t, which relates the ionic radii of the constituent ions according to

$$t = \frac{r_\mathrm{A} + r_\mathrm{X}}{\sqrt{2}\,(r_\mathrm{B} + r_\mathrm{X})},$$

where r_A, r_B, and r_X denote the effective ionic radii of the A-site cation, B-site cation, and halide anion, respectively.[72] For ideal cubic perovskites, t is close to unity, while stable three-dimensional perovskite structures are typically observed for $0.8 < t < 1.0$.[73–76] Deviations from this range favor octahedral tilting or alternative lower-dimensional polymorphs.

Optical and electronic properties are largely determined by the adopted crystal structure.[77] The photoactive perovskite polymorph corresponds to the three-dimensional corner-sharing coordination network of BX_6 octahedra, commonly referred to as the perovskite α-phase (**Figure 2.5 A/B**). In formamidinium-based lead iodide perovskites, this phase adopts a cubic or slightly distorted tetragonal symmetry and exhibits a direct bandgap that is well suited for photovoltaic applications. In contrast, the photoinactive δ-phase (**Figure 2.5 C-E**) represents a non-perovskite polymorph, involving face-sharing or edge-sharing BX_6 units. This structural rearrangement results in a substantially wider bandgap and inferior charge-transport properties, rendering the δ-phase optically and electronically unsuitable for solar cell operation. The transformation from the α-phase to the δ-phase is therefore highly detrimental to device performance and is therefore closely associated with degradation processes in PSCs. The relative stability of the α- and δ-phases is determined by a combination of thermodynamic and kinetic factors, including temperature,

[e] This composition is derived from the $CaTiO_3$ structure which was first identified by Gustav Rose and named after the Russian mineralogist Lev Perovski.[71]

lattice strain, and the size and dynamics of the A-site cation.[78–80] At room temperature, the photoactive α-phase of $FAPbI_3$ is metastable[81] and tends to transform into the δ-phase unless stabilized through compositional engineering. Partial substitution of FA^+ with smaller cations such as Cs^+ or MA^+, as well as halide alloying with Br^- or Cl^-, have been shown to suppress the formation of the non-perovskite phase by tuning the effective tolerance factor and increasing lattice stability.[40,75,76,82]

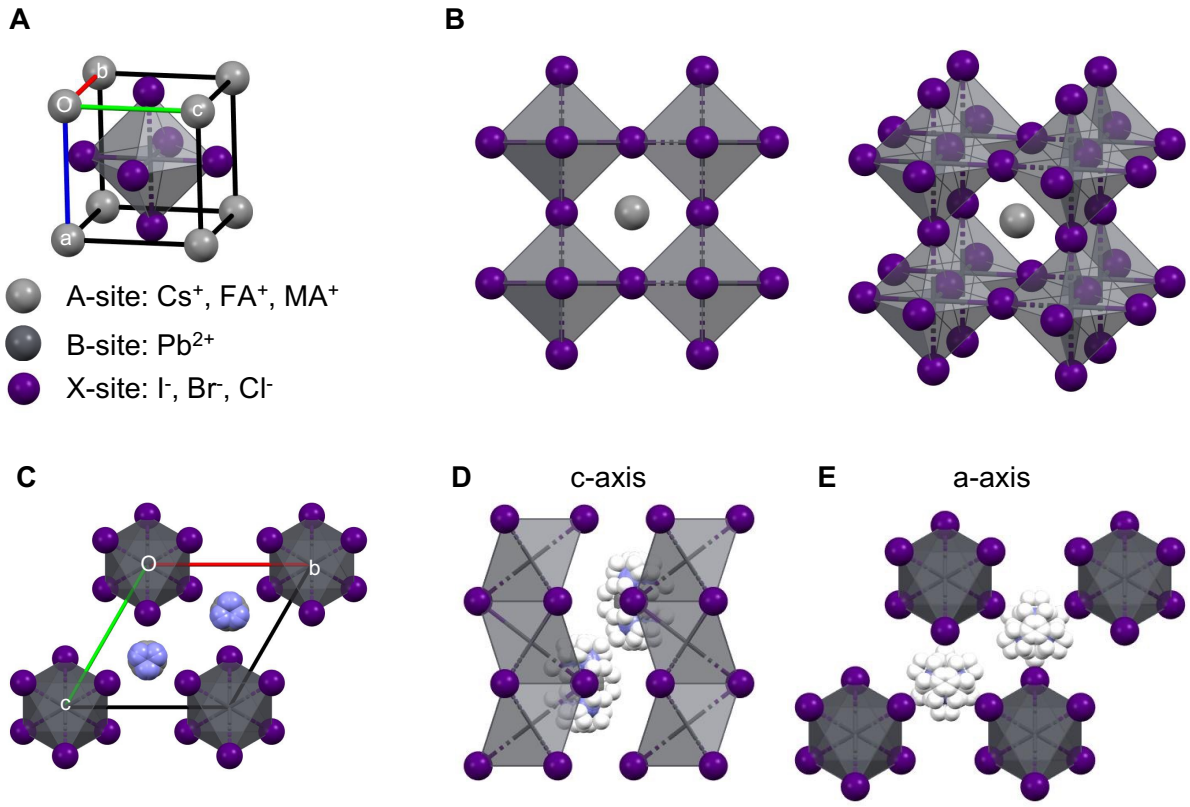

Figure 2.5: Crystal structure and polymorphism of hybrid metal halide perovskites. **A** Idealized α-phase ABX_3 perovskite unit cell. **B** Corner-sharing BX_6 octahedral network forming the three-dimensional photoactive perovskite α-phase. **C** Non-perovskite δ-phase (for $FAPbI_3$) characterized by face- or edge-sharing octahedra. **D,E** Structural views along the *c*- and *a*-axes, respectively, illustrating the different octahedral connectivity and A-site cation arrangement in the perovskite lattice.

2.2.2 Electronic and Optical Properties

Hybrid organic–inorganic lead halide perovskites exhibit exceptionally high optical absorption coefficients ($\alpha \sim 10^4$ –10^5 cm^{-1}) already close to the band edge, such that absorber thicknesses of only a few hundred nanometers are sufficient for near-complete absorption of above-bandgap photons.[83,84] Importantly, the absorption onset in metal halide perovskites is often strongly shaped by excitonic effects. Excitons can provide a pronounced enhancement of the oscillator strength near the bandgap and are therefore a key

microscopic origin of the very large optical absorption coefficient observed close to the absorption edge.[56] The magnitude of this excitonic enhancement depends on the exciton binding energy E_b and on Coulomb screening, which in lead-halide perovskites involves both electronic and lattice (phonon) contributions.[56]

The exciton binding energies of 3D lead halide perovskites are typically in the range of a few to several tens of meV at room temperature, although reported values depend on composition, crystal phase, and the frequency-dependent dielectric screening.[56–58] A useful trend for tandem-relevant WBG compositions is that excitonic resonances generally become more pronounced with wider bandgaps, because reduced electronic polarizability weakens Coulomb screening and strengthens the electron–hole interaction. Under typical solar-cell operating conditions, the majority of photoexcitations in 3D perovskites are free carriers rather than bound excitons, which can be rationalized by treating exciton formation $e + h \rightleftharpoons X$ as a chemical equilibrium (Saha picture): at the low injection levels relevant for 1 sun operation (photoexcited pair densities on the order of 10^{13}–$10^{14}\ \mathrm{cm}^{-3}$), the equilibrium fraction of excitons is predicted to be very small in 3D iodide- and bromide-based perovskites. Consequently, photogeneration readily yields mobile electrons and holes, enabling efficient charge collection without requiring strong internal electric fields.

Charge transport in hybrid perovskites is characterized by long carrier lifetimes and diffusion lengths, often exceeding hundreds of nanoseconds and several micrometers, respectively.[85,86] These properties are attributed to low densities of deep non-radiative defects and to strong dielectric screening, which mitigates Coulombic interactions between charge carriers and charged defects.[77,87–91] While free carriers dominate the carrier population in 3D perovskites under operating conditions, excitons can still play a disproportionate role in optical processes. They contribute strongly to band-edge absorption and can dominate luminescence even when they are a minority species.[56] Together, the tunable bandgap, strong optical absorption, predominantly free-carrier photogeneration at device-relevant injection levels, and favorable charge-transport characteristics position hybrid lead-halide perovskites as a uniquely versatile absorber class for high-efficiency single-junction and tandem photovoltaic devices.

2.2.3 Bandgap Engineering

The electronic structure of hybrid metal halide perovskites can be rationalized within a molecular orbital picture that links the atomic orbitals of the constituent ions to the formation of the valence and conduction bands. In the photoactive α-phase, hybridization within the corner-sharing BX_6 octahedral framework leads to band edges that are predominantly derived from the inorganic sublattice.[92,93] Photoemission and inverse photoemission measurements combined with DFT show that the valence band maximum (VBM) is dominated by halide p states (I $5p$ or Br $4p$), with smaller contributions from Pb $6s$/$6p$ states, while the conduction band minimum (CBM) is dominated by Pb $6p$ states with only minor halide contributions.[94]

In this picture, the VBM is primarily associated with antibonding interactions between halide p orbitals (X_p) and the metal s orbital states (M_s), whereas the CBM is largely formed by antibonding metal p states (M_p) with smaller contributions from halide states (often X_s).[93] Consequently, the fundamental bandgap is mainly determined by the energetic separation between the halide p dominated VBM and the metal p

dominated CBM. In addition to these bonding and antibonding states, defects can introduce trap states within the band structure. In lead halide perovskites, the antibonding character of the VBM is commonly associated with defect-mediated shallow trap states forming close to the band edges or being resonant with the bands, rather than deep within the gap.[92] While such defects can contribute to non-radiative recombination, dielectric screening in perovskites can reduce their capture cross sections, limiting their impact in high-quality films.[92]

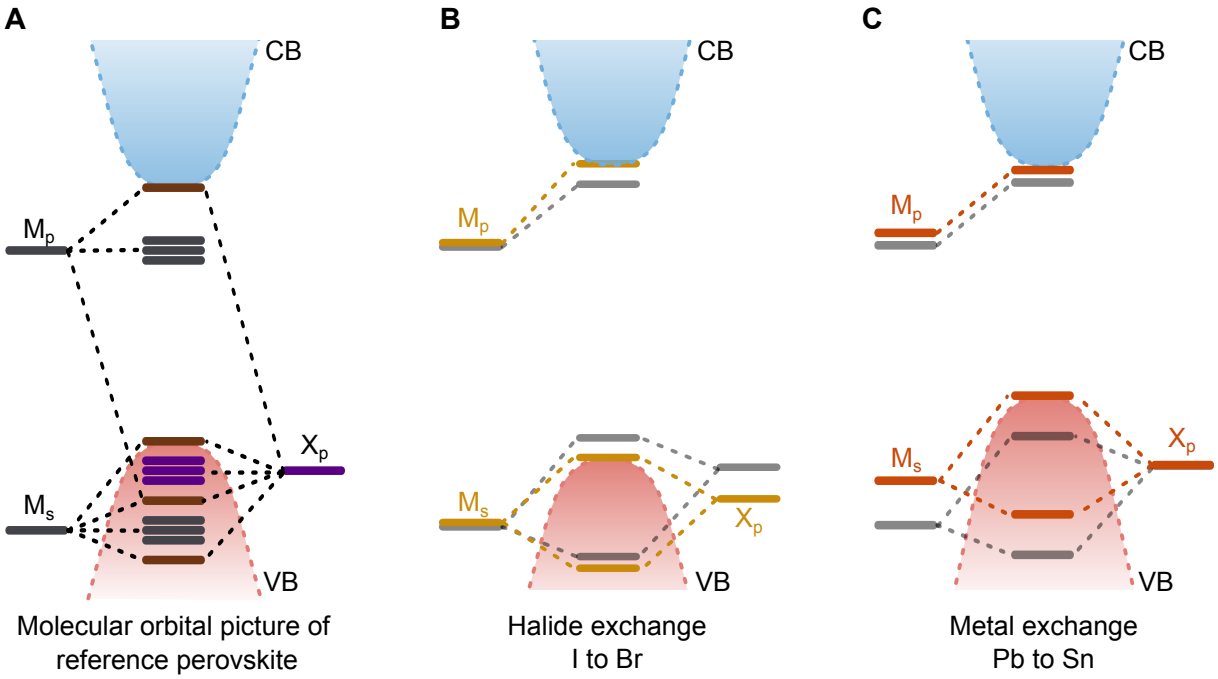

Figure 2.6: Molecular-orbital picture of band formation and bandgap engineering in hybrid metal halide perovskites. **A** For a reference ABX_3 perovskite in the photoactive α-phase, hybridization within the corner-sharing BX_6 framework yields antibonding band-edge states: the VBM is dominated by halide p orbitals (X_p) with contributions from the metal s orbitals (M_s), whereas the CBM is dominated by metal p orbitals (M_p) with minor halide contributions. **B** Halide exchange ($I^- \rightarrow Br^-$) lowers the halide-p orbital energy, shifting the VBM downward and widening the bandgap.[93] **C** Metal exchange ($Pb^{2+} \rightarrow Sn^{2+}$) modifies the metal-orbital energies and typically narrows the bandgap relative to Pb-based compositions.[93,94] VBM: Valence band maximum, CBM: conduction band minimum

Bandgap engineering in hybrid perovskites can be understood as a direct consequence of modifying the relative energies of these contributing atomic orbitals. Halide exchange is the most widely used tuning mechanism. Substituting iodide with bromide lowers the energy of the halide p orbitals (consistent with the electronegativity trend $I < Br < Cl$), shifting the VBM downward and widening the bandgap.[93] Conversely, reducing the bromide content and increasing the iodide fraction raises the VBM and narrows the bandgap.

Metal-site substitution provides an additional degree of freedom for bandgap control. Replacing Pb^{2+} with Sn^{2+} shifts the metal-derived orbital states and generally results in a narrower bandgap relative to lead-based perovskites.[93]

Overall, the molecular-orbital framework provides an intuitive understanding of bandgap engineering in hybrid metal halide perovskites: halide substitution primarily tunes the valence-band position, while metal substitution can alter both band edges.[93] This orbital-level picture underpins the compositional strategies used throughout this work to tailor perovskite absorbers across a wide bandgap range for single-junction, tandem, and multi-junction photovoltaic applications.

2.3 Fundamentals of Vapor-Phase Deposition of Perovskite Thin Films

Vacuum-based deposition relies on the sublimation or evaporation[f] of precursor materials and their subsequent transport through the gas phase toward a substrate held at reduced pressure. The equilibrium vapor pressure of a material, and thus its achievable deposition rate, is described by the Clausius–Clapeyron relation,

$$\ln p = -\frac{\Delta H_{\mathrm{sub}}}{RT} + C,$$

which links the vapor pressure p to the sublimation enthalpy ΔH_{sub} and the source temperature T. The Clausius–Clapeyron relation highlights the exponential increase of vapor pressure with temperature. Elevating the source temperature is thus an important lever to increase the effusion rate and consequently the achievable deposition rate.

The transition between ballistic transport and collision-dominated transport in vacuum-based deposition can be quantified by the mean free path λ_{mfp}, representing the average distance traveled by a gas-phase particle between collisions. In the molecular flow regime relevant to high-vacuum evaporation, the number density n is sufficiently low that λ_{mfp} often exceeds the source-to-substrate distance (SSD). Within kinetic gas theory, the mean free path of a particle in a dilute gas is given by

$$\lambda_{\mathrm{mfp}} = \frac{1}{\sqrt{2}\, n\sigma}, \tag{2.27}$$

where σ denotes the collision cross section and the factor $\sqrt{2}$ accounts for the relative motion of collision partners. For identical hard-sphere particles of diameter d, $\sigma = \pi d^2$ and the mean free path can be written as

$$\lambda_{\mathrm{mfp}} = \frac{1}{\sqrt{2}\, n\pi d^2} = \frac{k_{\mathrm{B}} T}{\sqrt{2}\, \pi d^2\, p}, \tag{2.28}$$

[f] Many scientific publications are using the terms “sublimation” and “evaporation” interchangeably. In this thesis, processes are termed either as sublimation or evaporation, if the phase transition occurs from solid to gas phase or from the liquid phase to the gas phase, respectively.

after substituting the ideal-gas relation $n = p/(k_{\mathrm{B}}T)$. For collisions between two different species A and B with hard-sphere diameters d_A and d_B, the cross section is $\sigma_{AB} = \pi\left((d_A + d_B)/2\right)^2$. The corresponding mean free path of species A in a background gas of species B with number density n_B can be written as

$$\lambda_{\mathrm{mfp,A}} = \frac{1}{n_B\,\sigma_{AB}\sqrt{1+\frac{m_A}{m_B}}} = \frac{4k_{\mathrm{B}}T}{p_B\pi\,(d_A+d_B)^2\,\sqrt{1+\frac{m_A}{m_B}}}, \tag{2.29}$$

where m_A and m_B are the particle masses and p_B is the partial pressure of species B. In the special case $A = B$, this expression reduces to the identical-particle result, since $\sigma_{AB} = \pi d^2$ and $\sqrt{1 + m_A/m_B} = \sqrt{2}$.

An idealized Knudsen effusion cell is a thermally controlled effusion source designed to deliver a well-defined and stable molecular or atomic flux under high-vacuum conditions. The source material is contained in a crucible that is heated uniformly, establishing thermal equilibrium between the condensed phase and its vapor. Effusion occurs through a small orifice whose diameter is much smaller than the mean free path of the effused species, therby ensuring molecular flow in the Knudsen regime. Under these conditions, the effusing flux is determined solely by the equilibrium vapor pressure of the material and the cell temperature, and can be described by kinetic gas theory. The resulting particle flux is highly directional and proportional to the vapor pressure inside the cell, which is governed by the Clausius–Clapeyron relation. Owing to the well-defined geometry and thermal isolation, Knudsen cells enable precise control over deposition rate, high temporal stability, and reproducible material delivery, making them a standard source concept for vacuum deposition of inorganic and organic thin films in research and industrial-scale systems.

2.3.1 Thin-film Nucleation and Layer Growth Mechanisms

Thin-film formation proceeds through a sequence of elementary steps (**Figure 2.7**). All following descriptions follow Brune *et al.*[95] First, incident species adsorb to the substrate surface at a rate k_{A} and may desorb with rate k_{D} (**Figure 2.7 A**). Following adsorption, adatoms diffuse on the surface and form stable nuclei through collision and aggregation (**Figure 2.7 B**), which subsequently grow by continued adatom capture and incorporation at the nucleus perimeter (**Figure 2.7 C**). The competition between adatom–substrate interactions, adatom–adatom interactions, and the relevant surface and interface energies determines the macroscopic growth mode. Strong adatom–substrate bonding promotes Frank–van–der–Merwe growth with layer-by-layer film formation (**Figure 2.7 D**), typically expressed by a surface-energy balance of $\mathrm{SE}_{\mathrm{substrate}} \geq \mathrm{SE}_{\mathrm{film}} + \mathrm{SE}_{\mathrm{interface}}$. Weaker wetting favors Volmer–Weber growth, where islands form directly on the substrate (**Figure 2.7 E**; $\mathrm{SE}_{\mathrm{substrate}} < \mathrm{SE}_{\mathrm{film}} + \mathrm{SE}_{\mathrm{interface}}$). An intermediate case is Stranski–Krastanow growth, in which an initial wetting layer forms before the growth transitions to island formation after a critical thickness, for example due to strain accumulation or changes in surface energy balance (**Figure 2.7 F**). These nucleation and growth pathways control film morphology, crystallographic

texture, and porosity and therefore constitute a key determinant of film formation for vapor-deposited perovskite thin films.

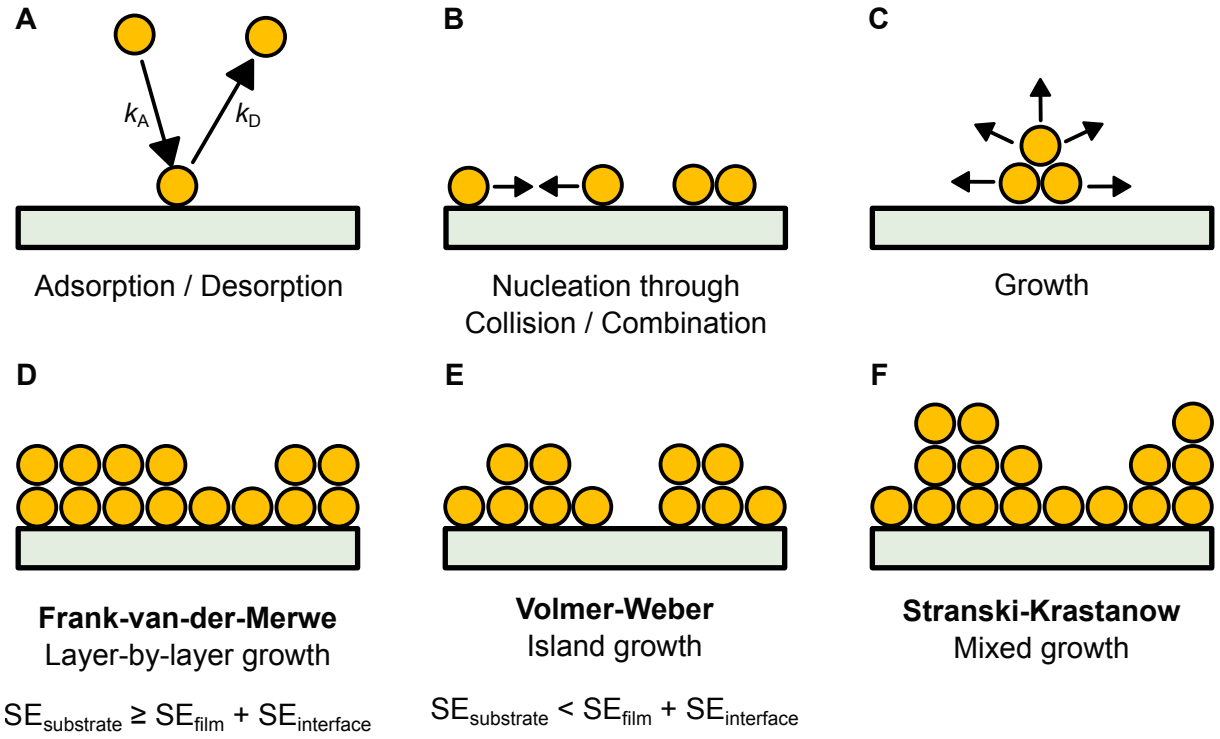

Figure 2.7: Illustration of elementary thin-film formation steps and resulting growth modes in vacuum deposition. **A** Adsorption and desorption of incident species with adsorption rate k_{A} and desorption rate k_{D}. **B** Nucleation through surface diffusion followed by collision/aggregation of adatoms into stable clusters. **C** Growth of stable nuclei by continued adatom capture and incorporation. **D** Frank–van–der–Merwe (layer-by-layer) growth under favorable wetting conditions ($SE_{\mathrm{substrate}} \geq SE_{\mathrm{film}} + SE_{\mathrm{interface}}$). **E** Volmer–Weber (island) growth under poor wetting conditions ($SE_{\mathrm{substrate}} < SE_{\mathrm{film}} + SE_{\mathrm{interface}}$). **F** Stranski–Krastanow (mixed) growth, where an initial wetting layer transitions to island growth after a critical thickness.

A central kinetic parameter controlling island growth dynamics is the surface diffusion coefficient D_{S}, which determines how far an adatom can migrate before either desorbing or being incorporated into a nucleus. A higher D_{S} increases the probability that an arriving adatom reaches an existing island (growth) rather than meeting another adatom to form a new nucleus (nucleation), which lowers the island density and promotes coalescence into larger features. Conversely, increasing the deposition rate raises the local supersaturation and increases the likelihood of adatom-adatom collisions, thereby increasing island density and typically yielding finer-grained, rougher films. This competition between growth and nucleation produces a characteristic scaling in which island density increases with deposition rate and decreases with diffusion (often expressed as $N \propto (R/D_{\mathrm{S}})^{\frac{1}{3}}$), linking controllable process parameters such as substrate temperature (through D) and flux (through R) to the resulting morphology.

Ostwald ripening and Smoluchowski ripening are two complementary coarsening mechanisms that affect the late-stage thin-film evolution, influencing final morphology, roughness, and microstructure. In Ostwald ripening, smaller islands shrink while larger islands grow because the chemical potential of atoms at highly curved surfaces is higher (Gibbs–Thomson effect). Material is transported by adatom diffusion on the surface (or *via* the vapor) from small to large islands, leading to an increasing mean island size and a reduction of the island density over time. In contrast, Smoluchowski ripening proceeds through the physical motion of entire islands. Islands diffuse on the substrate, collide, and merge into larger aggregates. The relative mobility of adatoms versus clusters, together with the competition between deposition flux, surface diffusion, and binding to the substrate, dictates which ripening mechanism dominates.

2.3.2 Considerations for Co-Deposition of Perovskite Thin Films

Vapor-deposition methods are attractive for perovskite absorbers because they are solvent-free, compatible with multilayer stacks, and offer precise control of thickness and uniformity over large areas.[39] The hybrid perovskite growth is governed by the coupled interplay of vapor transport and surface reactions: volatile organic salts (*e.g.*, MAI, FAI) can desorb or decompose, so that the incorporated stoichiometry may deviate from the nominal flux ratio.

The target composition is commonly adjusted by controlling the relative deposition rates of the individual precursors. However, the incorporated stoichiometry is set by the effective flux at the substrate, the sticking probability (often quantified by the sticking coefficient $0 \leq a \leq 1$), and desorption of weakly bound species. Since sticking and surface reaction kinetics are substrate and temperature dependent, identical QCM rate setpoints can yield different compositions and interfacial phases on different surface terminations. When the mean free path λ_{mfp} becomes comparable to the SSD, gas-phase collisions can reduce and redistribute the arriving flux relative to QCM readings, making background pressure control central to stoichiometry control, especially for MAI deposition.[41,96,97]

QCMs are widely used to monitor deposition rates in vacuum deposition processes by measuring the frequency shift of a piezoelectric quartz resonator caused by mass accumulation on its surface. For thin, rigid, and uniformly distributed films, the deposited mass Δm can be directly related to the frequency change Δf *via* the Sauerbrey equation[98]

$$\Delta f = -\frac{2 f_0^2}{A\sqrt{\rho_q \mu_q}} \Delta m,$$

where f_0 is the fundamental resonance frequency of the crystal, A the active area, and ρ_q and μ_q are the density and shear modulus of quartz, respectively. However, the Sauerbrey relation assumes a rigid film that couples elastically to the oscillating crystal. For soft or viscoelastic films, a correction using the acoustic impedance mismatch (Z-factor) between the film and quartz is required, which depends on the density ρ_f and shear modulus μ_f of the deposited material. This limitation is particularly relevant for perovskite precursor materials. For example, PbI_2 forms platelet-like crystallites during deposition,

resulting in a porous film morphology that can lead to deviations between the measured QCM signal and the actual deposition rate. Similarly, organic precursors such as MAI or FAI tend to form comparatively soft films, for which viscoelastic effects can influence the effective mechanical properties of the deposited layer and thus the QCM response. Further, impurities in the organic precursor powder can substantially influence the QCM reading, such as phosphorus-containing compounds sometimes present in MAI.[99–102]

Substrate-Dependent Nucleation and Growth

The substrate strongly influences the nucleation density, preferred crystal orientation, grain-growth mode, and even the incorporation of the organic precursor into the perovskite framework. Systematic break-off and morphology studies identify an early Volmer–Weber (island) growth stage followed by coalescence and Ostwald ripening. Critically, the subsequent evolution toward high-quality, columnar grains is highly substrate dependent.[44] These substrate effects are particularly relevant for device integration, as they imply that a process optimized on one transport-layer stack may not translate directly to another.[43,44,103]

Precursor Decomposition and Background Pressure Effects

Repeatability in FA-based co-deposition is strongly affected by the thermal stability of FAI. Mass-spectrometry measurements show that FAI can generate volatile degradation products (notably hydrogen cyanide and triazine) under thermal stress and that severe decomposition occurs at elevated source temperatures. Further, the FAI incorporation rate depends on the chamber background pressure, and the tooling factor[g] becomes pressure dependent. At higher pressures the QCM near the substrate can detect substantially lower effective rates, even when the source-side QCM indicates stable flux. This provides an initial mechanistic explanation for why nominally identical rate setpoints can lead to different compositions across tools and across time. Local pressure gradients and collision frequencies close to the organic source alter the effective transport and may promote further degradation reactions.[97]

Gradients and Stoichiometry drift

Even within a single deposition run, composition can drift with time through gradual changes in background pressure or organic cation incorporation. Co-deposited $MAPbI_3$ films deposited under slowly varying pressure conditions exhibit thickness-dependent MAI deficiency (I:Pb ratio changes), which becomes more prominent for thick films and can create differently doped regions across the absorber. Such gradients can modify the internal field distribution and impact carrier dynamics, implying that deposition kinetics and stoichiometry control influence both morphology and electronic properties of the perovskite thin film.[104,105]

[g] Deposition rate ratio between a QCM near the source and a QCM near the substrate to compensate for chamber geometry

2.3.3 Considerations for Two-Step Perovskite Thin Film Deposition

Two-step deposition is a widely used route to fabricate high-quality halide perovskite absorber layers, and it has been particularly important for FA-based compositions.[106–108] A PbI_2-rich inorganic scaffold is deposited first, followed by deposition of the organic cations, either by vapor deposition or solution-based processes. Conversion to the perovskite proceeds by precursor interdiffusion and reaction, and film quality is ultimately determined by how efficiently FA^+ infiltrates the inorganic scaffold and how intermediate phases evolve into the 3D perovskite network.

Diffusion-Limited Conversion

In sequential deposition, the rate-limiting step is often the infiltration and diffusion of FAI (or its ionic species) through the inorganic scaffold. Here, it is useful to distinguish between porosity, tortuosity, and permeability when describing transport through thin films. Porosity quantifies the fraction of void space available for infiltration, tortuosity captures how convoluted the transport pathways are relative to a straight path, and permeability reflects the overall ease with which species are transported through the thin film as a result of both factors. Thus, even highly porous PbI_2 can exhibit slow infiltration if pathways are poorly connected or highly tortuous, whereas lower porosity films with well-aligned channels may still enable efficient transport. In a simple picture, the process begins with wetting of the PbI_2 surface by the FAI solution, followed by penetration into voids or grain boundaries, and then diffusion into the bulk. The relevant transport length scale is set by the PbI_2 thickness and tortuosity, while the effective diffusion coefficient depends on solvent choice, and the density of fast pathways such as grain boundaries.

A porous or vertically connected PbI_2 morphology typically promotes rapid and more complete conversion because it enables deeper precursor access and reduces the time required for FA^+ to reach the bottom interface. Conversely, dense PbI_2 often leads to a reaction front that advances slowly from the top surface downward, increasing the likelihood of residual PbI_2 or compositional gradients if thermal annealing is insufficient. Practically, this motivates solvent/additive engineering during PbI_2 deposition to tune the inorganic scaffold porosity and coordination chemistry so that subsequent FAI infiltration results in uniform conversion across the full film thickness.[109–114]

While the above description is often rationalized using Fick's laws with a scalar diffusion coefficient, this approximation is generally insufficient for solid-state conversion processes.[115,116] In crystalline solids, diffusion is intrinsically anisotropic and is further complicated by microscopic features such as grain boundaries and voids. Consequently, the diffusivity is more appropriately described by

$$\overline{\mathbf{J}} = -\overline{\mathbf{D}}\,\nabla c, \tag{2.30}$$

where $\overline{\mathbf{J}}$ is the diffusive flux, c the concentration of the diffusing species, and $\overline{\mathbf{D}}$ the anisotropic diffusion tensor

$$\overline{\mathbf{D}} = \begin{bmatrix} D_x & D_{xy} & D_{xz} \\ D_{yx} & D_y & D_{yz} \\ D_{zx} & D_{zy} & D_z \end{bmatrix}.$$

This distinction is particularly relevant for layered PbI_2, where transport parallel and perpendicular to the inorganic sheets can differ by orders of magnitude, such that the direction of preferential diffusion relative to the film normal influences whether conversion proceeds uniformly through the thickness or remains confined to a reaction front near the top surface.

Moreover, the interdiffusion process during thermal conversion is rarely governed by lattice diffusion alone. Instead, the experimentally observed effective transport rate reflects a combination of anisotropic intragrain diffusion through interstitial or vacancy-mediated jumps and diffusion along microstructural fast pathways, most notably grain boundaries, dislocations, and porous networks. Because these features provide lower activation barriers and higher free volume, they can dominate the overall flux even when their volumetric fraction is small, thereby controlling the penetration depth of FA^+/I^--bearing species and the time required to homogenize composition across the PbI_2 layer. As a result, scaffold engineering (grain size, boundary density/chemistry, and vertical connectivity) does not merely change the geometric tortuosity, but can qualitatively change the diffusion mechanism and hence the uniformity and completeness of the perovskite formation.

Formation Mechanism and Intermediates in FA-based Perovskite Thin Films

The conversion reaction PbI_2 + FAI $\rightarrow$ $FAPbI_3$ is a complex multi-step solid-state reaction.[117] Perovskite formation commonly proceeds through (i) intercalation of FA^+ into layered PbI_2, (ii) formation of low-dimensional (layered/adduct) intermediates, and (iii) rearrangement into the corner-sharing PbI_6 octahedral network of the 3D perovskite. Kinetically, the earliest perovskite nuclei tend to form near the FAI/PbI_2 interface. Continued conversion then depends on ion transport to the reaction front and on dissolution–recrystallization events that allow structural reorganization.[118]

Role of Moisture in the Conversion Process

A notable feature of sequential deposition (both hybrid and PVD/PVD processes) is its sensitivity to ambient moisture. In controlled amounts, water can assist conversion and crystallization by increasing ionic mobility and facilitating interfacial reaction pathways. Mechanistically, water can weakly solvate FAI and enhance its transport into the PbI_2 scaffold, coordinate to lead iodide and lower kinetic barriers for structural rearrangement, and promote dissolution–recrystallization that yields larger grains and improved coverage. Consequently, moderate relative humidity (RH) can accelerate perovskite formation and improve film morphology.[117,119–121] Excessive amounts of moisture can, however, be detrimental to perovskite film

formation. At high RH, water promotes hydrate formation and can drive FA-based perovskites toward non-photoactive phases or accelerate degradation.

3 Experimental Methods

This chapter outlines the experimental procedures used in this thesis to fabricate and evaluate perovskite thin films and solar cells, covering both single-junction and perovskite/silicon tandem architectures. It summarizes the key process routes (co-deposition, hybrid two-step, and selected solution steps), including substrate preparation, transport-layer formation, absorber deposition, passivation, and electrode integration. The chapter then details the optoelectronic, structural, and chemical characterization methods used to link processing to device performance, ranging from current-density–voltage trends and external quantum efficiency to atomic force microscopy, scanning electron microscopy, grazing-incidence wide-angle scattering and X-ray diffraction, and advanced analytics such as inductively coupled plasma optical emission spectroscopy, Knudsen effusion mass spectrometry, time-of-flight secondary ion mass spectrometry, and synchrotron-based X-ray emission spectroscopy along with computational density functional theory simulations.

3.1 Fabrication Methods

3.1.1 Process Parameters for Device Fabrication

Throughout the course of this work, different deposition routes and device architectures were investigated. Relevant information regarding all fabrication steps is summarized in the following section for single-junction (**Figure 3.1**) and tandem devices.

Single-Junction Solar Cells

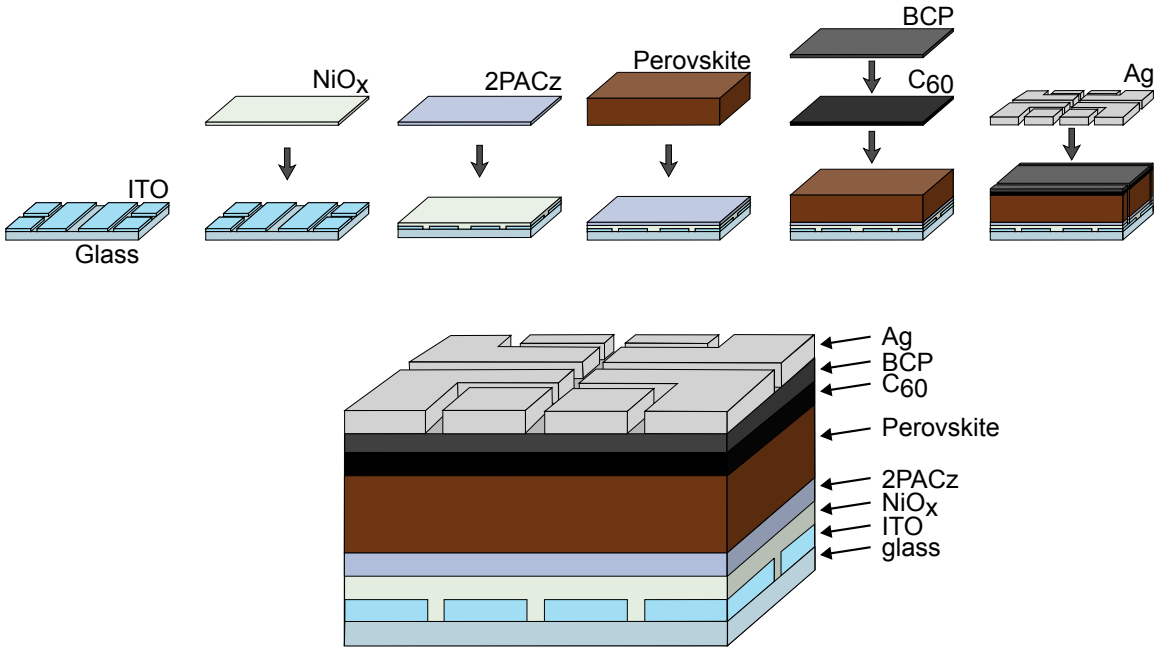

Figure 3.1: Schematic illustration of the single-junction perovskite solar cell architecture, showing the layer-by-layer device stack and corresponding deposition sequence from glass/ITO to the Ag top electrode.

Substrate Preparation and Cleaning

Different types of glass/ITO substrate were used throughout this work: In Chapter 5, glass substrates with 120 nm thick indium tin oxide (ITO) coating (sheet resistance 15 Ω/□, Luminescence Technology, CAS: 50926-11-9) and were cut in 16 mm × 16 mm. For Chapter 6, glass substrates with ITO coating (Shangyang Technology) were used. Two different types of glass thicknesses were used with 1.1 mm thickness for Chapter 6.2 and 0.7 mm for Chapter 6.5. Substrates with thickness of 1.1 mm already had a anti-reflective coating, however, the manufacturer does not disclose details about the used material or thickness.

Substrates were cleaned in an ultrasonic bath with acetone and isopropanol for 20 min each followed by an oxygen plasma treatment.

Hole Transport Layer Deposition

In case of Co-Deposition of Perovskite Thin Films (Chapter 5)
Solution-processed SAM-HTLs: A thin layer of 2PACz was deposited on the ITO substrate by dispensing 75 µL 2PACz solution (0.5 mg mL^{-1} in anhydrous EtOH) on the substrate with a resting time of 5 s followed by rotation at 3000 rpm for 30 s. The substrates were then annealed at a temperature of 100 °C for 10 min. A second washing step was used to remove any unbound molecules. Here, 150 µL of pure EtOH was dynamically dispensed onto the substrate within 2 s at 3000 rpm for a total rotation time of 30 s. The substrates were then annealed at 100 °C for 10 min.

Evaporated SAM-HTLs: Evaporated 2PACz thin films were fabricated *via* vapor deposition from a crucible in an OPTIvap system (M. Braun Inertgas-Systeme GmbH, Dresden) as described by Farag *et al.*[122] All films were deposited at a base pressure of 5×10^{-6} mbar , with rates of 0.15-0.25 Å s^{-1}. Bulk SAM-HTLs had a final thickness of 4 nm. A washing step was used to remove any unbound molecules with 150 µL of pure EtOH dynamically dispensed onto the substrate within 2 s at 3000 rpm for a total rotation time of 30 s. The substrates were then annealed at 100 °C for 10 min.

In case of Hybrid Two-Step Deposition of Perovskite Thin Films (Chapter 6)
A 5 nm thick NiO_x film was sputtered from a NiO_x target (4 inch, 99.99 % pure, Kurt J. Lesker Company) using 100 W power (7.95 W in^{-2} power density) in a gas mixture of Ar and O_2 on the ITO substrate with a fixed flow rate of 0.2 sccm for O_2 and a variable flow rate of Ar to achieve the set pressure of 1 mTorr. Then, a thin layer of 2PACz was deposited on the ITO/NiO_x substrate by dispensing 75 µL 2PACz solution (0.5 mg mL^{-1} in anhydrous EtOH) on the substrate with a resting time of 5 s followed by rotation at 3000 rpm for 30 s. The substrates were then annealed at a temperature of 100 °C for 10 min. A second washing step was used to remove any unbound molecules. Here, 150 µL of pure EtOH was dynamically dispensed onto the substrate within 2 s at 3000 rpm for a total rotation time of 30 s. The substrates were then annealed at 100 °C for 10 min.

Perovskite Thin Film Deposition

In Case of Co-Deposition
For perovskite thin film deposition, a PEROvap system (M. Braun Inertgas-Systeme GmbH, Dresden) integrated into a nitrogen glovebox was used. The deposition rates of individual materials were monitored independently using four QCMs. To minimize background deposition, the cooling shield surrounding all sources was maintained at -25 °C. Prior to initiating heating, the chamber was evacuated for 60 min,

yielding a typical base pressure at the start of heating of 3×10^{-6} mbar. Throughout deposition, the rate of each material was stabilized by manually adjusting the source temperature. The substrate temperature was fixed at 18°C, and the substrate rotation speed was held constant at 10 rpm for all processes. During co-deposition, the inorganic rates were: PbI_2 = 0.23 Å s^{-1}, CsI = 0.025 Å s^{-1}, and $PbCl_2$ = 0.01 Å s^{-1}, adapting an established recipe of Lohmann *et al.*[123] The FAI deposition rate was adjusted to optimize device performance, reflected in the "equivalent FAI rate". All films were annealed at 140°C for 10 min in a nitrogen-filled glovebox.

In Case of Hybrid Two-Step Deposition

Vapor-based deposition of inorganic perovskite precursor materials was performed using a PEROvap system (M. Braun Inertgas-Systeme GmbH, Dresden) integrated into a nitrogen glovebox (Figure 3.2). Individual QCMs were used to measure the rate of each material. A cooling shield, surrounding all sublimation sources, was set to −20 °C. Prior to the heating process, the system was evacuated, yielding a typical base pressure at the start of heating of $< 3 \times 10^{-6}$ mbar. For each process, the deposition rates were kept constant by an automated process. The substrate temperature (18 °C) was kept constant for all experiments.

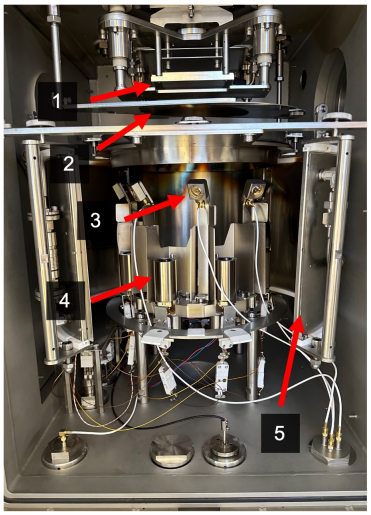

Figure 3.2: Optical photograph of the used PEROvap system (M. Braun Inertgas-Systeme GmbH, Dresden) used for the inorganic scaffold deposition in this thesis. 1) Substrate station with temperature control, 2) Closed substrate shutter, 3) QCM holder, 4) Sublimation crucible source, 5) Cooling shield. QCM: Quartz crystal microbalance

In a subsequent step, the organic cation solution was deposited *via* a spin-coating process. In a dynamic spin coating process, 100 µL of the organic cation solution was dispensed at a rotation speed of 4000 rpm

for 30 s. The spin-coating process took place in an N_2-filled glovebox. An overview of process parameters for different targeted perovskite absorber bandgaps are summarized in **Table 3.1**, **Table 3.2** and **Table 3.3**.

Table 3.1: Optimized layer thicknesses and nominal inorganic scaffold composition

Target bandgap [eV]	CsCl [nm]	$PbBr_2$ [nm]	PbI_2 [nm]	Nominal inorganic scaffold composition [-]
1.52	5	0	300	$Cs_{0.03}PbI_2Cl_{0.03}$
1.70	30	0	300	$Cs_{0.18}PbI_2Cl_{0.18}$
1.84	30	40	246	$Cs_{0.18}PbI_{1.64}Br_{0.36}Cl_{0.18}$

Table 3.2: Parameters of organic cation solution

Target bandgap [eV]	FAI [%]	FABr [%]	Organic molarity [M]	FAI [mg/mL]	FABr [mg/mL]	MACl (10 $\%_{rel}$) [mg/mL]
1.52	100	0	0.75	129	0	15
1.70	35	65	0.75	45	61	15
1.84	10	90	0.75	13	84	15

Table 3.3: Nominal perovskite composition

Target bandgap [eV]	Nominal perovskite composition [-]
1.52	$Cs_{0.03}FA_{0.97}Pb(I_{0.99}Cl_{0.01})_3$
1.70	$Cs_{0.18}FA_{0.82}Pb(I_{0.76}Br_{0.18}Cl_{0.06})_3$
1.84	$Cs_{0.18}FA_{0.82}Pb(I_{0.57}Br_{0.37}Cl_{0.06})_3$

Process for a target bandgap of 1.52 eV:
Static deposition rates of 1.0 and 0.1 Å s^{-1} of PbI_2 and CsCl, respectively, were used for the deposition of the inorganic scaffold. First, 5 nm of CsCl was deposited, followed by 300 nm of PbI_2. A solution of FAI in a mixture of anhydrous EtOH and DMSO (97:3 V/V) was prepared with MACl added as an additive at a ratio of 10 mol% relative to the total amount of FA^+. The substrates were annealed at 150 °C for 20 min at a relative humidity of 30 % in a humidity-controlled glovebox.

Process for a target bandgap of 1.70 eV:
Static deposition rates of 1.0 Å s^{-1} and 0.1 Å s^{-1} of PbI_2 and CsCl, respectively, were used for both

sequential and co-deposition of the inorganic scaffold. In the case of co-deposition, a film thickness of 300 nm was set as the final film thickness for PbI_2, terminating the deposition. The final thickness of CsCl was 30 ± 1 nm. For sequential deposition, first 30 nm of CsCl was deposited, followed by 300 nm of PbI_2. A solution of FAI (35 %), FABr (65 %) in anhydrous EtOH was prepared with MACl added as an additive at a ratio of 10 mol% relative to the total amount of FA^+ following the established reciple of Li *et al.* and Er-raji *et al.*[117,124] The substrates were annealed at 150 °C for 20 min at a relative humidity of 30–40 % in a humidity-controlled glovebox.

Process for a target bandgap of 1.84 eV:
Static deposition rates of 1.0, 0.5, and 0.1 Å s^{-1} of PbI_2, $PbBr_2$, and CsCl, respectively, were used. All materials were deposited sequentially with final thicknesses of 30 nm for CsCl, 40 nm for $PbBr_2$, and 246 nm for PbI_2. A solution of FAI (10 %), FABr (90 %) in anhydrous EtOH was prepared with MACl added as an additive at a ratio of 10 mol% relative to the total amount of FA^+. The substrates were annealed at 150 °C for 20 min at a relative humidity of 40 % in a humidity-controlled glovebox.

Surface Passivation Deposition

In case of Hybrid Two-Step Deposited Perovskite of Bandgap 1.70 eV
A solution of $PDAI_2$ and BAI was prepared by first dissolving 4 mg of $PDAI_2$ under heating at 50 °C in anhydrous EtOH. The solution was then transferred to a second vial containing 4 mg of BAI. The mixture was agitated to yield a stock solution of 1 mg mL^{-1} with respect to the content of $PDAI_2$. The stock solution was diluted to a concentration of 0.3 mg mL^{-1} by adding pure EtOH. For application of the surface passivation, 100 µL of the diluted solution was dispensed on the substrate with a resting time of 5 s, followed by rotation at 4500 rpm for 30 s. The substrates were then annealed at 100 °C for 5 min.

Electron Transport Layer and Back Electrode Deposition

As the electron transport layer, 20 nm of C_{60} and 5 nm of bathocuproine (BCP) were thermally sublimed and deposited using an Ångstrom EvoVac system at a rate of 0.1–0.2 Å s^{-1} at a pressure of approximately 10^{-6} mbar. Subsequently, 100 nm of Ag was thermally evaporated using a shadow mask to define an active area to 10.5 mm^2, resulting in PSCs with four pixels per substrate.

Tandem Solar Cells

Silicon Bottom Cells

Substrate Preparation and Cleaning

The silicon bottom cells were subsequently cleaned by statically dispensing around 200 µL each of acetone and isopropanol onto the substrate followed by rotation at 1800 rpm for 30 s.

Back Contact Deposition

For deposition of the back contact, 300 nm of Ag was thermally evaporated using a shadow mask with dimensions of 13 × 13 mm at a rate of 1.5 Å s^{-1}.

Hole Transport Layer Deposition

For the HTL layer, a 15 nm thick NiO_x film was sputtered from a NiO_x target (4 inch, 99.99% pure, Kurt J. Lesker Company) using 100 W power (7.95 W in^{-2} power density) in a gas mixture of Ar and O_2 at 1 mTorr on the Si/ITO substrate with a fixed flow rate of 0.2 sccm for O_2 and a variable flow rate of Ar to achieve the set pressure. Then, a thin layer of 2PACz was deposited on the ITO/NiO_x substrate by dispensing 180 µL of 2PACz solution (1 mg mL^{-1} in anhydrous EtOH) on the substrate with a resting time of 5 s followed by rotation at 3000 rpm for 30 s. The substrates were then annealed at a temperature of 100 °C for 10 min. A second washing step was used to remove any unbound molecules. Here, 360 µL of pure EtOH was dynamically dispensed onto the substrate within 2 s at 3000 rpm for a total rotation time of 30 s. The substrates were then annealed at 100 °C for 10 min.

Perovskite Absorber Deposition

Static deposition rates of 1.0 and 0.8 Å s^{-1} of PbI_2 and CsCl were used, respectively. First 50 nm of CsCl were deposited, followed by 500 nm of PbI_2. A 0.75 M solution of FAI (35%), FABr (65%) in anhydrous EtOH was prepared with MACl added at a ratio of 10 mol% relative to the total amount of FA^+. Then, 180 µL of the organic cation solution was dynamically deposited onto the substrate at a rotation speed of 4000 rpm.[117,124] The substrates were annealed at 150 °C for 20 min at a relative humidity of 30–40% in a humidity-controlled glovebox.

Electron Transport Layer Deposition

As electron transport layer, 20 nm of C_{60} was thermally sublimed and deposited using an Ångstrom EvoVac system at a rate of 0.1–0.2 Å s^{-1} at a pressure of around 10^{-6} mbar.

Atomic Layer Deposition (ALD)

A 20 nm SnO_2 layer was deposited using a glovebox-integrated showerhead ALD system (Arradiance GEMStar XT). N_2 served as both the carrier and purge gas, while TDMASn and H_2O (in-house, Milli-Q) were used as precursor and oxidant, respectively. The TDMASn source was heated to 70 °C while the TDMASn carrier line was maintained at 130 °C during operation. Before deposition, the chamber was evacuated to $\sim 10^{-6}$ mbar and stabilized at the target temperature for 10 min to ensure sample equilibration. SnO_2 films were deposited over 200 ALD cycles using the following sequence: a 0.5 s TDMASn pulse

followed by a 12 s purge at 50 sccm, then a 1.0 s H_2O pulse followed by a 12 s purge at 50 sccm. The chamber temperature was set to 90 °C.

Transparent Conductive Oxide Deposition

For the TCO layer, a ∼40 nm thick IZO film was sputtered from a $In_2O_3 : ZnO$ target (4 inch, 99.99% pure, 90:10 wt% In_2O_3:ZnO, Kurt J. Lesker Company) using 190 W power (15.10 W in^{-2} power density) in a gas mixture of Ar and O_2 (1.3%) at 1.1 mTorr.

Front Electrode Deposition

A front electrode of 600 nm Ag was thermally evaporated using a shadow mask with 6 grid fingers (150 μm wide) to define an active area of 1 cm^2 and complete the tandem device.

3.2 Characterization

3.2.1 Investigation of Sublimation Characteristics

Duran Tube Sublimation Setup

Vacuum sublimation in a spatially resolved Duran tube setup was used to study the thermal stability and volatility of perovskite precursor materials under conditions relevant for vacuum processing. The setup enables separation of sublimed material into distinct fractions along the temperature and pressure gradient, allowing identification of decomposition, preferential sublimation, and volatile by-products. This provides practical guidance for selecting suitable precursors and defining safe sublimation conditions for reproducible vacuum-deposited perovskite photovoltaics.

Sublimation experiments of perovskite precursor materials were performed by Dr. Stefan Auschill at M. Braun Inertgas-Systeme GmbH, Dresden. The material was loaded into a Duran tube (**Figure 3.3**) which was evacuated to a base pressure of $\sim 10^{-6}$ mbar. Harvesting zones were defined by equidistant rings. An external cooling loop was placed before the outlet to the vacuum pump to collect any volatile species. For all experiments in **Chapter 4**, materials between harvesting zones 3-12 were collected as the main fraction. Harvested material were subjected to further analysis. Materials were used without further purification: FAI (GreatCell Solar, ≥99.99%), MAI (GreatCell Solar, ≥99.99%), and PbI_2 (TCI, 99.99%, trace metal basis).

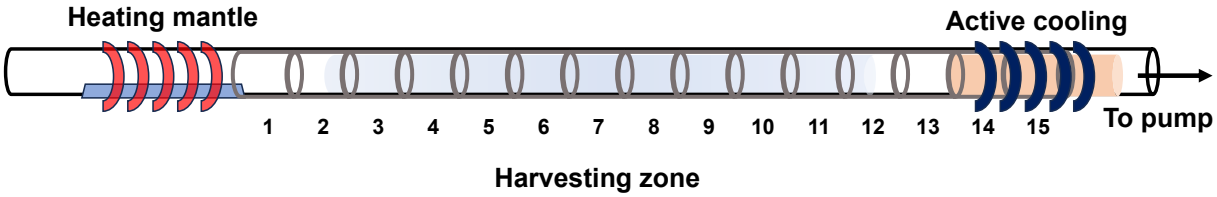

Figure 3.3: Schematic of the Duran tube sublimation setup. Material is loaded and sublimed with the help of an external heating mantle. Equidistant rings define individual harvesting zones. External active cooling deposits volatile species.

Vapor Flux Distribution of Perovskite Precursor Materials

Vapor deposition on a static substrate holder was used to quantify material-specific vapor flux distributions under realistic high-vacuum processing conditions. Practically, using this method provides a thickness gradient from which the vapor flux distribution is derived.

Vapor deposition of perovskite precursor materials was performed in a nitrogen glovebox-integrated PEROvap system (M. Braun Inertgas-Systeme GmbH, Dresden). Individual QCMs were used to measure the rate of each material independently. A cooling shield, surrounding all sublimation sources, was set to -20 °C. The substrate temperature (18 °C) was kept constant for all experiments. Prior to the heating process, the system was evacuated to a base pressure of 5×10^{-6} mbar. For all processes, the rate of each material was kept constant in a manual process by varying the source temperature. The experimental setup features a 300 mm vertical distance between the sublimation source and the substrate. The point source and the center of the substrate were positioned off-axis, approximately 165 mm apart, without a tilt towards the substrate. Emission characteristics were determined without rotating the substrate. The film thickness was around 300 nm for all materials. A schematic of the used setup and resulting vapor flux distribution is depicted in **Figure 3.4**. Deposition rates during sublimation were: FAI: 1.0 Å s^{-1}, PbI_2: 13.0 Å s^{-1}, and CsI: 10.0 Å s^{-1}. The lateral distance from the source to the QCM was 75 mm, which was used for scaling from the thickness distribution to the static deposition rate profile. For all experiments, cylindrical 10 cm^3 crucibles were used, with a material loading of 3 g for PbI_2 and CsI, and 2 g for FAI. Materials for this study were used without further purification: FAI (GreatCell Solar, $\geq$99.99%), PbI_2 (TCI, 99.99%, trace metals basis), CsI (TCI, $\geq$99.0% (titration)).

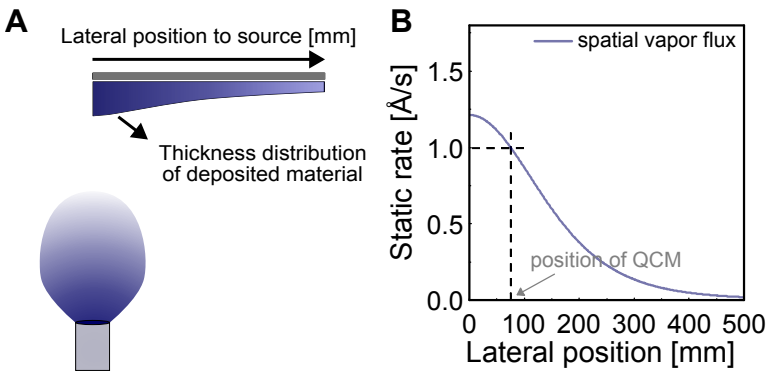

Figure 3.4: **A** Spatial vapor flux distribution across the substrate, showing the lateral thickness profile and **B** static deposition rate as a function of position relative to the source, with the QCM location indicated as the point of normalization. QCM: quartz crystal microbalance

3.2.2 Optoelectronic Characterization

Current Density–Voltage (*J–V*) Measurements

Current–voltage (*J–V*) measurements were used as the primary method to evaluate the photovoltaic performance of single-junction perovskite solar cells. They provide direct access to key device parameters such as open-circuit voltage (V_{OC}), short-circuit current density (J_{SC}), fill factor, and power conversion efficiency, while stabilized maximum power point tracking allows reliable assessment of steady-state device performance and hysteresis-related effects.

The *J–V* characteristics of the SJ-PSCs were measured with a class AAA xenon-lamp solar simulator (Newport Oriel Sol3A) with a scan rate of 0.6 V s^{-1} using a sourcemeter (Keithley 2400) under the air-mass 1.5 global (AM1.5G) spectra (100 mW cm^{-2}). The solar simulator irradiation intensity was calibrated using a certified Si solar cell (Fraunhofer ISE, calibrated 2024) equipped with a KG5 bandpass filter (Schott). Device parameters of the light-soaked PSCs were used for evaluation. The stabilized PCE of the PSCs was determined by measuring the photocurrent at the maximum power point (MPP) for example, 300 s using a perturb-and-observe algorithm under continuous AM1.5G illumination. Measurements were performed in an N_2-filled glovebox without a shadow mask.

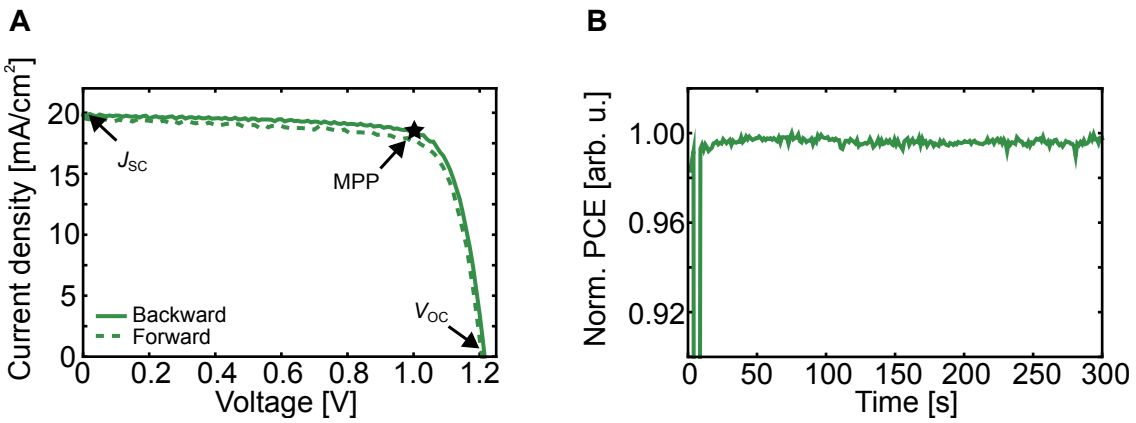

Figure 3.5: **A** *J–V* characteristics of the perovskite solar cell under illumination, showing forward and backward scans with characteristic photovoltaic parameters of J_{SC}, V_{OC} and **B** stabilized power conversion efficiency measured at MPP. *J–V*: Current density–voltage, MPP: maximum power point

External Quantum Efficiency (EQE)

External quantum efficiency (EQE) measurements were used to spectrally resolve the photoresponse of the perovskite solar cells and to independently determine the photocurrent contribution across the absorption range. From the EQE onset, the optical bandgap of the perovskite absorbers can be extracted.

The EQE was measured using a PVE300 photovoltaic QE system (Bentham EQE system). A chopping frequency in the range of 560–590 Hz with an integration time of 500 ms was used to acquire spectra in a wavelength range from 300 to 850 nm. An illumination spot with a diameter of 0.74 mm was used to average over possible variations in the EQE spectra. TSCs were measured over a wider spectral range (300-1200 nm) with a 750 ms integration time and a larger illumination spot of 2.0×2.0 mm. The subcells were measured individually, using bias light: the perovskite top cell with 780 nm and 940 nm LEDs, and the Si bottom cell with a 465 nm LED and a white light source. The bandgap of all processed perovskite thin films was determined based on the first derivative of the EQE curves near the absorption edge (maximum of d(EQE)/d(E)) according to Krückemeier *et al.*[125]

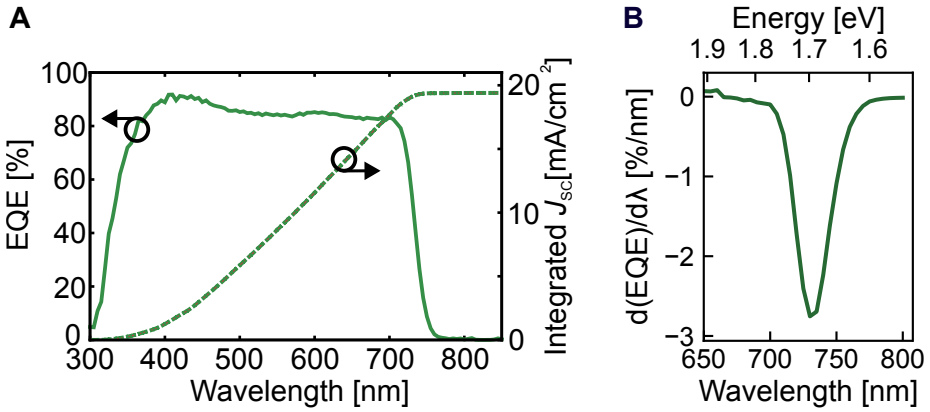

Figure 3.6: A External quantum efficiency (EQE) spectra of the perovskite solar cell, showing the wavelength-dependent response and the integrated short-circuit current density, with **B** the optical bandgap extracted from the EQE onset according to Krückemeier *et al.*[125]

Transmittance and Reflectance Spectroscopy

Optical transmittance and reflectance measurements were used to determine the absorption characteristics of perovskite and inorganic scaffold thin films. These data provide information on optical losses and enable correlation of film thickness and composition with the absorber's spectral response relevant for photovoltaic performance.

Transmittance and reflectance spectra of the perovskite thin films were measured using a PerkinElmer Lambda 1050 spectrophotometer equipped with a double monochromator and a modulated source. A chopper frequency of 46 Hz was applied.

3.2.3 Material Characterization

Atomic Force Microscopy (AFM)

Atomic force microscopy (AFM) was used to assess the surface morphology and roughness of perovskite thin films. The extracted RMS roughness values provide insight into nanoscale film uniformity.

AFM images were obtained using a NanoWizard II setup (JPK Instruments) with an example is shown in **Figure 3.7**. The scanning area was 5 µm × 5 µm. For each sample, 2–3 measurements were performed, and the average root-mean-square (RMS) roughness value was determined.

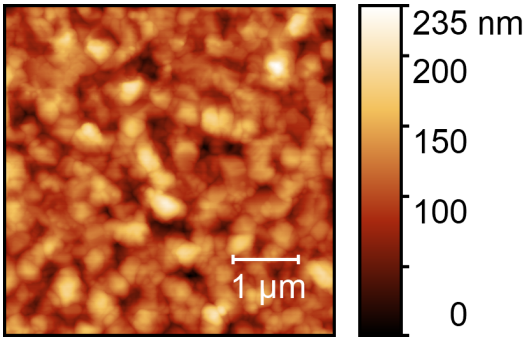

Figure 3.7: Representative AFM image with height and lateral scale bar. AFM: Atomic force microscopy

Confocal Scanning Microscopy (CSM)

Confocal scanning microscopy (CSM) was used to characterize the three-dimensional surface topography of perovskite thin films. This technique provides complementary information on large-area height variations and film uniformity, which is relevant for assessing macroscopic coating quality. Confocal scanning microscopy measurements were carried out using a MarSurf 3D system as displayed in **Figure 3.8**. All measurements were conducted by Julian Petry and Richard Thelen.

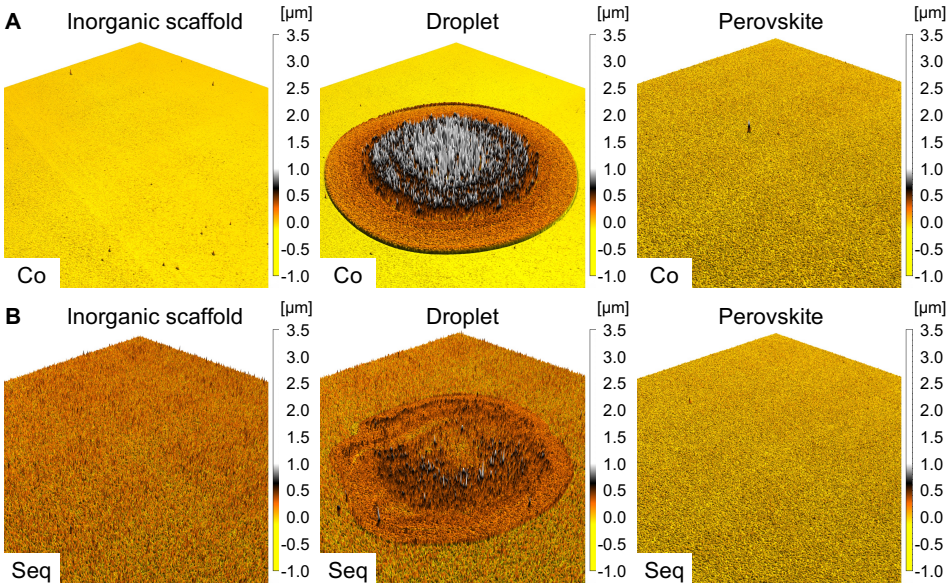

Figure 3.8: Representative CSM measurements of picoliter droplets deposited on inorganic scaffolds. CSM: Confocal scanning microscopy

Grazing-Incidence Wide-Angle X-ray Scattering (GIWAXS)

Grazing-incidence wide-angle X-ray scattering (GIWAXS) was used to analyze the crystallographic structure and orientation of perovskite thin films. The resulting reciprocal-space maps and azimuthal intensity profiles provide information on phase composition, preferred crystal orientation, and texture, enabling correlation of film microstructure with optoelectronic properties and device performance. All measurements were conducted by Dr. Tonghan Zhao at IMT/KIT.

GIWAXS measurements were performed on a Bruker D8 Advance equipped with a Cu X-ray source (40 kV, 40 mA), a Göbel mirror, a 0.5 mm micro mask, and a 0.3 mm snout on the primary track, as well as an Eiger2 R 500K 2D detector on the secondary track. The incidence angle was fixed at 1.5°. All acquired images were first projected onto a virtual detector directly behind the goniometer circle using a home-developed program in MATLAB.[126] The experimentally acquired data were then reshaped into 2D diffractograms (**Figure 3.9 A**) in reciprocal space using the open-access software GIXSGUI.[127] Corresponding azimuthal intensity profiles are integrated along the Debye-Scherrer ring (**Figure 3.9 B**).

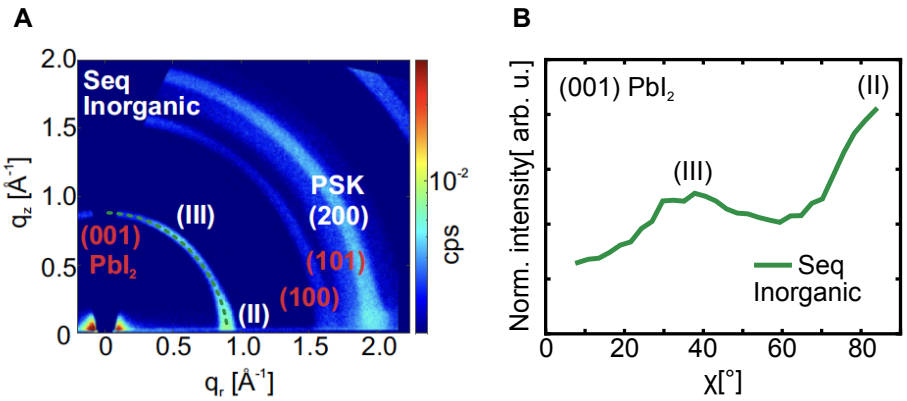

Figure 3.9: GIWAXS analysis of the perovskite film: **A** 2D GIWAXS pattern highlighting characteristic perovskite and PbI_2 diffraction features, and **B** corresponding azimuthal intensity profile showing the angular distribution of the (001) PbI_2 reflection. GIWAXS: Grazing-incidence wide-angle X-ray scattering

Picoliter Droplet Deposition

Picoliter droplet dispensing was used to deposit precisely controlled amounts of organic cation solution onto inorganic scaffolds to study organic cation infiltration. Deposition was conducted by Raphael Pesch at LTI/KIT.

Picoliter droplets were dispensed using an optical contact angle and drop contour analyzer (OCA 200, DataPhysics Instruments GmbH) equipped with a picoliter dosing system (PDDS). Cartridges capable of jetting approximately 50 pL droplets were employed. An organic cation solution in ethanol with optimized molarity was used in each case.

Scanning Electron Microscopy (SEM)

Scanning electron microscopy (SEM) was used to investigate the surface morphology and cross-sectional layer structure of perovskite thin films and devices. The images provide information on grain structure, film coverage, and layer thickness, which are critical for understanding charge transport and device performance. All measurements were conducted by Dr. Alexander Diercks at LEM/KIT.

Field emission top-view SEM images (examples shown in **Figure 3.10**) were taken with a scanning electron microscope (Zeiss LEO Gemini 1530) with an in-lens detector and an aperture size of 20-30 µm. For cross-sectional analysis, the edges were covered with a 3 nm thick platinum layer deposited by sputtering to prevent charging. The applied acceleration voltages for surface and cross sectional analysis range between 5 and 10 kV.

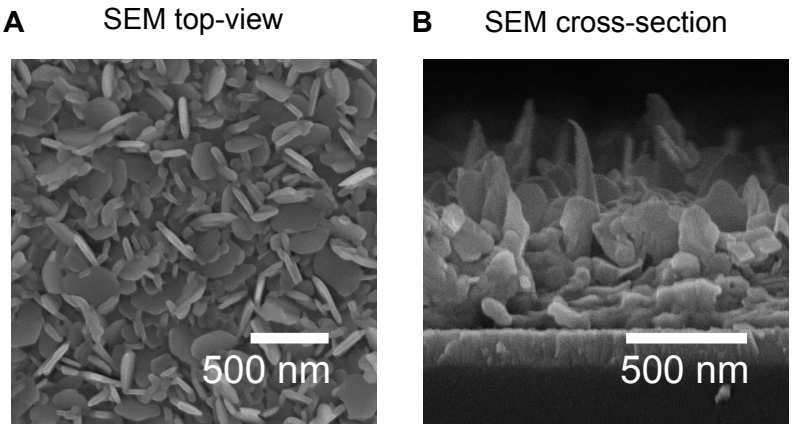

Figure 3.10: SEM images of the perovskite thin film showing **A** top-view morphology and **B** cross-sectional structure. Scale bars = 500 nm. SEM: Scanning electron microscopy

White-Light Interferometry (WLI)

White-light interferometry (WLI) is a non-contact optical profilometry technique used to determine film thickness and surface topography with nanometer-scale precision. In WLI, broadband light is directed onto the sample and the reflected signal from the film surface is interfered with a reference reflection. The resulting interference pattern provides a quantitative map of surface height, enabling extraction of film thickness and roughness. Measurements were conducted by Dr. Alexander Diercks and Richard Thelen at IMT/KIT. In **Chapter 4**, the thickness of deposited FAI layers was measured using a Bruker WLI system (Contour GT-X500, Bruker; **Figure 3.11**). Step heights at coated edges were quantified using the combined white-light interferometry and phase-shift imaging mode (UXI). Measurements were performed with a 5× objective in combination with a 0.55× field-of-view lens (working distance of the 5× objective: 6.7 mm). The illumination intensity was set between 0.15 and 0.18%. Data were evaluated using Bruker Vision64 software.

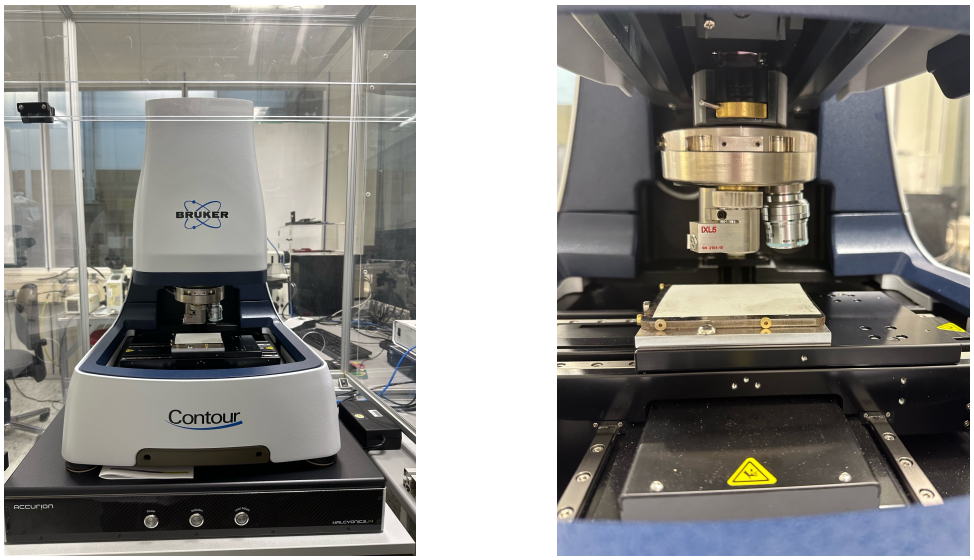

Figure 3.11: Setup used for WLI measurements. WLI: white light interferometry

X-ray Diffraction (XRD)

X-ray diffraction (XRD) was used to identify the crystalline phases and structural evolution of inorganic scaffolds and converted perovskite thin films. The diffraction patterns provide insight into phase purity, crystallization, and perovskite conversion, which are essential for correlating processing conditions with film structure and device performance. All measurements were conducted by Dr. Thomas Feeney (**Chapter 5**) and Ronja Pappenberger (**Chapter 6**) at IMT/KIT.

X-ray diffraction measurements of the inorganic scaffolds and perovskite thin films (Representative example in **Figure 3.12**) were performed using a Bruker D2 Phaser system with Cu K_α radiation ($\lambda = 1.5405$ Å) in Bragg–Brentano configuration with a LynxEye detector. Diffraction patterns were recorded for half-stacks of glass/ITO/HTL/PVK.

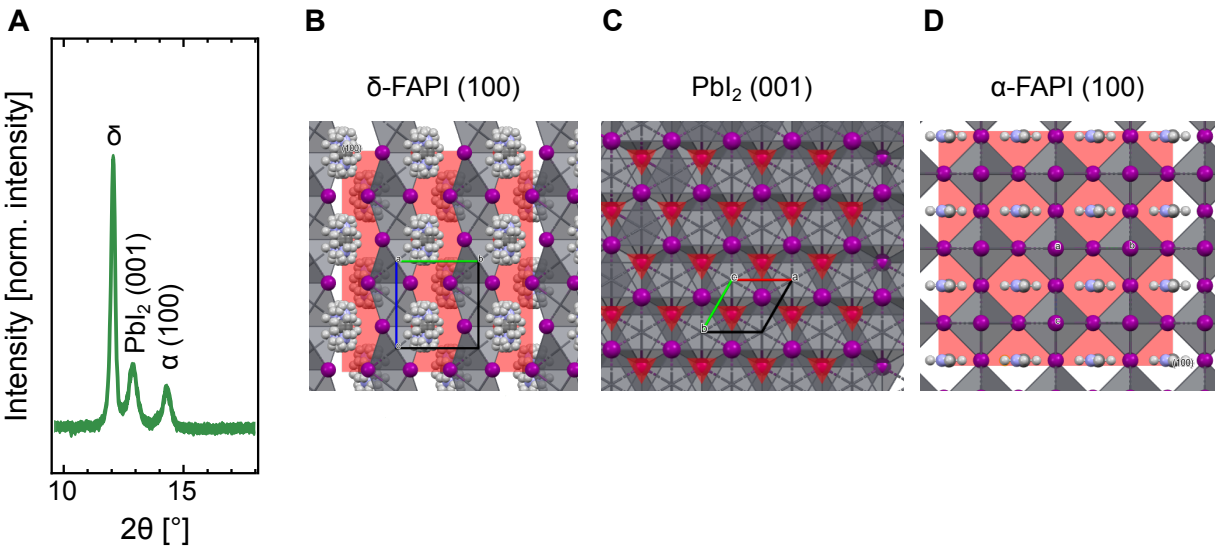

Figure 3.12: **A** XRD pattern of a representative $CsFAPbI_3$ thin film, showing characteristic reflections attributed to the photoinactive hexagonal δ-$FAPI_3$ phase, residual PbI_2, and the photoactive cubic α-$FAPI_3$ phase. (**B-D**) Schematic crystal structures corresponding to the δ-$FAPI_3$ (100), PbI_2 (001), and α-FAPI (100) planes, respectively, illustrating the structural origin of the observed diffraction peaks. XRD: X-ray diffraction

3.2.4 Chemical Characterization

Inductively Coupled Plasma Optical Emission Spectroscopy (ICP-OES)

Inductively coupled plasma optical emission spectroscopy (ICP-OES) was used for quantitative elemental analysis of lead and iodine in inorganic precursor materials. This technique enables precise determination of stoichiometry and elemental ratios, allowing verification of compositional changes arising, for example, from material sublimation. All measurements were conducted by Dr. Sara Rose Kimmig at AWG/KIT.

A stock solution (Inorganic Ventures) was prepared with the following concentrations: Pb:I (500 µg mL^{-1} Pb, 100 µg mL^{-1} I) in 1% (v/v) triethanolamine (TEA, Sigma-Aldrich®, BioUltra, ≥99.5%) and 0.07% (w/v) ethylenediaminetetraacetic acid (EDTA, Merck Millipore, Supelco®). PbI_2 solids were digested using a solution of 1% (v/v) TEA and 0.07% (w/v) EDTA in Milli-Q water. Approximately 2–4 mg of PbI_2 was dissolved into 40 mL of matrix solution and ultrasonicated for 2 h at 50 °C to ensure complete dissolution. Linear calibrations of both Pb and I were generated using five calibration standard concentrations, yielding $R^2 \geq 0.999$. Lead and iodine concentrations were determined by ICP-OES using a Thermo iCAP 7000 Dual View instrument. Iodine and lead were measured in both radial and axial views at wavelengths 178.276 nm for I and 220.353 nm or 216.999 nm for Pb, respectively. Radial view yielded the most reliable results for both elements. Procedural blanks for Pb and I yielded <0.001% and <0.01%, respectively, of the reported sample concentrations. The relative standard deviation (RSD) of measurements was within acceptable thresholds.

Knudsen Effusion Mass Spectrometry (KEMS)

Knudsen effusion mass spectrometry (KEMS) was used to analyze the volatile species and decomposition products released from perovskite precursor materials under controlled thermal conditions. This technique provides direct insight into sublimation and decomposition pathways, enabling assessment of precursor stability and suitability for vapor-based perovskite photovoltaic processing.

Knudsen effusion mass spectrometry was performed using a FINNIGAN MAT 271 instrument at Forschungszentrum Jülich, with detailed specifications given by Bischof *et al.*[128] Measurements were conducted by Julian Petry and Amedeo Morsa.

The apparatus (**Figure 3.13**) consists of four main components: a Knudsen cell (KC), an electron impact ion source, a single-focusing magnetic sector-field mass spectrometer, and a detection system comprising a secondary electron multiplier and an ion counter.[129] Samples were placed inside an alumina liner (height: 8 mm; outer diameter: 6.4 mm; wall thickness: 0.5 mm), which was inserted into an iridium Knudsen cell (height: 8.5 mm; outer diameter: 7.8 mm; wall thickness: 0.2 mm). The KC was covered with a lid containing a central 0.4 mm orifice to allow molecular effusion. Heating was performed at a rate of 10 K min^{-1}. To maintain thermal stability, the KC was insulated by two nested tantalum heat shields with axial openings. Radiation heating was achieved with a tungsten wire wrapped around the KC.[129,130] A $W_{97}Re_3/W_{75}Re_{25}$ thermocouple, integrated into the KC holder, monitored the temperature. The chamber was maintained at $\sim 10^{-6}$ mbar using a turbomolecular pump, while the mass spectrometer compartments were kept under ultra-high vacuum ($\sim 10^{-9}$ mbar) with ion getter pumps. A shutter mechanism allowed separation of sample signal and background. Ionization was achieved *via* an electron beam from an incandescent cathode (60–70 eV; 0.468 mA emission current), intersecting the effusing molecular beam perpendicularly. The detection system used the ion counter for large ion fluxes and the secondary electron multiplier for smaller fluxes.

Between 60-100 mg of powder was loaded per measurement. Measurements were performed in isothermal and polythermal modes. Materials were used as received: FAI (GreatCell Solar, $\geq$99.99%), PbI_2 (TCI, 99.99%, trace metals basis), CsI (TCI, $\geq$99.0% titration).

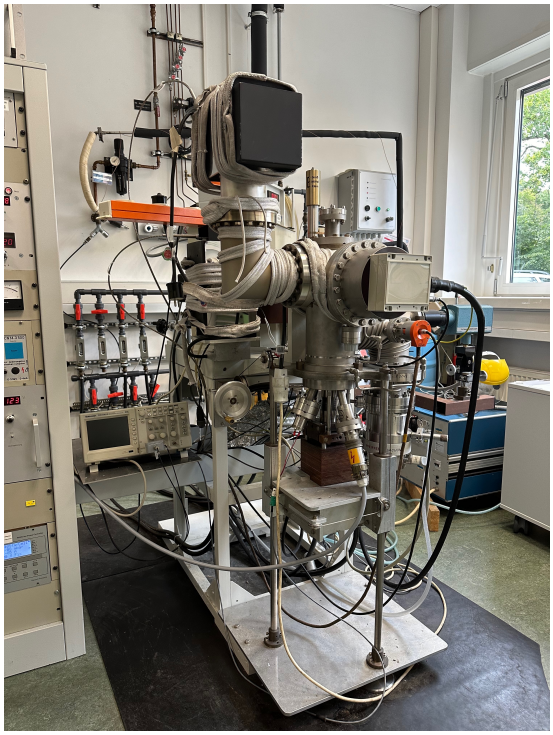

Figure 3.13: Used setup for KEMS measurements at FZ Jülich. KEMS: Knudsen effusion mass spectrometry

Nuclear Magnetic Resonance Spectroscopy (NMR)

Nuclear magnetic resonance (NMR) spectroscopy was used to probe the organic material composition and interaction pathways in solution. The spectra provide information on chemical purity and potential degradation or reaction products.

^{1}H-NMR spectra were recorded in dry DMSO-d_6 (Deutero GmbH) using a Bruker Avance III 300 spectrometer at 300 MHz and 298 K at the Institute for Organic Chemistry at the University of Heidelberg with assistance of Pascal Merten or using a Bruker AVANCE 400 spectrometer at 400 MHz and 298 K at the Institute for Organic Chemistry at KIT by Dr. Andreas Rapp, Despina Savvidou and Tanja Ohmer-Scherrer. Chemical shifts are reported in parts per million (ppm) relative to residual solvent signals (δ_{H} = 2.50 ppm, δ_{C} = 39.52 ppm).[131]

Thermogravimetric Analysis (TGA) and Differential Scanning Calorimetry (DSC)

Thermogravimetric analysis (TGA) combined with differential scanning calorimetry (DSC) was used to investigate the thermal stability, mass loss, and phase transitions of inorganic perovskite precursor materials. These measurements provide insight into sublimation, decomposition, and phase transitions under atmospheric and reduced-pressure conditions, supporting the definition of suitable temperature

windows for vacuum-based perovskite processing. Measurements were conducted by Dr. Carolin Fischer at the company NETZSCH.

TGA/DSC measurements of PbI_2 (TCI, 99.99%, trace metals basis) were performed using a NETZSCH STA 449 F3 Jupiter® equipped with a SiC furnace. The heating rate was 10 K min^{-1}. Samples were weighed in 85 µL Al_2O_3 crucibles. For reduced-pressure measurements, a rotary vane pump was used ($\sim 10^{-2}$ mbar), while high-vacuum conditions were achieved with an additional turbomolecular pump ($\sim 10^{-4}$ mbar).

Time-of-Flight Secondary Ion Mass Spectrometry (ToF-SIMS)

Time-of-flight secondary ion mass spectrometry (ToF-SIMS) was used to obtain depth-resolved chemical information of perovskite thin films and multilayer stacks. This technique enables identification of elemental and molecular species as a function of depth, providing insight into composition gradients, interdiffusion, and interface chemistry that are critical for understanding device performance and stability.

ToF-SIMS measurements were carried out by Dr. Alexander Welle at INT/KIT on a TOF.SIMS5 instrument (ION-TOF GmbH, Münster, Germany) equipped with a Bi-cluster primary ion source and a reflectron-type time-of-flight analyzer. The process parameters used are summarized in **Table 3.4**. The UHV base pressure during analysis was $<7{\cdot}10^{-8}$ mbar. For high mass resolution, the Bi source was operated in "high current bunched" mode, providing short Bi_3^+ primary ion pulses at 25 keV with a lateral resolution of 4 µm and a target current of 0.31–0.35 pA at 10 kHz repetition rate. The 1.5 ns pulse length enabled a mass resolution of $m/\Delta m \approx 6500$ for $^{208}Pb^+$. The primary ion beam was rastered over a 200×200 μm^2 field of view, with 128×128 data points recorded. Mass calibration was based on Li^+, Na^+, $^{204}Pb^+$, $^{206}Pb^+$, Cs_2^+, $^{37}Cl^-$, PO_2^-, CsI_2^-, and PbI_2^-. Depth profiling was performed in dual-beam interlaced mode using Ar_{1500}^+ ions at 10 keV over a 500×500 μm^2 area (7.4-7.5 nA target current). Sputter ion fluence was used as a relative depth scale, though deviations from linearity may occur due to differing erosion rates across layers. Secondary ion intensities were normalized to their respective maxima, with care taken to exclude detector-saturated signals.

Table 3.4: Parameters for ToF-SIMS measurements of inorganic scaffolds and perovskite layers fabricated using the hybrid route presented in **Chapter 6**. ToF-SIMS: time-of-flight secondary ion mass spectrometry

	Positive polarity	**Negative polarity**
Primary ion source	Bi_3^+, 25 keV, pulse bunching, 1.5 ns pulse length, 100 μs cycle time	
Target current [pA]	0.31–0.35, 10 kHz repetition rate	
Field of view [μm^2]	200×200	
Lateral resolution [pixel]	128×128	
Mass scale calibration	Li^+, Na^+, $^{204}Pb^+$, $^{206}Pb^+$, Cs_2^+	$^{37}Cl^-$, PO_2^-, CsI_2^-, PbI_2^-
Sputter ion	Ar_{1500}^+, 10 keV, 7.4–7.5 nA	
Crater size [μm^2]	500×500	
Measurement conditions	interlaced	

3.2.5 Density Functional Theory (DFT) Simulations

Density functional theory (DFT) simulations were used to provide an atomistic understanding of phase stability and energetic trends in formamidinium-based lead halide perovskites. By including entropic contributions associated with organic cation dynamics, these calculations rationalize the temperature-dependent stability of different perovskite phases and support experimental observations of preferred phase formation and stability. All DFT simulations were conducted by Dr. Abderrezak Torche, Dr. Michelle Ernst and Prof. Dr. Ganna Gryn'ova at HITS/KIT.

General description. All computations were performed using density functional theory (DFT) as implemented in the Quantum ESPRESSO package with the PBE exchange–correlation functional.[132] Core electrons were modeled using ultrasoft pseudopotentials, a plane-wave cutoff energy of 55 Ry was applied, and dispersion corrections were included at the DFT-D3 level.[133] Structural relaxations were carried out using the conjugate gradient method, with a convergence threshold on the forces of 10^{-3} atomic units.

Determination of entropic contributions. The entropy argument of Chen *et al.*[134] was used to explain the stability of α-$FAPbI_3$ above room temperature. Assuming that the formamidinium (FA^+) cation is geometrically restricted within the hexagonal δ-$FAPbI_3$ unit cell (as suggested by X-ray analysis),[134] the Gibbs free energy of δ-$FAPbI_3$ is equal to its internal energy,

$$G^{\delta} = E^{\delta}_{\mathrm{DFT}}.$$

For cubic α-$FAPbI_3$, the FA^+ cation undergoes random rotation within the cubic unit cell, contributing an entropic term to the Gibbs free energy:

$$G^{\alpha} = E^{\alpha}_{\mathrm{DFT}} - T \times S,$$

where T is the temperature and S is the entropy of FA^+, given by

$$S = \frac{3}{2} k_B \times \left\{ 1 + \ln \left(0.478 \times k_B T \times (I_1 I_2 I_3)^{\frac{1}{3}} \right) \right\}.$$

Here, k_B is the Boltzmann constant, and I_i are the principal moments of inertia of FA^+: 11.644, 60.161, and 71.806 u Å^2, with $u = 1.6605 \times 10^{-27}$ kg.[134] At $T = 18°\mathrm{C}$, the entropic contribution amounts to -253 meV.

3.2.6 X-ray Emission Spectroscopy (XES)

X-ray emission spectroscopy (XES) was used to probe the local chemical environment and bonding of nitrogen-containing organic components in perovskite-related materials. The element-specific sensitivity of XES enables direct insight into electronic structure and chemical integrity of organic cations. In the context of this thesis, XES was used to quantify the substrate-dependent organic cation uptake for co-deposited perovskite films. All measurements were conducted by Dr. Dirk Hauschild and Dr. Constantin Wansorra with support of Prof. Dr. Clemens Heske and Prof. Dr. Lothar Weinhardt.

For XES measurements, the samples were prepared at KIT, sealed under dry nitrogen, transported to Beamline 8.0.1 of the Advanced Light Source (Lawrence Berkeley National Laboratory), and introduced into the SALSA endstation[135] without exposure to air. N K-edge emission spectra were acquired using a high-transmission soft X-ray spectrometer,[136] with the energy scale calibrated against BN and $CaSO_4$ standards.[137]

A 2PACz reference powder (TCI America, purity >98.0%) was pressed into a pellet inside a nitrogen-filled glovebox. Significant beam-induced spectral changes were observed in the static measurement (*i.e.*, no scanning) and were minimized by scanning the sample under the X-ray beam at 600 μm s^{-1}, corresponding to an effective exposure time of 50 ms per spot. Control measurements confirmed that artifacts observed under static exposure were absent in the scanned data.

3.3 List of Materials

Table 3.5: List of materials used in this thesis. The supplier names stand for Tokyo Chemical Industry Co. Ltd (TCI), Dyenamo, Sigma-Aldrich, Greatcell Solar Materials (Greatcell), Luminescence Technology Corp. (Lumtec) and VWR International (VWR).

Name	Chemical formula	Purity [%]	CAS No.	Supplier
Lead(II) iodide	PbI_2	99.99	10101-63-0	TCI
Lead(II) bromide	$PbBr_2$	99.99	10031-22-8	TCI
Formamidinium iodide (FAI)	CH_6IN_2	99.99	879643-71-7	Greatcell
Methylammonium chloride (MACl)	CH_6ClN	99.99	593-51-1	Dyenamo
Formamidinium bromide (FABr)	CH_6BrN_2	99.99	146958-06-7	Dyenamo
n-Butylammonium iodide (BAI)	$C_4H_{12}IN$	>99	36945-08-1	Greatcell
Propane-1,3-diammonium iodide ($PDAI_2$)	$C_3H_{12}I_2N_2$	high	120675-53-8	Greatcell
Cesium iodide	CsI	>99	7789-17-5	TCI
Cesium chloride	CsCl	>99	7647-17-8	TCI
[2-(9H-carbazol-9-yl)ethyl]phosphonic acid (2PACz)	$C_{14}H_{14}NO_3P$	98	20999-38-6	TCI
(4-(7H-dibenzo[c,g]carbazol-7-yl)butyl) phosphonic acid (4PADBCz)	$C_{24}H_{22}NO_3P$	98	2882156-63-8	Lumtec
Fullerene-C_{60}	C_{60}	99.5	99685-96-8	Sigma-Aldrich
Bathocuproine (BCP)	$C_{26}H_{20}N_2$	99.5	4733-39-5	Lumtec
Magnesium fluoride	MgF_2	99.9	7783-40-6	Sigma-Aldrich
Lithium fluoride	LiF	99.9	7789-24-4	ChemPur
Ethanol (EtOH)	C_2H_6O	99.8	64-17-5	VWR
Silver	Ag	-	7440-22-4	-
Gold	Au	-	7440-57-5	-

4 Industrialization of Perovskite Thin Film Fabrication for Photovoltaics: Strategies to achieve High-Throughput Vapor Deposition Processes

As perovskite photovoltaics transition from laboratory-scale demonstrations toward pilot-line manufacturing, the central criterion is no longer record efficiency alone, but whether perovskite thin films can be deposited reproducibly and at industrially relevant fabrication throughput. Here, vapor deposition offers a mature and scalable tool chain, making it a promising candidate for industrial fabrication of perovskite solar cells. However, the industrial feasibility of adopting vapor deposition for perovskite thin films is governed by precursor thermochemistry, source utilization, deposition-route choice, and equipment demand. In this chapter, the challenges associated with translating laboratory vapor deposition processes to industrially relevant fabrication are evaluated. Specifically, three complementary strategies to realize high-throughput vapor deposition processes are assessed: (1) maximizing deposition rates while identifying thermochemical stability limits of key precursor materials, (2) improving sublimation process effectiveness by evaluation of commonly used deposition routes in a linear source framework, and (3) quantifying the equipment demand required to meet pilot-line throughput targets of 1000 M10-sized wafers h^{-1}. Safe operational windows for rate maximization are derived for the key precursor materials (MAI, FAI, PbI_2, CsI) by systematically evaluating their thermal stability under realistic sublimation conditions. The limited thermal stability of FAI imposes a critical intrinsic bottleneck for maximizing the deposition rate. In addition, reproducible FAI deposition is shown to depend on the crucible geometry and precursor particle-size distribution. Commonly used deposition routes (co-deposition, partially sequential, and fully sequential) are evaluated in terms of process effectiveness, composition control, and source utilization. A bottom-up fabrication-throughput simulation then translates precursor rate limits and deposition route choice into equipment demand with implications for the required capital expenditure. By combining precursor thermochemistry, source engineering, and throughput modeling, this chapter establishes practical design rules for maximizing fabrication throughput and improving process effectiveness for translating vapor-deposited perovskites into scalable, economically viable photovoltaic production.

Parts of this chapter were published in the research article "Industrialization of Perovskite Solar Cell Fabrication: Strategies to achieve High-Throughput Vapor Deposition Processes" *EES Solar* (**2025**) by *Julian Petry*, Viktor Škorjanc, Alexander Diercks, Thomas Feeney, Amedeo Morsa, Sara Rose Kimmig, Jens Baumann, Frank Löffler, Stefan Auschill, Joshua Damm, Daniel Baumann, Felix Laufer, Jona Kurpiers, Michael Müller, Lars Korte, Steve Albrecht, Marcel Roß, Ulrich W. Paetzold and Paul Fassl*. Some figures in this chapter were reproduced or adapted from the original publication with permission from the Royal Society of Chemistry.[36] *Responsible lead and first author.
Julian Petry contributed to this work by developing the research plan and conceptual framework. Julian Petry led the project administration, investigation, data curation, formal analysis and methodology of this work. The original idea was conceived by Ulrich W. Paetzold and Julian Petry. The project was supervised by Ulrich W. Paetzold and Paul Fassl. The contributions of all authors according to the CRediT system are listed in **Table A.5**.

Part of this chapter (Section 4.3.1.1) was published in the research article "Particle Size Matters – Impact of Particle Size and Crucible Geometry on Sublimation Behavior of Formamidinium Iodide", *Adv. Mater. Technol.*, (**2025**), by *Julian Petry*, Alexander Diercks*, Thomas Feeney, Richard Thelen, Paul Fassl and Ulrich W. Paetzold*. Julian Petry and Alexander Diercks contributed equally to this work. Some figures in this chapter were reproduced or adapted from the original publication with permission from Wiley-VCH.[138] *Responsible lead and shared first author.
Julian Petry contributed to this work by conceiving the original idea and conducting the initial tests on the particle size distribution of FAI. Julian Petry and Alexander Diercks jointly developed the research plan. The project was supervised by Ulrich W. Paetzold and Paul Fassl. The contributions of all authors according to the CRediT system are listed in **Table A.6**.

Motivation and Contextualization

Perovskite/silicon (PVK/Si) tandem solar cells (TSCs) represent one of the most promising pathways to surpass the practical efficiency limits of single-junction silicon photovoltaics.[24,139] While record efficiencies have advanced rapidly, the decisive challenge has shifted from performance demonstration to manufacturability at industrial fabrication throughput demands. In monolithic tandem architectures, perovskite top cells must be deposited conformally onto commercially textured silicon bottom cells, which typically employ random pyramidal surface textures (2–5 μm height) to enhance light harvesting.[140–145] Achieving uniform, pinhole-free perovskite layers on these micron-scale features remains difficult for conventional solution-based processes,[139] frequently leading to incomplete coverage and performance losses.[146–148]

Vapor-deposition routes offer a technologically mature and scalable alternative, enabling conformal coating of complex topographies and homogeneous large-area films.[37,39,149–151] Their suitability for both single-junction PSCs and tandem integration has been demonstrated by several milestones: stable co-deposited devices exceeding 20% PCE with >1000 h operational stability,[40] conformal coatings on textured substrates with 15% PCE,[151] large-area vapor-deposited modules (16.6% PCE, 51 cm^2 aperture),[39] and sequentially deposited absorbers reaching 24.4% (*n-i-p* architecture) and 17.8% (*p-i-n* architecture).[106,152] Most recently, vapor-based perovskite top cells integrated into tandems have demonstrated 31.3% PCE, narrowing the PCE gap to conventional solution-based perovskite deposition.[153,154]

Despite these advances, pilot-line implementation of vapor-phase perovskite deposition is not constrained by efficiency alone, but by fabrication throughput and process transferability. Recent techno-economic analyses of PVK/Si tandems indicate that scale expansion alone is insufficient to close the cost gap to crystalline silicon, and that further reductions require process and materials innovation. This places fabrication throughput, source utilization, and equipment demand at the center of industrial relevance.[38,46,139,155,156] At industrial line speeds, the overall cycle time is governed by the slowest deposition steps, typically those requiring thick layers and/or thermally stable deposition rates.[a] In this context, achieving high deposition rates is not just a material property, but a key determinant of equipment demand and manufacturing cost. Achievable precursor flux directly determines required source dimensions, number of deposition stations, and thus the capital expenditure (CapEx).[38] This interplay between precursor thermochemistry, reactor design, and economic feasibility has not yet been quantitatively resolved for vapor-deposited perovskite thin films. Recent efforts to accelerate vapor deposition have demonstrated promising reductions in process time,[157,158] yet reported sublimation rates remain orders of magnitude below the $\sim$1000 nm min^{-1} range projected to be necessary for industrially relevant line speeds required for cost competitiveness compared to solution-based deposition.[38] A thorough assessment of deposition-rate limits and equipment demand under

[a] Cycle time is the processing time required per substrate, while fabrication throughput quantifies the number of substrates produced per unit time. In steady-state in-line production, the slowest process step defines the effective cycle time and therefore limits the fabrication throughput.

pilot-line conditions is therefore essential, as throughput and yield ultimately determine manufacturing cost and commercial viability.

However, a quantitative framework that links precursor-specific rate limits, deposition-route choice, and resulting equipment demand under industrial boundary conditions is still missing. Without such a framework, it remains unclear which process strategies can realistically enable cost-competitive, high-throughput vapor deposition at pilot-line scale. This chapter addresses *Research Objective 1* by deriving quantitative guidelines for industrial scale-up of vapor-phase perovskite deposition, and *Research Objective 4* by identifying intrinsic and reactor-induced factors that limit process transferability and repeatability. To establish a pilot-line reference, continuous operation at 1000 M10 wafers h^{-1} is assumed, corresponding to $\sim$8.76 million wafers a^{-1}. This pilot-line scale fabrication throughput is a first step towards gigawatt peak (GWp) lines with demands of 14000 wafers h^{-1}.

To systematically address this gap, the problem must be decomposed into its fundamental determinants: the intrinsic material limits to increasing deposition rates, the route-dependent process effectiveness and the resulting equipment demand required to meet a defined throughput target. Scaling strategies are classified into vertical scale-up and horizontal scale-out. Vertical scale-up aims to increase throughput by maximizing deposition rates, but is fundamentally constrained by the thermochemical stability of precursor materials. Further, improving the source utilization increases the effective deposition rate without the need of additional equipment. Horizontal scale-out increases capacity through additional or enlarged sublimation sources, which alleviates rate limitations at the expense of increased equipment complexity and CapEx.

To systematically address fabrication throughput, the analysis is structured along three complementary strategies.

Strategy 1: Vertical scale-up through deposition-rate maximization. The thermochemical stability and sublimation behavior of key precursors (FAI and PbI_2) are examined to define safe operational windows for increasing source temperature and vapor flux. This establishes intrinsic material thermal stability limits that determine the potential of vertical scale-up throughput enhancement.

Strategy 2: Improvement of process effectiveness. Commonly applied deposition modes are evaluated within a linear source framework to quantify material utilization, compositional control, and effective source usage.

Strategy 3: Horizontal scale-out toward pilot-line throughput. Experimentally derived vapor-flux distributions from laboratory-scale point sources are translated into conceptual industrial linear-source configurations. Based on the spatial vapor-flux distributions, the number and dimensions of sources required to achieve a target throughput of 1000 M10 wafers h^{-1} are estimated, enabling direct assessment of equipment demand and capital expenditure implications.

By integrating precursor thermochemistry, source engineering, and throughput modeling within this framework, this chapter establishes a manufacturing-oriented basis for vapor-deposited perovskite thin

film fabrication. The identification of organic precursor sublimation as the dominant bottleneck further motivates the process-route decoupling and interface-control strategies developed in subsequent chapters, thereby advancing the overarching goal of robust, high-throughput, and economically viable perovskite photovoltaic manufacturing.

4.1 From Laboratory Processes towards Pilot Line Fabrication

Industrial linear-source configurations impose a change in the design space compared to laboratory point sources, which are not feasible for industrial application as illustrated in **Figure 4.1**. Because the substrate carrier is transported perpendicularly relative to the linear sources for in-line fabrication, achievable film uniformity and composition control depend on the spatial vapor-flux distribution, the overlap of the vapor fluxes of adjacent sources, and the degree to which deposition steps can be combined without sacrificing stoichiometric control. As a result, process choices such as co-deposition *versus* (partially) sequential deposition must be evaluated by both device performance and by their process effectiveness (*i.e.* maximizing the potential of a given setup) and demanded horizontal scale-out required to meet the target throughput. This motivates a quantitative process assessment of rate limits and source utilization under realistic constraints.

Accordingly, this chapter establishes operational boundaries for stable high-rate sublimation, quantifies precursor-specific vapor-flux profiles relevant to linear sources, and uses these inputs to estimate the linear-source scale required to achieve pilot-line-scale throughput.

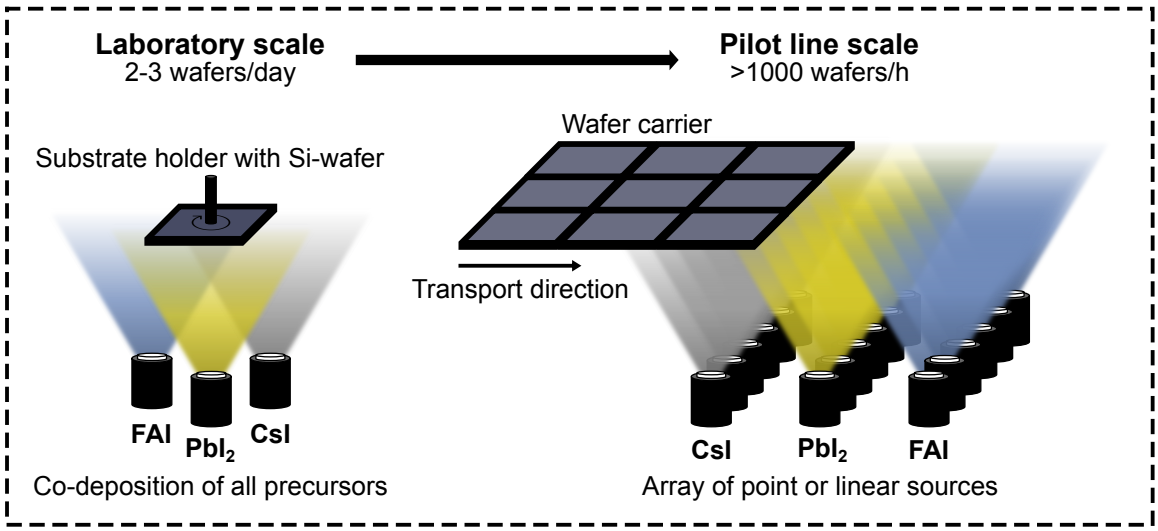

Figure 4.1: Comparison of laboratory- and pilot-scale production setups. Laboratory-scale fabrication commonly uses co-deposition of all precursors, with sublimation sources positioned off-center relative to the substrate to achieve material mixing. Pilot-scale production uses moving wafer carriers that pass perpendicularly through the array of industrial-scale point- or linear deposition sources. Reproduced/Adapted with permission from the Royal Society of Chemistry.[36]

4.2 Strategy 1: Vertical scale-up through Deposition-Rate Maximization

A strong lever to raise production throughput without introducing additional CapEx is to increase the effusion rate of perovskite precursor materials, whose potential is evaluated by maximizing the source temperature while mitigating thermal precursor decomposition. Potential limits on achievable effusion rate and throughput are addressed by establishing a fundamental understanding of precursor thermal stability under sublimation conditions before eventual thermal decomposition. This analysis is essential because the maximum thermally stable effusion rate directly defines the upper limit of achievable deposition rates and therefore sets the limit for vertical scale-up of fabrication throughput. Critical components in this context are PbI_2, CsI, FAI, and MAI, as they contribute most to common perovskite compositions.[159] Each component exhibits distinct sublimation behavior that can, in turn, constrain the achievable fabrication throughput. Accordingly, each material is sublimed at stepwise increasing temperatures in a Duran tube sublimation setup as depicted in **Figure 4.2**. Three fractions are harvested after sublimation: A crucible residue, a main fraction and volatiles deposited under active cooling. Harvested materials are analyzed to track potential compositional changes and identify potential decomposition products. Additionally, the evolving gas phase under sublimation is monitored to elucidate decomposition reactions at elevated temperature using Knudsen effusion mass spectrometry (KEMS).

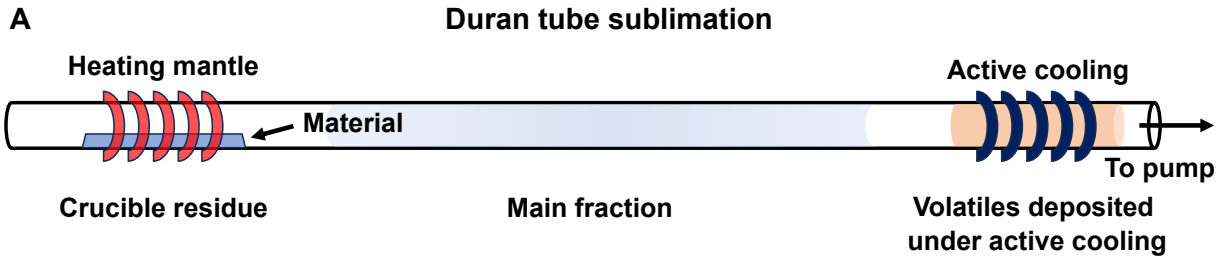

Figure 4.2: Illustration of the used Duran tube sublimation setup. Material is heated with a heating mantle and material deposits at different areas in the Duran tube. Active cooling deposits volatile species at the end of the Duran tube. Adapted with permission from the Royal Society of Chemistry.[36]

4.2.1 Thermal Stability of Organic Precursor Materials

Thermal Stability of Methylammonium Iodide

Controlled, reproducible sublimation of organic perovskite precursors is widely recognized as one of the most pressing challenges for the adaptation of vapor deposition.[97,99–102,158,160] The sublimation of MAI is frequently described as omnidirectional and cloud-like,[44] rendering rate control *via* a conventional quartz crystal microbalance (QCM) non-trivial.[102] Reported strategies to improve process control include tracking the MAI-induced background pressure and/or positioning a QCM to detect PbI_2 and MAI

simultaneously, thereby approximating the net $MAPbI_3$ formation rate.[101] At lower temperatures, MAI dissociation into methylamine and hydroiodic acid (HI) dictates the sublimation dynamics. Reliable rate control is challenging as the MAI sticking coefficient on the QCM depends on precursor purity, which can vary with synthesis route, further complicating reproducible rate control.[99–102] Several studies on MAI purity indicate strong effects of phosphorus-containing impurities on its sublimation characteristics, with methylammonium hypophosphite (MAH_2PO_2) and methylammonium phosphonate (MAH_2PO_3) being the most commonly observed impurities.[99–102] Thermal cracking of MAI has been observed above 170 °C with formation of methyl iodide (CH_3I) and ammonia (NH_3).[161,162]

To assess the thermal stability of MAI under sublimation conditions, MAI is sublimated in the previously described Duran tube setup in a temperature range of 160-240 °C. The collected fractions are analyzed by nuclear magnetic resonance (NMR) spectroscopy with corresponding ^{1}H-NMR and ^{31}P-NMR spectra are shown in **Figure 4.3**. No evidence of MAI decomposition is observed across this temperature window. This observation is unexpected given the comparatively low reported thermal stability of MAI.[163] It can be hypothesized that, during sublimation, a significant fraction of the supplied thermal energy is consumed by the phase transition from solid to vapor, thereby limiting further temperature increase of the material. As a consequence, excess thermal energy may be predominantly utilized for the phase transition rather than for heating the material. Phosphorus-containing species are detected among the volatiles condensed under active cooling at 180 and 200 °C and are assigned to MAH_2PO_2 based on characteristic ^{1}H resonances at 6.22 and 7.83 ppm.[100] A red-colored residue accumulates in the crucible upon heating, the identity of which remains unresolved because characterization is hindered by low solubility in common organic solvents.

Although MAI is not the primary focus for high-efficiency FA-based compositions, these findings highlight general challenges associated with organic precursor sublimation, which are directly relevant for FAI and other organic salts discussed in the following section.

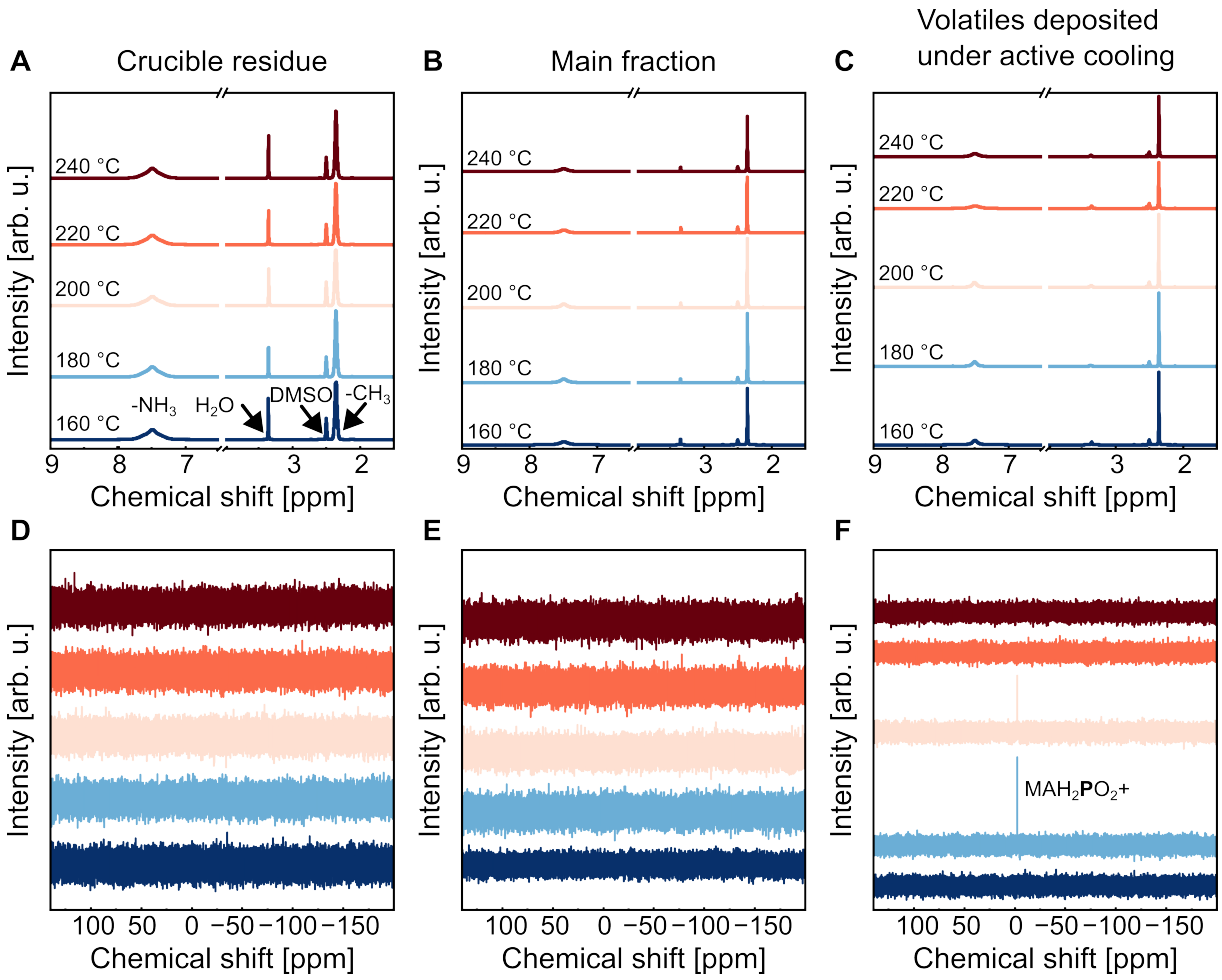

Figure 4.3: MAI remains thermally stable during sublimation between 160 and 240 °C, with only minor phosphorus-containing volatiles detected. ^{1}H-NMR (**A**-**C**) and ^{31}P-NMR (**D**-**F**) NMR spectra of fractions collected during MAI sublimation in the Duran tube setup in a temperature range of 160–240 °C are shown. No additional ^{1}H signals attributable to MAI decomposition products are observed across this range, while ^{31}P spectra of volatile fractions condensed at 180 and 200 °C reveal phosphorus-containing species assigned to MAH_2PO_2 based on characteristic ^{1}H resonances at 6.22 and 7.83 ppm.[100] Adapted with permission from the Royal Society of Chemistry.[36] NMR: Nuclear magnetic resonance

Thermal Stability of Formamidinium Iodide

The comparatively lower intrinsic thermal stability of MA-based perovskite thin films has motivated the adoption of FA-based compositions.[103,106,164,165] However, studies of FAI decomposition under sublimation conditions are scarce. Recent work indicates that thermal cracking of FAI occurs above ∼200 °C with fragmentation to 1,3,5-triazine, ammonia, and hydrogen cyanide. Critically, there is no experimental evidence that these cracking products are incorporated into the perovskite lattice.[97] Given its lower thermal stability compared to inorganic precursors, FAI is expected to impose a fundamental

limitation on achievable deposition rates and thus represents a critical bottleneck for high-throughput vapor deposition. Extending knowledge of the accessible temperature range of FAI sublimation is critical for maximizing the potential of effusion rate while mitigating thermal decomposition reactions. In a first step, FAI is sublimated in the Duran tube setup in a temperature range of 190-260 °C with optical photographs of the crucible residue, the main fraction, and the volatiles deposited under active cooling shown in **Figure 4.4**. Clear differences are apparent under visual inspection. The crucible residue shows progressive discoloration from colorless/off-white at low temperature to yellow and, above 240 °C, to gray/black, indicating precursor decomposition and coke formation. In contrast, the main fraction remains largely unchanged in visual appearance, showing only a slight off-white discoloration even at a temperature of 260 °C. The volatiles deposited under active cooling show the most significant discoloration and turn orange at 260 °C.

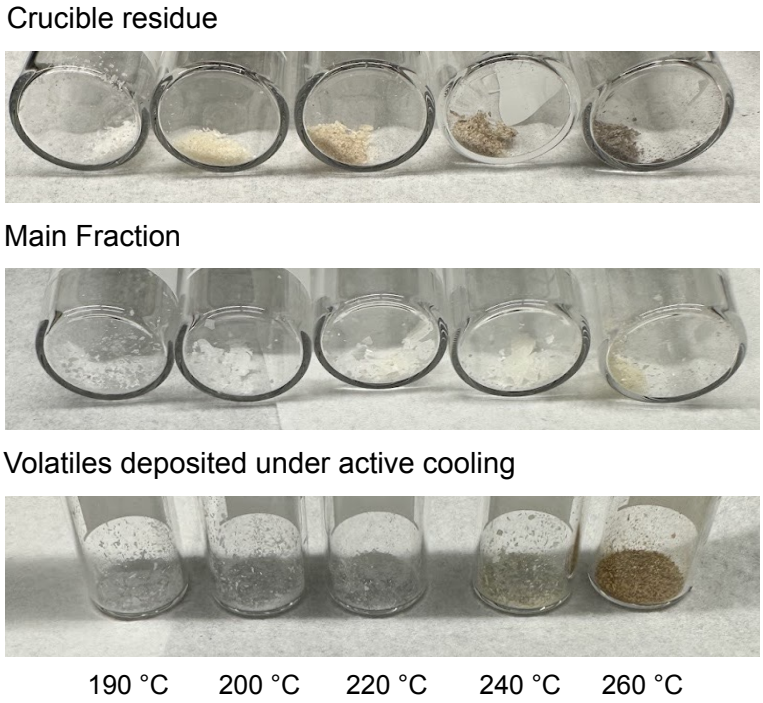

Figure 4.4: Optical photographs of FAI powder collected after Duran tube sublimation. Reproduced with permission from the Royal Society of Chemistry.[36]

The observations of material discoloration give a first indication of substantial chemical transformation of FAI at elevated temperatures motivating further investigations by NMR spectroscopy measurements with ^{1}H-NMR spectra depicted in **Figure 4.5 A-C**. Samples exposed to temperatures above 240 °C exhibit broadening of the characteristic amidine ^{1}H signal at 8.80 ppm, with additional peak splitting at 260 °C. This behavior is attributed to Lewis-acid effects.[103,166] In the present case, an increased hydroiodic acid (HI) content as a result of FAI dissociation is hypothesized. Consistently, the main fraction exhibits a yellow discoloration above 240 °C together with splitting of the 8.80 ppm amidine signal. An additional signal at 7.09 ppm, assigned to ammonium iodide (NH_4I), indicates formation of NH_3 and HI *via* FAI

dissociation/thermal cracking.[97] The detection of NH_4I is critical because deposition on a cold substrate could influence the perovskite formation. However, under typical operation the substrate is near room temperature, so NH_4I condensation is not expected. No additional impurities are detected for sublimation temperatures below 240 °C. Volatiles condensed under active cooling exhibit discoloration only for temperatures above 240 °C, while NH_4I is detected at all temperatures. Traces of FAI are observed above 240 °C, consistent with increased material transfer distance at higher temperature. In all cases, no characteristic 1,3,5-triazine ^{1}H signals are observed, likely due to its volatility and insufficient external cooling to allow for material deposition.

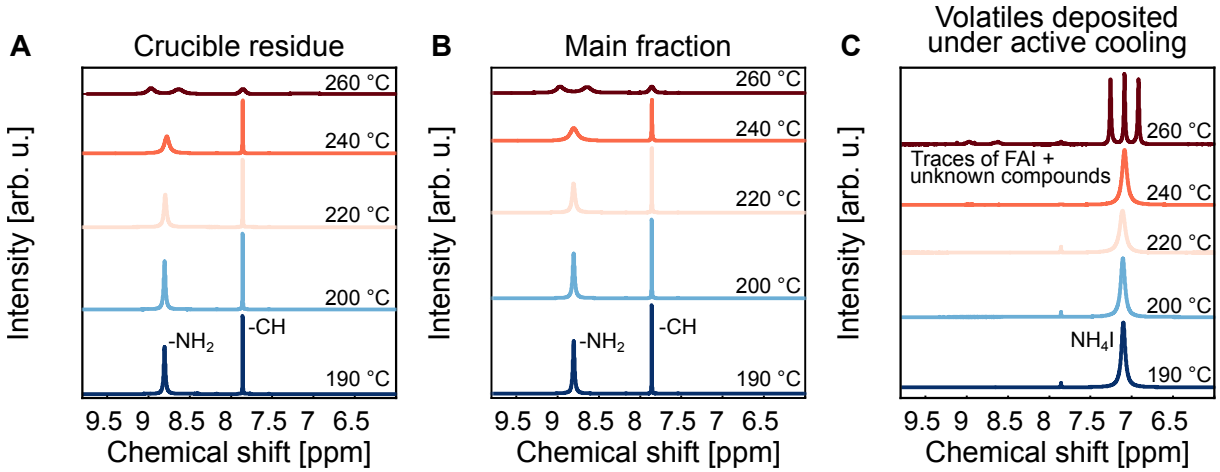

Figure 4.5: ^{1}H-NMR spectra of collected material for increasing sublimation temperatures. Characteristic FAI signals of -NH_2 and -CH signals are annotated. Ammonium iodide is observed in all fractions of the volatiles deposited under active cooling. Reproduced with permission from the Royal Society of Chemistry.[36] NMR: Nuclear magnetic resonance

The molecular identity of species effused from a point source is probed by KEMS as a function of temperature (**Figure 4.6**). A quasi-equilibrium within the source is maintained by using a semi-closed effusion cell with a small orifice, such that only a minor fraction of material is effused at any time, minimizing disturbance of the internal equilibrium.[167,168] For FAI, eight ionic signals, assigned to either molecular ions or fragments, are observed: NH_3^+ ($m/z = 17$), CN^+ ($m/z = 26$), HCN^+ ($m/z = 27$), FA^+ ($m/z = 44$), 1,3,5-triazine$^+$ ($m/z = 81$), I^+ ($m/z = 127$), HI^+ ($m/z = 128$), and I_2^+ ($m/z = 254$) (**Figure 4.6 A**).[b] The nominal m/z of NH_4^+ equals that of H_2O^+ (both $m/z = 18$), and thus cannot be deconvoluted. The mass spectrometry measurements are of qualitative nature, with absolute ion intensities not necessarily reflecting gas-phase abundances because of ion specific ionization cross sections. However, comparing temperature-dependent trends can reveal previously underexplored correlations of molecular generation channels. Specifically, HI^+, I^+, and triazine$^+$ follow a similar trend, whereas FA^+ and

[b] In mass spectrometry, m/z denotes the mass-to-charge ratio of an ionized species. Since fragments can be multiply charged and their trajectories in a magnetic field are influenced by both mass and charge, the detected signal is expressed as m/z rather than mass alone.

CN^+/HCN^+ display a common minimum near 130 °C followed by an increase that anti-correlates with I_2^+. Because FA^+ and HCN^+ are formed from FAI dissociation and thermal cracking, respectively, these trends indicate a coupled, multi-step gas phase reaction during FAI sublimation that includes triazine-forming channels.

Temporal stability of the material effusion is critical for industrial fabrication campaigns, which requires long-time and continuous deposition of material of same composition and quality. To assess the temporal stability of material effusion, isothermal KEMS is conducted at the two temperatures of 130 °C and 150 °C. At 130 °C, all ion intensities stabilized and remained constant within experimental accuracy. After ∼20 h, ≈95% of the material in the crucible is consumed (**Figure 4.6 B**). At 150 °C, rapid decrease of all ion intensities occurred within ∼5 h as the loaded material depletes (**Figure 4.6 C**).

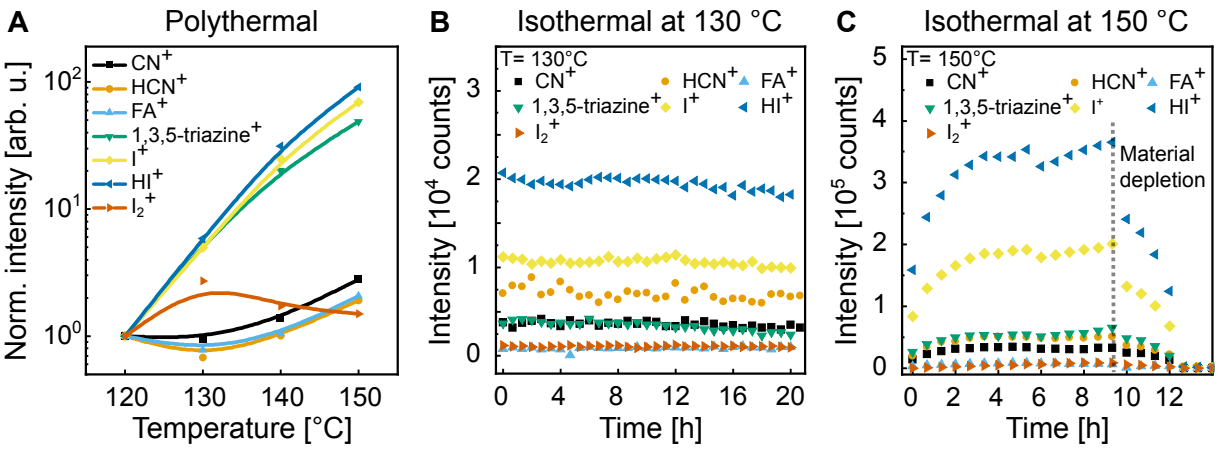

Figure 4.6: The gas-phase chemistry of FAI changes with temperature. **A** Polythermal KEMS measurements of pristine FAI with increasing temperature. Lines are guides for the eye. **B**/**C** Isothermal KEMS measurements at 130 and 150 °C, respectively. Adapted with permission from the Royal Society of Chemistry.[36] KEMS: Knudsen effusion mass spectrometry

To conclude, FAI sublimation above ∼220-240 °C results in significant material decomposition, including coke formation in the crucible residue, consistent with prior reports of FAI thermal cracking.[97] As the formed coke is not emitted from the crucible, this temperature window may represent a compromise between maximizing the effusion rate and limiting decomposition. Notably, discrepancies between the composition of deposited solids and the gas phase are observed: while the gas composition shifts with temperature, the main-fraction chemical composition remains identical, implying selective deposition of FAI from the vapor. A potential explanation is that additional species (*e.g.*, triazine-, HI-, or HCN-related products) do not co-crystallize with the FAI lattice due to differences in lattice constants and charge. In practice, this suggests that higher crucible temperatures might be tolerated to increase the effusion rate, as decomposition products either remain in the crucible in the form of coke or exhibit limited deposition on near-ambient temperature substrates (*e.g.*, NH_4I). Feeney *et al.* conducted a first study of the effect of the perovskite deposition rate on the actual performance of the device for FA-based perovskite solar cells, showing a decrease in device performance for higher perovskite deposition rates. Mitigation strategies

include using multiple crucibles for FAI or material preconditioning, achieving device performance comparable to the slower baseline process. Carbon-rich spit defects are observed resulting in shunted PSCs. This provides initial evidence that the emission of coke particles may depend on the specific source design and needs to be considered.[41] Other organic halide salts such as MACl, MABr, FABr, and FACl are not commonly used in vapor-phase perovskite deposition. To date, only two reports describe the use of sublimed MACl, either as a bulk additive in a sequential process or co-deposited together with MAI from a common MAI:MACl pellet.[169,170] Experiments performed with FABr showed limited suitability due to melting already at approximately 120 °C. In contrast, mixtures of MAI and MABr are utilized in close-space sublimation processes to enable bandgap tuning of the perovskite absorber. Further studies targeted to elucidate the thermal stability and usability of these compounds is necessary for adopting them in stable deposition processes.

4.2.2 Thermal Stability of Inorganic Precursor Materials

Because MAI/FAI are the most temperature-sensitive precursors, potential limitations of the inorganic deposition is often not considered in conventional co-deposition. However, considering a two-step route with decoupling of the FAI deposition, this assumption no longer necessarily holds as the inorganic scaffold can be deposited at substantially higher rates, requiring higher source temperatures and longer high-flux operation especially considering industrial high-throughput fabrication demands. In that regime, thermal degradation of inorganic precursors can become a practical limit to rate acceleration and reproducibility. This provides the rationale for a focused study of the thermal stability of inorganic precursors.

Thermal Stability of Cesium Iodide

Cesium is commonly incorporated into FA-based thin films to stabilize the photoactive α-perovskite phase with the A-site Cs fraction on the order of 5-20%.[103,171–173] Accordingly, the CsI sublimation rate is not expected to be a rate-limiting factor, especially compared to PbI_2 and FAI. Polythermal KEMS measurements are performed for CsI revealing temperature-dependent changes in gas-phase composition, with signals assigned to Cs^+, I^+, CsI^+, and the oligomeric ions Cs_2I^+ and $Cs_2I_3^+$ being identified (**Figure 4.7**). The normalized intensities of Cs^+, I^+, CsI^+, and Cs_2I^+ show a correlation, which indicates that sublimation of CsI proceeds in the form of $(CsI)_n$ clusters, which undergo fragmentation induced by electron-ionization in the mass spectrometer. The $Cs_2I_3^+$ signal emerged above ∼440 °C, reflecting the higher thermal energy required to release larger $(CsI)_n$ clusters from the $(CsI)_x$ lattice. Although the sublimation rate of CsI is not expected to limit the overall deposition process, the observed temperature-dependent changes in gas-phase composition may influence film formation through variations in the arriving species.

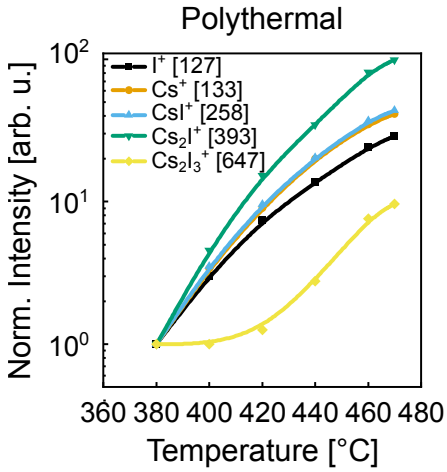

Figure 4.7: Polythermal KEMS measurement of CsI with observed species. Reproduced with permission from the Royal Society of Chemistry.[36] KEMS: Knudsen effusion mass spectrometry

CsCl and CsBr have been used as inorganic cesium sources in vapor-phase perovskite deposition in several studies,[107,124,154,174] with no reports of significant thermal decomposition under typical laboratory conditions. However, the reported deposition rates are generally low, and a systematic investigation of their sublimation behavior and stability at elevated fluxes relevant for industrial-scale processing remains necessary. A first investigation of the effect of increased CsCl deposition rate (range of 0.1 to 0.8 Å /s) in case of a hybrid-two step process shows no detrimental influence on device performance (**Chapter 6.3.1**).

Thermal Stability of Lead Iodide

In the following section, a critical assessment of safe operational guidelines for the sublimation of PbI_2 with respect to the maximum applicable source temperature is conducted. Particular attention is given to PbI_2, as its deposition can represent a throughput-limiting step in vapor-based perovskite fabrication. In typical thin-film stacks used for two-step deposition processes, PbI_2 constitutes the dominant fraction of the inorganic scaffold and therefore contributes substantially to the overall film thickness.[106,107,112,169,174] As thin film layers with thicknesses of several hundred nanometers are commonly required, comparatively high PbI_2 deposition rates are necessary to meet industrial cycle-time constraints and fabrication throughput demands. Consequently, any limitation in the maximum stable deposition rate of PbI_2 directly translates into reduced fabrication throughput.

A decomposition temperature of ∼872 °C is reported for PbI_2 under ambient conditions.[175] However, no systematic thermal stability assessment under reduced-pressure sublimation conditions has been reported to date. To fill this knowledge gap, PbI_2 is first sublimed at increasing temperatures under high-vacuum conditions ($<10^{-6}$ mbar). Material decomposition accompanied by the formation of metallic lead is observed when the source temperature exceeds 300 °C. Representative optical photographs of PbI_2 collected from the crucible at source temperatures below and above ∼300 °C are shown in **Figure 4.8**. The onset of

decomposition at approximately 300 °C is particularly critical, as it significantly constrains the maximum achievable effusion rate, especially in comparison to the reported ambient-pressure decomposition temperature of 872 °C.[175] This apparent contradiction suggests that the observed decomposition is not an intrinsic material limitation but rather a consequence of the specific experimental conditions, necessitating a detailed analysis of heat transfer and thermal equilibrium effects within the source.

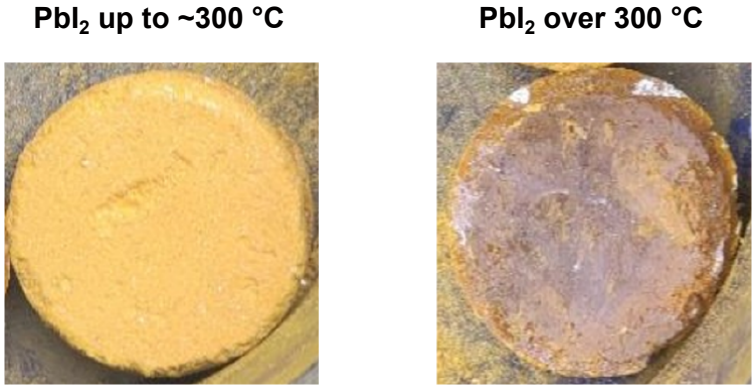

Figure 4.8: Optical photographs of PbI_2 recovered from a sublimation crucible after heating up to ∼300 °C and over 300 °C. For temperatures above ∼300 °C, formation of grey metallic lead is observed.

In order to understand the discrepancy between the observed decomposition at ∼300 °C and the reported decomposition temperature of 872 °C, thermogravimetric analysis (TGA) and complementary differential scanning calorimeter (DSC) measurements of pristine PbI_2 powder are conducted. Mass loss of PbI_2 is tracked *versus* temperature. A residual mass of ∼45% corresponds to complete decomposition (representing the Pb mass fraction of PbI_2), whereas values $< 45\%$ signify PbI_2 volatilization rather than stoichiometric decomposition. Under ambient pressure, the residual weight decreases slightly up to a temperature of 500 °C, which is associated with evaporation of residual water or solvents in the material (**Figure 4.9 A**). Melting of the material is indicated by an endothermic peak at a temperature of 403 °C and an enthalpy of 58.5 J/g, in agreement with the literature value of 402 °C.[175] A decrease of residual weight is observed for temperatures above 500 °C as a consequence of evaporation from the melted state. Lower process pressures are hypothesized to potentially accelerate PbI_2 decomposition as volatile iodide is removed from the system, effectively shifting the reaction equilibrium towards the decomposition products. At reduced pressures of $\sim 10^{-2}$ and $\sim 10^{-4}$ mbar, the first derivative of weight (d Weight) maximum shifted to 347 °C and 362 °C, respectively (**Figure 4.9 B**). The residual weights for both pressure ranges approach 0% as the material quantitatively sublimes from the solid state without evidence of degradation. Consequently, the pressure range does not influence the decomposition of PbI_2.

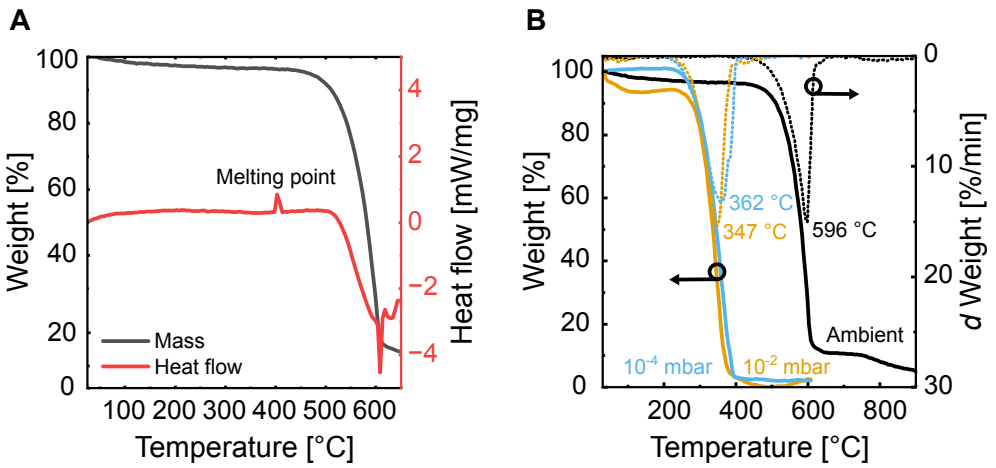

Figure 4.9: **A** TGA (black line) and DSC (red line) measurement of PbI_2. **B** TGA analysis under varying pressure ranges. Solid lines represent the weight and dotted lines the differential weight. Adapted with permission from the Royal Society of Chemistry.[36] TGA: Thermogravimetric analysis, DSC: differential scanning calorimeter, *d* Weight: first derivative of weight

A sublimation series using the Duran tube setup with a stepwise increasing temperature is conducted, which enables a more homogeneous and controlled temperature distribution within the material in the crucible. Subsequently, a compositional analysis of the harvested material *via* inductively coupled plasma optical emission spectroscopy (ICP-OES) measurements on crucible residue, main fraction, and volatiles deposited under active cooling is performed (**Figure 4.10**). PbI_2 material composition can deviate from the stoichiometric iodine to lead (I:Pb) ratio of 2 with values reported being in the range of the I:Pb ratio ∼1.8-2.1.[168] Temperature-induced changes in I:Pb can thus indicate a potential material decomposition. For the crucible residue, a slight apparent decrease was observed with temperature (I:Pb ratio of 2.05 to 2.02; **Figure 4.10 A**), near the analytical uncertainty. The I:Pb ratio of the main fraction remained constant within error (**Figure 4.10 B**), while the fraction of the volatiles deposited under active cooling presents a marginally higher I:Pb ratio of ∼2.04 (**Figure 4.10 C**). This observation implies that material decomposition does not occur in the probed temperature range. This is significant as it already exceeds the typical maximum operational temperatures of around 300 °C in the used laboratory setup by more than 150 °C, a strong lever to increase the deposition rate. It is hypothesized that the control and homogenization of the heat distribution within the crucible is decisive to mitigate material decomposition. The use of different crucible shapes (*i.e.* cylindrical *vs.* conical crucible) can improve the heat distribution, increasing the thermal decomposition threshold.[41]

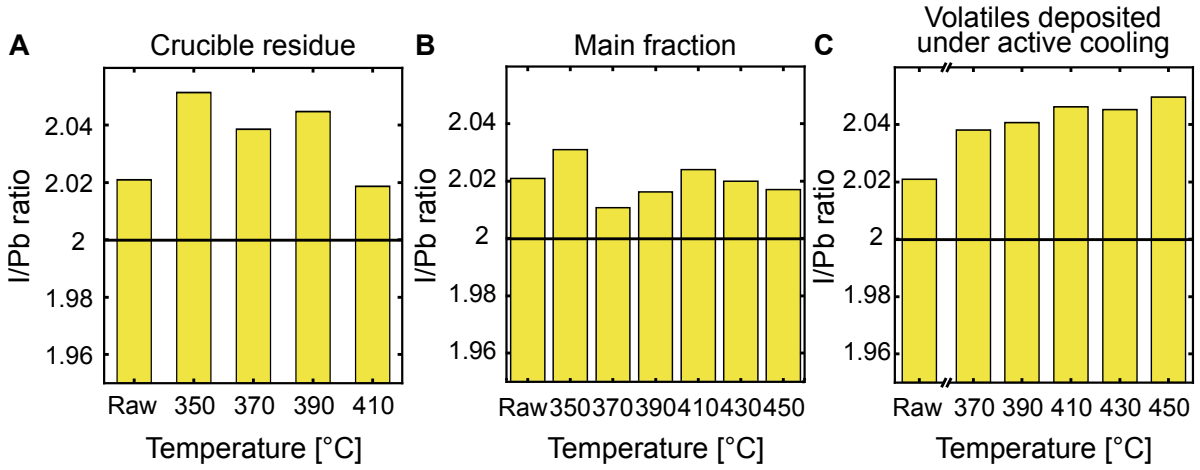

Figure 4.10: ICP-OES analysis of PbI_2 after sublimation at increasing temperatures. Reproduced with permission from the Royal Society of Chemistry.[36] ICP-OES: Inductively coupled plasma optical emission spectroscopy

Complementary investigation of potential gas phase reactions is performed by KEMS measurements where I^+ ($m/z = 127$), Pb^+ ($m/z = 208$), I_2^+ ($m/z = 254$), PbI^+ ($m/z = 335$), PbI_2^+ ($m/z = 462$), and PbI_4^+ ($m/z = 716$) ions are observed (**Figure 4.11 A**). I^+, Pb^+, PbI^+, and PbI_2^+ evolve in parallel, consistent with PbI_2 fragmentation due to the electron ionization process. I_2^+ and PbI_4^+ are detected at temperatures above ~275 °C, implying gas-phase oxidation of Pb^{II} to Pb^{IV}. A dimeric form of Pb_2I_4 is thermodynamically predicted by the FactSage database but is experimentally not observed.[176] Isothermal KEMS measurements at 250 °C show stabilized ion intensity within ~3 h and remained constant for ~25 h. At higher source temperatures of 270 °C, rapid material depletion occurred within ~4 h (**Figure 4.11 B**).

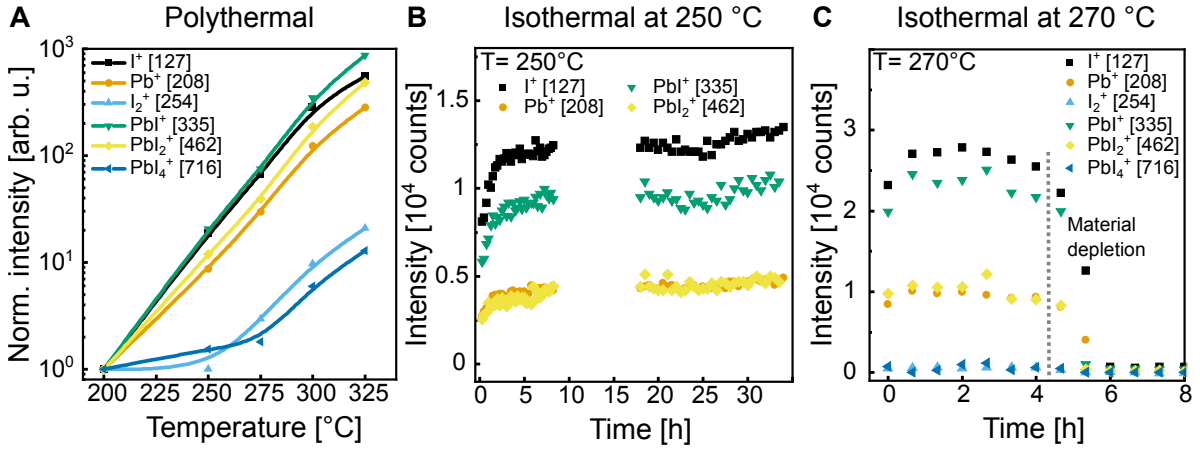

Figure 4.11: **A** Polythermal KEMS measurements of PbI_2 with increasing temperature. Lines are guides for the eye. **B**/**C** Isothermal KEMS measurements at 250 and 270 °C, respectively. In case of **B**, the measurement was restarted, explaining the missing data points. Adapted with permission from the Royal Society of Chemistry.[36] KEMS: Knudsen effusion mass spectrometry

Differences in the gas-phase and deposited material composition are observed, with the deposited main fraction remains compositionally invariant in the tested temperature range. This indicates a selective deposition of PbI_2 from the vapor, analogous to FAI. Additional species (*e.g.*, PbI_4) are unlikely to co-crystallize and can revert to PbI_2 + I_2 upon condensation. Across the explored temperature windows, no material decomposition is detected. Insufficient heat transfer and homogeneity in the crucible can explain the deviation of experimentally observed decomposition at source temperatures above 300 °C to the literature value under ambient conditions. No signs of pressure-related accelerated decomposition is observed. In conclusion, observed PbI_2 decomposition over 300 °C in laboratory-scale deposition sources is not an intrinsic material property but rather a consequence of limited heat homogenization within the crucible. With improved source design, higher effusion rates and thus higher deposition rates are achievable. To assess the potential impact of these findings on industrial fabrication, the achievable deposition rates under extended temperature ranges are estimated beyond the experimentally accessible window. In a first estimation, an extrapolation from the experimentally determined deposition rates to higher temperature ranges is conducted. In high vacuum ($\sim 10^{-6}$ mbar), raising the crucible temperature from 180 to 270 °C increased the QCM rate from 0.01 s^{-1} to 0.73 nm s^{-1} (**Figure 4.12 A**). Linear extrapolation implies deposition rates of $\sim$25 nm s^{-1} at 350 °C and $\sim$1800 nm s^{-1} at 450 °C, respectively, which represent the temperature limits determined *via* TGA and DTS experiments (**Figure 4.12 B**). Critically, deposition rates above a threshold of 1000 nm min^{-1} (or 16.7 nm s^{-1}) are cost competitive compared to conventional solution-based processes in terms of production cost ($ W^{-1}) and approach the range of CapEx parity, which is projected at 10 linear sources operating at 12 nm s^{-1} according to Abzieher *et al.*[38] This highlights the yet unused potential of increasing the PbI_2 deposition rate to industrially relevant levels.

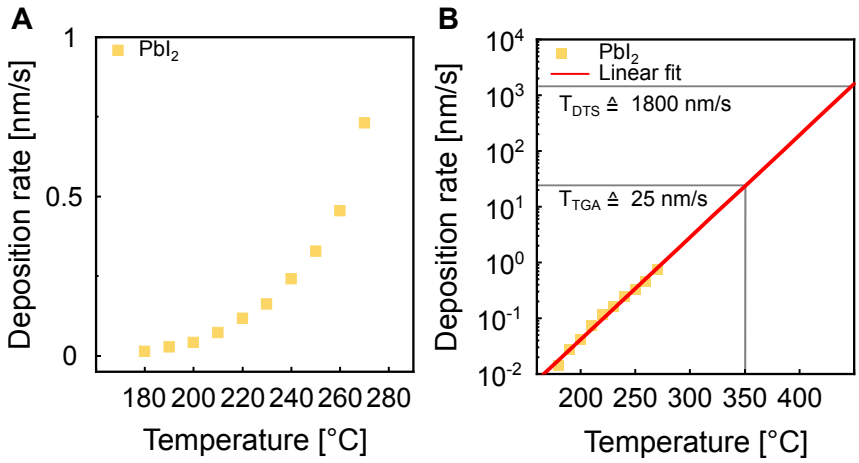

Figure 4.12: A Temperature dependent exponential increase of the static deposition rate of PbI_2. **B** Linear extrapolation of the expected static deposition rate for temperatures from TGA or Duran tube sublimation. Reproduced with permission from the Royal Society of Chemistry.[36] TGA: Thermogravimetric analysis, DTS: Duran tube sublimation

$PbBr_2$ and $PbCl_2$ are used as halide sources in vapor-phase perovskite deposition in several studies,[41,103,123] typically without indications of significant thermal decomposition under laboratory-scale conditions. However, reported deposition rates remain comparatively low, and their sublimation behavior and stability at the elevated fluxes required for high-throughput industrial fabrication requires systematic evaluation.

4.3 Strategy 2: Improvement of Process Effectiveness

While Strategy 1 defines the intrinsic upper limits of deposition rates, these limits alone do not determine fabrication throughput, as the effective utilization of the emitted vapor flux strongly depends on the deposition configuration and source geometry. This section focuses on improving the process effectiveness of vapor deposition, defined here as maximizing the achievable material utilization, uniformity, and controllability within the constraints of an existing deposition setup. Rather than altering the hardware, this strategy aims to optimize how material-specific sublimation characteristics are understood and exploited to enable scalable, industrially relevant vapor deposition.

4.3.1 Modeling of Material-Specific Vapor-Flux Distribution

Insights into the material-specific sublimation characteristics are represented by their respective vapor-flux distributions and are essential to simulate a linear sublimation source in the next step. Therefore, vapor-flux distributions of the relevant perovskite precursor materials CsI, PbI_2, and FAI are experimentally assessed.

Static depositions[c] are performed to produce a lateral thickness gradient on the substrate. The resulting thickness profile provides information on the angular distribution of the vapor flux. This gradient can be approximated by the following expression with:

$$t(x) = A \cdot \frac{\cos^n\left(\arctan\left(\frac{x}{x_h}\right)\right)}{R^2} = A \cdot \frac{\cos^n\left(\arctan\left(\frac{x}{x_h}\right)\right)}{x^2 + x_h^2}, \tag{4.1}$$

where $t(x)$ is the local thickness at lateral distance x from the source axis, x_h is the vertical source-to-substrate distance (SSD), n is an empirical exponent describing the angular broadening of the vapor flux, and A is a normalization factor related to the deposition rate. A derivation of the used expression is presented in Appendix A.1. Knowledge of this spatial vapor-flux distribution is critical for predicting film uniformity, material utilization, and ultimately the achievable dynamic deposition rates in industrial in-line processes. In the present system the vertical SSD is x_h= 300 mm. This expression provides a description of the measured deposition profiles and enables quantitative comparison between different materials and

[c] Static deposition rates (with unit [nm/s]) describe film growth on a stationary substrate under constant flux conditions, whereas dynamic deposition rates (with unit [nm · m/min]) account for substrate motion relative to the source, as in continuous in-line processing. The latter directly governs achievable line speed and production throughput in industrial fabrication.

crucible conditions. In particular, the exponent n reflects the focusing behavior of the vapor flux and thus represents a material- and source-dependent parameter that must be considered when simulating linear source configurations. It should be noted that this model assumes a perfect Knudsen-type effusion cell with an infinitely small orifice, where material effuses without disturbing the thermodynamic equilibrium in the crucible. In practice, open crucibles are used to increase the effusion rate, which leads to deviations from the idealized angular distribution and thus represents a limitation of the model.

4.3.1.1 Particle-Size Dependent Sublimation Behavior of FAI

In vapor-phase deposition, the physical form of the precursor can play a decisive role in determining sublimation behavior and vapor-flux distribution at the substrate. In contrast to conventional solution-based processing, where all precursors are fully dissolved and the initial particle size is therefore assumed to have no influence, the solid-state nature of vapor deposition introduces additional degrees of freedom related to powder properties. As demonstrated in this section, the particle-size distribution of FAI, together with crucible geometry, critically affects the emitted vapor-flux distribution and thus the reproducibility of the vapor deposition, representing an important but previously overlooked parameter in FA-based vapor deposition of perovskite thin films. The vapor flux from a conical crucible is schematically illustrated in **Figure 4.13 A**. Most reports on FA-based thermal sublimation processes use commercially available FAI from "Greatcell Solar Materials".[97,103,106,177,178] Control of the particle-size distribution in the crucible is inherently challenging, as the precursor is transferred manually (*e.g.*, with a spatula) from the bottle into the crucible, leading to an uncontrolled distribution of particle sizes. This variability is further amplified by granular convection (commonly referred to as “Brazil–nut effect”), where agitation of the dry powder causes larger particles to migrate upward (**Figure 4.13 B**). The resulting de-mixing alters the size distribution of particles transferred into the crucible, thereby affecting local sublimation dynamics. As a result, the effective particle-size composition in the crucible varies between experiments, altering sublimation behavior and negatively impacting repeatability. To control the particle size of the used FAI powder, analytical sieves with defined mesh sizes were used to separate the precursor material into three main fractions: small ($100 - 200\,\mu$m), mid ($200 - 500\,\mu$m), and large ($500 - 800\,\mu$m) (**Figure 4.13 C**). The particle-size distribution varies significantly even between synthesis batches and between bottles from the same batch (**Figure 4.13 D**). Such inconsistencies in commercial precursor powders add another layer of complexity to the reproducible vapor deposition.

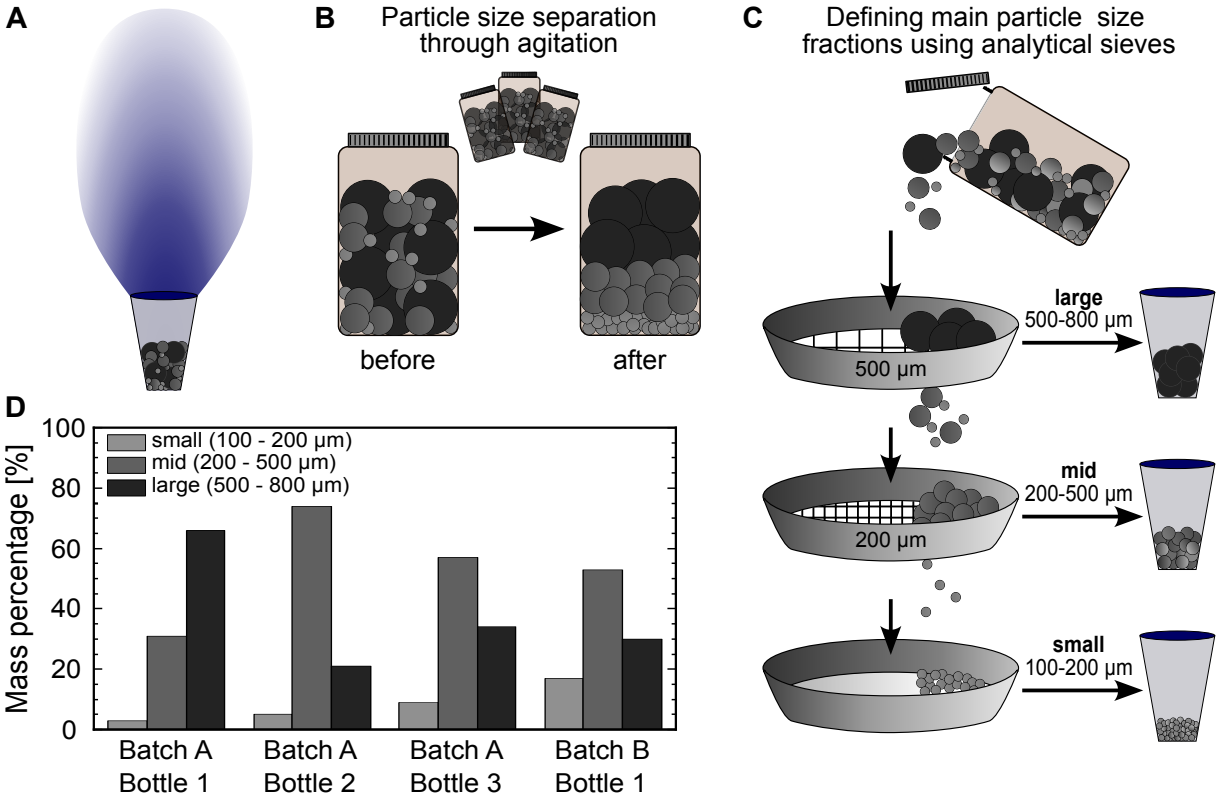

Figure 4.13: **A** Illustration of the FAI vapor flux emitted from a conical crucible. **B** Schematic of the granular convection process ("Brazil–nut effect") showing de-mixing of different particle sizes due to agitation inside a precursor bottle. **C** Procedure to define the main particle-size fractions (small: $100 - 200\,\mu$m; mid: $200 - 500\,\mu$m; large: $500 - 800\,\mu$m) using analytical sieves of different mesh sizes. **D** Particle-size distribution of FAI from "Greatcell Solar Materials" for different bottles and fabrication batches. Reproduced with permission from Wiley-VCH.[138]

To assess the influence of particle-size fraction and crucible geometry on sublimation behavior, effusion characteristics of the three main fractions are examined for conical and cylindrical crucibles. (**Figures 4.14 A/D**) show the corresponding flux geometries. Static deposition is conducted at a nominal rate of $1\,\text{Å}\,\text{s}^{-1}$. For conical crucibles, the static deposition rate profile is found to depend strongly on the particle-size fraction (**Figure 4.14 B**). Given the variability of commercial FAI powders, deviations in the effective deposition rate at the substrate are therefore expected between experiments, negatively affecting repeatability. In contrast, cylindrical crucibles yield nearly identical static deposition rate profiles across all particle-size fractions (**Figure 4.14 E**), together with a de-focusing of the vapor flux compared to the reference conical crucible (**Figures 4.14 C/F**). Resulting fit parameters are summarized in **Table 4.1** . Control of the precursor particle-size distribution is therefore required to achieve reproducible sublimation with conical crucibles. Further, the crucible geometry is a decisive factor for repeatability by determining the effective vapor flux distribution at the substrate for a given nominal deposition rate. Overall, these results identify precursor particle-size distribution and crucible geometry as previously neglected key

control parameters for achieving reproducible FAI sublimation in vapor-deposition of perovskite thin films. Control of the particle-size distribution and choice of a cylindrical crucible geometry can overcome this limitation, improving the process repeatability. This sensitivity to particle-size distribution represents a critical limitation for process transferability from laboratory to industrial scale, where uncontrolled variations in precursor handling can lead to significant deviations in deposition behavior.

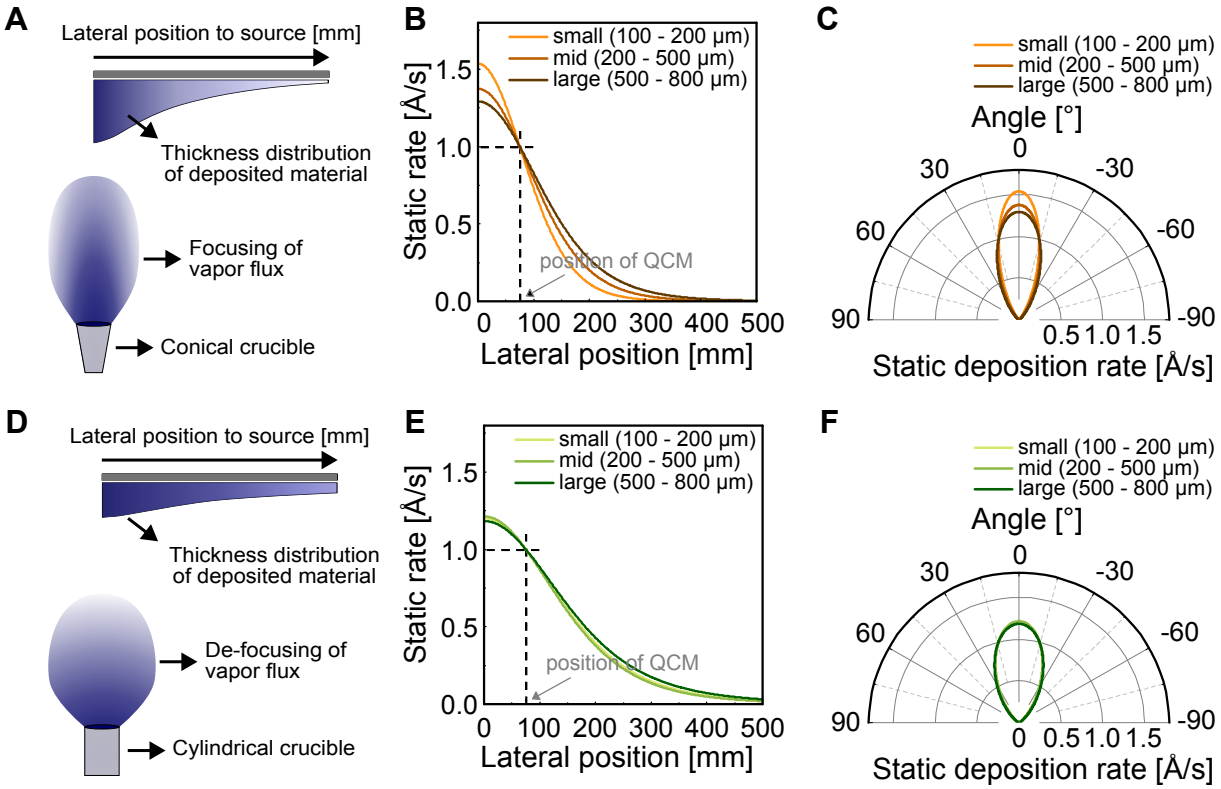

Figure 4.14: **A/D** Schematics of the FAI vapor flux and deposition on the substrate from conical and cylindrical crucibles, respectively. **B/E** Fitted static deposition rate profiles as a function of lateral position relative to the source for conical and cylindrical crucibles, respectively. **C/F** Angular emission dependence on particle size for conical and cylindrical crucibles, respectively. Reproduced with permission from Wiley-VCH.[138]

4.3.1.2 Vapor Flux Distribution of Perovskite Precursor Materials

An overview of the measured thickness gradients for FAI, PbI_2, and CsI is shown in **Figure 4.15 A-C** allowing for a qualitative comparison. Based on the previous findings, cylindrical crucibles are used for the following analysis of all perovskite precursor materials, due to their reduced sensitivity to particle-size fraction and vapor flux defocusing property. For FAI, size-selected powder with a particle size of 200–500 μm (mid fraction) is used. Source temperatures for CsI, PbI_2 and FAI are chosen to maximize deposition rate while remaining below the respective decomposition point.

Table 4.1: Fitting parameters and static deposition rate of FAI for different particle sizes and crucible geometries.

Material	QCM rate [nm s^{-1}]	A [arb.u.]	Exponent n
Conical			
FAI (small)	0.10	$1.10 \cdot 10^8$	12.15
FAI (mid)	0.10	$7.96 \cdot 10^7$	8.46
FAI (large)	0.10	$6.92 \cdot 10^7$	6.45
Cylindrical			
FAI (small)	0.10	$4.51 \cdot 10^7$	4.05
FAI (mid)	0.10	$4.34 \cdot 10^7$	4.33
FAI (large)	0.10	$3.69 \cdot 10^7$	4.52

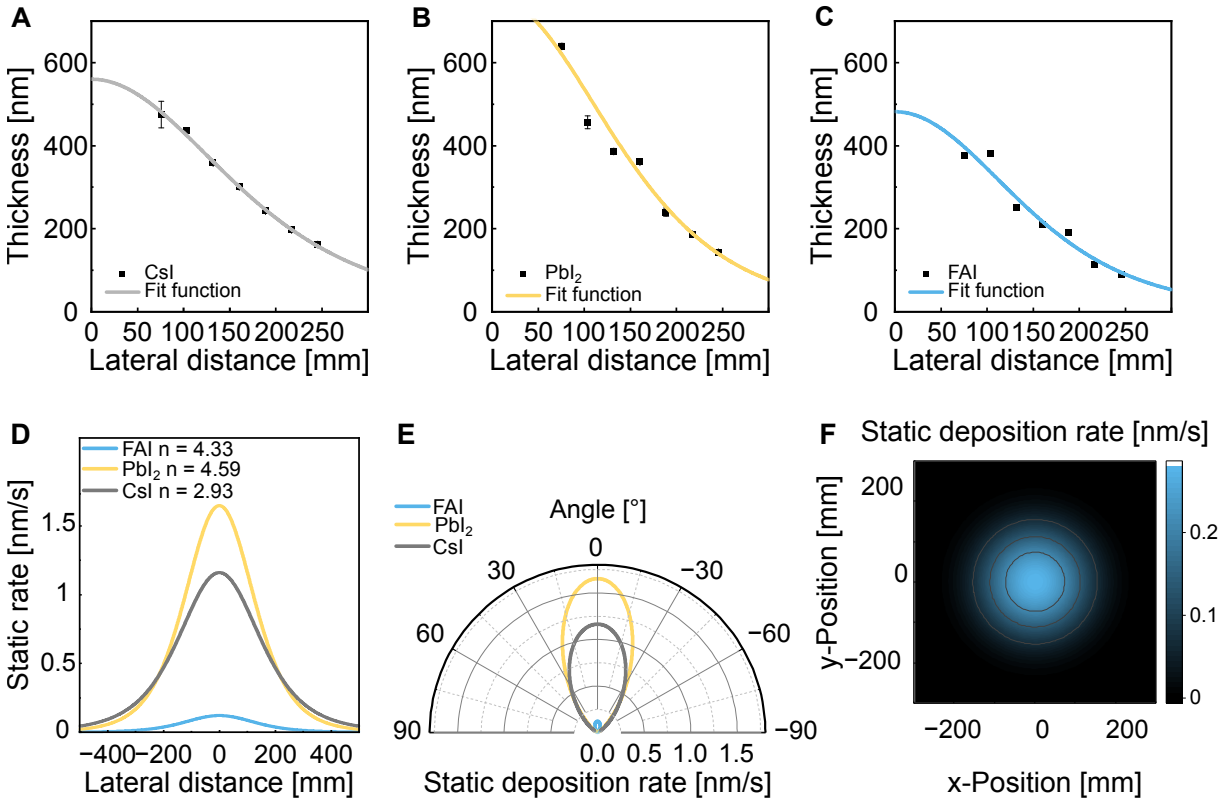

Figure 4.15: Comparison of vapor flux distributions of perovskite precursor materials. **A**-**C** Thickness gradient of CsI, PbI_2 and FAI after static deposition. **D**/**E** Fitted vapor flux distribution for all materials in cartesian and polar coordinates. **F** Spatial static deposition rate map for FAI. Adapted with permission from the Royal Society of Chemistry.[36]

Static thickness gradients of CsI, PbI_2, and FAI were approximated with Eq. 4.1, yielding material- and geometry-specific parameters. For better comparability across materials, the thickness gradients are converted into lateral static deposition-rate profiles by normalizing to the static QCM rate and position (at 75 mm lateral distance) (**Figure 4.15 D-E**). The fitted parameters are summarized in Table 4.2. For FAI, PbI_2, and CsI the exponents n are 4.33, 4.59, and 2.93, respectively, with corresponding full width at half maximum (FWHM) distances of 112 mm, 145 mm, and 170 mm. The extracted exponents indicate a more focused vapor-flux distribution for FAI/ PbI_2 and broader vapor-flux distribution for CsI. The lateral deposition rate profile can be converted to the corresponding spatial deposition rate map assuming rotational symmetry of the effused vapor flux, as shown for FAI in **Figure 4.15 F**. Static deposition rates at the QCM position and rates at FWHM are included in **Table 4.2**. In the next section, these deposition rate profiles are utilized to model a linear source, enabling horizontal scale-out estimation and prediction of dynamic deposition rates and throughput.

Table 4.2: Fitting parameters and static deposition rate of different perovskite precursor materials.

Material	QCM rate [nm s^{-1}]	A [arb.u.]	Exponent n	FWHM distance [mm]	Static rate at FWHM [nm s^{-1}]
FAI (mid)	0.10	$4.34 \cdot 10^7$	4.33	112	0.14
PbI_2	1.35	$6.84 \cdot 10^7$	4.59	145	0.83
CsI	1.00	$5.04 \cdot 10^7$	2.93	170	0.58

4.3.2 Adaptation of Point-Source Emission to Industrial Linear Sources

Motivated by the requirements on throughput and material utilization for industrial perovskite fabrication, commonly used deposition routes are scrutinized for their applicability in industrial context using linear sources.

Scale-up to larger substrates or higher throughput is achieved by the linear alignment of multiple point sources and by transporting the substrates perpendicularly relative to the array. The transition from point to linear sources introduces further considerations, including material utilization and potential fabrication throughput limitations induced by one or more precursor materials. For point sources, uniform material composition is achieved by off-center placement of the sources relative to a rotating substrate. However, this approach is impractical for in-line processing using linear sources. A possible configuration involves orienting multiple linear sources inclined toward a common point (**Figure 4.16 A**), resulting in material gradients that may affect perovskite properties. Uniformity can be improved by the addition of apertures, however at the cost of reduced material utilization. Whether an aperture is required is determined by the system's sensitivity to compositional variations.[124,179] A further consequence of the co-deposition configuration is that the overall deposition rate is limited by the slowest component, as all other deposition rates must be adjusted relative to it.

Because both FAI and MAI are prone to thermal decomposition, decoupling the deposition of the organic precursors from the inorganic precursors is desirable to maximize production throughput. Partial mitigation of rate limitation due to FAI/MAI deposition is achieved when using a two-step deposition process. In the first step, an inorganic scaffold is deposited, followed by deposition of an organic-cation layer and conversion to the final perovskite phase *via* an additional thermal annealing step. Two variants of the inorganic-scaffold step are distinguished: co-deposition (type A) and sequential deposition (type B) (**Figure 4.16 A-C**). In the literature, co-deposition is predominantly used to form the inorganic scaffold in both PVD/PVD and hybrid PVD/solution-based processes.[29,111,117,124,169,180,181] Conversely, the highest material utilization can be achieved by fully sequential sublimation. In this method, the material flux is directed onto the substrate carrier without the use of an aperture, and a "pseudo" sequential deposition is produced owing to partial overlap of the vapor fluxes.

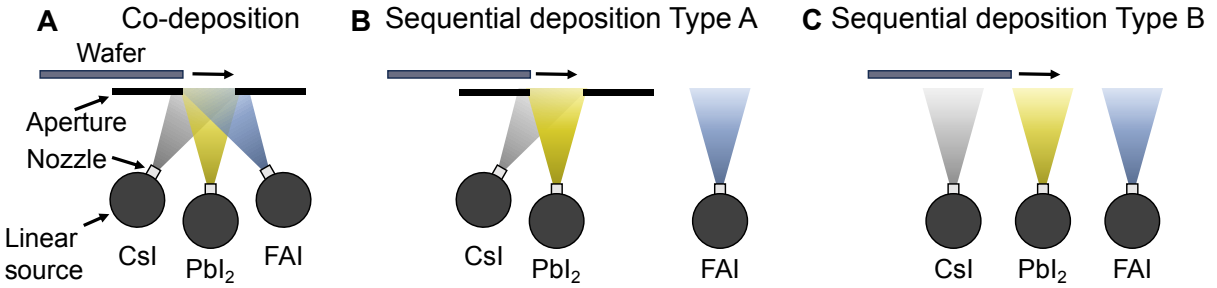

Figure 4.16: Comparison of different linear source arrangements for **A** co-deposition and **B**/**C** sequential deposition. For sequential deposition, two types are differentiated: Type A with co-deposited inorganic scaffolds and Type B using fully sequential layer deposition. Reproduced with permission from the Royal Society of Chemistry.[36]

To conclude, the fully sequential deposition (Type B) shows the highest process effectiveness as all sources can be operated at maximum deposition rate and will be considered as the baseline process in the next section to quantify differences in required horizontal scale-out to achieve a pilot-line fabrication throughput. The observation of the highest process effectiveness for the fully sequential deposition diverges with the current research focus, mostly relying on co-deposition of all perovskite materials[40,41,43,103,154,182] which can hinder the industrial transfer.

4.4 Strategy 3: Horizontal scale-out toward Pilot-Line Throughput

Having established both the intrinsic rate limits (Strategy 1) and the effective utilization of vapor flux (Strategy 2), these parameters can now be combined to quantitatively estimate the equipment demand required to reach industrial fabrication throughput. To reach an industrially relevant fabrication throughput, sole vertical scale-up strategies of single deposition sources are not sufficient, requiring additional deposition sources in a horizontal scale-out strategy. The horizontal scale-out required to reach industrially relevant fabrication throughput is simulated by arranging multiple point sources in series, building on the

limits of vertical scale-up discussed before. While effective, this strategy requires substantial additional CapEx and must therefore be evaluated for economic viability. The number of linear sources needed to achieve a fabrication throughput of 1000 M10-sized wafers h^{-1} is estimated, which is considered as a minimum threshold for a pilot-scale line. A realistic throughput estimate requires precise definition of boundary conditions such as the source layout, deposition mode, material composition, target film thickness, wafer format, deposition width, and line speed. As dynamic deposition rates of perovskite precursor materials are not reported in the academic literature, a bottom-up approach is adopted based on the previously determined experimental spatial vapor fluxes. A conceptual linear source is constructed by an array of equidistant point sources. The point-source model is derived from the corresponding spatial vapor-flux distribution density maps of FAI, PbI_2, and CsI (**Figure 4.17**). To maximize process effectiveness and material utilization, fully sequential deposition (type B) is selected as the baseline. A $Cs_{0.17}FA_{0.83}PbI_3$ perovskite thin film is used as an approximate composition, where FAI and PbI_2 are the rate-limiting constituents. Target layer thicknesses of 30 nm (CsI), 300 nm (PbI_2), and 300 nm (FAI) are chosen to represent a commonly used double-cation perovskite thin film.[106,183] It is noted, that tandem integration requires perovskite thin films with wider bandgaps of around 1.68 eV, which is realized by substituting PbI_2 with $PbBr_2$.[41,154] However, as a simplification, only CsI, PbI_2 and FAI are considered here. In 2024 the dominant wafer format was M10 (182×182 mm^2) with $> 60\%$ market share,[184] and is therefore considered for this analysis. For further contextualization, the assumed throughput of 1000 M10 wafers h^{-1} corresponds to a Si-wafer consumption of $\sim$8.76 million wafers a^{-1} under continuous operation and can be translated into an annual module output depending on the assumed cell efficiency. For a silicon single-junction bottom cell operating at 25% efficiency, this throughput corresponds to a power output of $\sim$73 MWp a^{-1}. If the current 34.85% laboratory record for perovskite/Si tandems is adopted, the annual power output increases by $\sim 39\%_{\mathrm{rel}}$ to $\sim$101 MWp a^{-1}.[26]

A deposition width of 800 mm is assumed, accommodating three M10 wafers side by side. To mitigate edge effects, the linear sources are extended 100 mm beyond the deposition area on both sides (**Figure 4.18 B/D**). To maintain $< 2\%$ non-uniformity across the central wafer region (200-400 mm), more than five point sources are required which are placed equidistantly along the central 600 mm interval. A 50 mm source-to-source spacing is used for the throughput calculation, equal to 13 point sources included per linear source and maximizing deposition rate within practical limits. Additional real-world factors such as maintenance, material refilling, source heat-up/ cool-down, pumping to high vacuum, and substrate handling/loading can further reduce the fabrication throughput but are not considered here as they depend on the exact process layout.

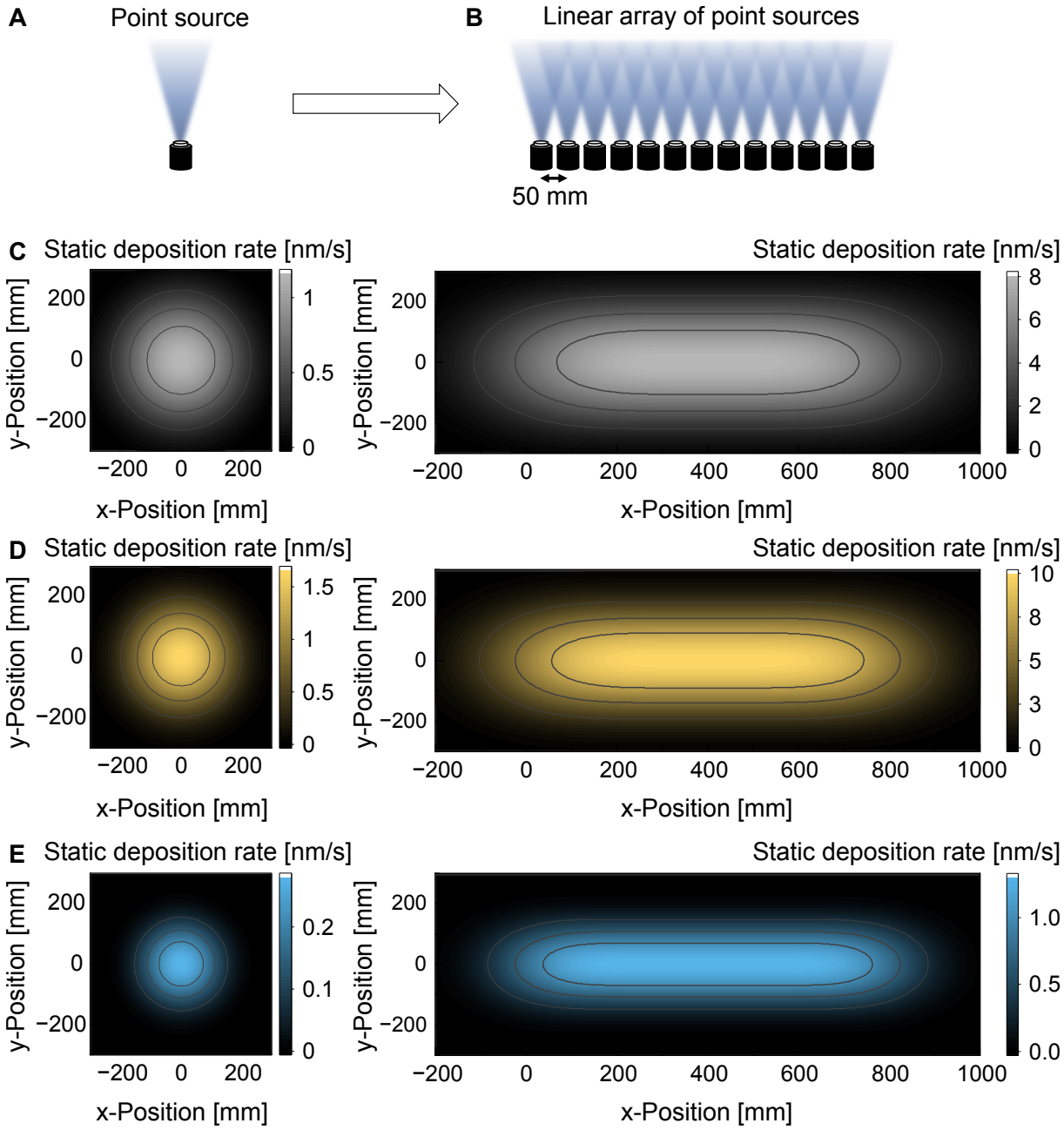

Figure 4.17: A/B Schematic representation of the approach to conceptualize an array of point sources. Resulting spatial static deposition rate maps for **C** CsI, **D** PbI_2 and **E** FAI for a single point source and the corresponding linear array of point sources. Reproduced with permission from the Royal Society of Chemistry.[36]

The cumulative thickness deposited on a moving substrate is obtained by integrating the static profile along the transport direction. Given the comparatively low deposition rate of FAI, it is anticipated that the organic precursor will dominate the overall equipment demand. At a line speed of 1 m min^{-1}, a single linear source deposits ∼159 nm (CsI), ∼173 nm (PbI_2), and ∼17 nm (FAI) (**Figure 4.18**).[d]

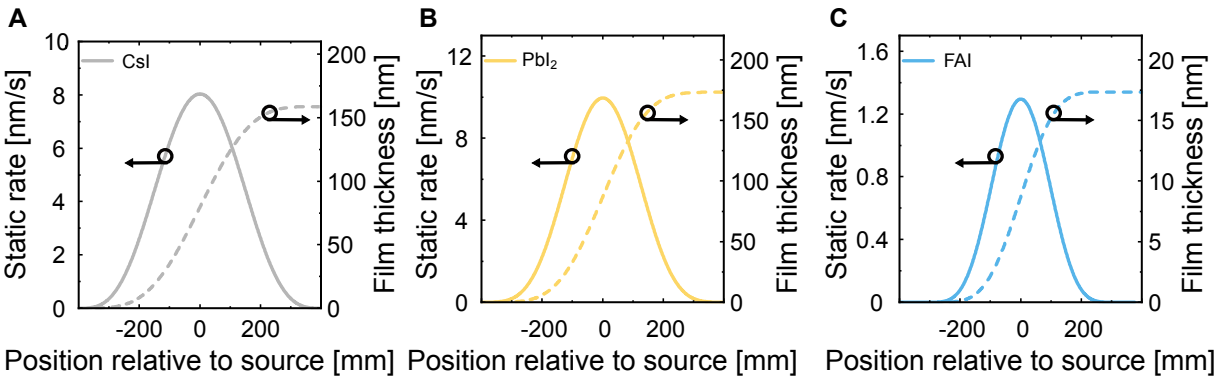

Figure 4.18: Extracted static deposition rate profiles and the corresponding expected film thickness deposited per conceptualized linear source at the central wafer position at 600 mm for a substrate velocity of ∼1 m/min for CsI **A**, PbI_2 **B** and FAI **C**. Note different y-axis scales. Adapted with permission from the Royal Society of Chemistry.[36]

Consequently, one linear source is sufficient for the CsI target thickness of 30 nm, whereas 2 and 18 linear sources are required for 300 nm PbI_2 and 300 nm FAI, respectively. Consequently, a total demand of 21 linear sources in series is needed to meet the target thicknesses at a fabrication throughput of 1000 M10-sized wafers/h in continuous operation (**Figure 4.19**). This result provides a quantitative benchmark for pilot-line implementation and directly links laboratory-scale deposition characteristics to industrial equipment requirements. These values are based on laboratory-scale sources operated at experimentally determined maximum deposition rates. Industrial linear sources operated at higher source temperatures, especially for FAI and PbI_2, are expected to deliver higher dynamic rates, reducing the number of required sources.

For comparison, the demand of deposition sources for co-deposition and partial sequential deposition type A are also evaluated. The total number of linear sources required is 54 for co-deposition and 22 for partial sequential deposition (Type A), respectively, *versus* 21 for fully sequential deposition (Type B). This corresponds to an increased equipment demand of $\sim 157\%_{\mathrm{rel}}$ (co-deposition) and $\sim 5\%_{\mathrm{rel}}$ (type A) relative to type B, underscoring the direct relation of process effectiveness to CapEx. The high number of FAI sources identifies the sublimation of organic precursors as a critical bottleneck towards the industrialization of vapor-based perovskite fabrication.

[d] The deposition width of 600 mm allows simultaneous processing of three M10-sized wafers side-by-side. Therefore the length of 333.3 M10-sized wafers (one third of the target 1000 M10-sized wafers) need to be transported along the transport direction per hour. The line speed considers the physical dimensions of the used wafer size and an additional margin of 5 mm on each side to compensate for the wafer carrier. With this information the required line speed is calculated to be around 1 m/min.

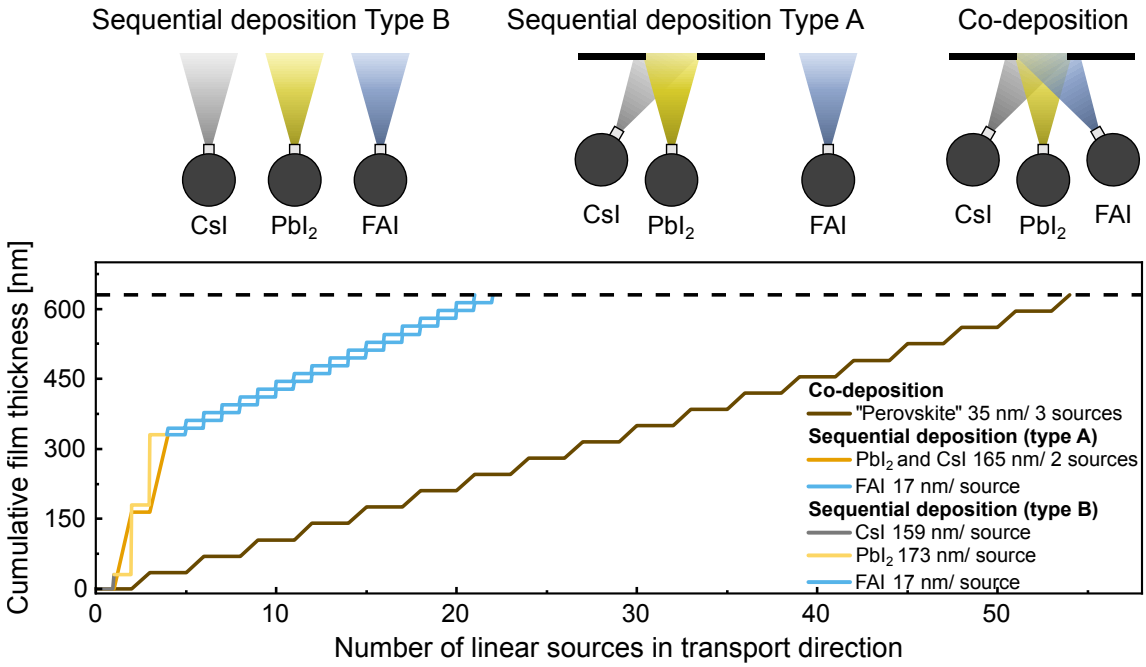

Figure 4.19: Estimation of horizontal scale-out for a fabrication throughput of 1000 M10-sized wafer per hour. Number of linear sources required to achieve a cumulative film thickness of 630 nm (30 nm CsI, 300 nm PbI_2 nm and 300 nm FAI) for different deposition modes. Reproduced with permission from the Royal Society of Chemistry.[36]

Alternatives to increase the organic deposition rate include hybrid two-step routes, in which the inorganic scaffold is vapor-based and the organic cations are introduced by solution or alternative vapor-phase methods.[111,112,117,185] Solution-based conversion allows for additive engineering with green, non-toxic solvents and has delivered certified tandem PCEs >31%, though its industrial suitability requires further study.[29,186,187] Scalable vapor-phase options include close-space sublimation (CSS), continuous flash sublimation, vapor-transport deposition (VTD), and chemical vapor deposition (CVD).[188–193] Furthermore, process metrology and control are more complex for co-deposition than for fully sequential operation and should be considered in any scale-out strategy. Accurate, reliable thickness and composition metrology remains a challenge for industrial vapor processing. The QCM lifetime can impose a limiting factor, particularly for PbI_2, and organic-rate monitoring is susceptible to precursor impurities in case of MAI.[99–102] *In situ* reflectance measurements can non-invasively track thickness, but may be limited on textured substrates.[194,195] As perovskite-based photovoltaics is not yet a mature technology, in-line quality control is essential. *In situ* photoluminescence (PL) has proven effective for sublimed perovskites,[196,197] and *k*-imaging provides additional information on spatially resolved radiative and non-radiative recombination.[198] Machine-learning assisted PL imaging is particularly attractive for high-throughput lines due to the large data volume and potential for recommendation feedback loops.[199,200] More advanced options such as *in situ* X-ray diffraction measurements can detect changes in crystallization and phase formation, complementing optical metrologies.[201,202]

4.5 Discussion Towards GWp Fabrication Throughput

The previous section outlines strategies to achieve a pilot-line scale fabrication of perovskite thin films. However, large-scale fabrication of Si-based tandem devices is expected to reach the GW_p- (gigawatt peak) scale, significantly increasing the demand for deposition sources to meet industrial throughput requirements.[203] At such manufacturing scales, production is typically distributed across multiple deposition lines in order to provide machine redundancy and reduce downtime. For the following considerations, a minimum throughput of 10.000 G12-sized (210 mm × 210 mm) wafers h^{-1} is assumed. The use of larger G12 wafers renders the calculation more future-proof as the industry continues to adopt larger wafer formats.

Based on this assumption, the required number of deposition sources for CsI, PbI_2, and FAI is estimated for both a single production line and three parallel production lines. For a single production line, a throughput of 10.000 wafers h^{-1} corresponds to a line speed of approximately 6 m min^{-1}. When the production is distributed over three parallel lines, each line requires 3.333 wafers h^{-1}, corresponding to a line speed of about 2 m min^{-1}. In these calculations, deposition rates obtained from laboratory-scale equipment are used. In industrial-scale deposition sources, however, significantly higher deposition rates can be expected as stated before.

The target layer thicknesses are assumed to be 50 nm for CsI, 500 nm for PbI_2, and 500 nm for FAI. These values account for the lower effective thickness on commercially available textured Si bottom cells. As a first approximation, only PbI_2 is considered in the calculations, although in practice a fraction of PbI_2 must be substituted with $PbBr_2$ to achieve tandem-relevant bandgaps.[41,154]

4.5.1 From Substrate Cleaning to Inorganic Scaffold Deposition

A potential production line up to the inorganic scaffold deposition is illustrated in **Figure 4.20**. In the first processing step, Si bottom cells are cleaned to prepare them for subsequent deposition processes. The cleaned substrates are then transferred into vacuum *via* a two-stage transfer chamber. The first stage operates at rough vacuum, after which the substrate carriers are moved into a second chamber where they are pumped down to high vacuum. The chamber colors indicate the vacuum state with grey signaling rough vacuum (<10^{-1} mbar) and black high vacuum (<10^{-5} mbar).

Subsequently, a thin NiO_x adhesion layer is deposited by a sputter process. The NiO_x and SAM-HTL layers are very thin and therefore not rate-limiting for the overall process throughput. A NiO_x/2PACz bilayer has demonstrated high performance in various two-step fabrication routes.[204] Recently, the deposition of ultrathin 2PACz layers by evaporation was demonstrated,[205] which could eliminate the need for an additional washing step typically required in solution-processed SAM deposition used for vapor-deposited perovskite thin films.[43,103,107]

In the next step, CsI and PbI_2 are deposited using the fully sequential route (Type B), as it has the highest process effectiveness as discussed previously. For a single production line, the calculations indicate that 2 CsI sources and 17 PbI_2 sources are required. When the production is distributed over three parallel lines, each line requires 1 CsI source and 6 PbI_2 sources. It is noted that the static deposition rates are conservative and consistent with the previous section, while extrapolation suggests a substantially higher deposition rate potential, especially for PbI_2.

An important consideration in the design of such production lines is the vacuum level required for each processing step. Transferring substrates from ambient conditions into high vacuum can limit the overall fabrication throughput, as the cycle time of the transfer chamber may become the rate-limiting step. This cycle time can be reduced by introducing additional vacuum buffer chambers, although this increases the capital expenditure (CapEx). Furthermore, frequent transitions between different vacuum levels increase the power consumption of the pumping systems, thereby raising the operational expenditure (OpEx) both of which are key determinants for the economic viability. This system-level relevance is consistent with recent techno-economic analyses, which identify equipment demand, energy consumption, and vacuum processing complexity as key cost drivers in tandem module manufacturing, emphasizing that improvements in process throughput and integration are essential for achieving cost-competitive production.[38,46,156]

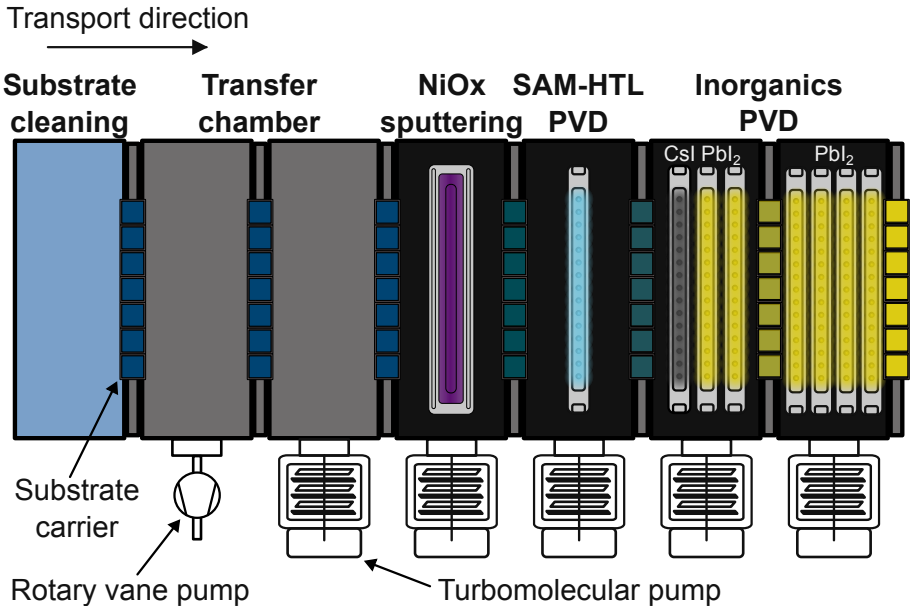

Figure 4.20: Schematic illustration of a potential GW_P-scale production line for the deposition of inorganic precursor layers on Si bottom cells. The process flow proceeds from left to right and begins with substrate cleaning of the Si bottom cells mounted on substrate carriers. The substrates are subsequently transferred into vacuum through a two-stage transfer chamber consisting of a rough-vacuum stage followed by a high-vacuum stage, pumped by rotary vane and turbomolecular pumps. After vacuum transfer, the NiO_x hole-transport layer is deposited by sputtering, followed by the deposition of a SAM-based HTL by evaporation. In the subsequent inorganic PVD section, CsI and PbI_2 precursor layers are deposited using multiple deposition sources arranged along the transport direction. The substrate color indicates the progress of subsequent depositions. SAM-HTL: Self-assembled monolayer hole transport layer, PVD: physical vapor deposition

4.5.2 Organic cation deposition

Vapor deposition of the organic cations (PVD route) was identified as a critical bottleneck in the previous sections. When considering a single production line, approximately 172 FAI linear deposition sources would be required to meet the target throughput of 10.000 wafers h^{-1}. Even when the production is distributed over three parallel production lines, about 57 FAI sources per line are still required. While such an approach is technically feasible, it becomes economically unattractive due to the large number of deposition sources required and associated costs for vacuum chambers, maintenance and increased chance of failure. Potential industrial production line layouts for the organic cation deposition are illustrated in **Figure 4.21**. These approaches differ fundamentally in their impact on equipment demand, process complexity, and integration into existing production lines, requiring a trade-off between throughput, cost, and process compatibility.

Strategies to increase the deposition speed of the organic cations include hybrid two-step processes (Hybrid route) in which the organic cations are supplied by a solution-based deposition step. Several scalable solution-processing techniques exist, including inkjet printing, spray coating, slot-die coating, and blade coating.[112,174,206] Among these approaches, inkjet printing is already widely used in industrial manufacturing and benefits from a mature tool chain. To achieve the required fabrication throughput at a given line speed, the number of print nozzles can be scaled accordingly.[207] However, slot-die and blade coating are inherently optimized for continuous roll-to-roll processing and can introduce challenges when transferred to wafer-based fabrication. While inhomogeneities at the coating front can be mitigated in foil-based roll-to-roll processes by excluding affected regions, wafer-based processing requires uniform film formation across the entire substrate. In this case, solution backflow and meniscus instabilities can propagate across the coating area, leading to thickness variations on every wafer and thereby potentially impacting yield and process reproducibility.[208–210]

A second emerging strategy is CSS (CSS route),[211–214] in which the SSD is reduced to only a few millimeters, drastically increasing the effective deposition rate. In this approach, the conversion time of the inorganic scaffold into the perovskite thin film becomes the critical parameter, and the source length must be adjusted to match the desired fabrication throughput. The process can be performed under rough vacuum conditions, thereby reducing the number of turbomolecular pumps required. However, it should be noted that this method has not yet reached industrial maturity and still requires significant engineering development to be adapted for perovskite thin films, while it is an established method for cadmium telluride thin-film photovoltaics.[215]

All two-step deposition routes require an additional annealing step under ambient conditions to improve the perovskite film quality.[112,117,121] This represents a disadvantage of the approach because the vacuum environment of the production line must be broken, requiring additional transfer chambers. Consequently, both CapEx and OpEx increase.

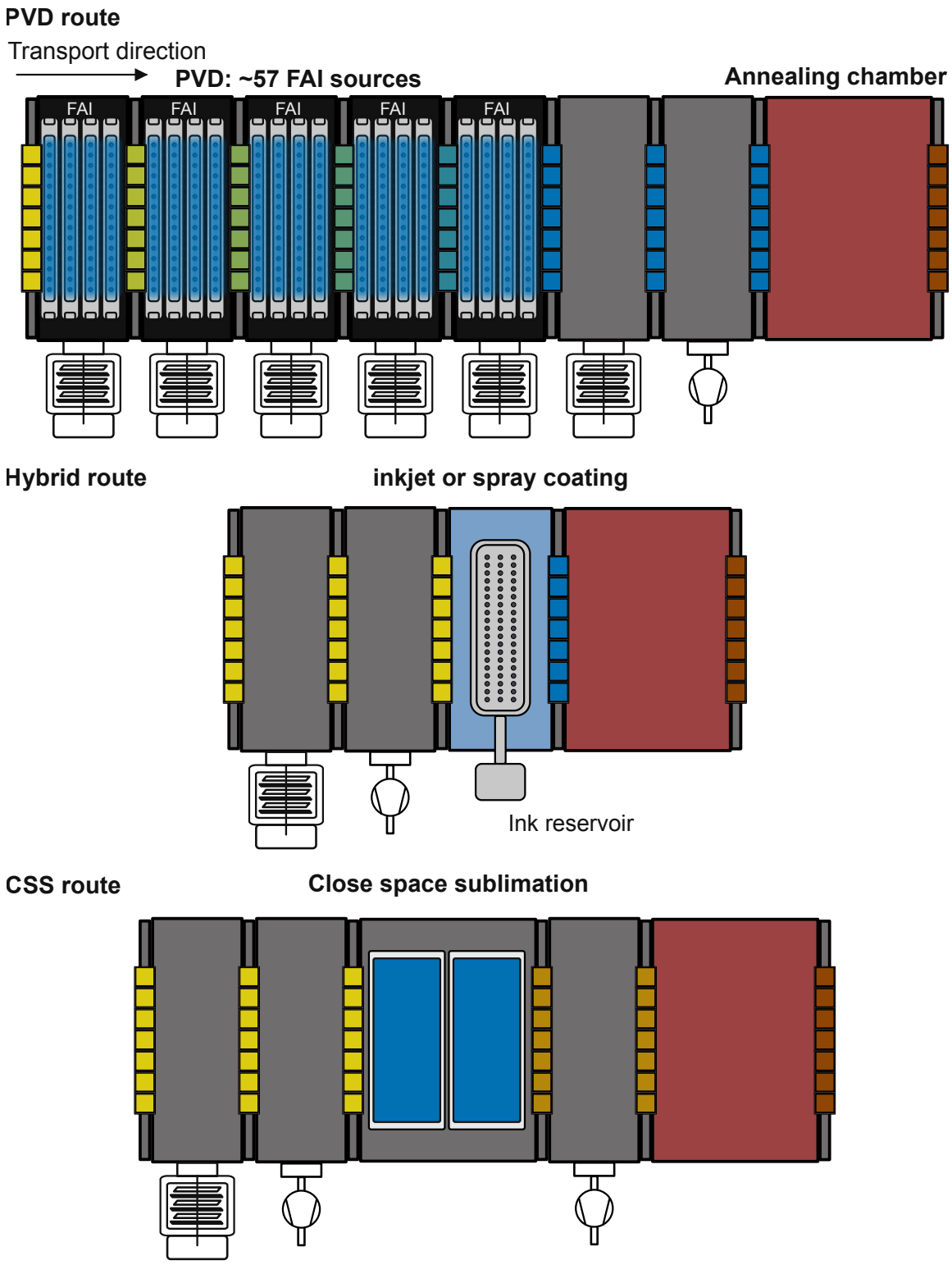

Figure 4.21: Schematic illustration of different strategies for supplying organic cations during GW_p-scale perovskite tandem solar cell fabrication. Top: Direct vapor deposition of FAI using a large number of deposition sources (approximately 57 sources per production line) followed by an annealing chamber. It is noted that only 20 sources are depicted here. Middle: Hybrid two-step process in which the organic cations are deposited by inkjet printing or spray coating. Bottom: CSS approach. For all approaches, a subsequent annealing step is required. The substrate color indicates the progress of subsequent depositions. CSS: Close space sublimation, GW_p Gigawatt peak

4.5.3 Final Processing Steps to complete Tandem Device Architecture

To complete the tandem device architecture, additional functional layers must be deposited on top of the perovskite absorber. These include an ETL, typically based on C_{60} and deposited by PVD methods, followed by a protective SnO_2 buffer layer deposited by atomic layer deposition (ALD), and finally a TCO deposited by sputter deposition.

The SnO_2 buffer layer serves as a protective barrier during the subsequent sputter deposition process of the TCO, preventing plasma-induced damage to the underlying perovskite layer. However, conventional ALD processes are characterized by relatively low film growth rates,[216] which can limit fabrication throughput in high-volume production environments. An alternative approach is spatial atomic layer deposition (SALD), which is compatible with in-line manufacturing and enables significantly higher dynamic deposition rates compared to conventional ALD.[217]

Following TCO sputter deposition, the front electrode is formed by screen printing of a metallic contact grid. Screen printing is a well-established industrial technique widely used in silicon solar cell manufacturing and offers high throughput and low cost. Overall, the deposition methods required for these final processing steps are industrially mature and compatible with large-scale photovoltaic production.

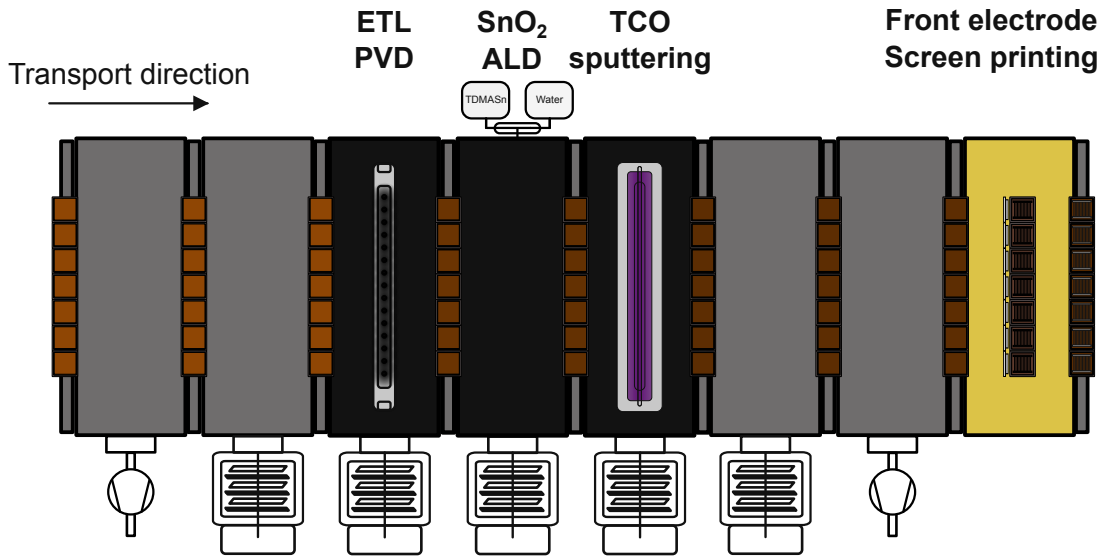

Figure 4.22: Schematic illustration of the final processing steps in a GW-scale perovskite–Si tandem solar cell production line. Substrates move from left to right along the transport direction. First, the electron transport layer, typically based on C_{60}, is deposited by physical vapor deposition. Subsequently, a thin SnO_2 buffer layer is deposited by atomic layer deposition. Finally, the front electrode is formed by screen printing of a metallic contact grid. The substrate color indicates the progress of subsequent depositions.

Looking beyond the GW_p scale considered here, future photovoltaic manufacturing facilities are expected to operate at production capacities of 10 GWp or higher. At such scales, deposition equipment must

sustain significantly higher line speeds, which requires high dynamic deposition rates and short cycle times across all process steps. Large-area deposition sources must therefore deliver stable and uniform vapor fluxes while operating reliably under continuous high-throughput conditions. In parallel, auxiliary processes such as substrate transfer, vacuum pumping, and thermal treatment must be carefully engineered to avoid becoming throughput bottlenecks. Furthermore, fast in-line process metrology will be required to monitor film thickness, composition, and uniformity at high line speeds, ensuring stable process control in large-scale tandem production.

4.6 Summary

The adaptation of vapor-based perovskite deposition from laboratory-scale toward industry-scale solar cell fabrication requires maximizing the fabrication throughput, which demands thorough understanding of the physical material limits to accelerate deposition rates and identification of the process route that can offer the highest process effectiveness in an industrial in-line linear source setup. In this context, three complementary strategies are assessed in this chapter: maximizing sublimation rates, improving process effectiveness through optimized source geometries and deposition modes, and finally horizontal scale-out *via* multiple linear sources in series.

First, the thermal stability of key perovskite precursor materials (MAI, FAI, CsI and PbI_2) is evaluated under realistic sublimation conditions using a Duran tube setup followed by complementary chemical analysis. MAI is shown to remain intact between 160-240 °C, with only minor phosphorus-containing impurities detected in volatile fractions. For FAI, significant decomposition, coke formation, and NH_4I formation set in above ∼220-240 °C. Importantly, the main deposition fraction remains chemically unchanged, suggesting selective deposition of FAI from the gas phase. PbI_2 and CsI are found to be thermally robust up to much higher temperatures under reduced pressure. PbI_2 in particular can be sublimed without decomposition up to a temperature of at least 450 °C when heat distribution in the crucible is well controlled. Extrapolating the measured PbI_2 rates suggests that static deposition rates from ∼25 to ∼1800 $\mathrm{nm\,s^{-1}}$ are accessible, the latter exceeding the target range of ∼1000 $\mathrm{nm\,min^{-1}}$ for cost competitiveness compared to conventional solution-based processes. This extrapolation underlines the potential of optimized source design to increase fabrication throughput. In this context, the present results are particularly relevant because the extrapolated PbI_2 deposition rates enter the range that has been projected to be economically competitive with solution-based manufacturing, indicating that further rate increases are not only technologically feasible within the thermal stability window but also directly relevant for achieving industrially viable throughput.

To optimize source geometries and precursor powder properties, material-specific vapor-flux distributions of CsI, PbI_2, and FAI are quantified. In case of FAI, the crucible geometry and particle-size distribution strongly influence the vapor flux focusing, which influences process reproducibility. A technological analysis of the particle-size dependent FAI sublimation behavior demonstrates that cylindrical crucibles combined with size-selected FAI powder improve the deposition homogeneity of FAI on the substrate

and enhance process repeatability. Using experimentally derived static deposition rate profiles of CsI, PbI_2, and FAI, different deposition schemes (co-deposition, partially sequential (type A), fully sequential (type B)) are assessed in terms of material utilization, composition control, and suitability for industrial linear source setups. In this context, a fully sequential deposition offers the highest process effectiveness together with simplified process metrology.

Finally, a bottom-up simulation is used to estimate how many linear sources are required to deposit a representative perovskite thin film at a fabrication throughput of 1000 M10-sized wafers/h. For a fully sequential (type B) deposition process, one linear source for CsI, two for PbI_2, and eighteen for FAI are required (21 in total) for the target pilot-line fabrication throughput, highlighting that organic precursor sublimation is the critical bottleneck. Comparing the required horizontal scale-out to the partial sequential deposition or co-deposition, reveals a $5\%_{rel}$ and $270\%_{rel}$ increased demand of sublimation sources, respectively. This finding signifies the direct influence of deposition route choice on the equipment demand and thus economic viability of this technology. Overall, the chapter connects detailed precursor thermochemistry, source engineering, and throughput modeling into a coherent framework that translates laboratory-scale sublimation processes into realistic process design guidelines for industrial perovskite manufacturing. As an outlook, the translation of these findings toward GW_p-scale manufacturing highlights the importance of integrating perovskite deposition processes into continuous in-line production concepts. At such scales, fabrication throughput is governed by both achievable deposition rates and the interplay between line speed, process cycle times, and transitions between different vacuum environments. Consequently, future development efforts must focus on deposition technologies and process flows that allow stable operation at high line speeds while reducing the frequency of vacuum interruptions and enabling scalable, high-throughput in-line processing.

Overall, the results demonstrate that industrial scalability of vapor-deposited perovskite thin films is governed by precursor thermochemistry, source design, and process configuration. While inorganic precursor deposition can be significantly accelerated through improved source engineering, the limited thermal stability and controllability of organic precursors remain the dominant bottleneck. Consequently, achieving industrially relevant fabrication throughput requires both maximizing deposition rates and rethinking deposition strategies and process integration. The framework established in this chapter provides a quantitative pathway for this transition, enabling the translation of laboratory-scale processes into scalable manufacturing concepts.

5 Understanding and exploiting interfacial interactions between phosphonic acid functional groups and co-deposited perovskites

Achieving robust and transferable vapor-deposition processes for perovskite photovoltaics requires precise control over the interfacial interactions that dictate early-stage nucleation and crystallization. For co-deposited perovskite thin films, variations in substrate surface chemistry can substantially shift the stoichiometric process window and influence the perovskite phase selectivity from the very first nanometers of growth. Such substrate-dependent effects introduce a critical source of variability that complicates process transferability across device architectures and fabrication routes. In this chapter, the influence of interfacial surface chemistry on growth mechanisms, organic precursor incorporation kinetics, and phase formation in co-deposited perovskite thin films is elucidated. Specifically, perovskite layers are deposited on the carbazole-based self-assembled monolayer hole-transport layer 2PACz while systematically varying the surface termination by comparing washed monolayers with unwashed ("bulk") 2PACz surfaces that retain exposed phosphonic-acid groups. X-ray diffraction analysis reveals pronounced substrate-driven phase selectivity with monolayer 2PACz yielding mixed δ/α-$FAPbI_3$ films, whereas bulk 2PACz promotes selective α-$FAPbI_3$ formation. Despite converting to α-$FAPbI_3$ after thermal annealing, the initial crystallization pathway strongly affects the stoichiometric process window required to achieve high device performance. By systematically varying the FAI deposition rate during co-deposition, a pronounced substrate dependence of the optimal process window is identified, where bulk 2PACz surfaces require substantially lower FAI rates to reach maximum photovoltaic efficiency. Soft X-ray emission spectroscopy at the N K-edge further reveals an increased effective incorporation rate of organic cations on phosphonic acid terminated surfaces. The mechanistic origin of this behavior is elucidated through water contact-angle analysis, ^{1}H-nuclear magnetic resonance spectroscopy titration experiments, and density functional theory simulations, which collectively indicate a hydrogen bonding interaction between phosphonic acid functional groups and interfacial iodide ions that promotes early α-phase nucleation and kinetically suppresses δ-phase formation. Building on this mechanistic understanding, a rational interface-engineering strategy is demonstrated using mixed SAMs composed of 2PACz and 1,4-butylenediphosphonic acid (4dPA), enabling controlled tuning of phosphonic-acid density at the substrate surface. This approach systematically suppresses δ-phase signatures while maintaining comparable device performance. By establishing how substrate surface chemistry alters stoichiometric process windows and crystallization pathways in co-deposited perovskites, this chapter provides design rules for engineering predictable and transferable vapor-deposition processes and highlights interfacial chemistry as a key determinant for repeatable growth dynamics in vapor-deposited perovskites.

Parts of this chapter were published in the research article "Understanding and Exploiting Interfacial Interactions between Phosphonic Acid Functional Groups and Co-Evaporated Perovskites" *Matter* (**2024**) by *Julian Petry*, Thomas Feeney*, Abderrezak Torche, Dirk Hauschild, Benjamin Hacene, Constantin Wansorra, Alexander Diercks, Michelle Ernst, Lothar Weinhardt, Clemens Heske, Ganna Gryn'ova, Ulrich W. Paetzold and Paul Fassl.* Julian Petry and Thomas Feeney contributed equally to this work. Some figures in this chapter were reproduced or adapted from the original publication with permission from Elsevier.[103]

Julian Petry contributed to this work by developing the research plan jointly with Thomas Feeney. Julian Petry provided initial experimental proof of the substrate dependent growth of co-deposited perovskite thin films on different self-assembled monolayers. Thomas Feeney fabricated all perovskite thin films and performed a systematic X-ray diffraction analysis that are presented in this chapter. *Responsible lead and shared first author. Julian Petry developed the research plan to investigate the interfacial interactions and acquired and coordinated experiments with external partners. DFT simulations were conducted by Abderrezak Torche and Michelle Ernst under supervision of Ganna Gryn'ova. XES measurements were performed by Dirk Hauschild with support of Constantin Wansorra, Lothar Weinhardt and Clemens Heske. The project was supervised by Ulrich W. Paetzold and Paul Fassl. The contributions of all authors according to the CRediT system are listed in **Table A.7**.

5.1 Motivation and Contextualization

For perovskite thin films fabricated by co-deposition, the first nanometers of crystallization are dictated by the chemical termination of the underlying substrate and even subtle surface changes can propagate into different perovskite phase selectivity, morphology and affect the process window.[40,43,44,218] This pronounced substrate-dependent growth is systematically investigated, for example by Abzieher *et al.*, who correlated substrate-perovskite interactions with changes in early-stage growth behavior and, consequently, film morphology and device performance.[44] For co-deposition, substrate-dependent growth implies a practical challenge: process recipes that yield high performance on one substrate cannot be easily transferred to different substrate types without re-optimization of the process conditions (*e.g.* relative organic-cation flux) and the overall stoichiometry window due to a shift in process window. This substrate effect is particularly relevant for vapor deposition, because excess bulk 2PACz remains at the HTL-perovskite interface during thin-film formation, whereas in solution-based perovskite processing such loosely bound material is typically washed away by the solvent during deposition, strongly reducing its impact on crystallization.[122]

This issue is particularly relevant for *p–i–n* architectures using carbazole-based phosphonic-acid self-assembled monolayer hole transport layer (SAM-HTL) materials from the nPACz family, which are widely adopted due to their near-lossless interface with the perovskite absorber.[219,220] In these systems, the surface termination can vary substantially depending on SAM preparation: a washed, well-defined monolayer presents a lower density of exposed phosphonic-acid (P–OH) groups compared to an unwashed, bulk surface which can contain residual physisorbed 2PACz[a] molecules. Pronounced differences in FA-based perovskite crystal growth have been reported for the SAM-HTL MeO-2PACz[b] depending on whether an ethanol washing step of the SAM-HTLs is applied, and hydrogen bonding involving phosphonic-acid functional groups and formamidinium cations has been proposed as a possible origin for differences in film formation.[40] While hydrogen bonding at perovskite interfaces is well established,[40,218,221] the specific underlying interfacial mechanism by which phosphonic-acid termination modifies organic-cation incorporation kinetics and phase selectivity during co-deposition remains elusive. This creates a practical need to re-optimize the organic-cation flux for each surface termination (monolayer *vs.* bulk), and a scientific need to identify the interfacial mechanism that causes such large shifts in film formation and process window. Resolving this surface dependence is therefore essential both for reliable process transfer and for leveraging rational interface design to control phase-pure, oriented perovskite growth.

This chapter addresses *Research Objective 2* and *Research Objective 4* by elucidating how interfacial surface chemistry governs early-stage crystallization, phase selectivity, and the effective stoichiometric process window during co-deposition, and by identifying substrate-dependent growth as a central limitation for process transferability and repeatability. First, substrate-dependent film formation is established by

[a] [2-(9H-Carbazol-9-yl)ethyl]phosphonic acid
[b] [2-(3,6-Dimethoxy-9H-carbazol-9-yl)ethyl]phosphonic acid

comparing perovskite layers co-deposited on washed (monolayer-like) 2PACz and unwashed (bulk) 2PACz using structural and morphological characterization techniques. Second, the practical consequence for process transfer is quantified by tracking the photovoltaic performance as a function of the equivalent FAI rate for each surface termination and identifying the shifted optimum. Third, the interfacial origin of the growth shift is elucidated by combining spectroscopy with solution-based ^{1}H-NMR titrations and density functional theory (DFT) simulations to identify the dominant interaction motif and its implications for incorporation kinetics and phase stability. Building on this understanding, a rational interface-design concept is demonstrated using a combination of two SAM materials which allows a controlled phosphonic-acid density, illustrating how fundamental insight can be translated into strategies to mitigate substrate dependence and enable reproducible co-deposition across relevant contact materials.

5.2 Observation of Substrate Dependent Preferential Growth on SAM-HTLs

The four source vapor co-deposition approach used for perovskite fabrication is illustrated in **Figure 5.1**, where PbI_2, FAI, CsI, and $PbCl_2$ are co-deposited under high vacuum. The as-deposited film consists of a mixed precursor phase in which the components are homogeneously distributed but not yet fully crystallized. A subsequent thermal annealing step activates interdiffusion and solid-state reaction, leading to the formation of the crystalline perovskite absorber layer.

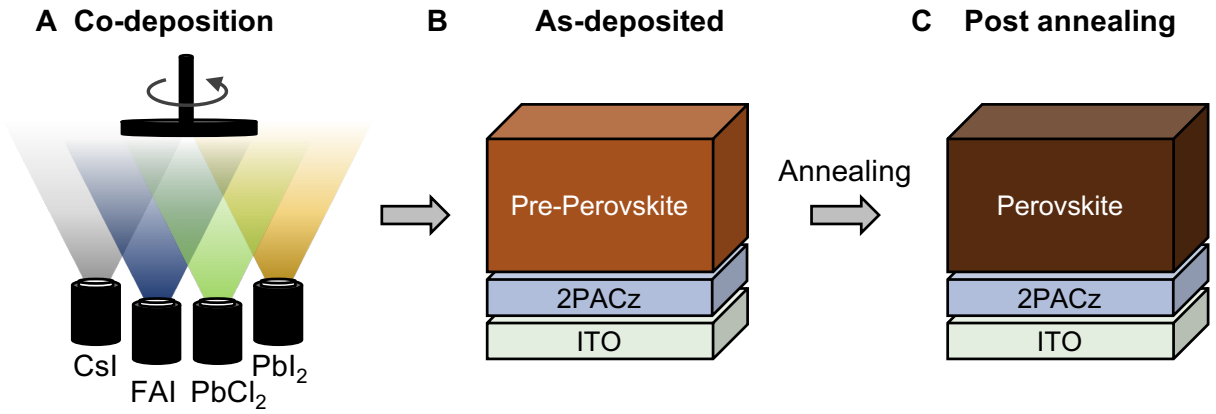

Figure 5.1: Schematic illustration of the co-deposition process for mixed-cation/mixed-halide perovskite formation. **A** Simultaneous deposition of PbI_2, FAI, CsI, and $PbCl_2$ onto an indium tin oxide (ITO)/2PACz substrate. **B** Formation of an as-deposited precursor ("pre-perovskite") thin film. **C** Post-deposition annealing yields the final perovskite thin film. ITO: Indium tin oxide

To investigate the substrate dependent growth in case of the evaporated 2PACz SAM-HTL, perovskite thin films are co-deposited on both a 2PACz monolayer and a bulk 2PACz layer, the former of which is fabricated by removing physisorbed, loosely bound 2PACz molecules *via* an additional washing step.

Perovskite thin films are analyzed using XRD measurements of both as-deposited and post-annealing perovskite thin films. As the contribution of other elements is low, the observed diffraction peaks are related to the parent $FAPI_3$ crystal structure as an approximation as no other diffraction peaks are observed. The nominal composition of the perovskite thin film is $Cs_{0.13}FA_{0.87}Pb(I_{0.95}Cl_{0.05})_3$.

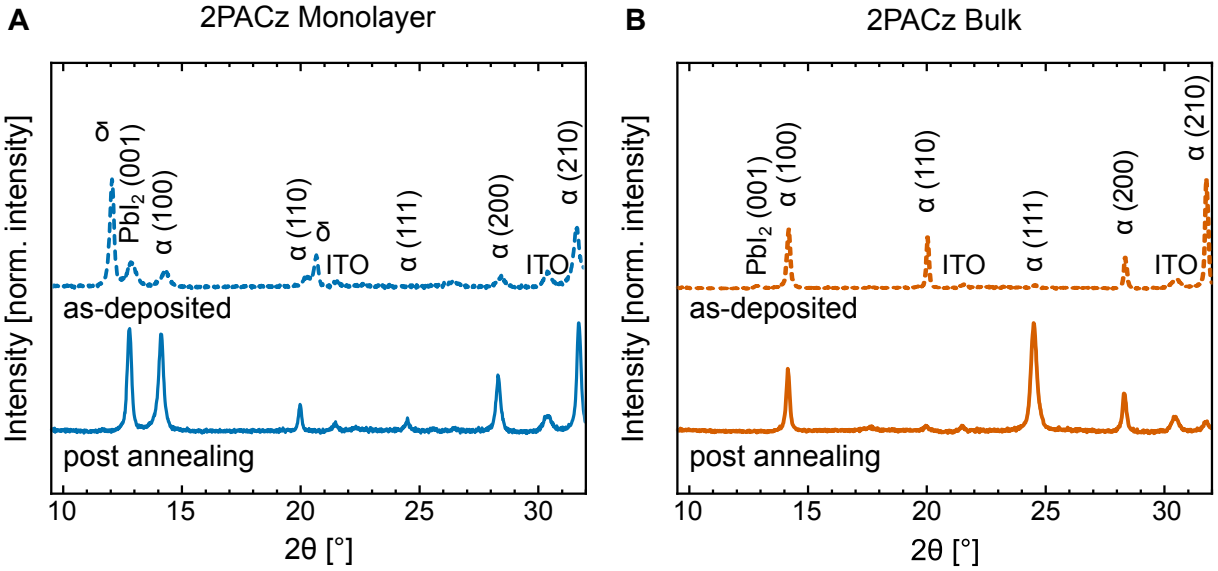

Figure 5.2: XRD analysis of the preferred crystal growth of perovskite thin films on monolayer **A** and bulk (unwashed) **B** solution-processed 2PACz. XRD patterns in panel **A** show perovskite thin films on monolayer 2PACz in the as-deposited and post-annealing state: in the as-deposited film, both δ- and α-perovskite reflections are observed together with residual PbI_2, whereas after annealing only α-perovskite and residual PbI_2 are detected. Panel **B** presents the corresponding XRD patterns for films on bulk 2PACz, where selective growth of the α-phase with only minimal residual PbI_2 is observed for both as-deposited and annealed perovskite thin films. Adapted with permission from Elsevier.[103] XRD: X-ray diffraction

In the as-deposited state, the perovskite layer on monolayer 2PACz exhibits mixed crystallization with both δ-$FAPbI_3$ and α-$FAPbI_3$ (100) signals together with residual PbI_2 (001), indicating that initial FAI incorporation and perovskite conversion are incomplete on this surface (**Figure 5.2 A**, dotted line). In contrast, growth on bulk 2PACz layers yields selective room-temperature formation of the α-phase (100) with only minimal residual PbI_2 (001), indicating a stoichiometric perovskite formation (**Figure 5.2 B**, dotted line). Post annealing, the monolayer-grown film converts to the α-phase (100) plane, but retains a comparatively strong PbI_2 (001) signal, whereas the bulk-grown film remains phase-pure α-phase (100) with little or no crystalline PbI_2 (001) plane (**Figure 5.2 A/B**, solid line). Residual PbI_2 is associated with increased V_{OC} but at the cost of reduced long-term stability.[222–225] Relative peak intensities reveal a clear difference in preferential orientation. Post-annealing perovskite thin films on bulk 2PACz show an increased α-$FAPI_3$ (111) signal relative to (100), whereas perovskite thin films on monolayer 2PACz crystallize primarily in the α-$FAPI_3$ (100) orientation with little contribution of the α-$FAPI_3$ (111) plane.

This indicates that bulk 2PACz promotes a recrystallization from purely (100)-oriented growth toward stronger contributions from secondary planes, which has been associated with a more columnar grain growth and improved charge extraction.[44]

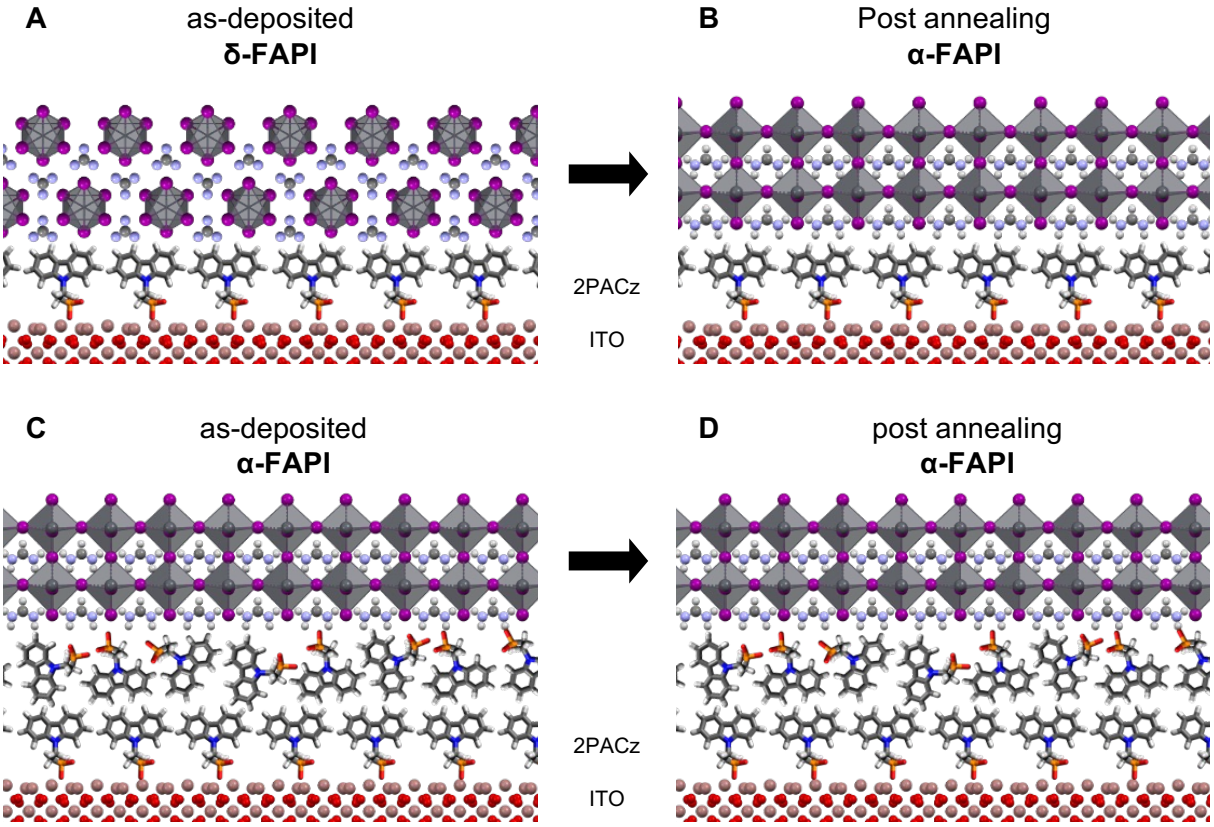

Figure 5.3: Schematic summary of XRD-derived observations for perovskite thin films on monolayer and bulk 2PACz. On monolayer 2PACz, the **A** as-deposited film consists predominantly of the δ-phase, which is converted **B** into the α-phase after annealing. In contrast, on bulk 2PACz, selective growth of α-FAPI is observed for both **C** the as-deposited and **D** annealed perovskite thin films. Adapted with permission from Elsevier.[103] XRD: X-ray diffraction

These observations of phase selectivity are illustrated in **Figure 5.3 A-D**. Panel **A** represents the monolayer case immediately after deposition, where δ-phase crystallites form primarily. Panel **C** depicts the bulk 2PACz case after deposition, where interfacial interactions drive direct α-phase nucleation and suppress δ-phase formation. Panels **B** and **D** show the annealed films on monolayer and bulk 2PACz, respectively, with both being converted to α-$FAPbI_3$. A substrate-dependent preference for α-phase nucleation and altered texture on bulk 2PACz are concluded from the XRD results, in agreement with findings of Ross *et al.*[40]

To assess whether the surface termination driven changes in phase selectivity and preferred growth direction from XRD can be observed at a microstructural level, cross-sectional and surface scanning electron

microscopy (SEM) are used. **Figure 5.4** shows SEM images of perovskite thin films grown on monolayer and bulk 2PACz in a top-view (top images) and cross-section (bottom images). Perovskite thin films deposited on monolayer and bulk 2PACz feature a comparable microstructure. Nevertheless, cross sectional SEM images still suggest a slight reduction in vertical grain boundaries for perovskite grown on bulk 2PACz, consistent with a weak tendency toward more columnar growth (**Figure 5.4** bottom). Top-view surface SEM images yield comparable average lateral grain sizes for both underlayers, namely 114 ± 5 nm on bulk 2PACz and 100 ± 3 nm on monolayer 2PACz, indicating that the SAM surface termination does not significantly influence the grain size. Notably, the perovskite thin films grown on monolayer 2PACz contain occasional grains with a substantially higher SEM contrast, a feature linked to Pb-rich domains, which is in agreement with the stronger residual PbI_2 signal observed by XRD for monolayer 2PACz. Taken together, the substrate-dependent differences in phase selectivity and residual PbI_2 indicate that the same nominal co-deposition process does not lead to the same effective precursor incorporation on monolayer and bulk 2PACz. This suggests that the interfacial surface chemistry modifies the effective FAI incorporation rate and thereby shifts the stoichiometric process window, which is quantified in the following section.

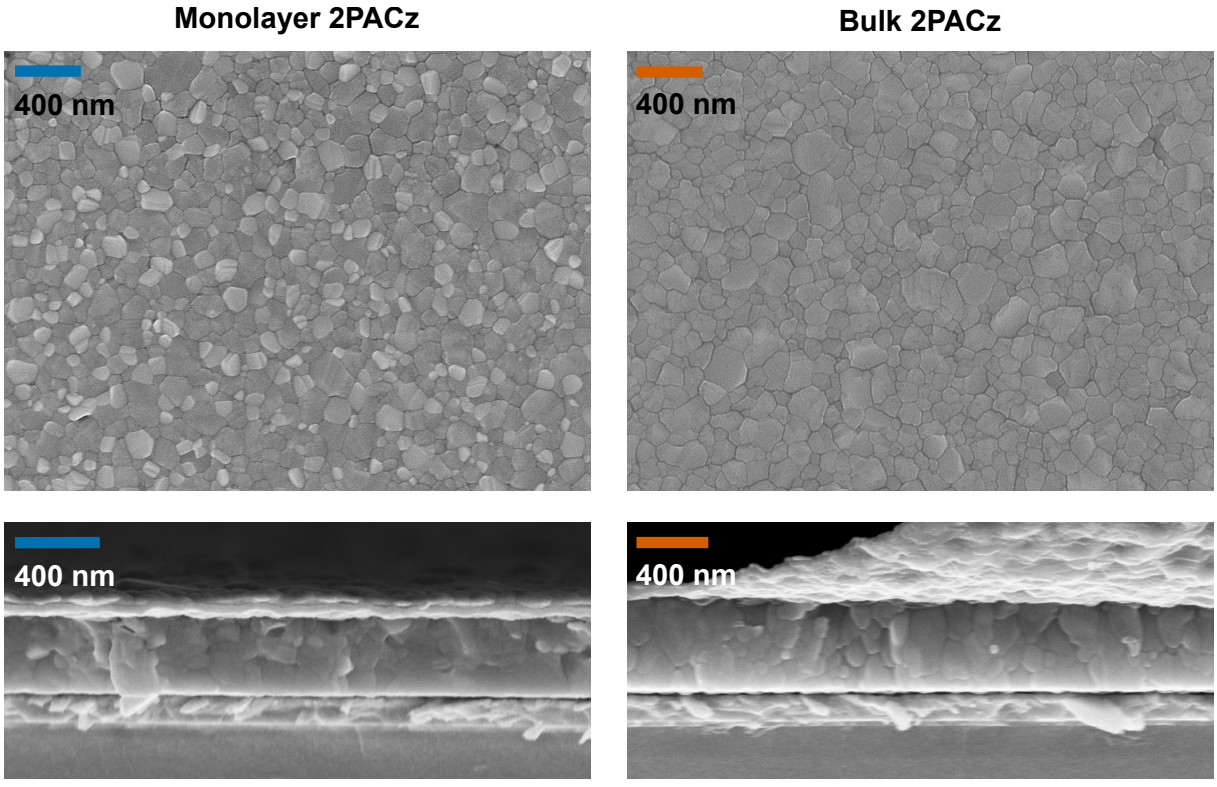

Figure 5.4: Top-view SEM images (top row) show comparable lateral grain sizes for perovskites grown on bulk and monolayer 2PACz. Cross-sectional SEM images (bottom row) reveal a slightly reduced density of vertical grain boundaries for films on bulk 2PACz. All scale bars correspond to 400 nm. Reproduced with permission from Elsevier.[103] SEM: Scanning electron microscopy

5.3 Substrate Dependent Effective FAI Incorporation Rate

XRD analysis of the deposited perovskite thin films already point towards a higher effective FAI incorporation rate reflected in the lower residual PbI_2 peak intensity. To quantify how the SAM interface influences the effective FAI incorporation rate during the co-deposition process, the perovskite stoichiometry is systematically optimized by changing the "equivalent FAI rate" and tracking the resulting device metrics. The equivalent FAI rate is an arbitrary unit which reflects the measured FAI deposition rate for a fixed deposition rate of the inorganic materials. As the sticking coefficient of FAI is substrate dependent, the actual measured QCM rate does not necessarily equal the substrate deposition rate. In the following, the used equivalent FAI rate is based on a previously developed deposition process and thus of arbitrary nature. Perovskite films with optimal stoichiometry, in regards of achieving the highest device performance, are analyzed by XES to quantify the FAI abundance in the perovskite absorber as an indicator of the effective FAI incorporation rate. In this way, XES serves as an independent validation of the substrate-dependent FAI incorporation behavior that is first inferred from the shifted device-level process window. Fundamental understanding of the surface-dependent perovskite growth is critical for the efficient development of co-deposition processes as it links the molecular scale SAM-perovskite interactions directly to the technological process window and the resulting optoelectronic perovskite properties.

5.3.1 Evidence of Substrate-Dependent Effective FAI Incorporation Rate

The effect of the different surface chemistries on the effective FAI incorporation rate is first assessed at the device level for the fixed nominal perovskite composition of $\mathrm{Cs_{0.13}FA_{0.87}Pb(I_{0.95}Cl_{0.05})_3}$ adapting a recipe by Lohman *et al.*[123] A series of co-deposition processes with increasing equivalent FAI rates[c] are fabricated to optimize the perovskite stoichiometry with the obtained PCEs being displayed in **Figure 5.5 A/B** for perovskite thin films deposited on monolayer and bulk 2PACz films, respectively. A strong substrate effect is observed in case of 2PACz for $\sim$ 23–30% lower FAI rates are required to reach peak PCE compared to the monolayer counterpart. This effect is also consistent for other members of the nPACz family such as MeO-2PACz and Me-4PACz[d] with detailed descriptions in the original publication.[103] In both monolayer (**Figure 5.5 A**) and bulk (**Figure 5.5 B**) series, the PCE remains high over a broad range and then collapses abruptly once the FAI content becomes too large, resulting in an FAI excess. This sharp drop is dominated by a pronounced decrease in J_{SC} and is characteristic of overstoichiometric, FAI-rich perovskite growth. Crucially, the onset of this drop occurs at much lower equivalent FAI rates for bulk 2PACz than for monolayer 2PACz, meaning that substantially less FAI is required to reach the same device performance. The observation that comparable device performances are achieved while requiring substantially lower amounts of FAI is important for industrial adaptation, considering that FAI deposition rate is limiting the fabrication throughput as laid out in the previous

[c] The inorganic precursor deposition rates are: PbI_2= 0.23 Å s^{-1}, $PbCl_2$= 0.01 Å s^{-1}, CsI= 0.025 Å s^{-1}

[d] [4-(3,6-Dimethyl-9H-carbazol-9-yl)butyl]phosphonic acid

Chapter 4. The widened high-PCE window for monolayer SAMs and the earlier collapse for bulk SAMs therefore provide direct evidence for a higher effective FAI incorporation rate on bulk 2PACz surfaces compared to the monolayer counterpart. **Figure 5.5 C/D** compares champion PCEs for 2PACz deposited by evaporation and by spin coating, for both monolayer and bulk surface terminations. Evaporation of SAM-HTLS is attractive as the lossless interface properties of nPACz materials can be implemented in a fully vapor-based device, simplifying process integration.[122] Despite different SAM preparation routes, the maximum performances are comparable when the equivalent FAI rate is optimized accordingly. Monolayer 2PACz yields champion PCEs of $\approx 17.0\%$ (solution processed SAM) and $\approx 16.7\%$ (evaporated SAM), while bulk 2PACz gives $\approx 16.2\%$ (solution processed SAM) and $\approx 16.0\%$ (evaporated SAM). It is speculated, that the slightly lower obtained PCEs on bulk SAM are caused by the higher resistance of the thicker HTL and non-ideal orientation of the bulk layer. However, the optimal equivalent FAI rates differ significantly between surface terminations with the monolayer optimum at a equivalent FAI rate of 1.05 for both deposition methods, whereas optima for bulk 2PACz occur at 0.8 (solution processed) and 0.6 (evaporated). Comparable champion efficiencies can be achieved on either surface type only after substantial, surface-specific optimization of the equivalent FAI rate, underscoring that the initial growth conditions set by the SAM interface decisively control the co-deposited perovskite formation pathway. At the same time, the higher optimal FAI rates on bulk SAMs imply a much higher effective FAI incorporation rate as compared to monolayer SAMs, which could be exploited to enable a higher overall deposition rates and thus improved fabrication throughput without sacrificing thin film quality.

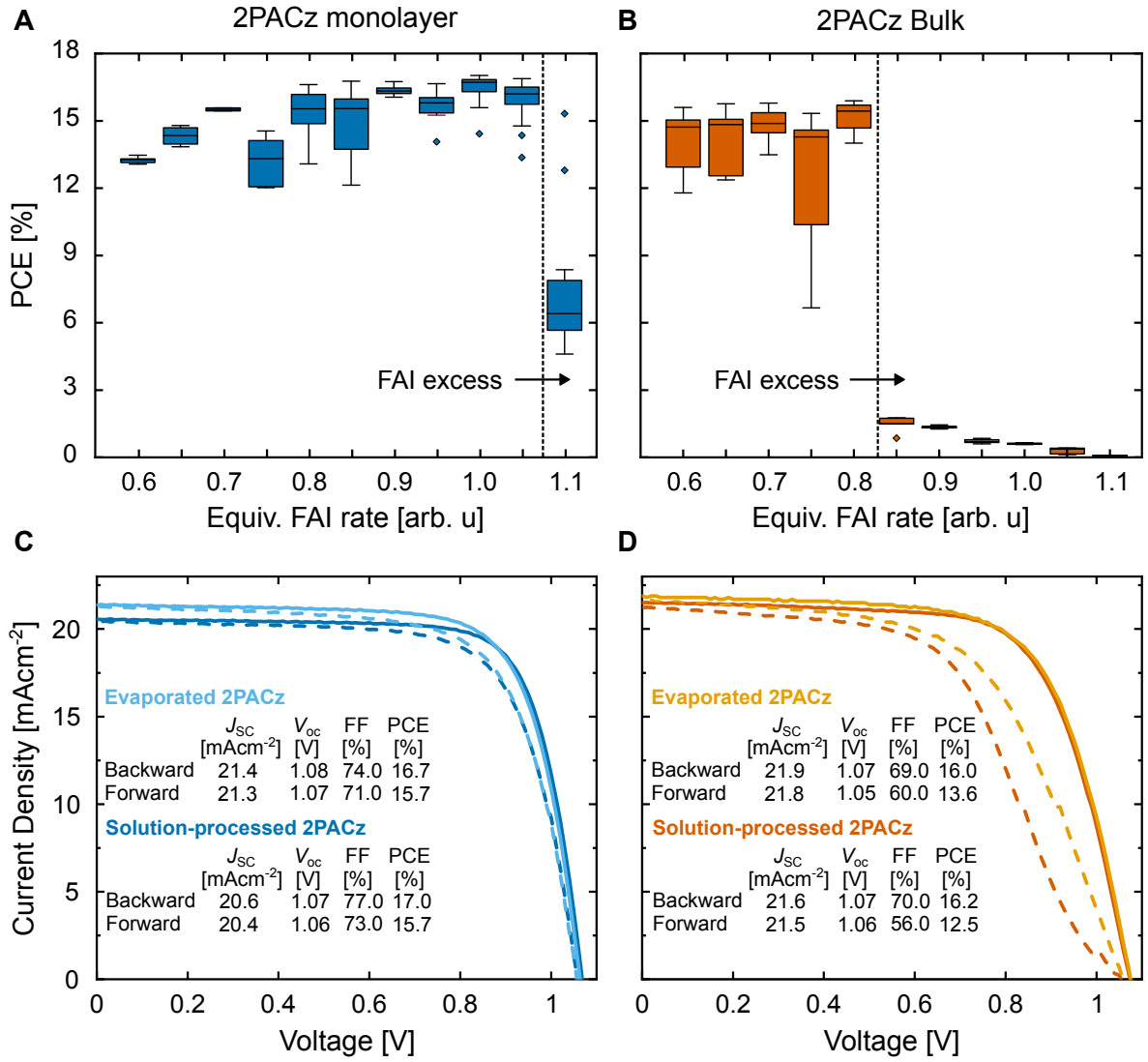

Figure 5.5: Panels **A** and **B** show statistical trends of the PCE using solution-processed 2PACz monolayer or bulk layer, respectively. For each series, the equivalent FAI deposition rate is varied from 0.60 to 1.10 Å s^{-1} in 0.05 Å s^{-1} steps, and only the backward J-V scan is shown. The number of devices per condition ranges from 4 to 16 (average $\approx$ 10), except for the 0.70 Å s^{-1} monolayer 2PACz condition, which includes 3 samples. Panels **C** and **D** display the J-V curves of champion pixels for devices based on monolayer and bulk 2PACz interfaces at their respective optimal equivalent FAI rates. Solid and dashed lines represent backward and forward scan, respectively. Adapted with permission from Elsevier.[103] PCE: power conversion efficiency

5.3.2 Quantification of Increased Effective FAI Incorporation Rate by X-ray Emission Spectroscopy

To directly probe whether exposed phosphonic acid groups present on the bulk 2PACz layer modify the effective FAI incorporation rate, soft X-ray emission spectroscopy (XES) measured at the N K edge is used. This technique provides element specific information of the occupied nitrogen-projected *p*-type density of states, and can detect changes in the local electronic environment together with a qualitative assessment of the abundance of the respective molecular entities.

Non-resonant N K XES spectra ($h\nu = 420$ eV) are collected for two substrate configurations: evaporated bulk 2PACz and evaporated monolayer 2PACz (washed to remove bulk material). On each substrate thin films of around $\sim$25 nm of either FAI or FA-based perovskite are deposited. Reference spectra of bare ITO, pressed-powder 2PACz, bulk $FAPbI_3$, and FAI (taken from a prior work of Kamal *et al.*)[226] are used to interpret the measured stacks with all data presented in **Figure 5.6 B**. The reference N K XES of ITO shows only a weak, broad feature centered near 394 eV, which is attributed to trace nitrogen incorporated during ITO preparation or contamination from the cleaning process. In contrast, 2PACz exhibits a pronounced multi-peak fingerprint with its dominant emission at $\sim$398 eV. This main peak corresponds to decay from the highest occupied molecular orbital localized on the carbazole nitrogen into the N 1s core hole, while the lower-energy shoulders are related to deeper-lying molecular orbitals. The FAI reference spectrum provides a distinct N K edge signature of the FA^+ cation. When incorporating FA^+ cations in perovskite structure, subtle changes of the spectrum reflect hybridized FA^+- and halide-derived valence states.

For the as-prepared substrates, the spectra of both 2PACz/ITO samples are a superposition of the ITO background and the 2PACz molecular signal. The bulk 2PACz/ITO spectrum contains the 2PACz multi-peak structure, indicating that evaporated bulk 2PACz retains the same chemical motif as the powder reference. By contrast, the monolayer 2PACz/ITO spectrum is dominated by the ITO contribution, implying that the monolayer signal is below the detection limit of the substrate background, consistent with an ultrathin SAM. After deposition of 25 nm FAI or 25 nm of perovskite, both stacks display the FA-related N K fingerprint in their respective local environment. Importantly, for both FAI and perovskite thin films, the spectra measured on bulk 2PACz show substantially higher nitrogen-emission intensity than those on monolayer 2PACz, with the difference being most pronounced for the perovskite/bulk-2PACz sample. This intensity contrast indicates a larger fraction of FA-material in the probed region when growing on bulk 2PACz, a direct experimental proof of an increased FAI incorporation rate. These fit fractions provide a qualitative measure of the abundance of the corresponding nitrogen-containing species but are not strictly proportional to the absolute nitrogen concentration due to possible differences in the photoionization cross-sections of the individual compounds. To quantify these contributions, each stack spectrum is modeled as a linear superposition of the corresponding 2PACz/ITO substrate spectrum and either the FAI or perovskite reference with results depicted in **Figure 5.6 B**. The spectrum of FAI on monolayer 2PACz is reproduced by $0.85\times$2PACz $+0.14\times$FAI, whereas FAI on bulk 2PACz requires a larger FAI fraction, $0.90\times$2PACz $+0.20\times$FAI. An analogous trend is observed for the corresponding perovskite samples where monolayer 2PACz yields $1.0\times$2PACz$+0.09\times$perovskite, while bulk 2PACz yields $1.0\times$2PACz$+0.35\times$perovskite. This deconvolution of the respective contribution confirms that both

FAI adsorption and incorporation in the perovskite lattice during crystallization are enhanced on bulk 2PACz featuring exposed phosphonic acid functional groups.

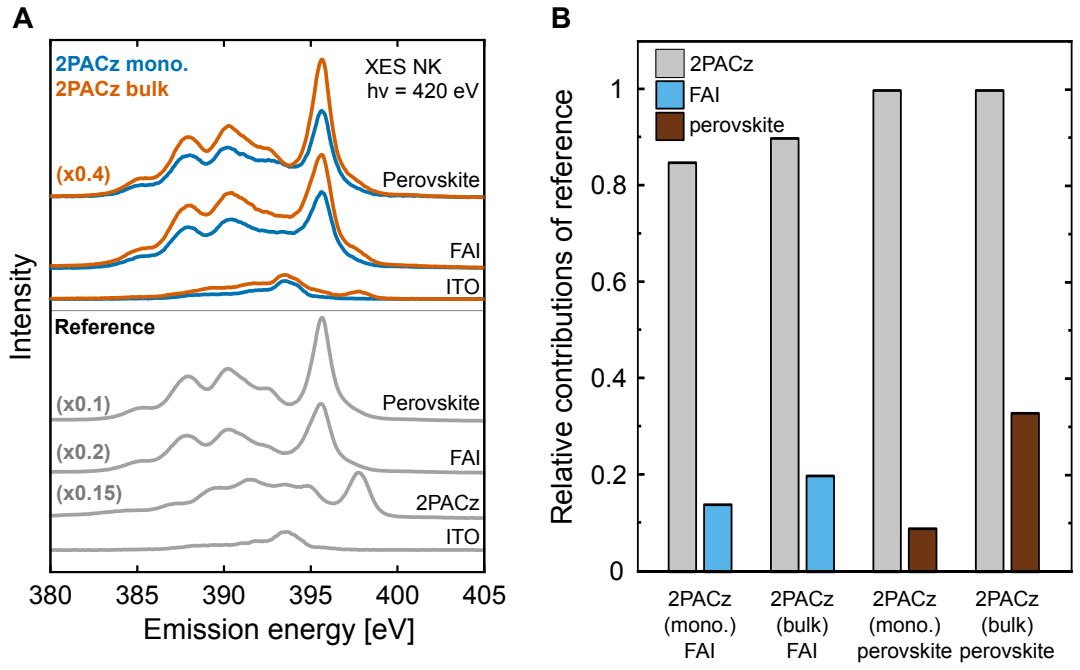

Figure 5.6: A Non-resonant N K-edge XES spectra ($h\nu = 420$ eV) of ~25 nm FAI and ~25 nm $Cs_{0.13}FA_{0.87}PbI_3$ perovskite thin films deposited on bulk or monolayer 2PACz, together with reference spectra of 2PACz (pressed powder pellet), ITO, FAI,[226] and $FAPbI_3$. Where indicated, spectra are multiplied by the listed factor for better visual comparison. **B** Relative contributions of the respective reference components obtained from linear-combination fits used to reproduce the spectra in **A**. These fit fractions provide a qualitative measure of the abundance of the corresponding nitrogen-containing species but are not strictly proportional to the absolute nitrogen concentration due to possible differences in the photoionization cross-sections of the individual compounds. Adapted with permission from Elsevier.[103] XES: X-ray emission spectroscopy, ITO: indium tin oxide

5.4 Investigation of Interfacial Interactions Pathways

To move from an empirical substrate effect to an exploitable design rule, it is important to understand the fundamental interfacial mechanism that governs perovskite phase selectivity during co-deposition. In this section, the mechanistic origin of the substrate-dependent growth behavior of the perovskite absorber on 2PACz is elucidated. First, liquid-state ^{1}H-NMR provides a preliminary assessment of the molecular interaction of FAI and 2PACz. Second, DFT calculations model the relevant α- and δ-$FAPbI_3$ surfaces in contact with 2PACz, allowing the mapping of spatial non-covalent interaction (NCI) energies and to compare phase-dependent binding motifs. Building on these insights a kinetic chemical trapping mechanism is postulated. These insights are utilized for a rational interface design by engineering

monolayer SAMs with controlled densities of exposed phosphonic acids, thereby validating the universal applicability of this hydrogen bonding interaction pathway. This multi-scale approach establishes a coherent mechanistic link between specific hydrogen bonding motifs at the SAM-perovskite interface and the observed phase selectivity.

5.4.1 Surface Polarity to Probe the Density of Phosphonic Acid Functional Groups

Water contact-angle (CA) measurements provide a simplified way to qualitatively assess the density of phosphonic acid functional groups, which is decisive for the earliest stages of co-deposited perovskite growth. In this framework, a low contact angle signals a polar, hydrophilic surface as a result of exposed phosphonic acid (P–OH) groups, whereas a high contact angle indicates a monolayer-type surface dominated by the non-polar carbazole head group. Thus, this method provides a first indication of the surface termination.

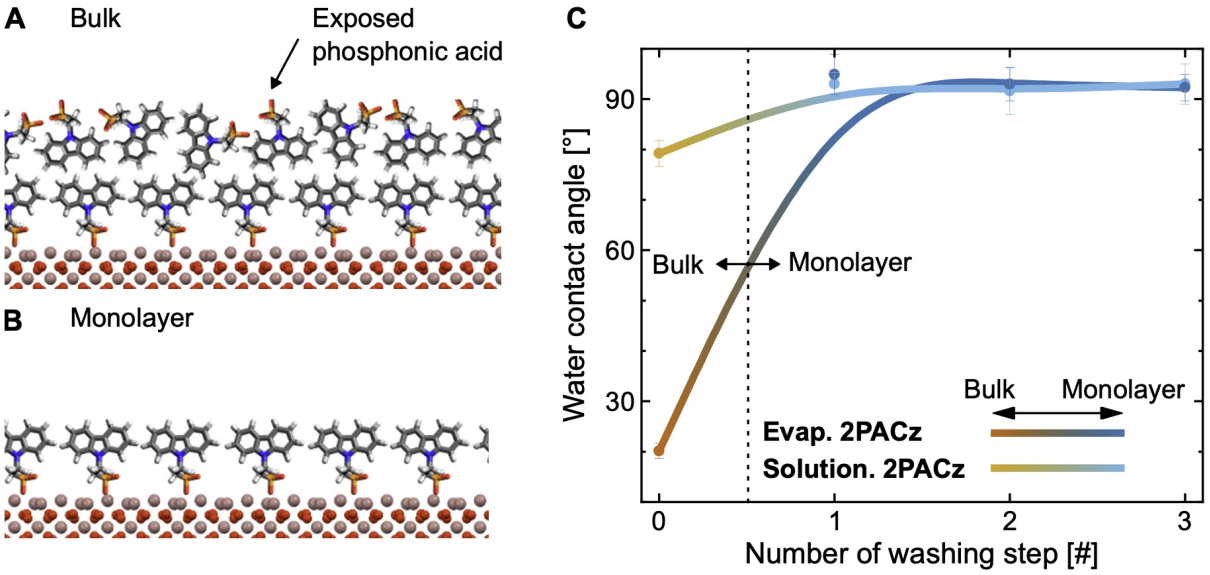

Figure 5.7: **A/B** Schematics of a bulk 2PACz film comprising a chemisorbed SAM-HTL on ITO with an physisorbed bulk overlayer and **B** a washed monolayer SAM. **C** Water CA *versus* successive washing steps for evaporated and solution-processed 2PACz: the as-prepared evaporated film shows a low CA ($\sim 25°$) indicating a highly polar, acid-terminated surface, whereas the unwashed solution-processed film yields a CA of $\sim 79°$. After one washing step, both surfaces converge to a CA of $\sim 92°$ and remain constant, evidencing removal of bulk material. Adapted with permission from Elsevier.[103] CA: Contact angle, ITO: indium tin oxide

Figure 5.7 **A** and **B** schematically depict the two present limits: **A** an unwashed "bulk" 2PACz film, where an additional, loosely bound 2PACz molecules form a bulk layer with P–OH functional groups oriented toward the top interface, *versus* **B** a washed monolayer where such free molecules are removed and

phosphonic acids are largely buried at the anchoring ITO interface. **Figure 5.7 C** shows the measured water CA as a function of the number of washing steps. As-prepared evaporated 2PACz is highly hydrophilic (CA= $\sim 25°$), while for solution-processed 2PACz, a higher CA of $\sim 79°$ is observed. After a single washing step, both converge to the same high contact angle of $\sim 92°$ and remain unchanged with further washing, demonstrating that the strong polarity difference originates from removed bulk 2PACz material, particularly in the evaporated 2PACz case. Therefore, the CA data directly support the initial claim of bulk 2PACz material with free phosphonic acids at the HTL-perovskite interface. Especially in case of evaporated 2PACz the difference between unwashed and washed layers is drastic, indicative of a high surface coverage of free phosphonic acid functional groups.

5.4.2 Identification of Main Interfacial Interaction Pathway

A solution-based mixture of 2PACz and FAI is utilized as an analog system to probe the interfacial interactions *via* liquid-state ^{1}H-NMR spectroscopy. Prior studies postulate that P–OH/FAI interaction occurs between P–OH$\cdots$FA$^+$ with bonding to the amidine moiety.[40] By tracking concentration-dependent chemical shifts and splitting patterns upon mixing 2PACz with FAI in a ^{1}H-NMR titration[e], these scenarios can be distinguished, allowing the the dominant interaction to be identified. **Figure 5.8 A** shows the reference spectra of 2PACz before addition of FAI. Aromatic resonances of the carbazole moiety together with a distinct phosphonic-acid P–OH signal at $\sim$8.8 ppm are observed. **Figure 5.8 B** shows the reference spectra of FAI before (top spectrum) and after addition of 0.5 equiv. 2PACz (bottom spectrum). For pure FAI, two characteristic signals are assigned to the formamidinium CH and NH_2 protons showing the expected integral ratio of 1 to 4, respectively. Upon mixing with 0.5 equiv. 2PACz, the amidine resonance splits into two non-equivalent signals, corresponding to the *cis*- and *trans*-oriented NH protons of FA$^+$ (denoted NH_{cis} and NH_{trans} in inset of **Figure 5.8 B**). The NH_{trans} protons show additional splitting into a doublet with a vicinal coupling constant of $J_{trans} \approx 15.2$ Hz, consistent with hindered rotation and partial planarization of the amidinium unit. As the J_{cis} coupling constant is expected to be smaller in comparison to J_{trans}, the NH_{cis} splitting is not resolved. The CH resonance exhibits splitting into a triplet of triplets, reflecting coupling to the now-inequivalent amidine protons, with $J_{cis} \approx 6.4$ Hz and $J_{trans} \approx 15.1$ Hz.[f] **Figure 5.8 C** tracks the spectra for FAI:2PACz mixtures as the 2PACz fraction is increased. The key observation is a pronounced downfield shift of the P–OH resonance: relative to the 2PACz reference at $\sim$8.8 ppm, the P–OH peak appears near $\sim$6.8 ppm for 0.5 equivalents of 2PACz and shifts progressively to $\sim$9.8 ppm at 2.0 equivalents. In contrast, all other signals related to 2PACz and FAI remain constant position. **Figure 5.8 D** summarize these trends by comparing the chemical shift *versus* added 2PACz equivalents. It is apparent that only the P–OH signal exhibits a systematic shift,

[e] The non-interacting solvent d_6-DMSO is used for this experiment to limit solvent-solute interactions

[f] The observed splitting of the FA$^+$ resonances arises from reduced rotational averaging of the amidinium unit upon addition of 2PACz, which renders the *cis*- and *trans*-oriented NH protons magnetically non-equivalent on the NMR timescale. Each NH proton couples vicinally to the adjacent CH proton. For the *trans*-NH this coupling ($J_{trans} \approx 15$ Hz) is sufficiently large to resolve a doublet, whereas the smaller J_{cis} coupling is only weakly resolved. The CH proton, in turn, couples to both non-equivalent NH protons with different coupling constants (J_{cis} and J_{trans}), resulting in a triplet of triplets pattern.

whereas the FA^+ related CH, NH_{cis}, and NH_{trans} signal positions remain constant. Concluding, the absence of FA^+ peak shifts alongside the selective shift of the P–OH proton indicates that the dominant interaction in solution is between the phosphonic acid and the halide component of FAI. This supports an P–OH$\cdots$I hydrogen bonding pathway rather than direct bonding to the previously assumed positively charged FA^+ cation,[40] providing the first qualitative evidence for the iodide-mediated interfacial interaction pathway. Further measurements of the FAI:Me4PACz and FAI:MeO-2PACz systems are presented in the original publication, showing a comparable trend of the P–OH proton signal shift. This represents the first generalization of the hydrogen bonding pathway across the nPACz family.

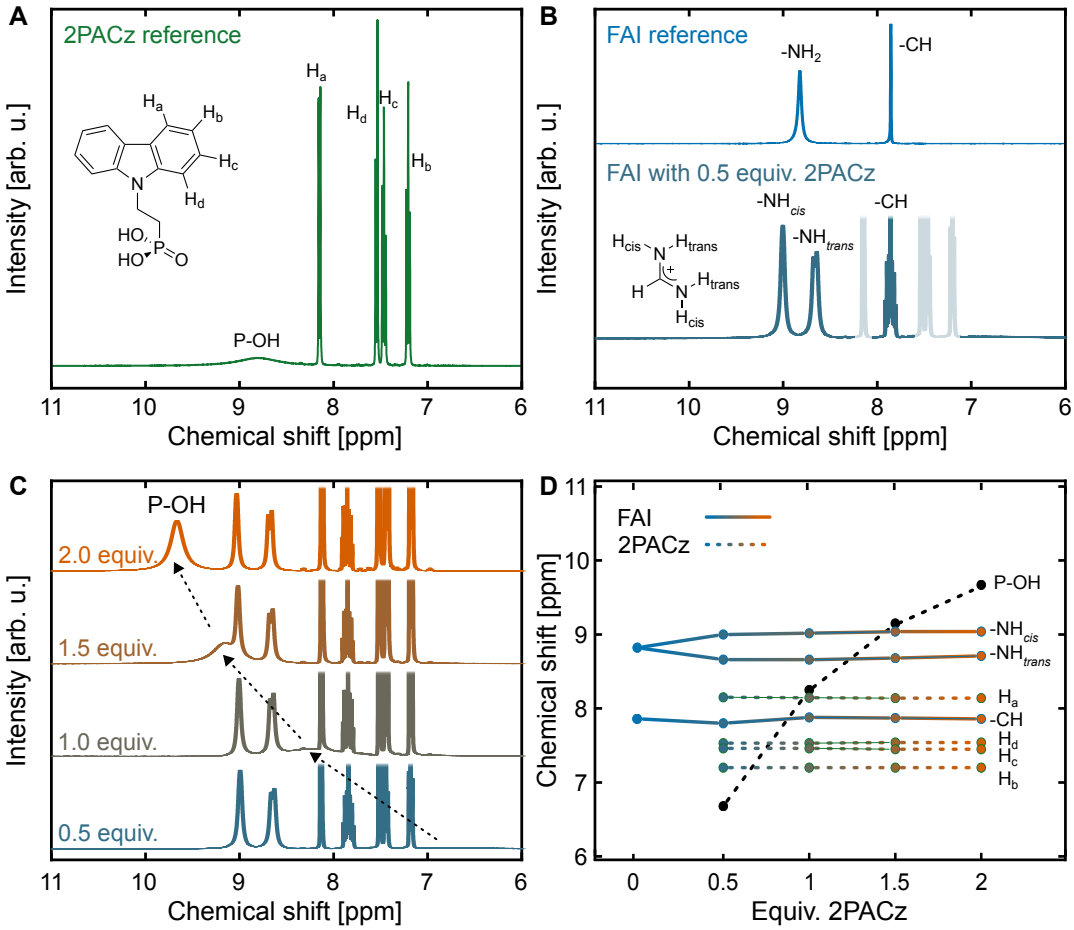

Figure 5.8: **A** Reference ^{1}H-NMR spectrum of 2PACz, showing the aromatic resonances of the carbazole motif and a distinct phosphonic acid P–OH signal at $\sim$8.8 ppm. **B** ^{1}H-NMR spectra of pure FAI before (top) and after addition of 0.5 equiv. 2PACz (bottom). Signals attributed to 2PACz in the mixture spectrum are shown with reduced opacity for clarity. Upon mixing, the CH and NH_2 resonances split into non-equivalent NH_{cis}/NH_{trans} and a triplet-of-triplets CH signal, respectively. **C** Stacked ^{1}H-NMR spectra of FAI:2PACz mixtures recorded at increasing 2PACz fractions. **D** Concentration-dependent chemical shifts of the P–OH, FA^+ CH, NH_{cis}, and NH_{trans} protons as a function of added 2PACz equivalents. Adapted with permission from Elsevier.[103] NMR: Nuclear magnetic resonance

5.4.3 Computational Analysis of Interfacial Interactions Mechanism

To rationalize the experimentally observed substrate dependent growth of the initial perovskite crystallization, and in particular the α-phase stabilization on bulk 2PACz, complementary DFT simulations are conducted. The aim is to obtain an atomistic picture of how exposed phosphonic acid groups in 2PACz interact with perovskite surfaces, and to test how such interactions result in the phase selectivity observed. All calculations are performed with the PBE functional including D3 dispersion corrections, and $FAPbI_3$ was used as a representative FA-based perovskite model in contact with a simplified 2PACz molecule. Only the cubic α-$FAPbI_3$ and hexagonal δ-$FAPbI_3$ polymorphs were considered, since other low-temperature polymorphs are less relevant for standard thin film growth at room temperature. It is first simulated, whether phosphonic-acid binding intrinsically prefers one $FAPbI_3$ phase over the other by analyzing vertical potential energy profiles. Three relevant 2PACz configurations (anionic (A), neutral (N), and *trans* (T)) are chosen and positioned above FA- and Pb-terminated (100) slabs of both α- and δ-$FAPbI_3$ (**Figure 5.9**).

In all cases, the strongest interactions, as reflected by the lowest NCI value, are detected at a 2PACz to perovskite distance of roughly 2 Å, consistent with non-covalent bonding rather than chemisorption. The depth and shape of the potential energy curves are similar for the two phases. Equivalent trends are found for Pb-terminated slabs, indicating that the chemical affinity of 2PACz toward the perovskite surface is not phase selective for α- and δ-$FAPI_3$ phase. It should be noted that slightly deviating potential energy profile is obtained for Pb-terminated α-$FAPI_3$ surfaces when interacting with neutral 2PACz. It is hypothesized, that this effect is not indicative of chemisorption but rather an effect of slightly different 2PACz positioning on the surface as the energy profile depth is in the same range as of the other simulated scenarios. A summary of the simulated NCI energies is given in **Table 5.1**. There is no consistent trend of NCI energies when comparing the binding energy on FA^+ or Pb-terminated surfaces. However, the binding energy of 2PACz to α-$FAPI_3$ is slightly lower compared to the corresponding δ-$FAPI_3$ surfaces. As the NCI stabilization of 2PACz on δ-phase is greater than the one of α-phase, it does not explain the difference in initial selective crystal growth of α-phase on bulk 2PACz.

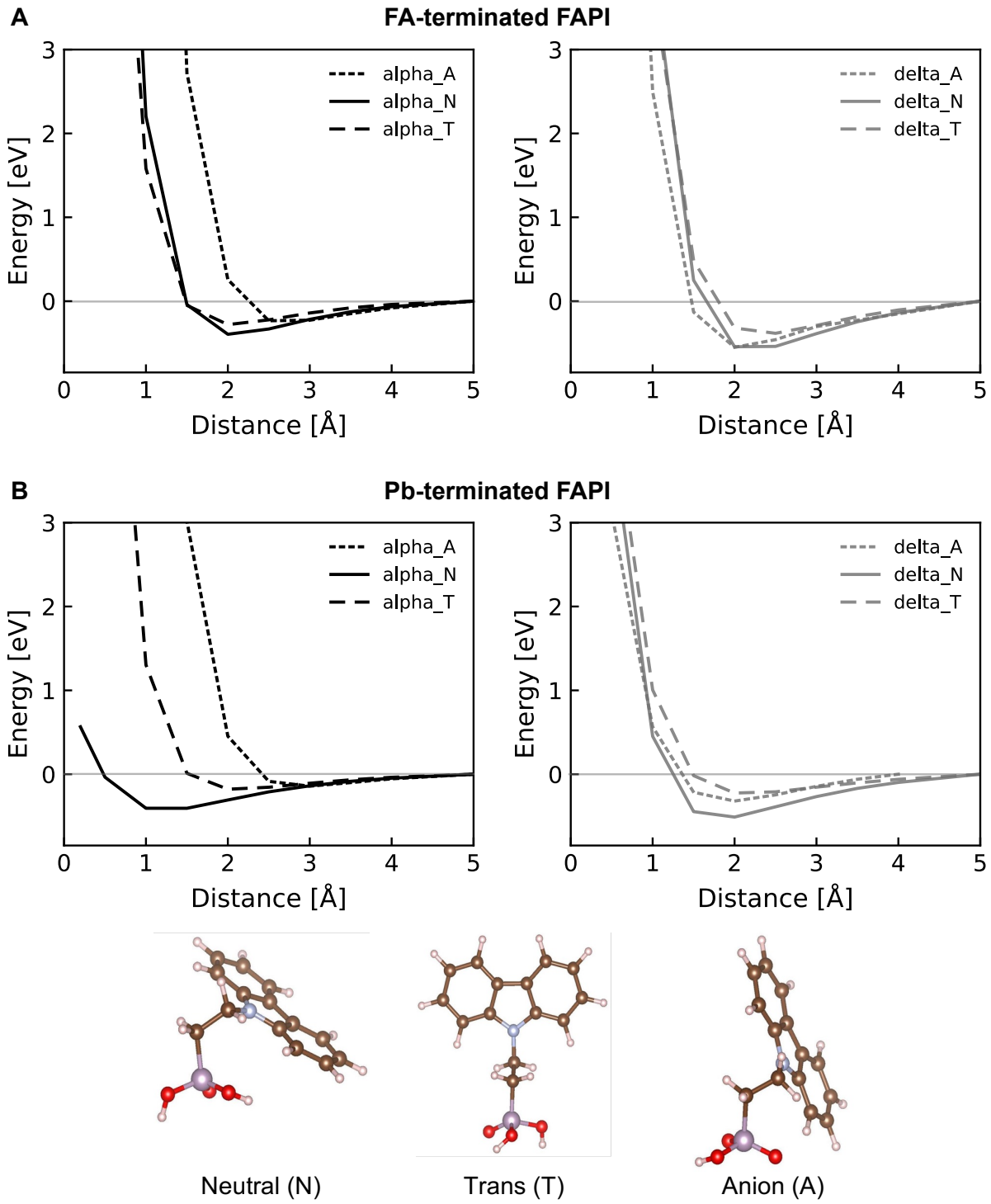

Figure 5.9: Vertical potential-energy profiles as a function of the distance between 2PACz and FA^+- or Pb-terminated (100) slabs of α- and δ-$FAPbI_3$ are shown. For each surface, three 2PACz configurations (anionic (A), neutral (N), and *trans* (T)) are placed above the perovskite and the NCI energy is evaluated. In all cases, the energy minima occur at 2PACz–surface separations of approximately 2 Å. The corresponding NCI energies extracted from these profiles are summarized in **Table 5.1**. Adapted with permission from Elsevier.[103] NCI: Non-covalent interaction

Table 5.1: Summary of non-covalent interaction (NCI) energies for α-FAPI and δ-FAPI. Both FA^+- and Pb-terminated (100) surfaces and three 2PACz configurations (anion (A), neutral (N), and *trans* (T)) are considered. NCI: Non-covalent interaction

	α-FAPI			δ-FAPI		
Surface termination	A	N	T	A	N	T
	NCI energy [eV]					
FA^+-terminated	-0.23	-0.39	-0.28	-0.55	-0.54	-0.38
Pb-terminated	-0.14	-0.41	-0.18	-0.32	-0.51	-0.22

To capture lateral local differences in NCI energies and to identify the relevant interaction geometries, the NCI energy is scanned by translating a 2PACz molecule across a 3×3 $FAPI_3$ superlattice along the (100) plane at a fixed vertical distance of 2 Å. The resulting spatial NCI energy maps are depicted in **(Figure 5.10 A/B)** for α- and δ-phase, respectively. A larger maximum stabilization is observed for δ-$FAPbI_3$ (up to ~ 720 meV) compared to α-$FAPbI_3$ with up to ~ 470 meV stabilization. Thus, phosphonic-acid binding thermodynamically favors the δ-phase. The geometries at the energy minima for both phases feature shortened P–$OH\cdots I^-$ contacts between the phosphonic acid and iodide ions at the surface (**Figure 5.10 C/D**), while contacts to FA^+ or Pb sites remain comparatively long. This observation directly supports the NMR-based conclusion that interfacial hydrogen bonding primarily involves phosphonic acids and halides, rather than the organic cation. Crucially, these results show that the interfacial phosphonic-acid interaction alone does not explain the experimentally observed preference for α-$FAPbI_3$ formation on bulk 2PACz. Instead, they indicate that the observed phase selectivity cannot arise from a simple thermodynamic surface preference and must therefore be understood in terms of the early-stage growth energetics and conversion kinetics.

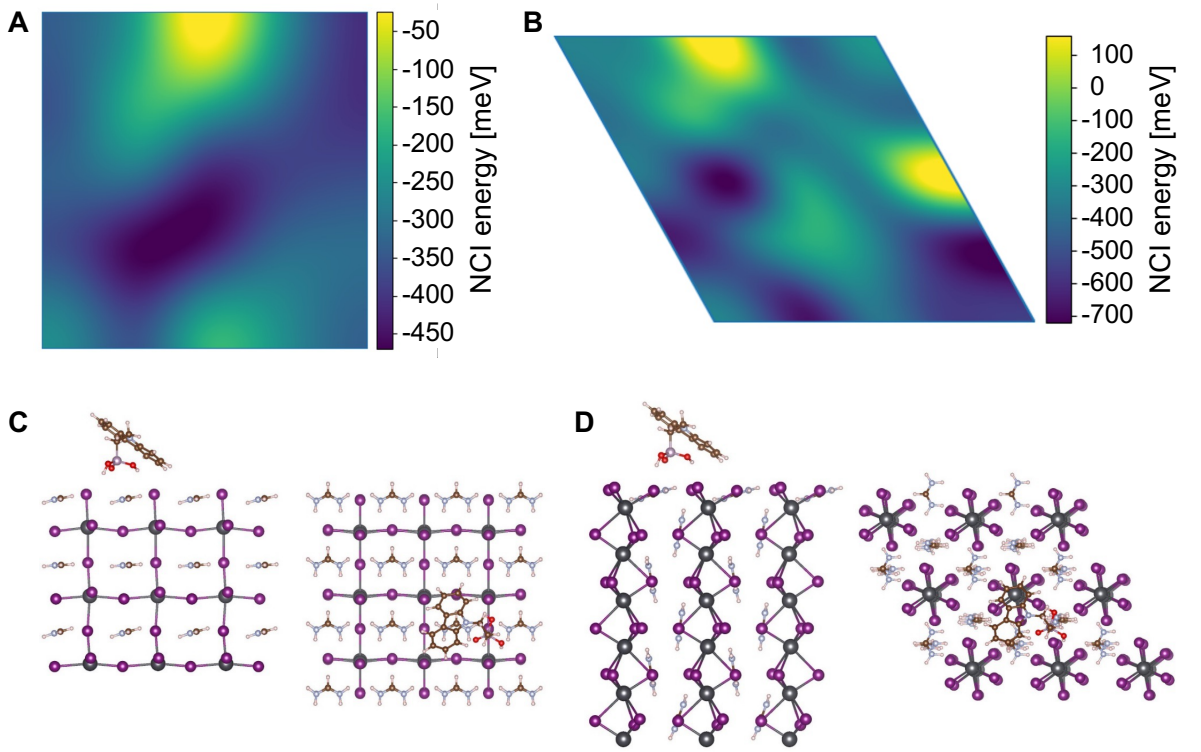

Figure 5.10: Non-covalent interaction maps show spatially varying 2PACz binding strengths on α- and δ-$FAPbI_3$ (100) surfaces. **A/B** Calculated NCI energy maps of α-$FAPbI_3$ and δ-$FAPbI_3$, respectively, at a fixed vertical distance of 2 Å. Representative geometries at the energy minima for **C** α-$FAPI_3$ and **D** δ-$FAPbI_3$, with shortened P–OH$\cdots$$I^-$ contacts. Reproduced with permission from Elsevier.[103]

As the differences in NCI energy of 2PACz on bulk α- and δ-phases do not explain the observed trends in growth behavior, further investigation into the thermodynamics of the initial film growth conditions are conducted. Relative energies of thin perovskite slabs are simulated with one unit cell of δ-$FAPbI_3$ as the thermodynamic reference point (**Figure 5.11 A**). All simulations are performed at a temperature of 0 K to exclude entropic effects and in absence of any surface functionalization. Here, the cubic phase is thermodynamically favored, with α-$FAPbI_3$ showing a 30 meV lower energy compared to δ-$FAPbI_3$ for thicknesses below $\sim$ 33 Å and lower energies at the monolayer-limit thickness of $\sim$ 16 Å. In other words, the δ-$FAPbI_3$ phase is thermodynamically favored in the bulk limit, whereas α-$FAPbI_3$ phase is favored in the monolayer limit, resembling the early crystal growth. Including temperature effects further increase the energetic difference of the two phases, as FA^+ can rotate freely in α-$FAPbI_3$ whereas it is geometrically fixed in δ-$FAPbI_3$,[227] effectively increasing the entropic contribution in α-$FAPbI_3$.[228–230] The entropy term stabilizes the α-phase by about -253 meV at 18° C. Consequently, δ-$FAPbI_3$ is only thermodynamically preferred in the bulk limit. This computational analysis is validated by comparing the XRD spectra of 25 nm thin co-deposited perovskite films on bulk and monolayer 2PACz showing exclusive growth of α-$FAPbI_3$ in the monolayer limit (**Figure 5.11 B**).

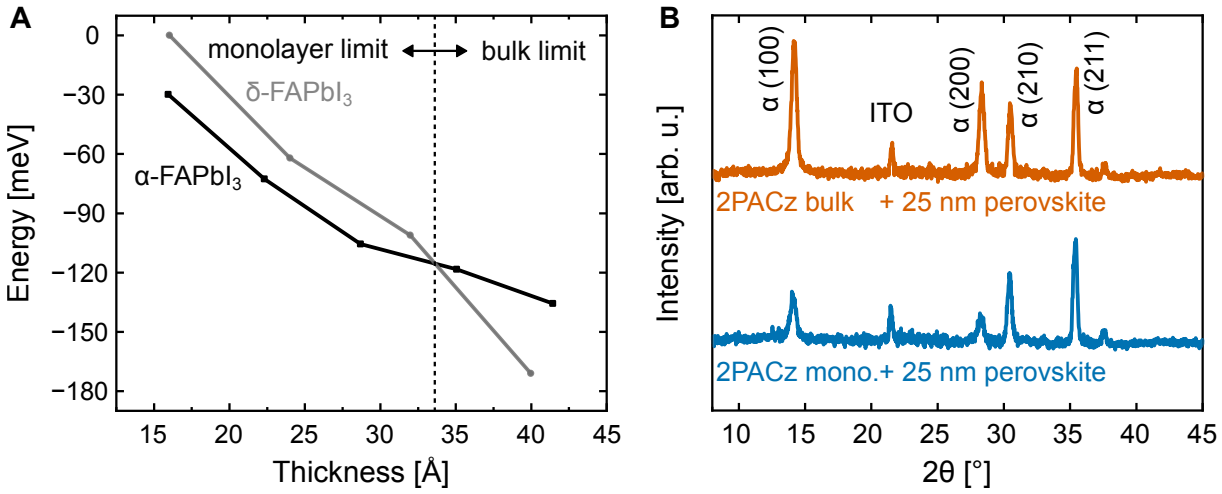

Figure 5.11: DFT slab calculations and XRD measurements demonstrate selectivity towards α-phase growth in monolayer limit. **A** Calculated relative energies of thin $FAPbI_3$ slabs as a function of film thickness. The α-$FAPbI_3$ and δ-$FAPbI_3$ polymorphs are compared for thicknesses down to the monolayer limit ($\sim$ 16 Å), showing lower energies for α-$FAPbI_3$ than for δ-$FAPbI_3$ below $\sim$ 33 Å. It should be noted, that the calculated energies relate to a temperature of 0 K and the energetic difference of α- to δ-phase is much higher at room temperature due to entropic stabilization of the α-phase. **B** XRD patterns of $\sim$ 25 nm co-deposited $FAPbI_3$ films grown on bulk and monolayer 2PACz, showing selective formation of α-$FAPbI_3$ in both cases. Reproduced with permission from Elsevier.[103]

The combined DFT results rationalize two key points: while monolayer $FAPbI_3$ is intrinsically stabilized in the α-phase during the earliest stage of growth, exposed phosphonic acids do not thermodynamically select this phase but instead modify the barrier for its subsequent conversion. On this basis, the experimentally observed α-phase selectivity on bulk 2PACz is interpreted as a kinetic rather than purely thermodynamic effect. Building on this computational analysis, a kinetic trapping mechanism for perovskite thin film growth on exposed phosphonic acids is proposed, as schematically depicted in **Figure 5.12**. Although phosphonic acids demonstrate a higher NCI energy on δ-$FAPbI_3$ compared to α-$FAPbI_3$, the perovskite initially forms as α-$FAPbI_3$ crystallites in the monolayer limit. Conversion to the hexagonal phase requires substantial lattice rearrangement and involves Pb-I bond breaking/forming.[81] When free phosphonic acid groups are present at the interface, the P–OH$\cdots$I hydrogen-bond network imposes an additional conversion barrier with each interacting 2PACz molecule that contributes on the order of 470 meV for α-$FAPbI_3$ resulting in an effective barrier increase of $N \times 470$ meV, with N the number of available phosphonic acids in contact with the perovskite surface. This increased activation energy kinetically traps the initially formed α-phase, explaining the selective and persistent α-$FAPbI_3$ growth on bulk 2PACz. DFT simulations reveal that phosphonic-acid binding to $FAPbI_3$ surfaces is not intrinsically phase selective and can thermodynamically favor the δ-phase. However, thin-slab energetics including entropic contributions stabilize α-$FAPbI_3$ in the monolayer limit. Interfacial hydrogen bonding is therefore proposed to kinetically hinder $\alpha \rightarrow \delta$ conversion and trap the photoactive α-phase during early growth.

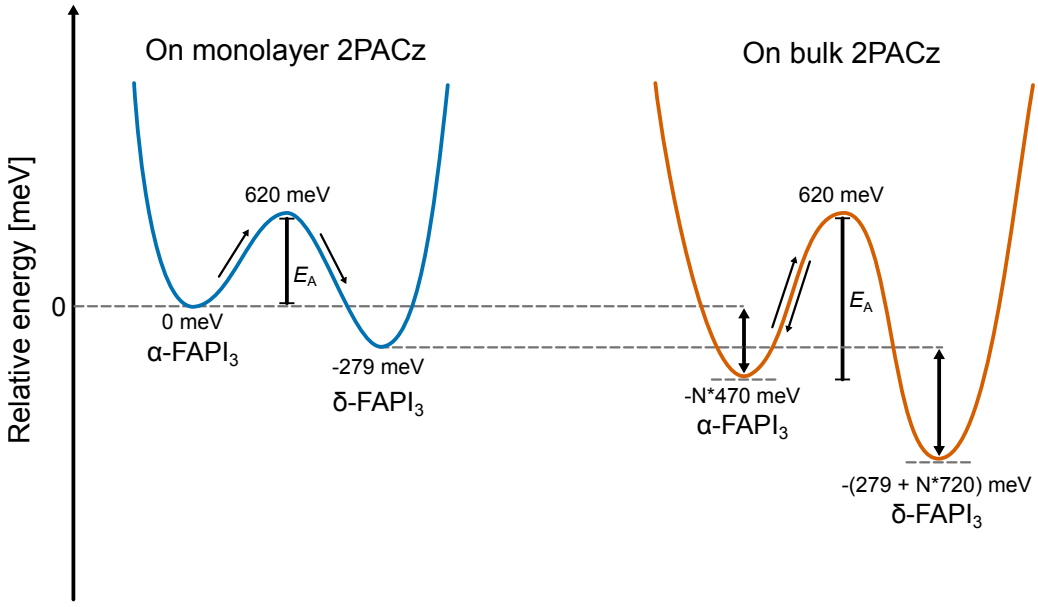

Figure 5.12: Energy diagram illustrating kinetic trapping and stabilization of α-FAPbI$_3$ on phosphonic-acid-terminated surfaces. Shown is a schematic comparison of the activation barriers for phase transitions with and without phosphonic acid functional groups. Reference activation energies in the absence of phosphonic acids are taken from Chen *et al.*[134] Reproduced with permission from Elsevier.[103]

5.5 Rational Surface Design to Control Phase Selective Perovskite Growth

Exposed phosphonic acids dictate the growth of co-deposited perovskite thin films. Consequently, if the proposed P–OH$\cdots$I$^-$ interaction pathway is indeed responsible for the substrate-dependent phase selectivity and shifted process window, then deliberately introducing exposed phosphonic acid groups into an otherwise washed monolayer should reproduce the same growth-directing effect. To test whether this effect can be introduced through rational design of the HTL surface, a monolayer SAM containing exposed phosphonic acids is engineered.

Building on the strategy introduced by Al-Ashouri *et al.* for Me-4PACz using 1,6-hexylenediphosphonic acid (6dPA) as a co-SAM, an analogous approach within the 2PACz system is utilized by partially substituting 2PACz with 1,4-butylenediphosphonic acid (4dPA), where 4dPA is chosen to compensate for the shorter linker for 2PACz in comparison to Me4PACz.[231] **Figure 5.13 A** illustrates this rational design strategy of the SAM surface, depicting the partial replacement of 2PACz by 4dPA within the monolayer. A subsequent washing step again removes unbound molecules, resulting in a phosphonic acid termination of the monolayer surface. Washed mixed SAMs are prepared with controlled 4dPA molar fractions (0%, 10%, 20%, 30%, and 60%), thereby deliberately tuning the surface density of exposed phosphonic acid sites. Co-deposited perovskite thin films at an equivalent FAI rate of 0.75 Å s^{-1} are

fabricated, a condition predicted to favor selective formation of α-$FAPbI_3$ when exposed phosphonic acids are available. **Figure 5.13 B/C** shows the XRD patterns of as-deposited perovskite films and post annealing, respectively. In the as-deposited state (**Figure 5.13 B**), increasing 4dPA content results in a progressive suppression of the δ-$FAPbI_3$ (001) peak accompanied with a rise of the α-$FAPbI_3$ (100) peak. A complete elimination of the δ-phase is observed at 60% 2PACz to 4dPA substitution, highlighting the universal applicability of the effect of exposed phosphonic acids. After thermal annealing (**Figure 5.13 C**), only α-phase signatures remain across the series, consistent with the expected conversion of any residual non-photoactive perovskite phase. In parallel, the residual PbI_2 (001) signal is suppressed as the 4dPA fraction increases, indicating reduced excess PbI_2 and therefore a higher effective FAI incorporation rate on surfaces rich in phosphonic acids, aligning with previous observations on bulk 2PACz.

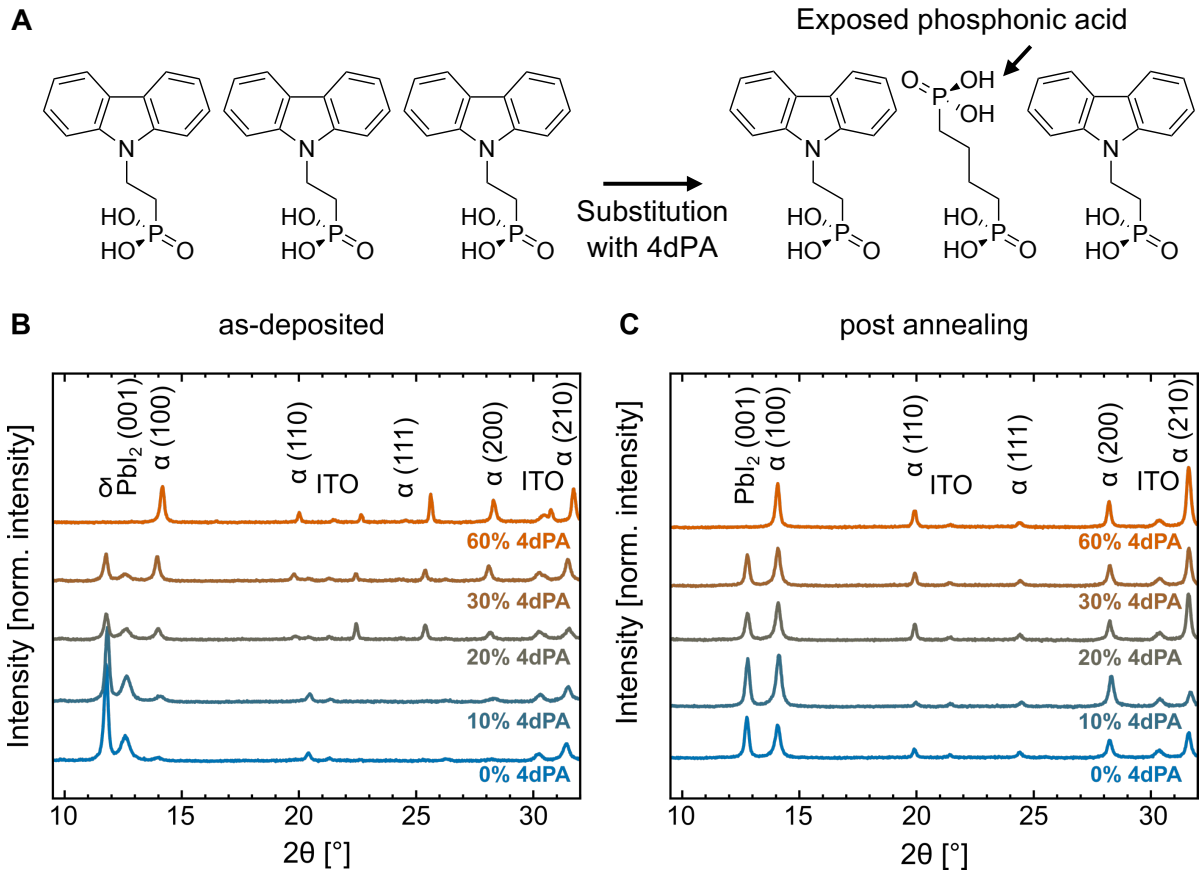

Figure 5.13: A Illustration of the rational SAM design strategy with exposed phosphonic acid sites. **B** XRD patterns of as-deposited perovskite films co-deposited at an equivalent FAI rate of 0.75 Å s^{-1} on the mixed SAM series, showing progressive suppression of the δ-$FAPbI_3$ peak. **C** XRD patterns of the same films post annealing, where only α-phase reflections are observed across all compositions, and the intensity of the PbI_2 (001) peak decreases as the 4dPA content in the SAM is increased. Adapted with permission from Elsevier.[103] XRD: X-ray diffraction, SAM: Self-assembled monolayer

Figure 5.14 summarizes the PSC performances incorporating these mixed monolayer SAMs. While low levels of substitution lead only to a modest reduction in performance, a pronounced drop in PCE emerges beyond 30% 4dPA, with the strongest loss at 60% substitution. This PCE reduction is primarily reflected in reduced J_{SC} and FF at high 4dPA content, indicative of impaired charge extraction at the HTL-perovskite interface. The trend is expected when comparing electronic properties of the two components. Whereas 2PACz is an electronically active hole transport layer, 4dPA acts essentially as an insulator, reducing the charge extraction capabilities at the interface. As a benchmark, perovskite deposition on bulk 2PACz yields PCEs comparable to those of mixed-SAM devices up to ∼30% substitution. The presented rational design strategy reinforces that exposed phosphonic acids can be introduced in a controlled manner to steer the α-phase growth, but that excessive replacement can compromise charge transport and thus device metrics. Through further chemical design, more conductive materials with the same diphosphonic acid motif can be envisioned, potentially enabling the same impact on crystallization while maintaining the beneficial charge extraction properties of SAM-HTLs.

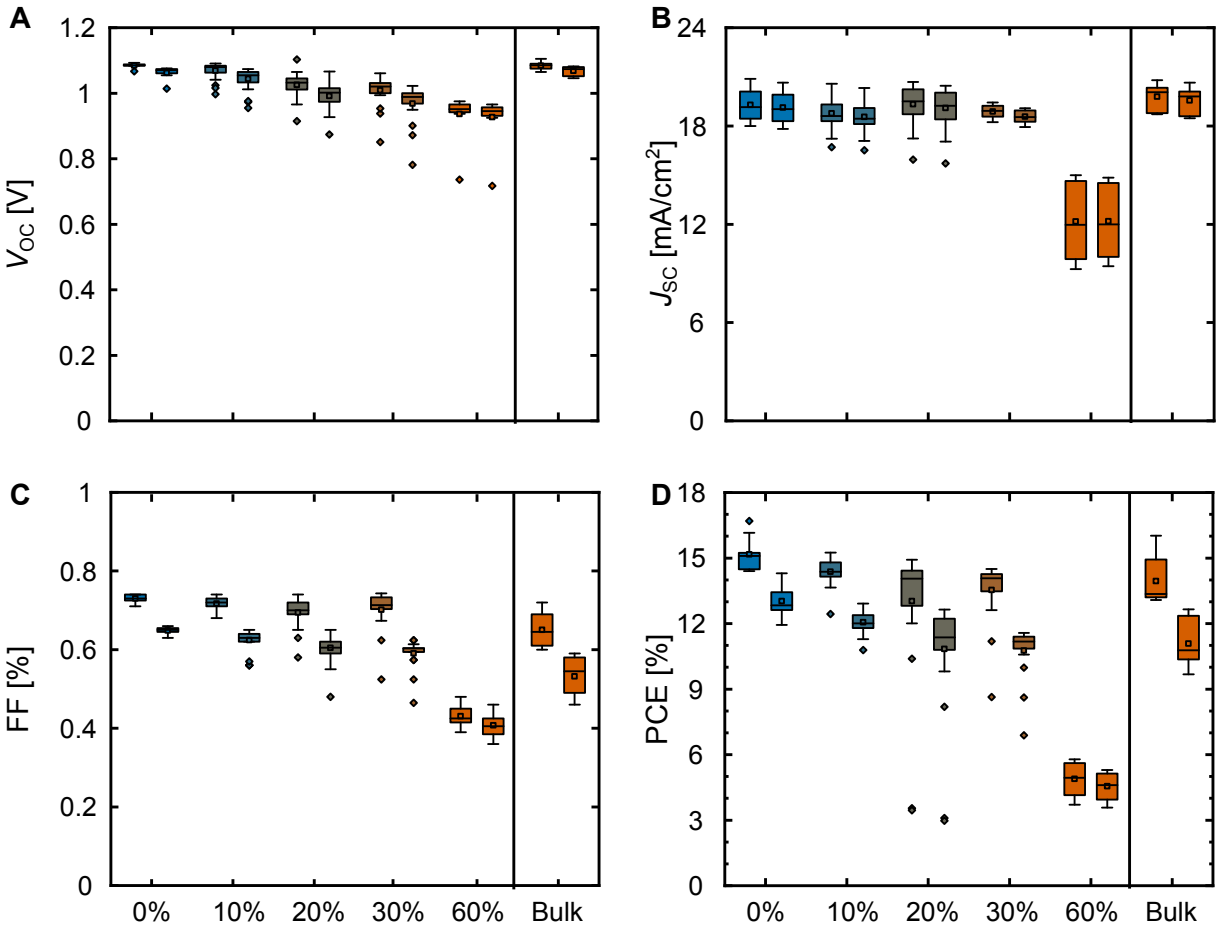

Figure 5.14: Photovoltaic device performances of the PSCs with increasing 4dPA content. As reference, PSCs using a bulk 2PACz layer are shown. The equivalent FAI rate is 0.75 Å s^{-1}. Adapted with permission from Elsevier.[103] PSCs: Perovskite solar cell

5.6 Summary

This chapter elucidates how interfacial surface chemistry controls early-stage crystallization, phase selectivity, and the effective stoichiometric process window during co-deposition, while identifying substrate-dependent growth as a central limitation for process transferability and repeatability. Specifically, the influence of exposed phosphonic acid functional groups in carbazole-based SAM-HTLs on the growth of co-deposited perovskite thin films is investigated by comparing washed 2PACz monolayers with unwashed bulk 2PACz layers containing additional loosely bound 2PACz molecules. This property of the SAM-HTL is specifically important for vapor-deposited perovskite thin films as

XRD analysis reveals pronounced substrate-dependent phase selectivity already in the as-deposited state. On monolayer 2PACz, co-deposited perovskite thin films crystallize into a mixed δ/α-$FAPbI_3$ phase with significant residual PbI_2, whereas on bulk 2PACz the photoactive α-phase forms selectively with only minor residual PbI_2. After thermal annealing, both thin films convert to α-$FAPbI_3$, although thin films on monolayer 2PACz retain higher residual PbI_2 content. Cross-sectional SEM further suggests a weak tendency toward more columnar growth on bulk 2PACz, while the overall lateral grain size remains comparable for both surface terminations.

At the device level, varying the equivalent FAI rate during co-deposition reveals a pronounced substrate dependence of the stoichiometric process window. Bulk 2PACz requires substantially lower equivalent FAI rates to reach optimum PCE, and the high-performance window collapses at lower FAI rates than for monolayer 2PACz, indicating a higher effective FAI incorporation rate on phosphonic-acid-terminated surfaces. Soft X-ray emission spectroscopy at the N K-edge supports this interpretation by showing higher FA-related nitrogen emission and a larger fitted FAI/perovskite contribution for thin films deposited on bulk 2PACz than on monolayer 2PACz.

Water contact-angle measurements confirm that bulk 2PACz presents a more polar, phosphonic-acid-terminated surface than the washed monolayer. To uncover the origin of the resulting substrate-dependent growth, liquid-state ^{1}H-NMR titrations show that only the phosphonic-acid P–OH resonance shifts systematically with the 2PACz:FAI ratio, while the FA^+ resonances remain essentially unchanged, indicating a dominant P–OH$\cdots I^-$ interaction pathway. DFT calculations support this interpretation by identifying short P–OH$\cdots I^-$ contacts at the interface and showing that phosphonic-acid binding is not intrinsically selective for the α-phase. Instead, additional thin-slab simulations demonstrate that ultrathin $FAPbI_3$ is intrinsically stabilized in the α-phase at low thickness, whereas the δ-phase becomes favorable only in the bulk limit. Based on these findings, a kinetic trapping mechanism is proposed in which exposed phosphonic acids increase the barrier for α- to δ-phase conversion, thereby stabilizing the initially formed α-phase during early growth.

Finally, a rational interface-design strategy is demonstrated by partially substituting 2PACz with the diphosphonic acid 4dPA to create mixed SAMs with tunable densities of exposed phosphonic acids. XRD analysis shows a gradual suppression of δ-$FAPbI_3$ and residual PbI_2 together with enhanced α-$FAPbI_3$ formation as the 4dPA fraction is increased, fully eliminating the δ-phase at 60% substitution. PSCs based on these mixed SAMs retain high PCEs up to $\sim$30% 4dPA, whereas higher fractions reduce performance

due to the insulating character of 4dPA. This finding is particularly relevant for vapor-deposition processes, in which excess bulk 2PACz can remain at the HTL-perovskite interface during thin-film formation, whereas analogous loosely bound material is expected to be washed away during solution-based processing. Overall, this chapter shows that phosphonic acid terminated interfaces directly influence effective FAI incorporation, phase selectivity, and the stoichiometric process window in co-deposited perovskites, and demonstrates how targeted interface engineering can be used to reduce substrate sensitivity, improve repeatability, and enable more predictable and transferable vapor-deposition processes.

6 Hybrid Two-Step Deposition of Perovskite Thin-Films

Hybrid two-step perovskite deposition represents a promising route for industrial perovskite thin-film fabrication because it decouples the rate-limiting organic-cation supply from the vapor-deposition step. Within this hybrid route, the deposition of the inorganic scaffold becomes a key process-design parameter that determines device performance, process repeatability, throughput potential, and transferability to industrial fabrication. In this chapter, a fully sequential inorganic scaffold deposition framework is established and benchmarked against the conventional co-deposition route for wide-bandgap perovskite thin-film fabrication. Both approaches achieve comparable device performance, with champion efficiencies of 20.3% for the sequential route and 19.3% for the co-deposition route at a wide bandgap of $\sim$1.70 eV targeted for tandem integration. The sequential route yields a high open-circuit voltage of 1.23 V, approaching 90% of the detailed-balance limit, and demonstrates improved batch-to-batch repeatability, highlighting its potential as a robust fabrication route for large-scale industrial manufacturing. The choice of deposition route itself is revealed as a scaffold-engineering parameter substantially influencing the microstructure formation. Sequential deposition produces a highly porous PbI_2 scaffold composed predominantly of vertically or tilted oriented platelets, whereas co-deposition yields a denser scaffold with horizontally aligned platelets. These microstructural differences directly influence organic-cation infiltration dynamics and the resulting elemental depth distribution within the perovskite thin film. Building on the sequential deposition framework, substantial acceleration of inorganic scaffold formation is demonstrated by reducing deposition times by 80%$_{rel}$ without compromising device performance, representing a critical step toward industrially relevant fabrication throughput. Compatibility with textured silicon substrates is further validated through a first perovskite/silicon tandem prototype achieving an initial efficiency of 24.1%. In addition, the modular architecture of the sequential process enables systematic bandgap engineering through independent control of halide supply from the inorganic scaffold and the organic precursor solution, allowing bandgap tuning from $\sim$1.70 eV to the target bandgaps $\sim$1.52 eV and $\sim$1.84 eV for future multi-junction integration. By linking deposition-route selection to scaffold microstructure, infiltration behavior, device performance, and throughput considerations, this chapter establishes the fully sequential inorganic scaffold deposition within the hybrid two-step route as a scalable and versatile process framework.

Parts of this chapter were published in the research article "Benchmarking Inorganic Deposition Routes for Hybrid Two-Step Processed Perovskite Solar Cells: A Materials Perspective", *Solar RRL*, (**2026**), by *Julian Petry*, Ronja Pappenberger*, Alexander Welle, Tonghan Zhao, Alexander Diercks, Raphael Pesch, Moritz Krause, Paul Fassl and Ulrich W. Paetzold*. Julian Petry and Ronja Pappenberger contributed equally to this work. Some figures in this chapter were reproduced or adapted from the original publication with permission from Wiley-VCH.[107] *Responsible lead and shared first author.
The research plan, including all fabrication of PSCs and characterization of thin-films were developed jointly by Julian Petry and Ronja Pappenberger. The project was supervised by Ulrich W. Paetzold and Paul Fassl. The contributions of all authors according to the CRediT system are listed in **Table A.8**.
This chapter also includes content produced during supervised master's theses of Moritz Krause,[232] Yan Hoppe[233] and Alex Mocanu.[234]

6.1 Motivation and Contextualization

For industrial implementation of perovskite photovoltaics, deposition routes must deliver both high device efficiencies and be compatible with scalable, repeatable, and high-throughput manufacturing. This requirement is particularly relevant for tandem integration on textured silicon bottom cells, where conformal coating, robust process windows, and compatibility with industrial in-line fabrication become decisive. In this context, hybrid two-step processing has emerged as a promising route because it combines the strengths of vapor deposition and solution processing: vapor deposition enables conformal and scalable formation of an inorganic scaffold on complex substrate topographies,[37,39,235–237] while solution-based conversion of the organic cations provides broad compositional tunability, additive engineering and exclusive use of green solvents.[111,117,124,146,180,238]

At the same time, **Chapter 4** identified a central bottleneck for the industrialization of fully vapor-phase perovskite deposition: the deposition of organic precursors is intrinsically limited by thermal stability, process controllability, and the resulting equipment demand at high fabrication throughput.[36,40,41,97,99–101,239] In particular, process-route modeling showed that fully sequential deposition is the most industry-aligned vapor-deposition strategy in terms of process effectiveness, source utilization, and process control. These findings directly motivate the hybrid two-step route studied in this chapter, where the rate-limiting and less controllable organic-cation deposition step is replaced by a solution-based conversion step, while the inorganic scaffold is still deposited by vapor deposition in an industry-compatible manner. Once the organic-cation supply is shifted to the solution step, the inorganic scaffold becomes the decisive vapor-deposition process that must combine device quality with industrial process effectiveness. This chapter thus addresses the *Research Objectives 2-4*.

Using the hybrid two-step route, high-performance PSCs have been demonstrated in tandem architectures, including micron-textured perovskite/Si tandems exceeding 31% PCE.[29,240] More recently, large-area perovskite/Si tandem solar cells using scalable solution processing have approached 28%.[174,206] Despite this strong industrial motivation, most reported hybrid two-step processes rely on co-deposition of the inorganic scaffold.[111,117,124,146,180,238] This creates a discrepancy between current laboratory practice and the industry-aligned process route requirements identified for industrial implementation in Chapter 4. A systematic investigation of fully sequential inorganic scaffold deposition within the hybrid two-step framework is therefore required.

Accordingly, this chapter addresses three questions central to implementation of the sequential deposition route:

- **Establishing and benchmarking the sequential route framework:** Can the hybrid two-step sequential route deliver perovskite quality and device performance comparable to the conventional co-deposited scaffold, and does it provide a more repeatable process window?

- **Acceleration of process throughput:** Are there fundamental limits to accelerate the sequential route through vertical scale-up and horizontal scale-out strategies? Does process acceleration compromise device performance?
- **Bandgap engineering:** Does the fully sequential framework enable facile bandgap tuning? How to develop recipes for mid bandgap (MBG, ∼1.52 eV) and ultra-wide bandgap (UWBG, ∼1.84 eV) perovskite thin films targeted for future triple-junction implementation?

6.2 Benchmarking Inorganic Scaffold Deposition Routes

Efficient WBG perovskite thin films with a target bandgap of ∼1.68 to 1.70 eV are central for implementation in tandem solar cells.[29,174,206,240] Further, scaffold engineering is a key lever in two-step perovskite processing: the inorganic scaffold morphology and porosity directly dictates the conversion kinetics in diffusion-limited two-step processes and ultimately the optoelectronic quality of the perovskite thin film.[106,112,121,174,241] Within this context, this section addresses whether a fully sequential vapor deposition of the inorganic scaffold can replace conventional co-deposition in the hybrid two-step route without compromising device performance, and to identify material-level differences arising from the choice of deposition route.

In the conventional co-deposition route (Co route), CsCl and PbI_2 are deposited simultaneously as illustrated in **Figure 6.1 A** (Co route). In contrast, the fully sequential vapor deposition of the inorganic scaffold (Seq route) is illustrated in **Figure 6.1 B** (Seq route). In this route, CsCl is deposited first, followed by deposition of PbI_2. The incorporation of CsCl into the scaffold has been shown to promote crystallization and enhance perovskite film quality.[242]

In the hybrid two-step routes, the inorganic scaffold is formed through vapor deposition of the inorganic precursors as depicted in **Figure 6.1 A/B** for the Co- or Seq route, respectively. The inorganic scaffold is composed of CsCl and PbI_2 in both cases. In a second step, conversion to the perovskite thin film by application of an organic cation solution, following established recipes by Er-raji *et al.*[117] and Li *et al.*[124], and subsequent thermal annealing under ambient condition as shown in **Figure 6.1 C**. A NiO_x/2PACz bilayer is used as the *p*-selective contact, which improves hole extraction and perovskite crystallinity relative to a 2PACz-only reference.[204] The half-stack architecture is glass/ITO/NiO_x/2PACz/perovskite. The perovskite thin film has the nominal composition $Cs_{0.18}FA_{0.82}Pb(I_{0.76}Br_{0.18}Cl_{0.06})_3$ with a target bandgap range of 1.68–1.70 eV (**Figure 6.1**). Further fabrication details are provided in the Experimental Section (**Chapter 3.1.1**).

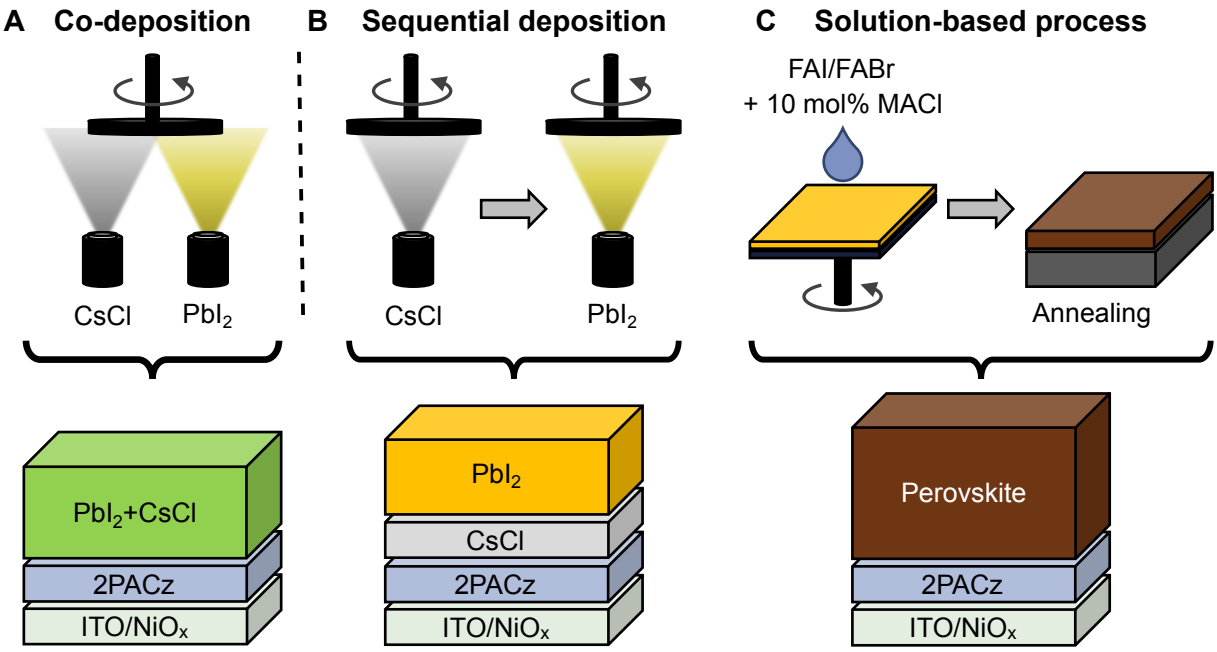

Figure 6.1: Schematic of the two hybrid two-step deposition process routes studied: **A** co-deposition (Co) and **B** sequential deposition (Seq) routes of the inorganic precursors CsCl and PbI_2, with the corresponding layer sequence depicted below each process. **C** Corresponding perovskite thin film obtained after deposition of the organic cation solution and subsequent thermal annealing under ambient conditions. Reproduced with permission from Wiley-VCH.[107]

The comparison therefore proceeds from device-level benchmarking to detailed materials analysis, linking route-dependent photovoltaic behavior to differences in scaffold morphology, crystal orientation, and elemental distribution.

6.2.1 Photovoltaic Performance of Perovskite Solar Cells

Device performance provides the first quantitative benchmark for comparing the two inorganic-scaffold deposition routes. Although the Co- and Seq routes follow fundamentally different process sequences, both routes yield PSCs with comparable PCEs when the conversion of the inorganic scaffold into the corresponding perovskite thin film is properly optimized by variation of the organic cation solution molarity.

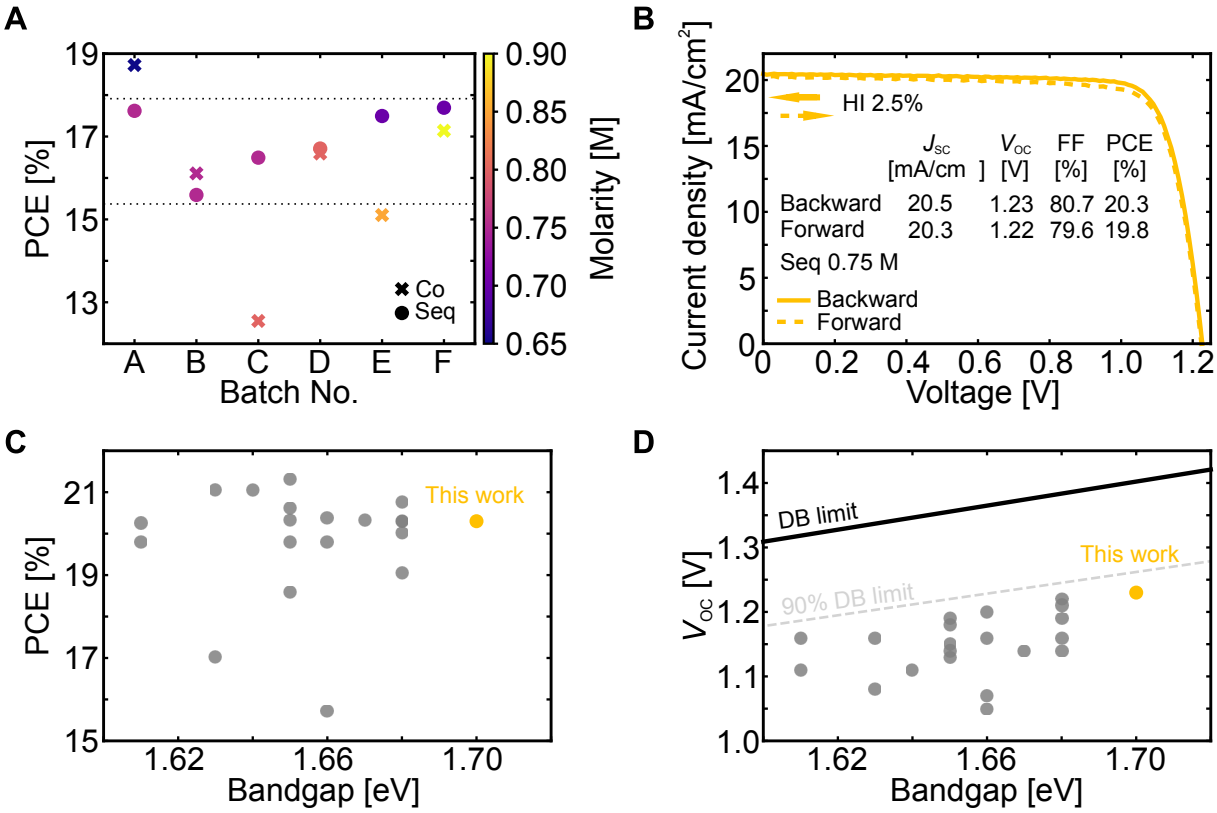

Figure 6.2: A Comparison of process repeatability for PSCs fabricated with co- (Co) and sequential (Seq) deposition of the inorganic scaffold. Shown are median PCE values of six consecutive batches. Within each batch, Co and Seq devices were fabricated in parallel. Symbol colors indicate the organic-cation molarity that yielded the highest PCE in the respective batch. **B** Representative champion PSC fabricated using the sequentially deposited inorganic scaffold (optimal organic-cation molarity: 0.75 M). **C** PCE *versus* bandgap and **D** V_{OC} *versus* bandgap for WBG (> 1.60 eV) hybrid two-step processed PSCs compiled from literature. Reproduced with permission from Wiley-VCH.[107] PSC: Perovskite solar cell, PCE: power conversion efficiency, HI: hysteresis index

To assess potential differences in process repeatability, six consecutive PSC batches are fabricated for both routes. For each batch, **Figure 6.2 A** summarizes the median PCE, while the symbol colors indicate the organic-cation molarity that produced the highest PCE within that batch. Two key observations are apparent. First, the Co route exhibits a pronounced batch-to-batch variability, whereas the Seq route provides more consistent performance across multiple batches, as indicated by the dotted horizontal line. Second, both deposition routes reach comparable efficiency levels. However, the Co route shows a substantially less consistent optimum in organic-cation molarity, which can lead to significant efficiency losses if the conversion conditions are not adjusted. This improved repeatability is particularly important for industrial manufacturing, where narrow and unstable process windows reduce the fabrication yield, and complicate stable high-throughput production.

Consistent with this trend, the optimal molarity for the Co route shifts between 0.65 M and 0.90 M across batches, while the Seq route retains a narrower optimum between 0.70 M and 0.80 M. Full batch-resolved trends are provided in **Figure A.1**. To exclude variations in the nominal inorganic scaffold as the dominant origin of these shifts, the final QCM thicknesses are monitored for each batch. Only minor variations of the CsCl QCM thickness are observed for Co route (30±1 nm), which rules out substantial changes in the intended scaffold composition (**Table A.1**).

A representative champion device obtained from the sequential route is shown in **Figure A.1 B**. For this device, a maximum PCE of 20.3% is achieved with $V_{\mathrm{OC}} = 1.23$ V, $J_{\mathrm{SC}} = 20.5$ mA cm^{-2} and $\mathrm{FF} = 80.7$ % and a bandgap of 1.70 eV (**Figure A.2 B**). This performance ranks among the highest reported efficiencies for hybrid two-step processed WBG PSCs and features a high V_{OC} approaching 90% of the detailed-balance limit for this bandgap (**Figure 6.2 C/D**; all values summarized in **Table A.2**). In addition, maximum power point (MPP) tracking confirms stable operation over 4000 s (**Figure A.2 C**). In comparison, the maximum PCE obtained for Co route is 19.3% with $V_{\mathrm{OC}} = 1.20$ V, $J_{\mathrm{SC}} = 19.8$ mA cm^{-2} and $\mathrm{FF} = 79.7$ %. Taken together, these results indicate that the Seq route is *on par* in terms of peak device performance, while also being preferable from a process perspective because it combines high efficiency with improved repeatability.

An initial stability screening was conducted under ISOS-L1 conditions (100 mW cm^{-2}, 25 °C, MPP tracking) for the optimal and second-best organic-cation molarities of each route (Co route: **Figure A.3**; Seq route: **Figure A.4**). The results (**Figure A.5**) indicate a strong dependence of device stability on the organic-cation molarity for both routes. Fractional deviations in perovskite stoichiometry are ascribed to influencing device stability, supporting this hypothesis.[243] These trends emphasize that conversion conditions critically affect both initial performance and operational stability, motivating further optimization and dedicated stability studies.

Unless stated otherwise, all subsequent material and device analyses in this section are conducted using Batch A (from **Figure 6.2**) and the respective optimal organic-cation molarities for perovskite conversion (0.65 M for Co route and 0.75 M for Seq route), allowing a representative and fair comparison at similar device performance. Detailed photovoltaic statistics for Batch A are provided in **Figure A.6** (Co route) and **Figure A.7** (Seq route), with the corresponding champion devices shown in **Figure A.8**. Both routes yield low hysteresis indices (HI) below 5%, which is favorable for *p-i-n* PSCs and indicates reliable device operation.[45] The EQE-derived bandgaps are shown in **Figure A.9** and the absorptance spectra in **Figure A.10**.

6.2.2 Microstructure and Morphology

This section compares route-dependent features from the optical appearance to the nanoscale structure and relates these features to the organic-cation uptake and thickness expansion upon conversion. Route-specific differences of the inorganic scaffolds are evident by visual inspection: co-deposition of inorganic precursors yields a smooth, featureless surface, whereas sequential deposition produces a distinctly rougher appearance

(**Figure 6.3 top row**). The corresponding perovskite thin films are comparable in appearance (**Figure 6.3 bottom row**).

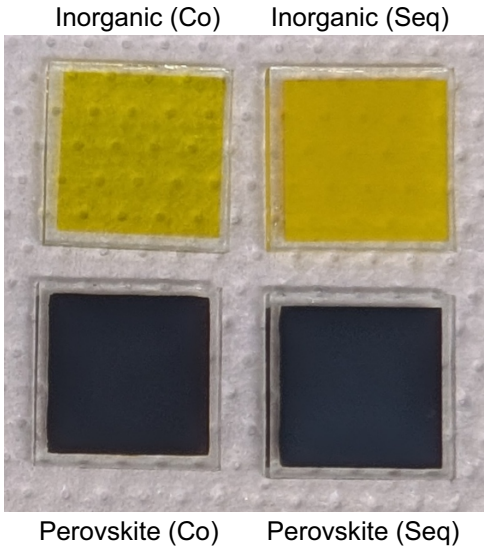

Figure 6.3: Optical photographs of the inorganic scaffolds and the corresponding perovskite thin films for Co- and Seq route. For the perovskite thin films, the respective optimal molarity of the organic cation solution is used. Reproduced with permission from Wiley-VCH.[107]

These macroscopic contrasts motivate a more detailed analysis by SEM and atomic force microscopy (AFM) (**Figure 6.4**). Top-view and cross-sectional SEM images confirm the pronounced route-dependent scaffold morphologies (**Figure 6.4 A/B**). The Co route inorganic scaffold is dense and uniform with a smooth surface structure and a thickness of $\sim$330 nm, consistent with QCM measurement and surface profilometry (**Figure 6.6**). Individual PbI_2 platelets are not discernible. In contrast, the Seq route inorganic scaffold exhibits a highly textured microstructure and an irregular topography that does not allow for reliable thickness determination from the SEM cross-section. From surface profilometry, an average thickness of 409 ± 4 nm is found, which is substantially thicker compared to Co route. Top-view and cross-section SEM images reveal vertically aligned PbI_2 platelets with two predominant orientations (vertical or tilted with respect to the substrate). AFM supports these observations, showing an order-of-magnitude increase in root-mean-square (RMS) roughness from 6.1 ± 0.1 nm (Co route) to 77.1 ± 0.4 nm (Seq route), indicative of a more open and textured surface. Despite these differences of the inorganic scaffold, the final perovskite thin films (prepared at the respective optimal organic-cation molarity) exhibit comparable microstructures and similar AFM roughness values of 29.6 ± 0.7 nm (Co route) and 26.8 ± 0.3 nm (Seq route) as depicted in **Figure 6.4 C/D**.

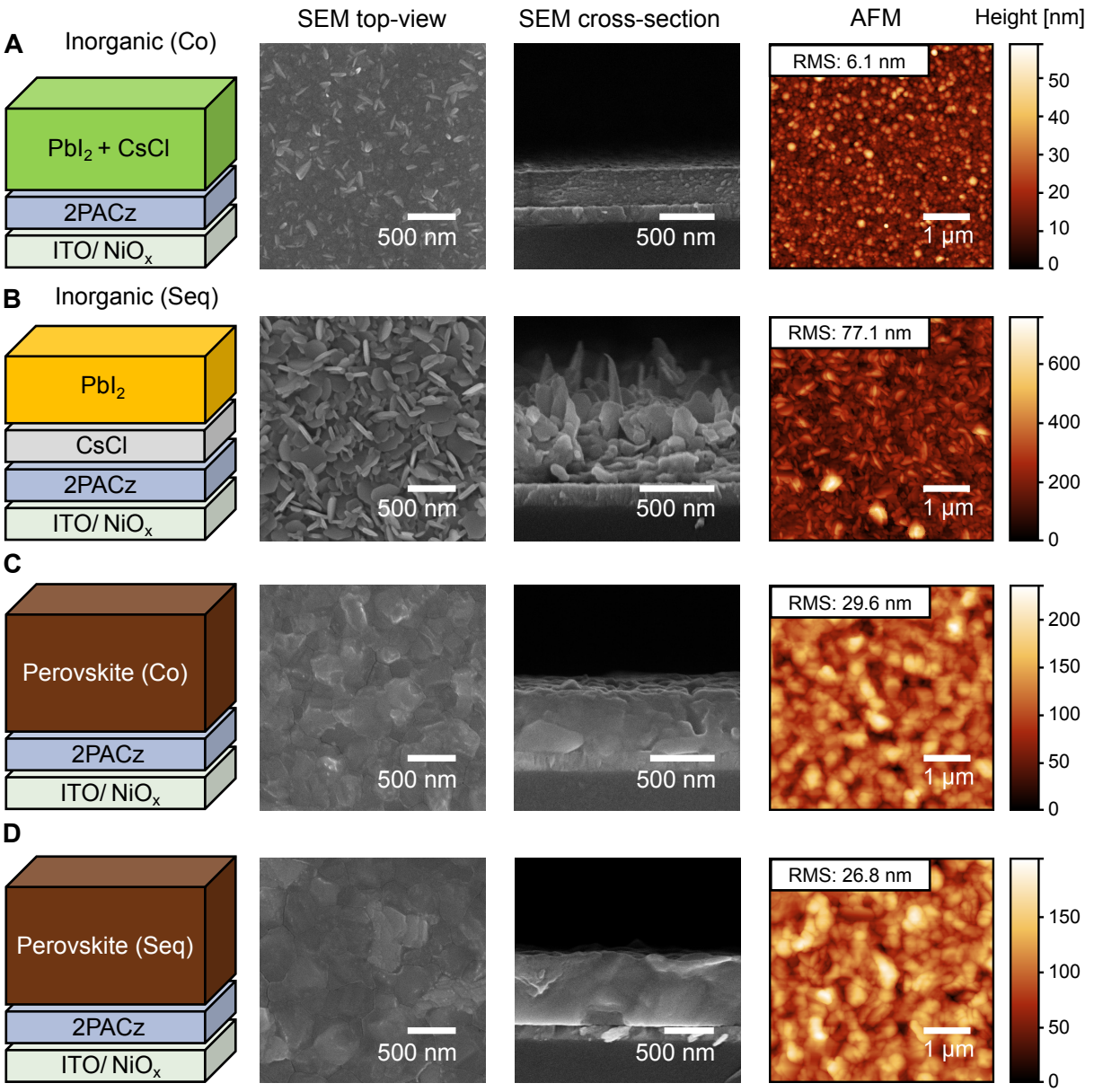

Figure 6.4: SEM- (top-view and cross-section) and AFM images of the inorganic scaffold for **A** Co- and **B** Seq route, as well as of the corresponding perovskite thin films with **C** Co- and **D** Seq route, respectively. For the perovskite thin films, the optimal molarity of the organic cation solution is used. Reproduced with permission from Wiley-VCH.[107] SEM: Scanning electron microscopy, AFM: atomic force microscopy

The substantially higher RMS roughness of the Seq scaffold suggests greater porosity which can enhance infiltration of the organic-cation solution during spin coating and thermal annealing.[112] This hypothesis is validated by dispensing a ∼50 pL droplet of the organic solution and tracking its residue by confocal scanning microscopy (**Figure 6.5**). On inorganic scaffolds of Co route, an accumulation of residual

crystalline organic salts is observed after drying, consistent with hindered organic cation infiltration due to reduced inorganic scaffold permeability. On inorganic scaffolds of Seq route, the organic cation residue is reduced, indicating more effective droplet absorption into the scaffold. Enhanced uptake is expected to promote more homogeneous perovskite conversion and is especially important for inkjet printing.[112,174]

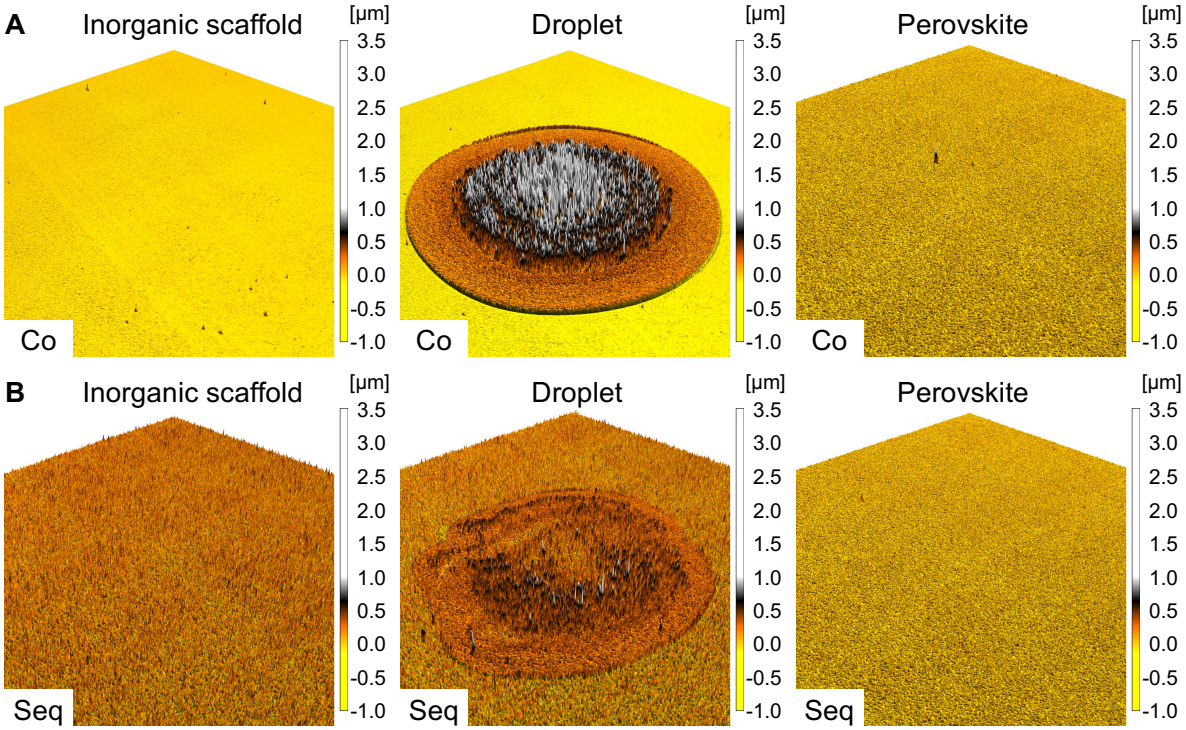

Figure 6.5: Confocal scanning microscopy analysis of a 50 pL organic-cation droplet dispensed onto inorganic scaffolds of **A** Co- and **B** Seq route . Residual crystalline salt accumulation at the droplet center on the Co route inorganic scaffold indicates limited absorption, while reduced residue on the Seq route inorganic scaffold evidences enhanced organic cation infiltration into the scaffold. Reproduced with permission from Wiley-VCH.[107]

Surface profilometry quantifies route-dependent thickness evolution and volumetric expansion (**Figure 6.6**). The inorganic scaffold thickness increases from 325 ± 4 nm (Co route) to 409 ± 4 nm (Seq route), and the corresponding perovskite thin-film thickness rises from 524 ± 4 nm (Co route) to 682 ± 5 nm (Seq route). The thickness expansion coefficients ($\mathrm{thickness_{perovskite}}/\mathrm{thickness_{inorganic}}$) are 1.62 (Co route) and 1.67 (Seq route), indicating slightly greater volumetric uptake during conversion for the Seq route. This expansion reflects the transformation of layered $\mathrm{PbI_2}$ into a three-dimensional perovskite lattice *via* incorporation of organic cations and mixed halides. A more porous inorganic scaffold, as present in the Seq case, offers increased accessible volume and transport pathways, consistent with the droplet-absorption results. The larger final thickness of the perovskite thin film for the Seq route is consistent with enhanced organic-precursor infiltration and reaction throughout the scaffold rather than predominantly surface-limited

conversion. Notably, despite this added thickness, SEM and AFM show comparable perovskite surface morphology for both routes, suggesting that the additional organic cation uptake primarily results in bulk expansion.

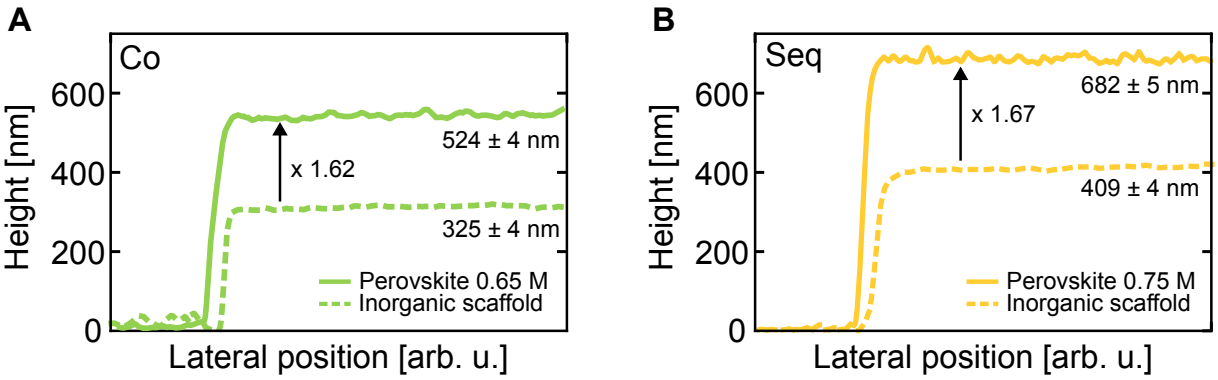

Figure 6.6: Surface profilometry of the inorganic scaffold and the perovskite thin film (optimal organic-cation molarity) for **A** Co- and **B** Seq route. The expansion coefficients ($\mathrm{thickness_{perovskite}}/\mathrm{thickness_{inorganic}}$) are 1.62 (Co route) and 1.67 (Seq route), evidencing slightly increased organic-cation uptake for Seq route. Reproduced with permission from Wiley-VCH.[107]

In summary, the deposition route strongly modifies the inorganic scaffold morphology and porosity, which in turn governs organic-cation uptake and thickness expansion during conversion. Corresponding perovskite thin films exhibit comparable surface morphologies.

6.2.3 Influence of Deposition Route on Preferred Crystal Orientation

While SEM reveals pronounced differences in scaffold morphology and platelet orientation between the Co and Seq routes, it does not provide direct information on crystal orientation. Because two-step conversion is diffusion-limited, such route-dependent scaffold morphology differences are expected to influence how the organic cation solution infiltrates the inorganic scaffold and how crystallographic features are transferred into the final perovskite thin film. This section thus evaluates how the deposition route influences preferred growth directions in the inorganic scaffold and the extent to which these textures are inherited by the final perovskite thin film. Grazing-incidence wide-angle X-ray scattering (GIWAXS) is used to resolve preferred orientation and crystallinity in thin films, using azimuthal intensity distributions of the (001) $\mathrm{PbI_2}$ reflection at $q = 0.9$ Å^{-1} for the inorganic scaffold and of the (100) α-phase perovskite reflection at $q = 1.0$ Å^{-1} for the corresponding perovskite thin films (**Figure 6.7**).[244]

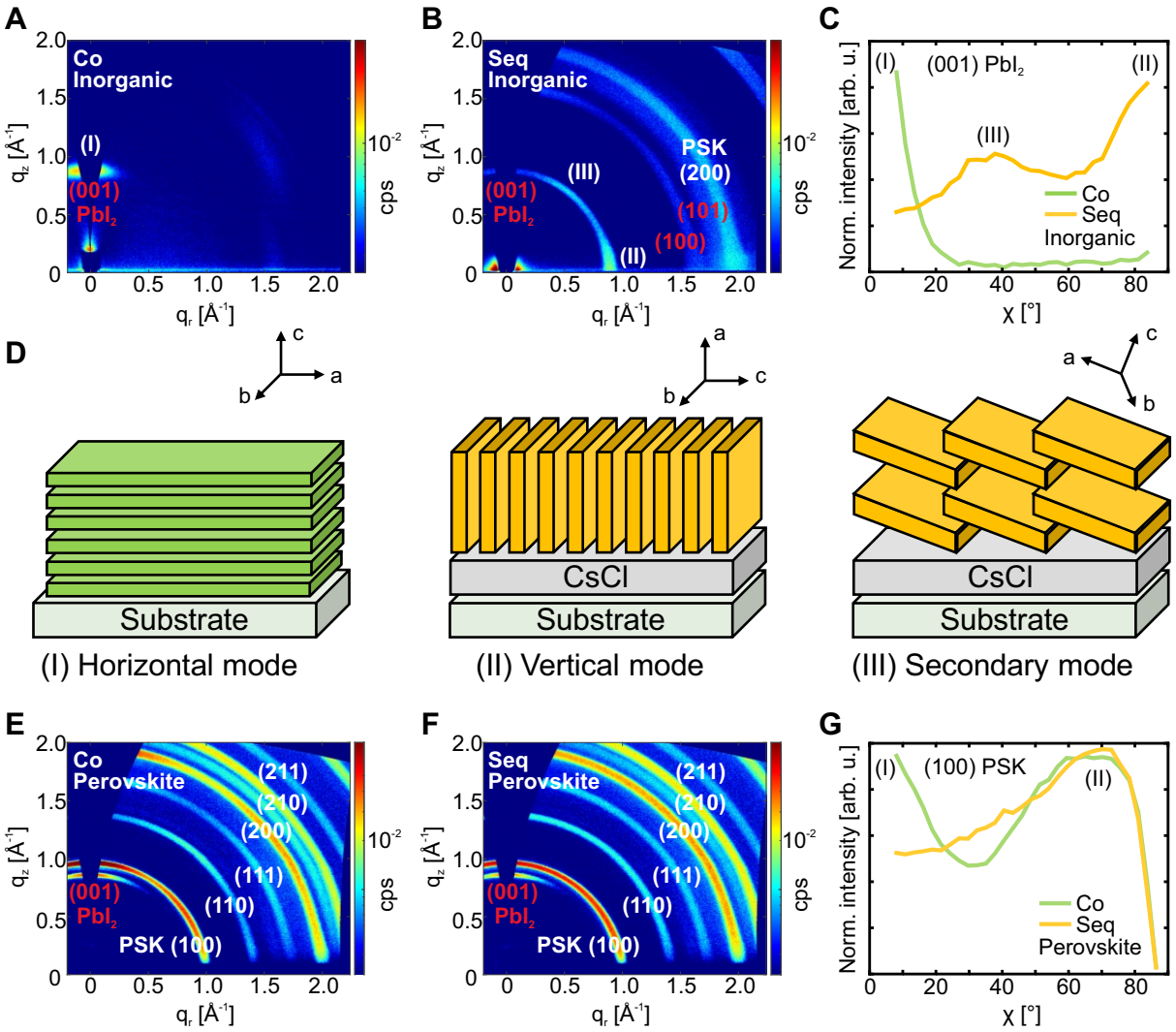

Figure 6.7: GIWAXS patterns of the inorganic scaffold deposited by **A** co- and **B** Seq route, and of the corresponding perovskite thin films prepared following the **E** Co- and **F** Seq route, respectively. **D** Schematic illustrating PbI_2 platelet orientations observed for the inorganic scaffold for Co route **(I)** and Seq route **(II)**/**(III)**. Distributions of crystallite orientation for the (001) PbI_2 plane in the inorganic scaffolds **C** and the (100) α-phase perovskite plane in the final films **G**. For the perovskite thin films, the optimal organic-cation molarity is used. Reproduced with permission from Wiley-VCH.[107] GIWAXS: Grazing-incidence wide-angle X-ray scattering

For an inorganic scaffold of the Co route, GIWAXS pattern indicates a preferred out-of-plane orientation of the (001) PbI_2 plane as depicted in **Figure 6.7 A**, corresponding to horizontally stacked PbI_2 platelets parallel to the substrate (mode **I** in **Figure 6.7 D**). The associated azimuthal distribution (**Figure 6.7 C**) is sharply concentrated around the out-of-plane direction, consistent with the dense, smooth morphology observed by SEM (**Figure 6.4**). In contrast, the Seq route produces a preferred in-plane orientation of the (001) PbI_2 plane (**Figure 6.7 B**), implying platelets that are vertically aligned relative to the substrate

(primary vertical mode **II**). A secondary tilted orientation at $\sim$40° (mode **III**) is apparent for the Seq route, in line with reports of surface-dependent PbI_2 growth on various hole-transport layers.[106,241] The fundamental growth mechanism resulting in the appearance of the secondary growth mode remains elusive and requires further investigation.

The distinct textures are consistent with intrinsic growth modes of PbI_2, where ionic bond formation along the (a,b)-plane is energetically favored over van der Waals–mediated c-axis stacking, leading to vertical alignment in vapor-deposited pure PbI_2.[245,246] Additionally, for the Seq route a feature at $q = 2.0$ Å^{-1} matches the (200) α-phase perovskite reflection, suggesting partial interfacial perovskite formation, initiated by spontaneous reactions between CsCl and PbI_2. For Co route perovskite thin films, GIWAXS shows a discrete Bragg spot of the (100) α-phase perovskite reflection near $\chi \approx 70°$ (**Figure 6.7 E,G**), indicating a pronounced preferred orientation. A secondary, smaller-angle Bragg feature is present for the Co route case (**Figure 6.7 G**), consistent with a templating (topotactic) conversion reaction whereby the horizontally aligned PbI_2 platelets imprint their preferred orientation during conversion to the corresponding perovskite thin film.[247,248] For Seq route perovskites, the (100) α-phase orientation is retained near $\chi \approx 70°$ (**Figure 6.7 F/G**), showing a broader distribution compared to Co route, reflecting the less ordered inorganic scaffold alignment (vertical/tilted platelets).

In summary, the deposition route exerts a strong influence on PbI_2 platelet orientation in the inorganic scaffold – horizontal for the Co route and predominantly vertical/tilted for Seq route – with a secondary $\sim$40° mode in the latter. Elements of this inorganic scaffold orientation are partially inherited by the perovskite, most notably the Co route specific secondary (100) α-phase feature consistent with a templating/topotactic conversion reaction. Both deposition routes feature a maximum at $\sim$70° which is hypothesized to result from the diffusion-limited nature of two-step conversion processes as described by Pettit *et al.*[241]

6.2.4 Elemental Distribution

Elemental distribution and diffusion within the inorganic scaffold govern the final local stoichiometry of the perovskite thin film.[121,249] Route-dependent differences of the inorganic scaffolds are therefore expected to manifest as distinct depth profiles and differences in mobility for metal cations, organic fragments, and halides. The central question is whether the route-dependent elemental depth distribution of the inorganic scaffold is erased during solution conversion or whether parts of the initial elemental depth profile remain imprinted in the final perovskite thin film. Qualitative elemental distribution as a function of depth for both the inorganic scaffolds and the corresponding perovskite thin films (**Figure 6.8** (positive polarity) and **Figure 6.9** (negative polarity)) are probed by Time-of-flight secondary ion mass spectrometry (ToF-SIMS) depth profiling. Signals associated with NiO_x from the underlying hole-transport layer (HTL) were used as positional references. Reported traces are normalized to highlight relative variations across the stacks.

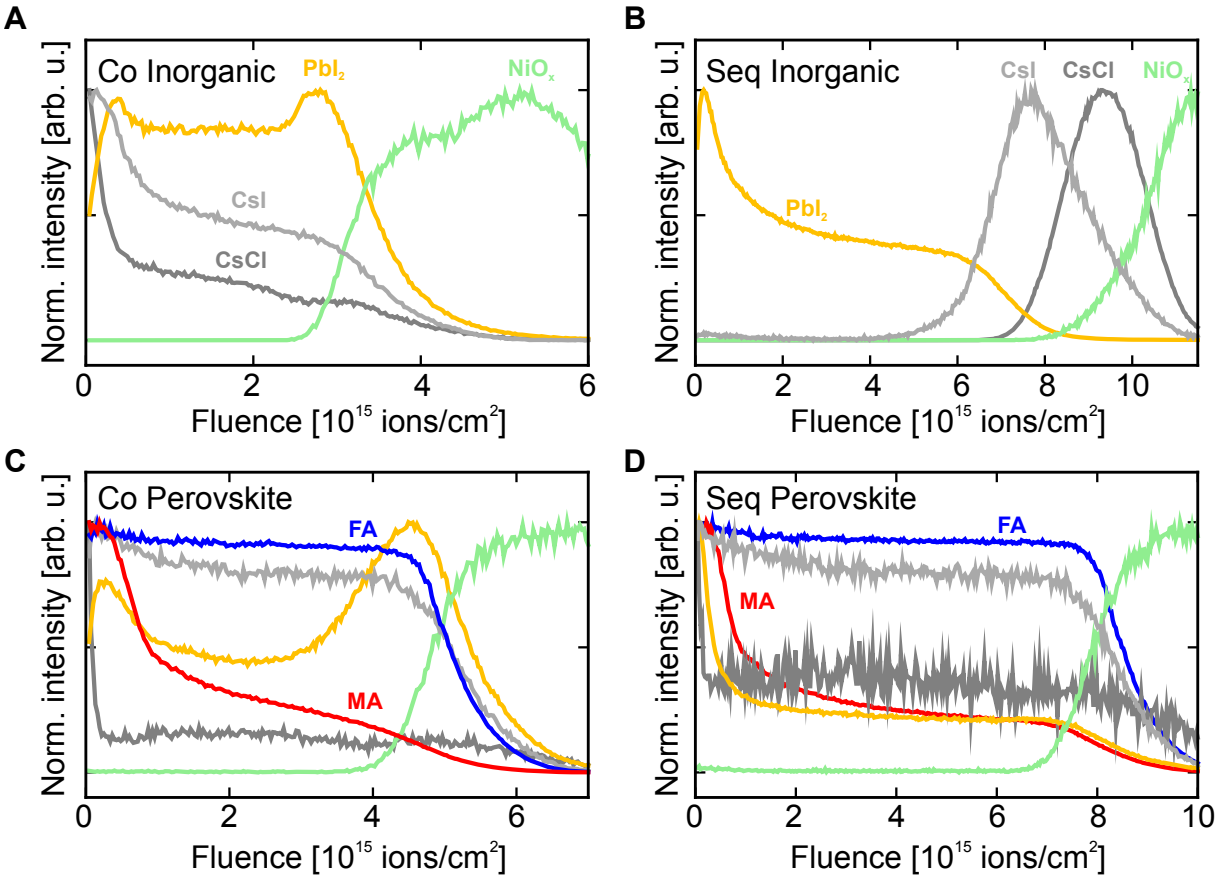

Figure 6.8: Normalized ToF-SIMS measurements (positive polarity) of the inorganic scaffold deposited by **A** Co- and **B** Seq route, and of the corresponding perovskite thin films prepared using **C** Co- and **D** Seq route, respectively. For the perovskite thin films, the optimal molarity of the organic cation solution is used. The following fragments are displayed: NiO_x: $\Sigma(^{58}Ni^+, ^{60}Ni^+)$; PbI_2: $\Sigma(^{206}PbI^+, ^{207}PbI^+, ^{208}PbI^+)$; **CsCl**: $Cs_3Cl_2^+$; **CsI**: CsI^+; FA: $CH_5N_2^+$; MA: $\Sigma(CH_4^+, NH_4^+, CH_2N^+, CH_3N^+)$. Reproduced with permission from Wiley-VCH.[107] ToF-SIMS: Time-of-flight secondary ion mass spectrometry

Starting with the inorganic scaffold, the Co route (**Figure 6.8 A**) shows CsI^+ and $Cs_3Cl_2^+$ concentration enriched near the top surface rather than uniformly throughout the layer, while a higher abundance of PbI-containing fragments are detected at both the top and bottom of the scaffold. The latter is hypothesized to result in a preferred nucleation of PbI_2 during co-deposition due to higher material flux. In contrast, expected layering is observed for the Seq route: a CsCl-rich region at the HTL interface (marked by Ni^+) and PbI-containing species concentrated towards the top, in agreement with the deposition order (**Figure 6.8 B**). A pronounced CsI^+ signal at the CsCl/PbI_2 interface indicates spontaneous diffusion of iodide into the CsCl lattice at the interface. After conversion to the corresponding perovskite thin films (**Figure 6.8 C/D**), Cs-related signals become largely uniform across the thin film for both routes, implying high Cs mobility (and/or rapid incorporation) during solution deposition/ thermal annealing steps. By contrast, PbI-related fragments largely preserve their original depth positions. For Co route perovskite

thin films they peak closer to the HTL side, while for Seq route perovskite thin films they remain more prominent towards the top surface. Organic fragments show distinct behavior with FA-fragments ($CH_5N_2^+$) appear homogeneous throughout the thin film, whereas MA-related fragments are found throughout the bulk material, indicating partial incorporation of MACl with accumulation at the surface. This observation is contrary to the common assumption that MACl is acting as a pure additive which is volatilized upon annealing.[110]

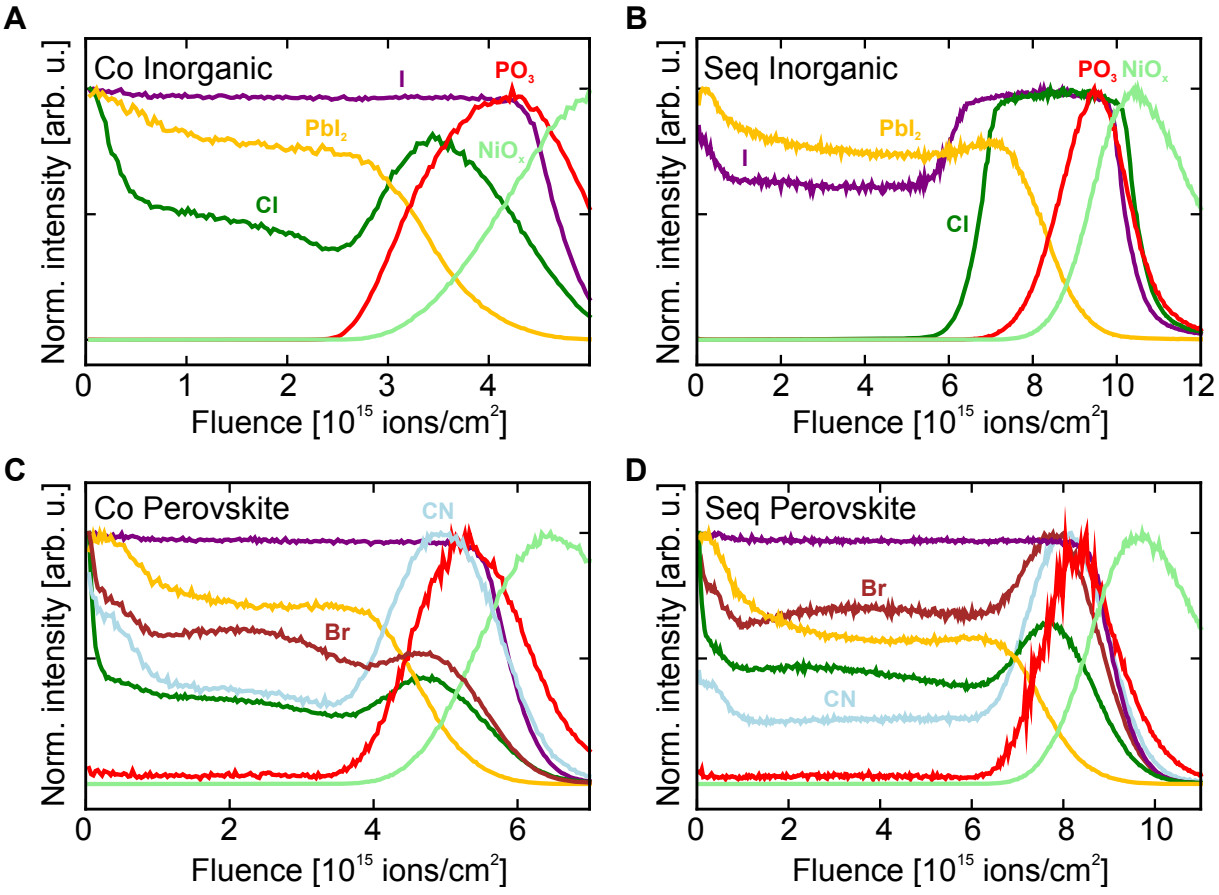

Figure 6.9: Normalized ToF-SIMS measurements (negative polarity) of the inorganic scaffold deposited by **A** co-deposition and **B** sequential deposition, as well as of the final perovskite thin films with **C** co-deposition and **D** sequential deposition of the inorganic scaffold. For the perovskite thin films, the optimal molarity of the organic cation solution is used. The following fragments are displayed: NiO_x: NiO_2^-; PO_3: $\Sigma(PO_3^-, PO_2^-)$; PbI_2: $^{207}PbI_3^-$; Cl: Cl^-; I: I^-; Br: Br^-; CN: CN^-. Reproduced/Adapted with permission from Wiley-VCH.[107] ToF-SIMS: Time-of-flight secondary ion mass spectrometry

In the inorganic scaffolds, iodide (I^-) is broadly distributed for Co route (**Figure 6.9 A**), whereas the Seq route shows an I^- accumulation at the HTL interface (**Figure 6.9 B**), consistent with I^- diffusion into the CsCl layer and the interfacial CsI^+ feature observed in positive polarity. Chloride (Cl^-) accumulates at

both interfaces for Co but predominantly at the bottom interface for Seq route, indicating lower overall halide mobility relative to I^- and stronger route-dependent localization for Cl^-. Halide distributions converge in the corresponding perovskite thin films (**Figure 6.9 C/D**). I^- distribution becomes essentially uniform across the thin film for both routes, while Cl^- and Br^- exhibit modest mid-depth accumulation. This homogenization aligns with the uniform Cs^+ distribution in positive polarity and suggests that solution conversion and thermal annealing erase much of the imprinted halide distribution, except for residual nuances in Cl^-/Br^- positioning that may influence local band-edge or defect chemistry. The deposition route imprints a layered elemental structure in the inorganic scaffold (especially for Seq route), including spontaneous interfacial CsI formation prior to annealing. During conversion, Cs^+ distributes efficiently and becomes homogeneous, whereas Pb-related fragments exhibit lower mobility and retain aspects of their initial depth localization. I^- diffuses readily (driving interfacial CsI in Seq route and uniform I^- in the corresponding perovskite thin films), while Cl^- and Br^- are comparatively less mobile and show residual, local accumulation within the thin film. These observations rationalize the observed differences in local scaffold composition and the largely homogenized, but subtly route-influenced, composition of the perovskite layer.

Conclusion

This section establishes that the choice of inorganic deposition route is a scaffold-engineering parameter that governs conversion behavior, repeatability, and ultimately the industrial relevance of the hybrid two-step route. Co- and Seq routes of the inorganic scaffold are benchmarked in a hybrid two-step route for a target bandgap range of ∼1.68 to 1.70 eV and it is demonstrated that both approaches can deliver comparable device efficiencies, with champion efficiencies of 20.3% (Seq route) and 19.3% (Co route), when the organic-cation conversion step is appropriately optimized. The Seq route yields improved batch-to-batch repeatability and a stable optimum in required organic-cation molarity compared to the Co route, demonstrating a more robust and controllable deposition and conversion process. Crucially, the deposition route functions as a previously underexplored scaffold-engineering parameter: already at the inorganic stage it defines microstructure, preferred crystal orientation, and elemental distribution, which collectively affect conversion kinetics. At the materials level, the Seq route produces a highly textured inorganic scaffold with predominantly vertical or tilted PbI_2 platelets, in contrast to the horizontal PbI_2 platelets resulting in a dense and smooth morphology for the Co route. The more porous inorganic scaffold for Seq route facilitates organic cation infiltration during solution deposition, leading to increased volumetric bulk expansion upon conversion. While both routes ultimately yield perovskite thin films with comparable surface morphology and device performance, elements of the scaffold properties are partially inherited by the perovskite, consistent with templating and topotactic aspects of two-step conversion. Elemental depth profiling further shows that sequential deposition imprints a layered inorganic structure prior to conversion, whereas subsequent solution processing and annealing largely homogenize the more mobile species such as Cs^+, I^- and FA^+ while retaining subtle depth-dependent trends for less mobile components such as Pb^{2+} and Cl^-. To conclude, fully sequential inorganic scaffold deposition is established as an industry-aligned

and tunable framework for repeatable fabrication of highly efficient PSCs. By enabling control over scaffold morphology, texture, and elemental distribution, the sequential route provides a robust process framework. Route-dependent inorganic scaffold engineering opens a new parameter space which motivates further exploration of the fully sequential deposition framework, specifically for the process acceleration, tandem integration, and bandgap engineering strategies investigated in the following sections.

6.3 Process Acceleration of Sequential Route Framework

Industrial adaptation of perovskite solar cell technologies requires fabrication routes that are compatible with high-throughput manufacturing.[36,38] Fabrication throughput is largely determined by the deposition rate of the perovskite precursor materials in vapor deposition processes. A fully sequential deposition route offers superior process effectiveness and control compared to co-deposition, as individual precursor steps are decoupled and can be optimized and maximized independently as discussed in Chapter 4. Building on the sequential route framework, a fully sequential inorganic deposition of the scaffold for a hybrid two-step perovskite formation process was established in the previous section.

While the sequential deposition route provides clear advantages in terms of controllability, scalability and process robustness, its initial implementation is time-intensive due to the low deposition rates which are adopted from co-deposition literature.[117,124] Importantly, these conservative rates are not intrinsic to the sequential route itself. Instead, the decoupling of CsCl and PbI_2 deposition steps enables systematic acceleration strategies that would be difficult to implement in a co-deposition route without influencing stoichiometry or process stability. This motivates a targeted acceleration of the inorganic scaffold deposition and investigation to which extent film quality and device efficiency are maintained.

Two complementary strategies are pursued to increase throughput within the sequential deposition framework. First, a vertical scale-up is pursued by increasing the effusion rates of CsCl and PbI_2 through elevated source temperatures, thereby exploiting unused deposition rate potential of the existing sources. Second, a horizontal scale-out strategy is introduced for PbI_2 by operating multiple sublimation sources in parallel. This strategy specifically targets PbI_2, as it contributes most to the overall film thickness of the inorganic scaffold, potentially limiting the fabrication throughput at large-scale manufacturing.

The overarching goal of these acceleration strategies is to reduce the total inorganic deposition time from the reference value of approximately 2×50 min (for CsCl and PbI_2, respectively) by $80\%_{rel}$ to below 20 min in total, while preserving the device performance achieved in the optimized baseline process. First, the limits of vertical rate scaling are explored for CsCl and PbI_2. Subsequently, horizontal scale-out is applied to the rate-limiting PbI_2 step. Here, PbI_2 represents the throughput-critical case because it dominates the scaffold thickness and therefore sets the practical acceleration limit. In this sense, the present section provides an experimental counterpart to the process effectiveness arguments developed in **Chapter 4**, by testing whether the predicted advantages of a fully sequential route can be translated into

accelerated thin-film fabrication without sacrificing device quality. The impact of accelerated inorganic scaffold deposition is evaluated based on photovoltaic characteristics and changes in film properties.

It should be noted that a different glass/ITO substrate type with improved optical properties is used for these experiments compared to the previous section. Further details are provided in the **Methods Section 3**. A constant organic cation solution molarity of 0.77 M is used, and $PDAI_2$:BAI is replaced by LiF, resulting in increased hysteresis compared to the baseline devices.[232]

6.3.1 Vertical Scale-up of CsCl Deposition Rate

Within the sequential deposition framework, CsCl deposition represents a first target for rate acceleration, as it forms only a thin layer and is fully decoupled from PbI_2 deposition. The reference CsCl deposition rate of 0.1 $Å s^{-1}$ was adopted from co-deposition literature to ensure comparability in the previous section (Section 6.2),[117,124] but does not reflect the practical rate limit of the sequential process. At this rate, deposition of a 30 nm CsCl layer requires approximately 50 min, excluding heating and stabilization times. The importance of CsCl deposition rate acceleration therefore is both an absolute throughput gain and a first experimental demonstration that the sequential route allows precursor-specific optimization without introducing the stoichiometric coupling that would complicate such acceleration in a co-deposition process.

Systematic vertical scale-up of the CsCl deposition rate demonstrates that this step can be accelerated by nearly an order of magnitude without compromising device performance. Increasing the rate from 0.1 $Å s^{-1}$ to 0.8 $Å s^{-1}$ results in no statistically significant change in median PCE, which remains in the range of 18.0 to 18.5% (Figure 6.10). Minor shifts in V_{OC} and J_{SC} suggest a slight change in the optimal organic cation concentration but do not indicate compromised of thin film quality.

No visual signs of CsCl degradation are observed in the sublimation crucible at the highest source temperature of approximately 470°C required for a deposition rate of 0.8 $Å s^{-1}$. Consequently, the CsCl deposition time is reduced from 50 min to 6.3 min without sacrificing device performance and within the thermal stability boundaries of CsCl. Further increases in the CsCl rate are possible but impractical in the present laboratory setup due to prolonged heating, cooling, and rate stabilization times at elevated source temperatures. When scaling to the fabrication throughput to pilot-line or GW_p demands, further increases of the deposition rate can decrease the number of required linear sources.

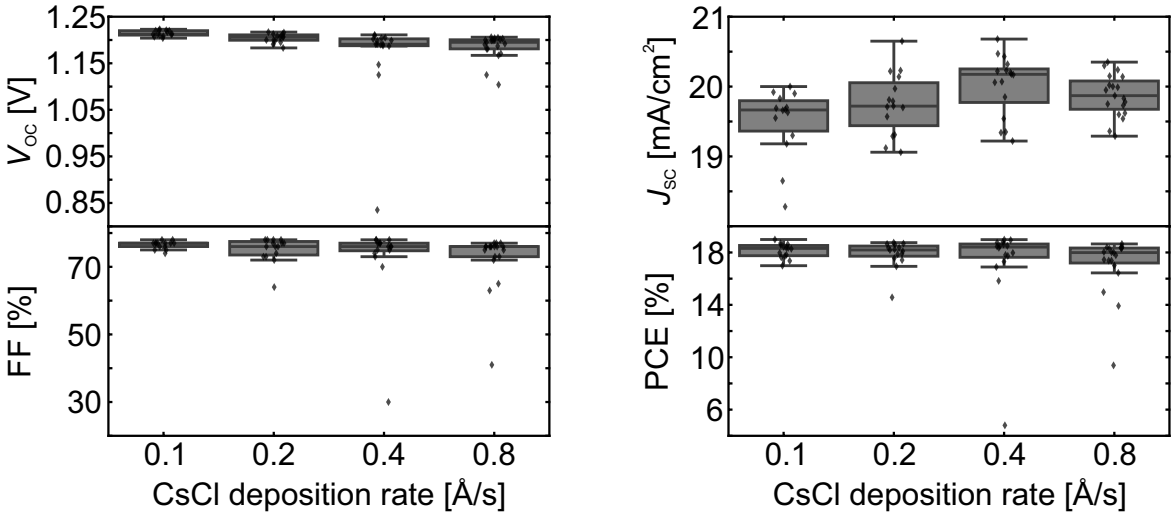

Figure 6.10: Statistical distribution (in total 66 devices) of the V_{OC}, FF, J_{SC} and PCE for increasing deposition rates of CsCl. The organic cation solution molarity is 0.77 M and 1 nm of LiF is used as surface passivation.[232]

6.3.2 Vertical Scale-Up and Horizontal Scale-Out of the PbI_2 Deposition Rate

PbI_2 contributes most to the overall layer thickness the inorganic scaffold and thus represents the primary bottleneck to the fabrication throughput. Vertical scale-up of the PbI_2 deposition rate from the reference value of 1.0 Ås^{-1} to 3.0 Ås^{-1} reduces the deposition time for a 300 nm layer from 50 min to approximately 17 min. Across this rate range, no systematic loss in photovoltaic performance is observed, with median PCEs remaining in the range of 16–17% (Figure 6.11). For all following experiments a CsCl deposition rate of 0.8 Ås^{-1} is used.

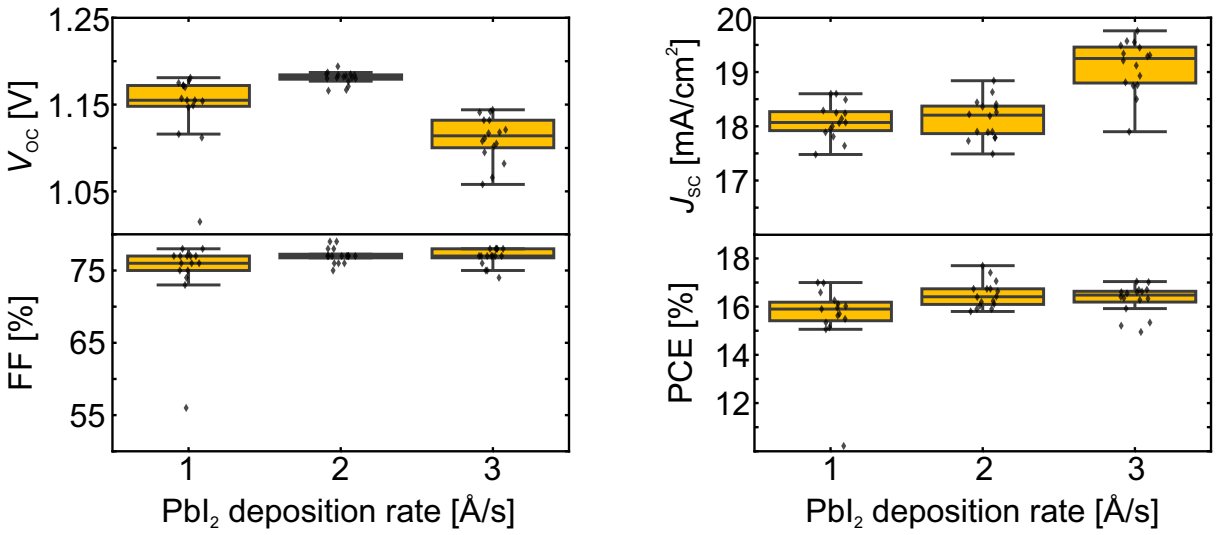

Figure 6.11: Statistical distribution (in total 49 devices) of the V_{OC}, FF, J_{SC} and PCE for increasing deposition rates of PbI_2. For this experiment, CsCl is deposited at a rate of 0.8 Ås^{-1}. The organic cation solution molarity is 0.77 M and 1 nm of LiF is used as surface passivation.[232]

At the highest rate of 3.0 Ås^{-1}, a decrease in V_{OC} accompanied by an increase in J_{SC} is observed. This behavior is consistent with a shift in the effective conversion conditions, arising from altered organic-cation infiltration (*e.g.* a slight FAI/FABr excess). While the deposition time is substantially reduced, further vertical scaling is limited by intrinsic material constraints with PbI_2 approaching thermal decomposition at source temperatures above ∼320°C and tool-specific factors such as reduced rate stability due to accelerated degradation of the QCM.

To overcome these single-source limitations, the fully sequential framework enables a facile implementation of horizontal scale-out strategies in which multiple PbI_2 sources are operated in parallel. Using two PbI_2 sources operated at 3.0 Ås^{-1} each results in an effective deposition rate of 6.0 Ås^{-1} and reduces the deposition time for a 300 nm layer to ∼8.3 min. The photovoltaic parameters are summarized in **Figure 6.12**. It is noted that this horizontal scale-out is practically a co-deposition process of two PbI_2 sources operated in parallel. As the vapor flux distributions of the two sources do not fully overlap, this is considered as an approximation of an in-line process but is a limitation of the used methodology. The key result is therefore the demonstration that the fully sequential route allows modular expansion of the rate-limiting PbI_2 step in a way that is compatible with industrial scale-out.

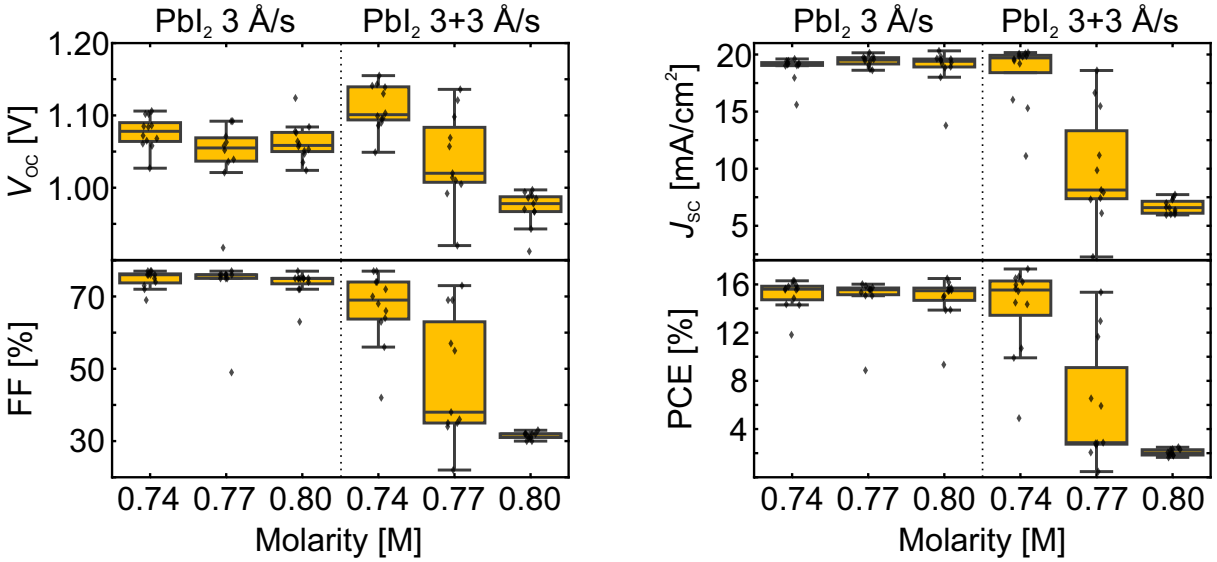

Figure 6.12: Statistical distribution (in total 70 devices) of the open-circuit voltage (V_{OC}), fill factor (FF), short-circuit current density (J_{SC}) and power conversion efficiency (PCE) for horizontal scale-out of the PbI_2 deposition rate using 3+3 $Å s^{-1}$.[232]

When transitioning from a single-source to a two-source configuration, the optimal organic cation solution molarity slightly shifts. At lower molarity (0.74 M), comparable or slightly improved device performance is achieved, whereas higher molarity (0.80 M) leads to pronounced losses in both J_{SC} and V_{OC}. These trends are attributed to less precise thickness control in the multi-source configuration, where small rate mismatches accumulate over time and necessitate re-optimization of the conversion step. Nevertheless, after tuning the organic cation concentration, comparable maximum PCEs are obtained. Overall, horizontal scale-out enables substantial acceleration of PbI_2 deposition while maintaining device performance, at the cost of reduced thickness control.

6.3.3 Analysis of Accelerated Process

When the inorganic deposition is accelerated, changes in growth kinetics can modify the morphology of the deposited layers and thereby influence the subsequent solution-based conversion step.[106,250] For CsCl, no change in the required organic cation solution molarity is observed over the investigated rate range, indicating that the CsCl morphology and its influence on the subsequent PbI_2 morphology remain largely unaffected by rate acceleration. In contrast, for PbI_2, a slight shift of the optimum organic cation solution molarity is observed at high deposition rates of 3.0 $Å s^{-1}$, accompanied by a decrease in V_{OC} and an increase in J_{SC}. This trend is consistent with enhanced organic cation uptake, which can occur if the inorganic scaffold becomes more porous, effectively increasing the permeability and thus organic cation infiltration. To elucidate the rate-morphology relationship, a SEM series (**Figure 6.13**) is conducted for three deposition rate combinations: **A** 0.1 $Å s^{-1}$ CsCl and 1.0 $Å s^{-1}$ PbI_2 (reference process), **B** 0.8 $Å s^{-1}$

CsCl and 3.0 Ås^{-1} PbI_2, and **C** 0.8 Ås^{-1} CsCl and 3.0+3.0 Ås^{-1} PbI_2. Across this series, the PbI_2 platelet size is observed to decrease with increasing deposition rate, while the films appear more compact at higher rates. Taken together, these observations provide a first indication that the porosity of the inorganic scaffold is altered upon rate acceleration, which rationalizes why the organic cation solution molarity needs to be re-optimized for PbI_2 at high rates. After tuning the organic molarity, the resulting perovskite layers exhibit a comparable appearance for all conditions. Since similar PSC performances are achieved, a comparable perovskite thin-film quality is expected across the investigated process windows.

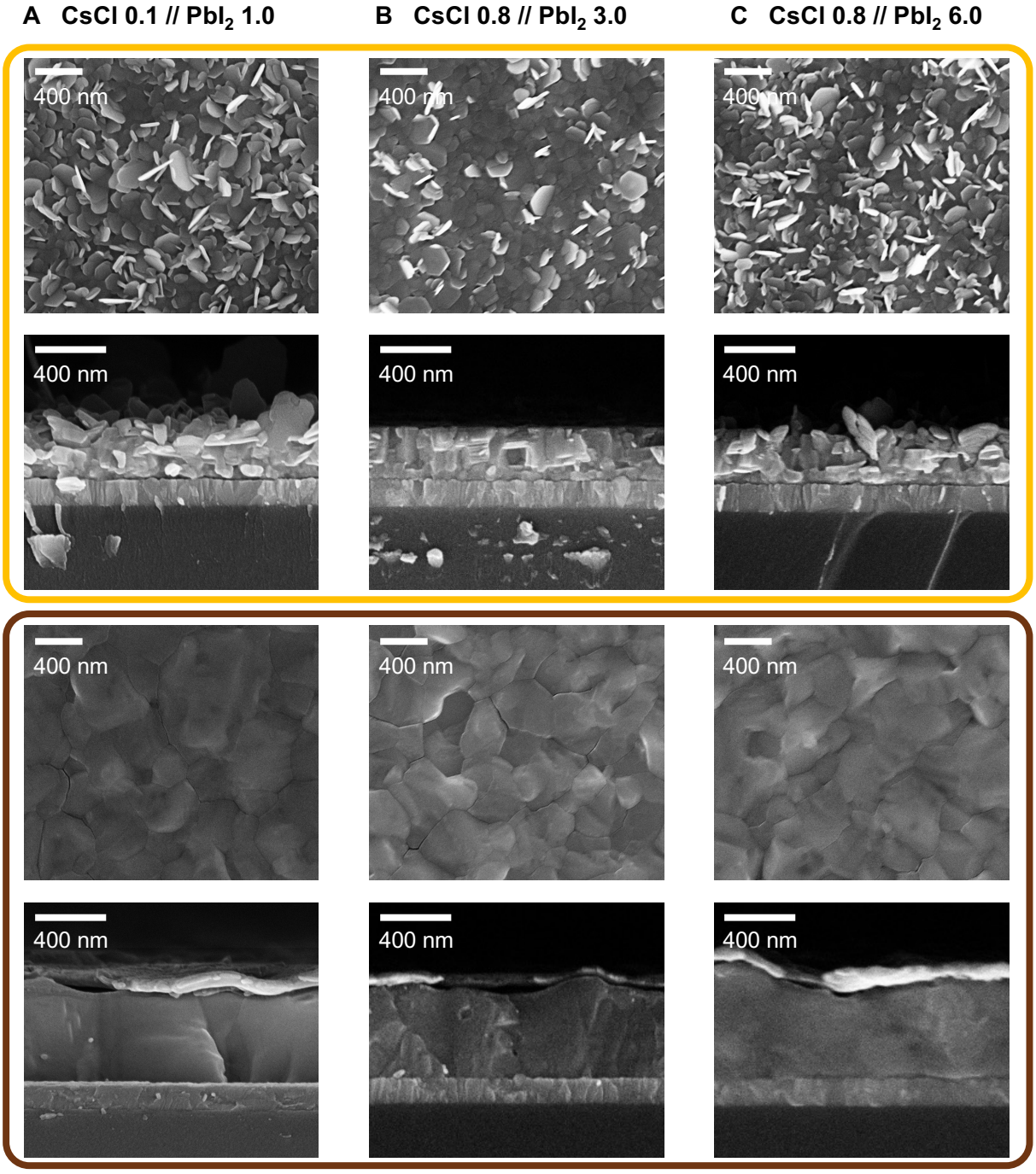

Figure 6.13: SEM images for increasing deposition rates of CsCl and PbI_2, given in Å/s. In each column top-view and cross-sectional SEM images of the inorganic scaffold (yellow frame) and corresponding perovskite thin films (brown frame) are depicted for the given combination of deposition rates.[232] Note: Full devices were used for cross-sectional SEM images with the ETL and Ag electrode visible as a top layer. SEM: Scanning electron microscopy, ETL: electron transport layer

Conclusion

Successful process acceleration is demonstrated for the sequential route framework with inorganic scaffold deposition time reduced by 80%$_{rel}$ to the baseline process while maintaining comparable device performance. Vertical scale-up is demonstrated by increasing the CsCl rate from 0.1 to 0.8 Ås^{-1}, whereby the CsCl deposition time is reduced from 50 min to 6.3 min without a significant change in median PCE. For PbI_2, the rate is increased up to 3.0 Ås^{-1}, for which no systematic efficiency loss is detected, but the maximum usable rate is limited by thermal decomposition and reduced rate-control stability. To further reduce the PbI_2 process time, horizontal scale-out is implemented using two sources (3+3 Ås^{-1}) in parallel, whereby 300 nm PbI_2 is deposited in 8.3 min. Here, a slight shift in the optimum organic cation solution molarity is observed and is attributed to less precise effective thickness control in the multi-source configuration. SEM trends indicate reduced PbI_2 platelet size and altered scaffold morphology at higher rates, which is consistent with the need for re-optimizing the organic conversion step while perovskite thin film appearance and achievable PSC performance remain comparable after tuning. In a broader context, the demonstrated rate acceleration of the sequential route framework indicates a clear pathway towards industrially relevant throughput without compromising device performance. The fully sequential hybrid two-step deposition process is thus well suited for high throughput inline manufacturing concepts using linear sources, as outlined in Chapter 4.

6.4 Transfer of Sequential Route Framework to Tandem Architectures

The compatibility of the sequential route framework with differently textured substrates is evaluated and compared to the conventional Co route. This comparison therefore tests whether the sequential route offers a more transferable inorganic-scaffold morphology across relevant substrate morphologies. In the context of perovskite/Si tandem solar cells, the formation of uniform and well-defined inorganic scaffolds on textured Si bottom cells is a key requirement for conformal thin film growth and reproducible device performance.[139,174]

Distinct differences in scaffold formation are observed depending on both substrate texture and deposition route. Optical photographs (**Figure 6.14**) provide a macroscopic comparison of film uniformity across planar **A/D**, nano-textured **B/E**, and micro-textured **C/F** Si surfaces. Inorganic scaffolds from the Co route are found to be more transparent with the underlying Si substrate visible through the inorganic scaffold. In contrast, inorganic scaffolds are visibly indifferent for the Seq route. These macroscopic differences provide a first indication that the deposition route interacts differently with substrate texturing and motivate the more detailed cross-sectional SEM analysis discussed below.

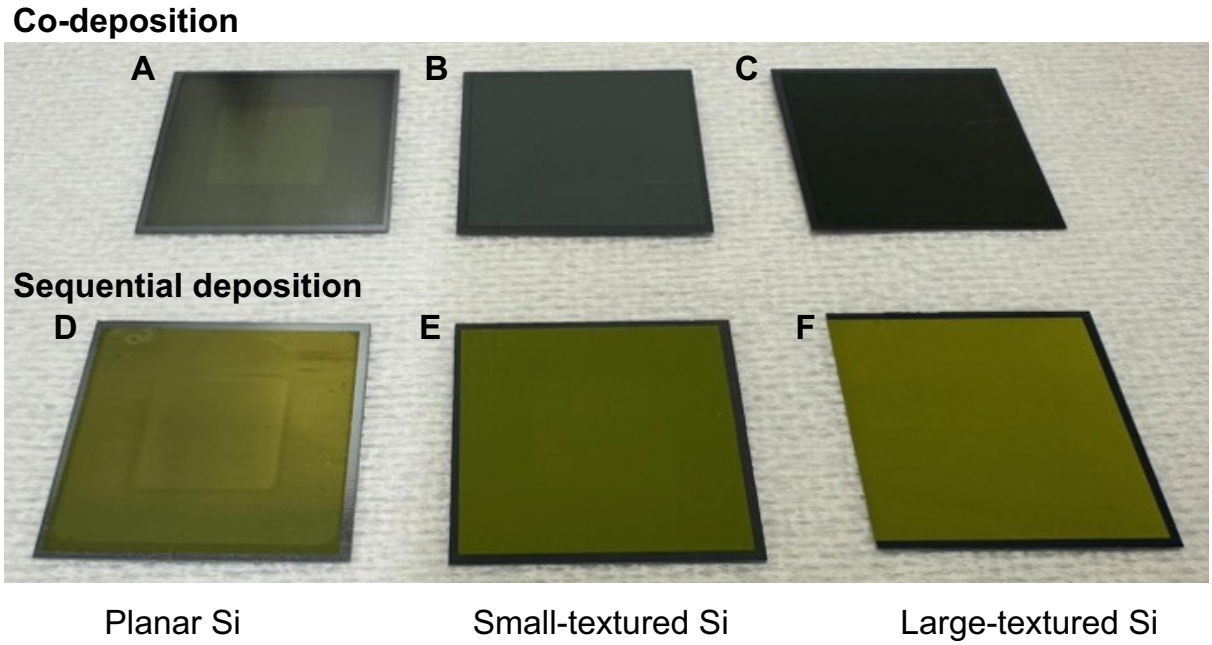

Figure 6.14: Optical photographs of the inorganic scaffold deposited by the Co- and Seq route on planar **A/D**, nano-textured **B/E**, and micro-textured **C/F** Si substrates. Reproduced with permission from Wiley-VCH.[107] Si: Silicon

The nano-scale growth morphology is further analyzed by cross-sectional SEM images (**Figure 6.15**). For Co route inorganic scaffolds, the layer morphology is influenced by the underlying substrate texture. A compact and uniform scaffold is obtained on planar substrates, whereas nano-textured surfaces yield an irregular intermediate morphology and micro-textured substrates promote growth of compact columns. The substrate-dependent growth in case of the Co route can complicate transfer between differently textured substrates. This sensitivity implies that process conditions optimized for planar substrates cannot be directly transferred to textured architectures, requiring additional re-optimization and increasing process complexity. In contrast, sequentially deposited inorganic scaffolds exhibit a similar microstructure across all investigated textures, without texture-dependent changes apparent. Importantly, conformal coverage of micro-structured Si textures is observed for the Seq route. This texture-independent growth behavior is highly advantageous for tandem fabrication, where reproducible coating of complex surface topographies is essential for achieving uniform thin film formation and consistent device performance.

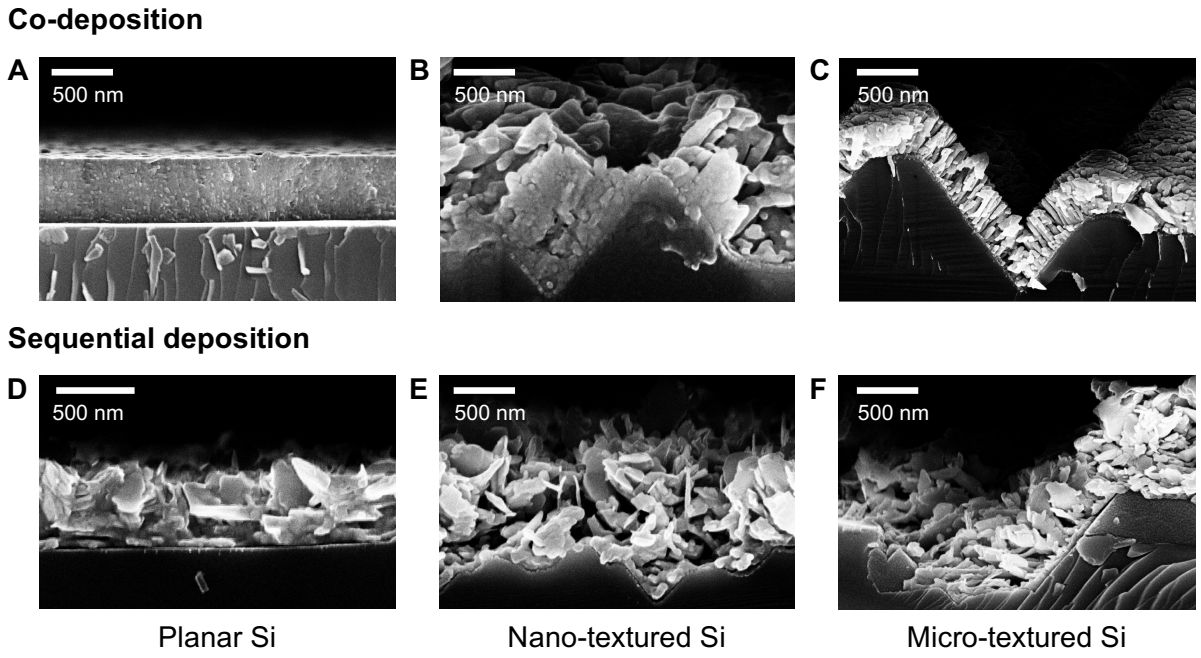

Figure 6.15: Cross-sectional SEM images of the inorganic scaffold deposited by the Co- and Seq route on **A/D**, small-textured **B/E**, and large-textured **C/F** Si substrates. Reproduced with permission from Wiley-VCH.[107]

The suitability of the sequential deposition route for tandem integration is further demonstrated by a representative perovskite/Si tandem prototype processed using this approach. The *J*–*V* characteristics and EQE spectra show functional tandem operation with a maximum obtained PCE of 24.1% and well-defined photocurrent contributions from the perovskite top cell and the silicon bottom cell, as evidenced by the EQE-derived current densities of the individual subcells. The tandem performance is mainly limited by low FF and V_{OC}, requiring further optimization of the perovskite thin-film formation and interfaces.

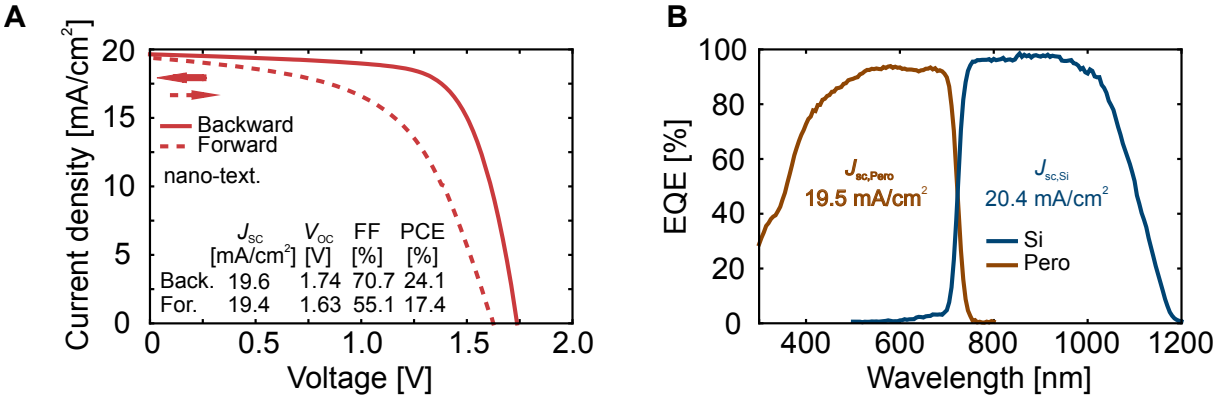

Figure 6.16: *J*–*V* characteristics and external quantum efficiency spectra of a representative perovskite/Si tandem solar cell processed using the sequential deposition route.

Conclusion

In summary, the sequential route framework is shown to be compatible with planar, small-textured (0.5 to 1 µm), and large-textured (2 to 5 µm) Si substrates, with the inorganic scaffold morphology being largely independent of substrate texturing. In contrast, the Co route exhibits pronounced texture-dependent growth behavior, leading to substantial morphological variations on textured surfaces. These observations suggest that the Co route may be more sensitive to substrate morphology, which could complicate process transfer between different substrate textures.

The comparatively texture-insensitive inorganic scaffold formation observed for the Seq route is favorable for conformal thin film growth on textured silicon and supports functional perovskite/Si tandem operation, as demonstrated by a representative tandem prototype. This apparent decoupling of scaffold formation from substrate topography is advantageous for industrial implementation, where uniform coating across varying surface morphologies is essential for maintaining high yield and reproducibility in high-throughput fabrication environments.

While the present tandem devices are not yet performance-optimized, the results highlight the sequential route framework as a promising and scalable pathway for integrating perovskite top cells on textured silicon bottom cells, motivating further optimization and development in dedicated tandem-focused studies. Beyond these initial prototypes, the sequential deposition route has been successfully combined with scalable inkjet printing for the organic cation solution deposition, enabling perovskite/Si tandem solar cells with efficiencies of up to 27.4% on large-textured Si bottom cells.[174]

6.5 Bandgap Engineering Towards Triple-Junction Application

Having established the sequential route scaffold-deposition framework, the next question is whether the same process architecture also provides compositional flexibility for future multi-junction device design.

In this section, the sequential route framework is extended for bandgap engineering with a focus on perovskite thin films for future triple-junction applications. The ability to deliberately tailor the thin film bandgap is a central requirement for realizing multi-junction architectures with optimized current matching and voltage addition.[251,252] The established ∼1.70 eV WBG perovskite recipe ($Cs_{0.18}FA_{0.82}Pb(I_{0.76}Br_{0.18}Cl_{0.06})_3$) is used as a reference point. Starting from this baseline, two target bandgaps are developed: a mid-bandgap (MBG) thin film with a target bandgap of ∼1.52 eV and an ultra-wide-bandgap (UWBG) thin film with a target bandgap of ∼1.84 eV. These bandgaps correspond to the mid- and top-cell thin films in a Si–PVK–PVK triple-junction architecture, respectively.[251] Bandgap tuning is realized by systematically modifying the relative halide composition (I^-, Br^-, and Cl^-) of the perovskite thin film. This is achieved either through adjustment of the halide ratios supplied by the organic cation solution during conversion or by modifying the halide composition of the inorganic scaffold (**Figure 6.17**).

The sequential route framework provides key advantages for this approach: First, the inorganic scaffold composition can be defined with high precision by independent control of each precursor deposition step. Second, the Seq route introduces an additional degree of freedom compared to Co routes. The spatial position of individual inorganic precursor materials within the inorganic scaffold stack can be deliberately selected.

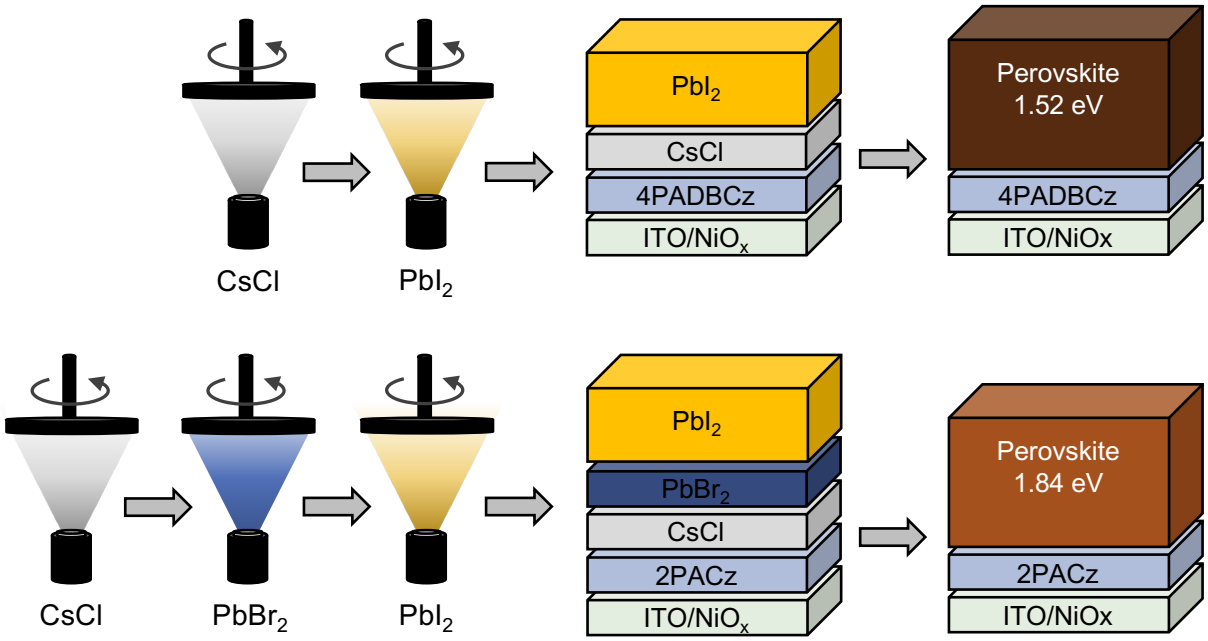

Figure 6.17: Schematic overview of the inorganic scaffold stacks used for bandgap engineering within the sequential route framework. 4PADBCz: (4-(7H-dibenzo[c,g]carbazol-7-yl)butyl) phosphonic acid

6.5.1 Process Development towards Target Bandgap of 1.52 eV

Bandgap narrowing towards the MBG target of 1.52 eV is achieved by systematically reducing the bromide content of the perovskite thin film and lowering the CsCl fraction supplied by the inorganic scaffold. The fully sequential hybrid two-step route enables both modifications to be implemented independently while maintaining an otherwise unchanged process flow.

Starting from the 1.70 eV baseline composition, the first step is the substitution of the FABr fraction in the organic cation solution by FAI. This increases the iodide content in the final perovskite thin film and results in a pronounced bandgap narrowing. Applying this strategy alone yields an iodide-rich perovskite with a nominal composition of

$$\mathrm{Cs_{0.18}FA_{0.82}Pb(I_{0.94}Cl_{0.06})_3},$$

corresponding to an EQE-derived bandgap of ∼1.57 eV. This intermediate composition provides a direct and controllable pathway from the WBG baseline to the MBG target, as reflected by the EQE onset and its first derivative shown in **Figure 6.18 A-C**.

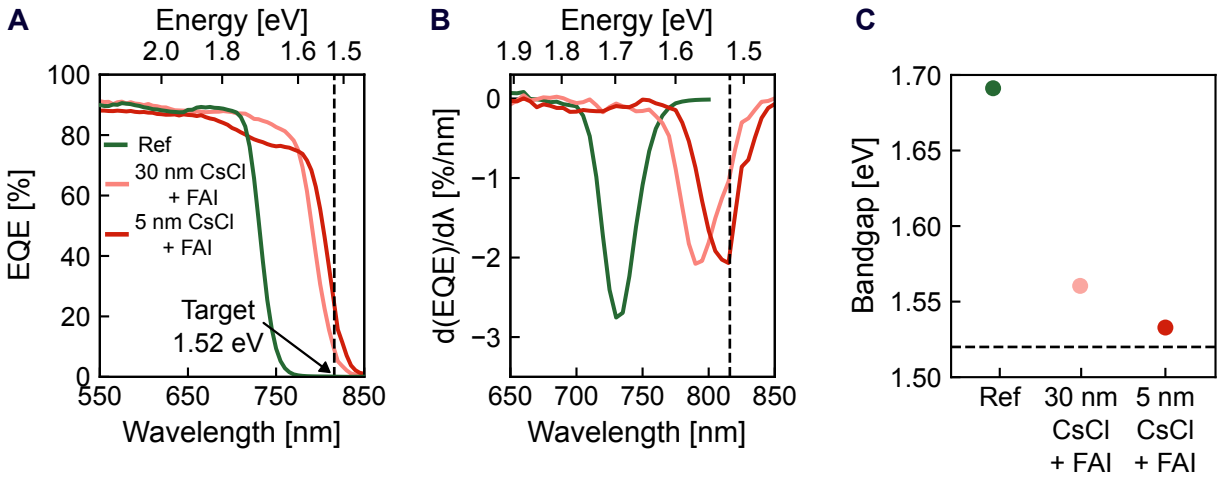

Figure 6.18: **A** EQE spectra of perovskite solar cells processed using I^--rich compositions for MBG thin films. Progressive bandgap narrowing from the 1.70 eV baseline towards ∼1.52 eV achieved by replacing Br^- from the organic cation solution and reducing the CsCl thickness in the inorganic scaffold. **B/C** First derivative of the EQE at bandgap edge and summary of extracted bandgaps towards the target value of 1.52 eV. 4PADBCz = (4-(7H-dibenzo[c,g]carbazol-7-yl)butyl)phosphonic acid. EQE: External quantum efficiency, MBG: mid bandgap

To further narrow the bandgap from ∼1.57 eV towards the target value of ∼1.52 eV, the Cl^- fraction is reduced by decreasing the CsCl thickness from 30 nm to 5 nm, while retaining the I^--rich organic solution. This adjustment lowers the incorporated Cs fraction, while preserving a small amount of Cs for phase stabilization, and results in a nominal perovskite composition of

$$Cs_{0.03}FA_{0.97}Pb(I_{0.99}Cl_{0.01})_3,$$

with the desired bandgap of ∼1.52 eV. The progressive bandgap evolution from the baseline through the intermediate state to the final target composition is summarized by the EQE spectra and extracted bandgaps in **Figure 6.18 A-C**.[233]

When replacing FABr by FAI, reduced solubility of the organic precursors in ethanol is observed, which can lead to precipitation of the organic salts at the pipette tip and process instability. Addition of small fractions (3 $\%_{vol}$) of DMSO to the organic cation solution improves solubility and processing robustness in this iodide-rich regime.[233] This observation is consistent with recent reports by Battran *et al.*, who independently demonstrated that DMSO addition can improve crystallization behavior in a comparable two-step hybrid perovskite process.[249] Using this adjusted process, a maximum PCE of 20.0% is achieved with V_{OC} = 1.08 V, J_{SC} = 23.6 mA cm^{-2} and FF = 78.3 % at the target bandgap of 1.52 eV as

summarized in **Figure 6.22**. Whereas the obtained V_{OC} approaches 90% of the DB-limit, the device performance is mainly limited by the comparatively low J_{SC} and FF, motivating further optimization of the perovskite thin-film formation and interfaces. This shows that the sequential route framework can be transferred from the WBG tandem regime to the MBG regime through targeted compositional adjustments while maintaining the underlying processing scheme.

6.5.2 Process Development towards Target Bandgap of 1.84 eV

For UWBG thin films, increased Br^- incorporation represents the primary strategy for bandgap widening. Within the sequential route framework, Br^- can be introduced through two independent pathways: *via* the organic cation solution during the conversion step and/or *via* tuning of the inorganic scaffold composition.

Balanced incorporation of bromide from both the inorganic precursor layer and the organic cation solution was found to be beneficial for WBG perovskite thin-film quality as described by Pappenberger *et al*. for a two-step solution-based process.[253] Motivated by this finding, the fully sequential route framework is used here to systematically explore these two bromide-supply pathways. First, independent increase of the bromide content in each layer is pursued, followed by a combined increase in both layers to assess their effectiveness for bandgap widening towards the UWBG regime of 1.84 eV.

Organic Cation Solution

As a first step, the influence of the organic cation solution composition is investigated while keeping the baseline inorganic scaffold of CsCl and PbI_2 unchanged. Increasing the FABr fraction relative to FAI systematically increases the Br^- content of the thin film and widens the bandgap approximately linearly, with a slope of about 0.02 eV per +10% FABr in the explored composition range. However, for the reference inorganic scaffold this approach saturates at a bandgap of approximately 1.75 eV and does not reach the UWBG target of 1.84 eV.[234]

The resulting bandgap evolution as a function of the FAI/FABr ratio is summarized in **Figure 6.19**, highlighting the limited tuning range achievable by modifying the organic solution alone.

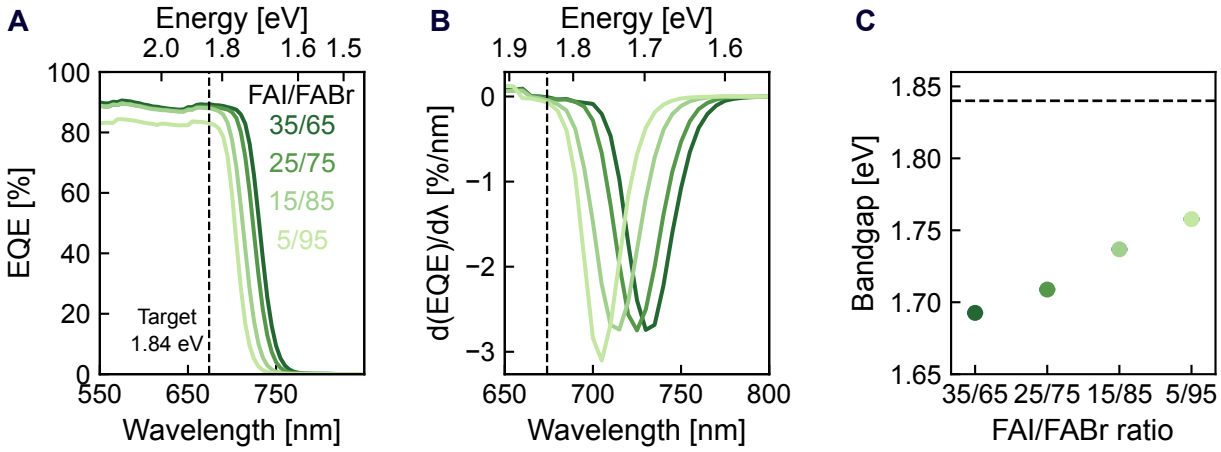

Figure 6.19: EQE-derived bandgap evolution as a function of the FAI/FABr ratio in the organic cation solution while keeping the inorganic scaffold unchanged. Increasing the FABr fraction systematically widens the bandgap but saturates below the UWBG target of 1.84 eV. EQE: External quantum efficiency, UWBG: ultra-wide bandgap

Inorganic Scaffold

To access the UWBG regime, the effect of Br^- addition is investigated by substitution of PbI_2 with $PbBr_2$ at a molar fraction of $15\%_{mol}$. The corresponding layer thicknesses are 255 nm of PbI_2 and 33 nm of $PbBr_2$. This substitution level is selected to approximately match the bromide content introduced by a 95/5 FAI/FABr ratio in the organic cation solution, thereby enabling a balanced comparison between organic- and inorganic-derived bromide incorporation. For this experiment, an organic cation ratio of 65/35 FAI/FABr (same as for the reference process) is chosen to retain sufficient headroom for further bandgap widening through subsequent compositional adjustments.

Importantly, both the amount and the spatial position of $PbBr_2$ within the inorganic scaffold strongly influences bromide incorporation during conversion. Specifically, a CsCl / $PbBr_2$ / PbI_2 stacking sequence (denoted "Mid") results in a more pronounced bandgap widening than depositing $PbBr_2$ on top of PbI_2 (denoted "Top").[234] It is hypothesized that Br^- is volatilized in form of FABr or MABr, reducing the effective Br^- concentration in the thin film. This effect could be more pronounced when $PbBr_2$ is introduced as the top layer.

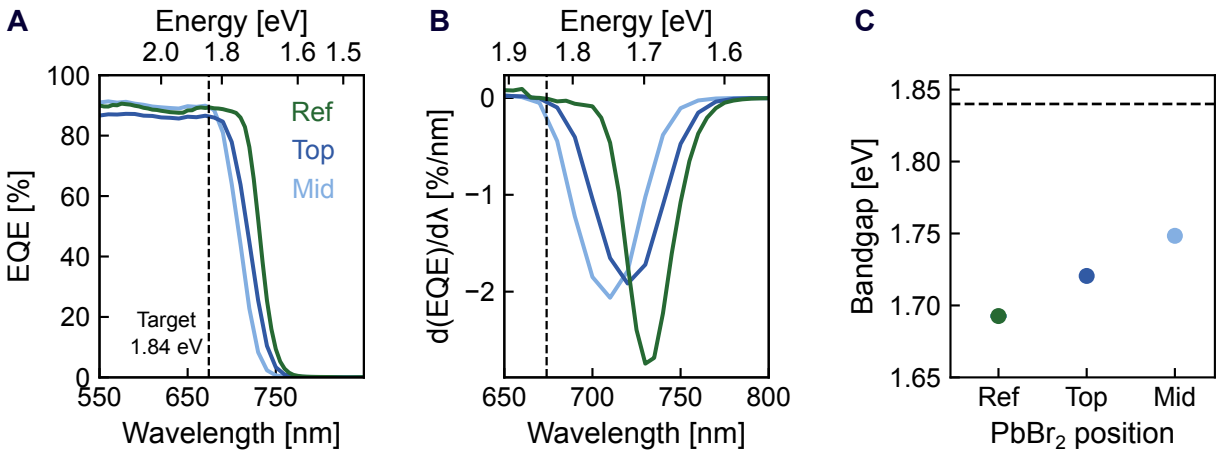

Figure 6.20: EQE-derived comparison of bandgap tuning achieved by incorporating $PbBr_2$ into the sequential inorganic scaffold using different stacking configurations. The figure highlights the influence of $PbBr_2$ position (*e.g.*, mid ($CsCl/PbBr_2/PbI_2$) *vs.* top ($CsCl/PbI_2/PbBr_2$) relative to PbI_2) on Br^- incorporation efficiency and the resulting bandgap. Here, $15\%_{mol}$ of PbI_2 is substituted by $PbBr_2$. EQE: External quantum efficiency

Combined Inorganic Scaffold and Organic Cation Solution

The target bandgap of 1.84 eV is achieved by combining bromide incorporation from both the inorganic scaffold and the organic cation solution. Specifically, $18\%_{\mathrm{mol}}$ of PbI_2 is substituted by $PbBr_2$ in the "mid" configuration, while the organic cation solution is adjusted to a high Br^- content with an FAI/FABr ratio of approximately 10/90. This combined tuning strategy yields a perovskite thin film with a nominal composition of

$$\mathrm{Cs_{0.18}FA_{0.82}Pb(I_{0.57}Br_{0.37}Cl_{0.06})_3},$$

corresponding to an EQE-derived bandgap of $\sim$1.84 eV.[234]

In the implemented process, the sequential inorganic scaffold consists of 30 nm CsCl / 40 nm $PbBr_2$ / 246 nm PbI_2, followed by deposition of the organic cation solution (FAI/FABr $\approx$ 10/90). The resulting EQE spectra confirming the UWBG perovskite thin-film formation and the desired bandgap are shown in **Figure 6.21**.

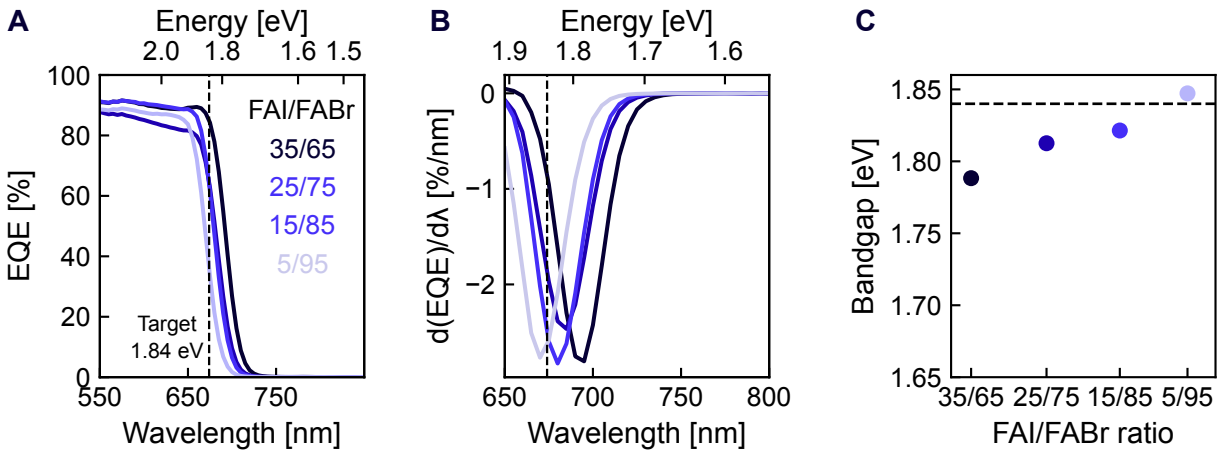

Figure 6.21: EQE spectra of UWBG perovskite thin films obtained by combining bromide incorporation in both the inorganic scaffold (*via* partial $PbBr_2$ substitution, $18\%_{mol}$) and the organic cation solution (high FABr fraction). The combined tuning strategy enables reproducible bandgaps up to ∼1.84 eV, exceeding the tuning range accessible by organic-only or inorganic-only modification. EQE: External quantum efficiency, UWBG: ultra-wide bandgap

While the targeted bandgap of 1.84 eV is reached reproducibly, the incorporation of $PbBr_2$ into the inorganic scaffold is accompanied by a pronounced reduction in photovoltaic performance, with maximum PCEs around ∼15.3%. This indicates that further optimization of interfaces, conversion conditions, and defect management is required to fully exploit the UWBG regime.[234] It should be noted that at the time of experiments, sputtered NiO_x was not accessible which significantly improved V_{OC} and FF when used as a bilayer with SAMs in previous experiments.[204]

Conclusion

This section demonstrates that the sequential route framework provides a versatile and modular framework for bandgap engineering across a wide compositional range relevant to future triple-junction applications. Starting from a 1.70 eV WBG reference thin film, systematic tuning towards both narrower and wider bandgaps is achieved by independently adjusting the halide supply from the organic cation solution and the inorganic scaffold. An overview of champion devices for the three bandgap regimes and a comparison to literature reports is displayed in **Figure 6.22**.

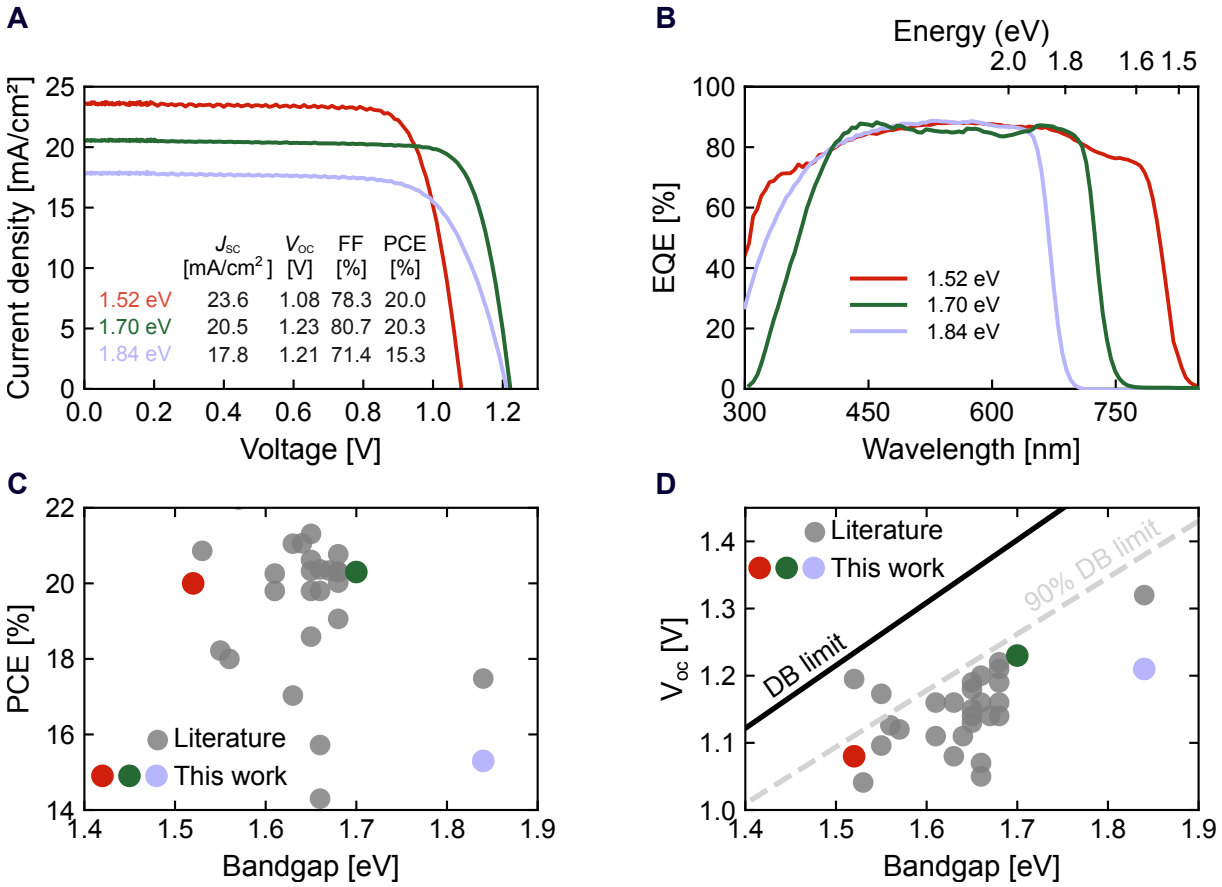

Figure 6.22: Overview of the accessible bandgap range achieved using the fully sequential hybrid two-step deposition process framework. **A** *J*–*V* characteristics and **B** EQE spectra for target bandgaps of 1.52 eV, 1.70 eV and 1.84 eV. **C/D** Comparison to PCEs and V_{OC} from the literature (Summarized in **Table A.3**). Note: Different substrate type was used for PSCs with a target bandgap of 1.70 eV explaining the different spectral EQE response at low wavelengths. *J*–*V*: Current-density–Voltage, EQE: external quantum efficiency

Bandgap narrowing towards the MBG regime is realized by reducing the Br^- and Cl^- content and lowering the Cs fraction supplied by the inorganic scaffold. This yields a perovskite thin film with a nominal composition of $Cs_{0.03}FA_{0.97}Pb(I_{0.99}Cl_{0.01})_3$, and an EQE-derived bandgap of ∼1.52 eV. In contrast, access to the UWBG regime requires the combined incorporation of Br^- from both the organic cation solution and the inorganic scaffold. By partially substituting PbI_2 with $PbBr_2$ in the sequential inorganic scaffold and using a Br^--rich organic solution, a perovskite thin film with a nominal composition of $Cs_{0.18}FA_{0.82}Pb(I_{0.57}Br_{0.37}Cl_{0.06})_3$ is obtained, yielding an EQE-derived bandgap of ∼1.84 eV. The sequential route enables high compositional control and deliberate positioning of inorganic precursor materials within the scaffold stack. These results position the fully sequential route framework as a promising pathway for bandgap engineering in future advanced multi-junction perovskite solar cell architectures.

6.6 Summary

This chapter demonstrates that fully sequential inorganic scaffold deposition can replace conventional co-deposition within the hybrid two-step route without sacrificing device performance, while offering clear advantages in repeatability, fabrication throughput potential, substrate transferability, and compositional control. Adopting the fully sequential route provides three central advantages: (i) improved process repeatability through decoupled deposition and higher control of individual precursor steps, (ii) a clear pathway to high fabrication throughput by independently accelerating rate-limiting depositions, and (iii) facile compositional engineering, enabling systematic bandgap tuning with minimal changes to the overall process flow.

A key outcome is the development and benchmarking of a sequential inorganic scaffold deposition (CsCl followed by PbI_2) against the conventional co-deposition route. Despite the fundamentally different scaffold formation pathways, both routes yield comparable WBG PSC performance after optimizing the organic-cation conversion step, with champion efficiencies of 20.3% (Seq route) and 19.3% (Co route) at a target bandgap of $\sim$1.70 eV. The performance obtained from the sequential route ranks among the highest reported efficiencies for hybrid two-step processed WBG PSCs and features a high V_{OC} approaching 90% of the detailed-balance limit for this bandgap. Further, the sequential route demonstrates improved batch-to-batch repeatability compared to the Co route which is crucial for reliable large-scale manufacturing. Beyond device performance metrics, the deposition route itself allows for inorganic scaffold engineering: sequential deposition yields a distinctly more textured and porous inorganic scaffold compared to co-deposition, facilitating organic cation infiltration. Sequential processing is further shown to be robust against process acceleration strategies that reduce inorganic scaffold deposition time by 80%$_{rel}$ compared to the baseline without a fundamental decrease in device performance. Compatibility with textured substrates relevant for tandem integration is demonstrated with a first TSC prototype reaching a PCE of 24.1% using the fully sequential deposition route.

Finally, the modularity of the sequential route framework enables bandgap engineering for multi-junction solar cell architectures. Starting from the $\sim$1.70 eV baseline, bandgaps are tuned to the MBG regime ($\sim$1.52 eV) and to the UWBG regime ($\sim$1.84 eV) by independently adjusting halide supply from the organic solution and/or the inorganic scaffold, with the additional degree of freedom of deliberate precursor positioning within the sequential stack. Notably, differences in bandgap tuning behavior are observed depending on the positioning of bromide within the inorganic scaffold. The mid configuration ($CsCl/PbBr_2/PbI_2$) reaches comparable bandgaps at lower FABr fractions in the organic cation solution than the top configuration ($CsCl/PbI_2/PbBr_2$), suggesting a more effective incorporation of Br^-.

Overall, this chapter positions fully sequential inorganic-scaffold deposition for the hybrid two-step route as an industry-aligned process framework that combines robust conversion control with scalability, throughput acceleration, and compositional tunability for next-generation tandem and multi-junction perovskite-based solar cells.

7 Conclusion and Outlook

7.1 Conclusion

Perovskite photovoltaics have matured to a stage at which the key challenge is no longer only the demonstration of high device efficiencies, but their reliable implementation in industrially relevant fabrication schemes, particularly for perovskite/silicon tandem architectures. This step toward manufacturing is still limited by narrow stoichiometric process windows, insufficient fabrication throughput, and pronounced route-dependent variability that often necessitates repeated process re-optimization. In this thesis, the translation challenge is addressed from a manufacturing-oriented perspective by considering perovskite thin films as process-limiting layers whose deposition must be reproducible, high-throughput, and compatible with realistic equipment constraints and source utilization. The coupled roles of process-route choice, source design, precursor thermochemistry, and interfacial interactions are analyzed to identify dominant process parameters and to derive stable operating windows and scalable process concepts for vapor-phase and hybrid perovskite fabrication. This thesis shows that industrial translation of perovskite photovoltaics is governed by both efficiency and by the coupled control of fabrication throughput, process transferability, and conversion robustness.

Research Objective 1: Derive guidelines for industrial scale-up
Industrialization requires that record efficiencies are reproduced at line speed, because throughput and yield largely determine production cost at scale. Deposition routes therefore have to be assessed in terms of device performance, compatibility with high-throughput in-line fabrication, and capital expenditure (CapEx). A manufacturing-oriented framework is established to connect laboratory deposition routes with industrial line-speed requirements for a target fabrication throughput of 1000 M10-sized wafers h^{-1}. Deposition-rate limitations, deposition-route dependent constraints on source demand and utilization together with equipment complexity are assessed. The deposition rate of volatile organic precursors such as FAI is constrained by low thermal stability, imposing a limit on fabrication throughput where high vapor fluxes must be balanced against material decomposition. In contrast, inorganic precursors such as PbI_2 can typically be deposited at substantially higher and more stable deposition rates, such that inorganic deposition is not intrinsically rate-limiting.

These process constraints become more pronounced when transitioning from laboratory point sources to industrial linear sources, where uniformity and stoichiometry have to be maintained across large widths at high substrate velocities, increasing the complexity of source layout and in-line control. Here, process-route choice determines how precursor-specific rate limits translate into equipment demand and, ultimately, economic viability. In co-deposition, precursor deposition rates are intrinsically coupled because stoichiometry must be maintained continuously by controlling the relative precursor deposition rates. Consequently, the maximum line speed is set by the slowest precursor. Any rate mismatch between

FAI and PbI_2 propagates directly into higher demand of deposition sources, more complex metrology requirements and increased downtime for source conditioning and refilling, all of which increase CapEx.

The commonly used co-deposition route is compared to route concepts with decoupled FAI deposition. In partial sequential routes, the inorganic components are co-deposited, followed by a separate organic deposition step. This separation allows the inorganic sources to operate close to their maximum stable rate. Fully sequential routes extend this decoupling further by separating individual precursor steps, enabling each source to be operated at its maximum stable rate without stoichiometric cross-coupling. A bottom-up throughput simulation reveals a stepwise increase in equipment demand for deposition of a representative perovskite absorber from fully sequential processing (baseline process) to partial sequential (+5%$_{rel}$) and co-deposition (+157%$_{rel}$). Across these deposition routes, the reduction in operated sources in series and the lower requirements of in-line stoichiometry control are direct levers to lower CapEx. Overall, process routes that decouple inorganic and organic deposition are identified as particularly attractive for industrial implementation because they enable higher line speed while simultaneously reducing equipment complexity and associated production costs.

In this way, a quantitative framework is established that links precursor thermochemistry, process-route choice, and source utilization to achievable deposition rates, equipment demand, and capital expenditure in high-throughput vapor-phase fabrication.

Research Objective 2: Elucidate interface- and process-induced layer growth mechanisms
Robust absorber formation requires understanding how phase evolution, incorporation kinetics, and microstructure depend on interface chemistry and process route. This is particularly important because early-stage crystallization in metal halide perovskites is highly sensitive to process conditions. Accordingly, interface- and route-induced growth mechanisms are resolved as determinants of phase selectivity and effective stoichiometric process windows in both vapor-only and hybrid two-step processing.
In vapor co-deposition of FA-based perovskites, substrate-dependent growth emerges as a decisive factor for both phase selectivity and effective FAI incorporation. Exposed phosphonic-acid functional groups in the nPACz material class stabilize the photoactive α-phase during the earliest crystallization stages and to suppress δ-phase formation under otherwise comparable conditions. Density-functional theory simulations support a kinetic interpretation in which phosphonic-acid groups interact predominantly *via* hydrogen bonding to surface iodides, thereby increasing the activation barrier for the $\alpha \rightarrow \delta$ transformation and kinetically trapping the initially formed α-phase. Device data reveal a pronounced substrate dependence of the effective FAI incorporation rate, requiring re-optimization of the relative FAI rate upon transfer between different substrate terminations. Excess-FAI regimes are accompanied by degraded photovoltaic metrics, most notably reduced J_{SC}. X-ray emission spectroscopy further supports substrate-dependent incorporation trends consistent with the device-derived shifts in the optimal FAI rate. To translate this substrate-dependent phase selectivity into a rational interface-engineering strategy, mixed self-assembled monolayers based on 2PACz and 4dPA allow deliberate tuning of the exposed phosphonic-acid surface density and thereby steer phase selectivity.
In hybrid two-step processing, the deposition route of the CsCl/PbI_2 inorganic scaffold is identified as

a previously overlooked scaffold-engineering parameter. Co-deposition yields a dense scaffold with predominantly horizontally aligned PbI_2 platelets, whereas fully sequential deposition produces a more textured and porous scaffold with predominantly vertical or tilted platelets. These route-dependent differences in microstructure, texture, and elemental depth distribution are shown to modify organic-cation uptake and infiltration during solution-based conversion, thereby providing a materials-level perspective for understanding conversion sensitivity in diffusion-limited two-step processes.

These findings clarify how interface chemistry and process-route choice govern phase selectivity, incorporation kinetics, and early-stage crystallization, thus defining the effective stoichiometric process window for perovskite absorber formation.

Research Objective 3: Assess industrially relevant vapor-deposition process routes
Industrial manufacturing demands process routes that combine high efficiency with repeatability, scalable throughput and compatibility with tandem-relevant substrates. Hybrid two-step perovskite fabrication is identified as an industry-aligned route combining conformal and scalable coating with fast deposition of organic precursors. In this context, deposition routes are benchmarked in terms of industrial process relevance, device performance, acceleration potential, and versatility for bandgap engineering.

A fully sequential inorganic-scaffold route is benchmarked against the conventional co-deposition route for wide-bandgap perovskite top-cell fabrication. Comparable device performance is achieved at a target bandgap of $\sim$1.70 eV, with champion efficiencies of 20.3% (Seq) and 19.3% (Co), indicating that an industry-aligned sequential route can match the performance level of the laboratory standard co-deposition route. The sequential route achieves device performance among the highest reported for hybrid two-step deposition of wide-bandgap perovskite thin films. Based on this sequential deposition framework, substantial acceleration of inorganic scaffold deposition is demonstrated without a fundamental loss in device performance, enabling a reduction of inorganic deposition time by $80\%_{rel}$ compared to the baseline process and directly addressing throughput constraints. Compatibility with textured silicon substrates is further demonstrated by a first perovskite/Si tandem prototype reaching 24.1%, supporting the applicability of the sequential framework and motivating dedicated tandem-focused optimization. Finally, the modular sequential route framework enables systematic bandgap engineering toward triple-junction-relevant absorbers by independent control of halide supply from the inorganic scaffold and/or the organic solution, yielding device efficiencies of 20.0% (1.52 eV) and 15.3% (1.84 eV).

Together, these results demonstrate that a fully sequential hybrid two-step framework can combine high device performance with improved repeatability, accelerated deposition, tandem compatibility, and modular bandgap tunability.

Research Objective 4: Identify factors limiting process transferability and repeatability
Industrial deployment requires both high peak performance and high yield over extended fabrication campaigns, which in turn demands process windows that are robust against drift in precursor condition, reactor state, and substrate properties. In perovskite deposition, limited repeatability and transferability

frequently demand recipe re-optimization when deposition tools, device stacks, or substrate properties are changed.

Exposed phosphonic-acid density is identified as a particularly challenging interfacial variable because it depends on substrate preparation, molecular packing, and processing conditions. Consequently, nominally identical deposition recipes can lead to shifts in effective FAI incorporation and phase selectivity. In hybrid two-step processing, repeatability is additionally constrained by route-dependent scaffold porosity, because infiltration pathways and conversion behavior are defined already at the inorganic stage. Here, the fully sequential scaffold route provides a broader and more stable conversion window than co-deposition, thereby reducing batch-to-batch variation. Finally, source design is found to directly affect flux reproducibility and tool-to-tool transferability. Conical and cylindrical crucibles impose different vapor-flux geometries and angular emission characteristics, such that the effective vapor flux at the substrate can change with crucible type and source loading. As a result, process drifts can occur over long deposition runs even when setpoint rates are maintained, because the effective precursor vapor flux at the substrate is influenced by changes in emission geometry.

Collectively, precursor thermochemistry, source design, interface-dependent incorporation kinetics, and route-defined scaffold microstructure provide a mechanistic basis for understanding and mitigating limitations in process transferability and repeatability under realistic manufacturing conditions.

Importantly, the four objectives do not describe isolated challenges, but coupled constraints of a single manufacturing problem. Precursor thermochemistry and source design define achievable deposition rates (*Research Objective 1*), which interact with process route choice (*Research Objective 3*) to determine equipment demand and scalability. At the same time, interface-controlled incorporation kinetics (*Research Objective 2*) and route-defined scaffold microstructure (*Research Objective 3*) jointly define the effective stoichiometric process window and conversion robustness (*Research Objective 4*). Industrial translation therefore requires coherent co-optimization across precursor chemistry, source design, interfaces, and process route, rather than isolated optimization of individual parameters.

By quantifying route-dependent throughput and equipment implications, resolving interfacial mechanisms that shift stoichiometric process windows and phase selectivity, and demonstrating a fully sequential hybrid two-step framework that combines improved repeatability, accelerated inorganic deposition, tandem compatibility, and modular bandgap tunability, this thesis establishes a manufacturing-oriented framework for perovskite thin-film fabrication, in which throughput, transferability, and conversion robustness are identified as the central, coupled constraints governing industrial scalability. Process-route choice, source design, and interface engineering are identified as the primary strategies to convert high-efficiency perovskite absorbers into repeatable, high-throughput, tandem-compatible manufacturing processes.

7.2 Outlook

The results of this thesis point to several research directions that are decisive for transferring vapor-based and hybrid perovskite deposition from laboratory demonstrations to large-scale manufacturing. Building on the framework developed in *Research Objectives 1–4*, future work should focus on four coupled priorities: long-term stability under realistic operation, scalable thin film deposition and tandem integration, scaffold engineering as a design space for perovskite conversion, and comprehensive process repeatability control. These challenges directly translate into cost and yield limitations at scale, making their resolution essential for reducing the levelized cost of electricity of perovskite-based technologies.

(1) Long-term stability under realistic operating conditions
High efficiencies have been demonstrated for perovskite single-junction and perovskite/silicon tandem devices, yet market entry is primarily limited by bankability, which requires proven long-term stability under realistic stress factors, including illumination, elevated temperature, and electrical bias. For wide-bandgap perovskites in particular, compositional instabilities and temperature-driven degradation pathways can compromise voltage and operational lifetime even when initial performance is high. Accordingly, stability qualification must move beyond short screening tests toward accelerated protocols with validated correlation to outdoor performance, including module-relevant encapsulation and interconnect concepts.

(2) Scalability of deposition and tandem-oriented process integration
Industrial translation requires that all functional layers are deposited by scalable methods that provide high throughput, good uniformity, and compatibility with tandem-relevant textured substrates. While spin coating enables controlled benchmarking in this thesis, future work should extend hybrid two-step processing toward scalable solution application of the organic-cation step (*e.g.*, meniscus coating, slot-die coating, spray coating, or inkjet printing), and similarly adopt scalable deposition concepts for transport layers and interlayers. In parallel, tandem integration should be advanced from prototype demonstrations toward monolithic, module-relevant implementations that combine conformal coating on textured silicon with reliable recombination layers, minimized parasitic absorption, and low interfacial recombination.

(3) Scaffold engineering as an underexplored design space for two-step conversion
The route-dependent scaffold microstructure identified in this thesis suggests that inorganic scaffold porosity, texture, and elemental distribution are central parameters influencing conversion kinetics and process robustness in diffusion-limited two-step processing. Future work should therefore broaden the scaffold-engineering parameter space beyond deposition sequence, including systematic variation of scaffold compositions, multilayer designs, and morphology-control strategies that tune the inorganic scaffold microstructure for optimal organic-cation infiltration. In addition, *in-situ* and operando diagnostics are particularly valuable for establishing links between deposition conditions, scaffold microstructure, and conversion pathways, for example, through synchrotron-based *in-situ* GIWAXS/XRD during vacuum deposition and subsequent conversion. A key objective is the development of predictive, experimentally accessible descriptors that enable estimation of the optimal conversion window from inorganic scaffold properties, reducing reliance on empirical parameter screening.

(4) Process repeatability and transferability as yield-limiting constraints
High-yield manufacturing requires robust process windows that remain resilient to drift in precursor condition, reactor state, and substrate properties over extended production runs. The sensitivities identified in this thesis indicate that repeatability is frequently limited by a small set of coupled factors: interface-dependent incorporation kinetics (*e.g.*, control of phosphonic-acid density), process-route defined inorganic scaffold microstructure that sets conversion behavior, precursor thermochemistry that constrains stable flux operation, and source-design-dependent emission characteristics that can shift the effective flux distribution at the substrate. Future work should therefore combine three elements: interface design to suppress unintended phase selectivity and incorporation shifts, process route concepts that decouple sensitive steps to stabilize stoichiometry and conversion and source and reactor designs that minimize process drift by controlling fill-level dependence, angular emission profiles, and precursor aging.

To conclude, these directions indicate that the industrialization of perovskite photovoltaics will depend less on isolated efficiency gains than on integrated process engineering, in which stability, throughput, transferability, and conversion robustness are co-optimized at line speed. The manufacturing-oriented framework established in this thesis, together with the sequential hybrid two-step route and the identified roles of interface chemistry, precursor thermochemistry, and source design, provides a foundation for advancing perovskite-based tandem and multi-junction photovoltaics toward scalable, repeatable, and high-yield manufacturing.

Appendix

A.1 Additional Data

Derivation of Expression to Fit Thickness Gradient for Vapor Flux Distributions

The angular vapor flux intensity $I(\theta)$ is proportional to $\cos^n(\theta)$, as expressed by the cosine law:

$$I(\theta) \propto \cos^n(\theta). \tag{A.1}$$

On a horizontal substrate holder, the angle θ is related to the distance x along the substrate holder and the height of the holder x_h using the tangent function:

$$\theta(x) = \arctan\left(\frac{x}{x_h}\right). \tag{A.2}$$

Substituting $\theta(x)$ into the cosine law relates the intensity to the effective angle at each point:

$$\cos^n(\theta(x)) = \cos^n\left(\arctan\left(\frac{x}{x_h}\right)\right). \tag{A.3}$$

Additionally, the vapor flux density decreases with the distance from the source (inverse square law), where the intensity decreases with the square of the distance from the source. The distance R from the source to a point x on the substrate is given by:

$$R = \sqrt{x^2 + x_h^2}. \tag{A.4}$$

Thus, the intensity at a given point x becomes:

$$I(x) = \frac{\cos^n\left(\arctan\left(\frac{x}{x_h}\right)\right)}{R^2} = \frac{\cos^n\left(\arctan\left(\frac{x}{x_h}\right)\right)}{x^2 + x_h^2}. \tag{A.5}$$

Assuming the thickness $t(x)$ is proportional to the corrected vapor flux distribution $I(x)$, a proportionality factor A is introduced:

$$t(x) = A \cdot \frac{\cos^n\left(\arctan\left(\frac{x}{x_h}\right)\right)}{R^2} = A \cdot \frac{\cos^n\left(\arctan\left(\frac{x}{x_h}\right)\right)}{x^2 + x_h^2}. \tag{A.6}$$

This expression is used to fit the vapor flux distribution from experimentally determined thickness gradients.

Benchmarking Inorganic Deposition Routes for Hybrid Two-Step Processed Perovskite Solar Cells: A Materials Perspective

A.1.0.1 Repeatability Study

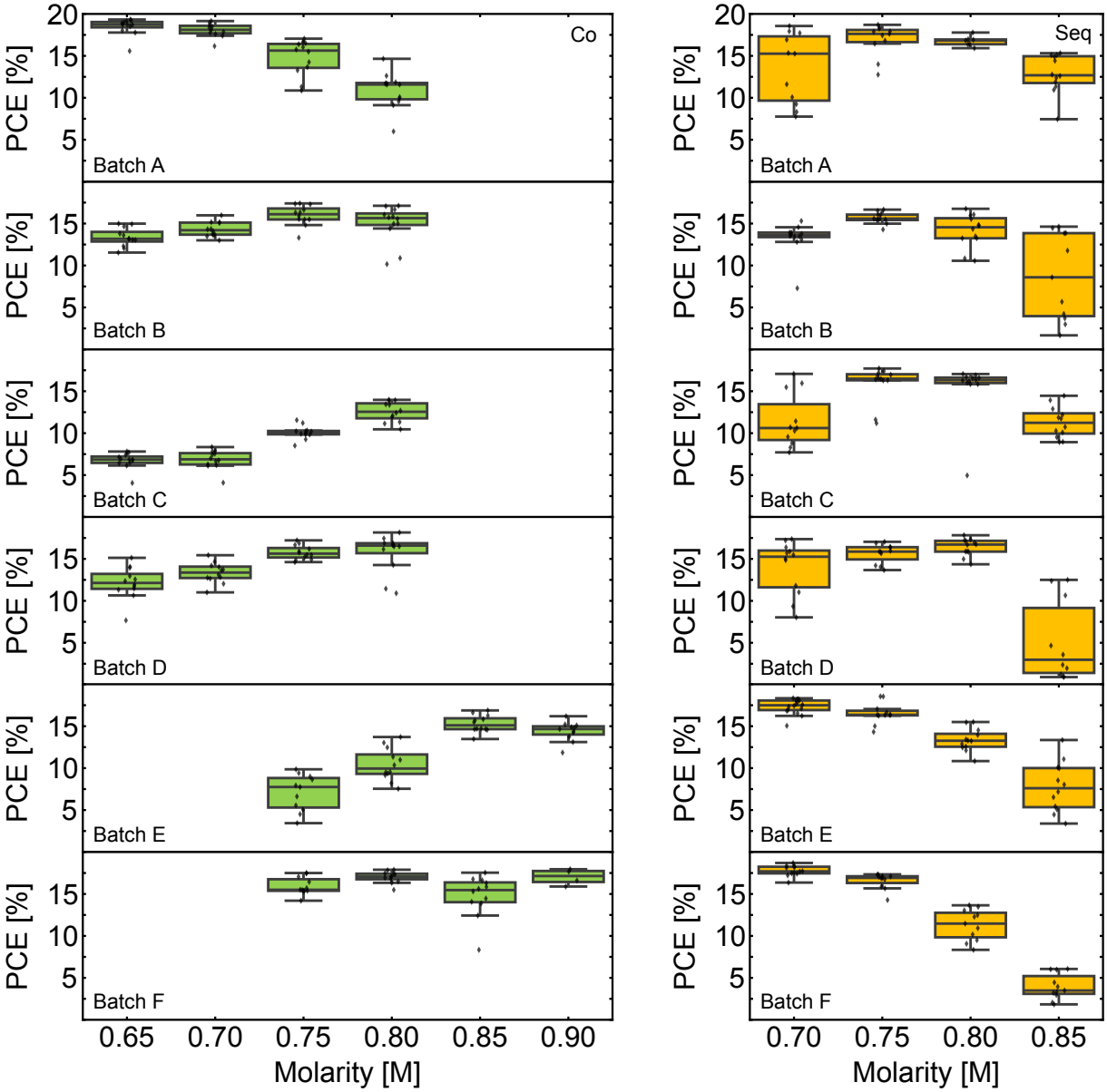

Figure A.1: Comparison of process repeatability of PSCs fabricated with Co- and Seq deposition of the inorganic scaffold. For each individual batch, Co and Seq PSCs were fabricated in parallel. Each batch comprises twelve pixels per organic cation molarity – for Co and Seq respectively. The rotation speed for the organic cation solution was increased from 4000 rpm in Batch A to 5500 rpm for Batch B-F to compensate for changed organic cation uptake after PeroVap maintenance. PSC: Perovskite solar cell, rpm: revolutions per minute

Table A.1: Final QCM thicknesses of CsCl and PbI_2 for co- (Co) and sequential (Seq) deposition over multiple batches. QCM: Quartz crystal microbalance

Batch No.	Seq		Co	
	Thickness [nm]		Thickness [nm]	
	PbI_2	CsCl	PbI_2	CsCl
A	300	30	300	not measured
B	300	30	300	29.7
C	300	30	300	30.2
D	300	30	300	29.7
E	300	30	300	29.7
F	300	30	300	30.1

A.1.0.2 Champion Device and Literature Comparison

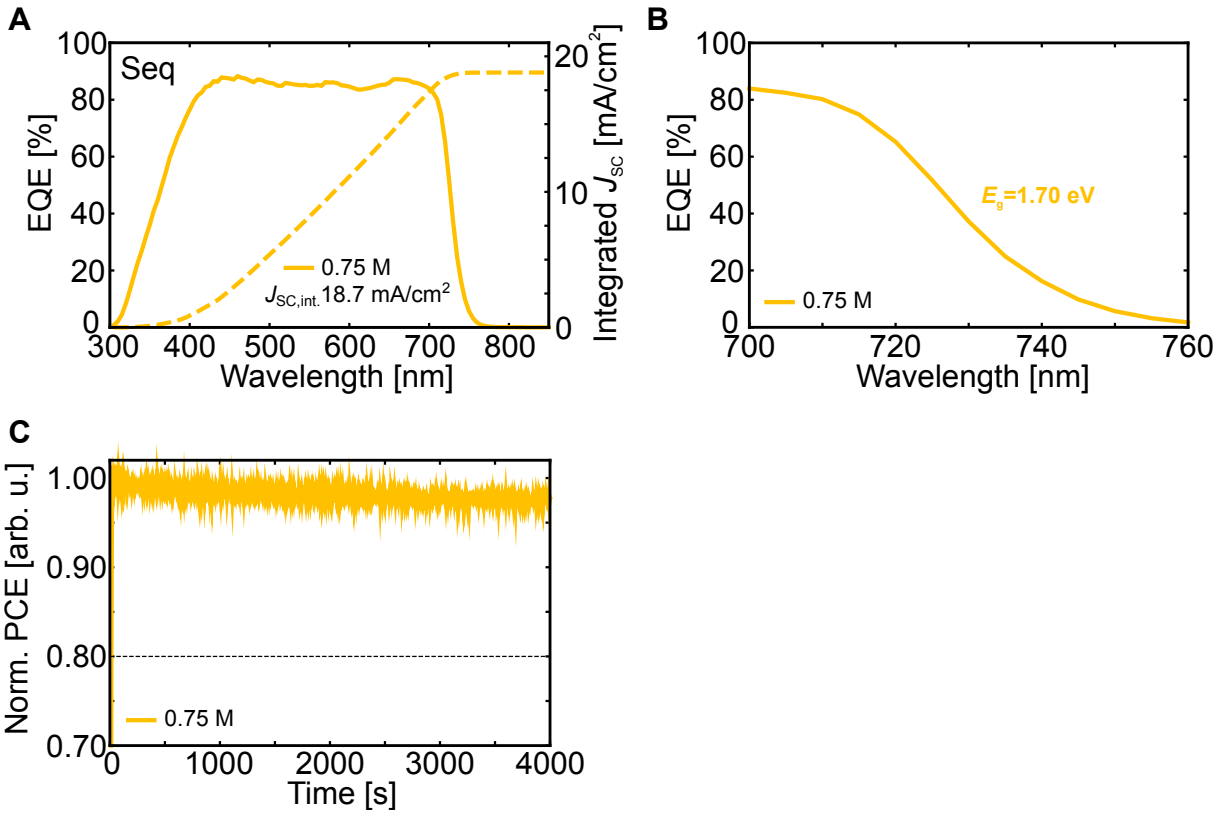

Figure A.2: **A** EQE spectrum as well as the corresponding integrated J_{SC}, **B** optical bandgap extracted from the inflection point of the EQE spectrum, and **C** MPP tracking for the champion PSC fabricated with sequential deposition of the inorganic scaffold. EQE: External quantum efficiency, MPP: maximum power point, PSC: perovskite solar cell

Table A.2: Literature overview for wide-bandgap PSCs based on hybrid two-step deposition. WBG: Wide bandgap PSC: perovskite solar cell

Author	Year	bandgap [eV]	PCE [%]	V_{OC} [V]	FF [%]	J_{SC} [mA/cm^2]	Reference
This work	2025	1.70	20.30	1.23	80.7	20.5	-
Pesch *et al.*	2025	1.66	19.80	1.20	79.2	20.8	[174]
Chen *et al.*	2024	1.65	20.33	1.19	81.2	21.09	[254]
Li *et al.*	2024	1.61	19.80	1.11	83.6	21.31	[255]
Liu *et al.*	2024	1.66	20.37	1.16	83.3	21.09	[240]
Yang *et al.*	2024	1.65	18.59	1.18	76.5	20.61	[256]
Zheng *et al.*	2024	1.68	20.77	1.22	81.5	20.98	[257]
Said *et al.*	2024	1.68	19.06	1.16	81.1	20.3	[258]
Xiong *et al.*	2023	1.68	20.02	1.14	81.2	21.64	[259]
Afshord *et al.*	2023	1.64	21.06	1.11	79.5	23.9	[181]
Afshord *et al.*	2023	1.67	20.34	1.14	80.9	22.06	[181]
Yang *et al.*	2023	1.63	21.05	1.16	78.97	22.98	[260]
Er-raji *et al.*	2023	1.66	15.72	1.07	78.4	18.78	[117]
Luo *et al.*	2023	1.68	20.30	1.19	81.6	20.9	[180]
Luo *et al.*	2023	1.68	20.30	1.21	80.8	20.9	[261]
Sun *et al.*	2023	1.65	20.62	1.13	80.2	22.77	[262]
Zhang *et al.*	2023	1.61	20.26	1.16	79.96	21.84	[263]
Er-raji *et al.*	2023	1.66	14.30	1.05	75.7	18	[109]
Mao *et al.*	2022	1.65	21.31	1.14	80.6	23.19	[204]
Li *et al.*	2021	1.63	17.03	1.08	80.3	19.59	[124]
Soltanpoor *et al.*	2020	1.65	19.80	1.15	82.8	20.8	[250]

Table A.3: Literature overview for MBG and UWBG PSCs based on hybrid two-step deposition. MBG: Mid bandgap, UWBG: ultra-wide bandgap, PSC: perovskite solar cell

Author	Year	bandgap [eV]	PCE [%]	V_{OC} [V]	FF [%]	J_{SC} [mA/cm^2]	Reference
This work (1.52 eV)	2025	1.52	20.00	1.08	78.3	23.6	-
This work (1.84 eV)	2025	1.84	15.30	1.21	71.4	17.8	-
Tan *et al.*	2023	1.52	24.27	1.19	83.34	24.4	[264]
Pesch *et al.*	2024	1.55	18.22	1.10	73.79	22.5	[174]
Fang *et al.*	2024	1.57	22.22	1.12	79.12	25.3	[265]
Golobostanfard *et al.*	2024	1.53	20.86	1.04	83.98	23.9	[266]
Wang *et al.*	2024	1.55	24.72	1.17	83.8	23.9	[267]
Battran *et al.*	2025	1.56	18.00	1.13	77.0	20.8	[249]
Wang *et al.*	2025	1.84	17.48	1.32	82.3	16.1	[268]

A.1.0.3 Stability Assessment

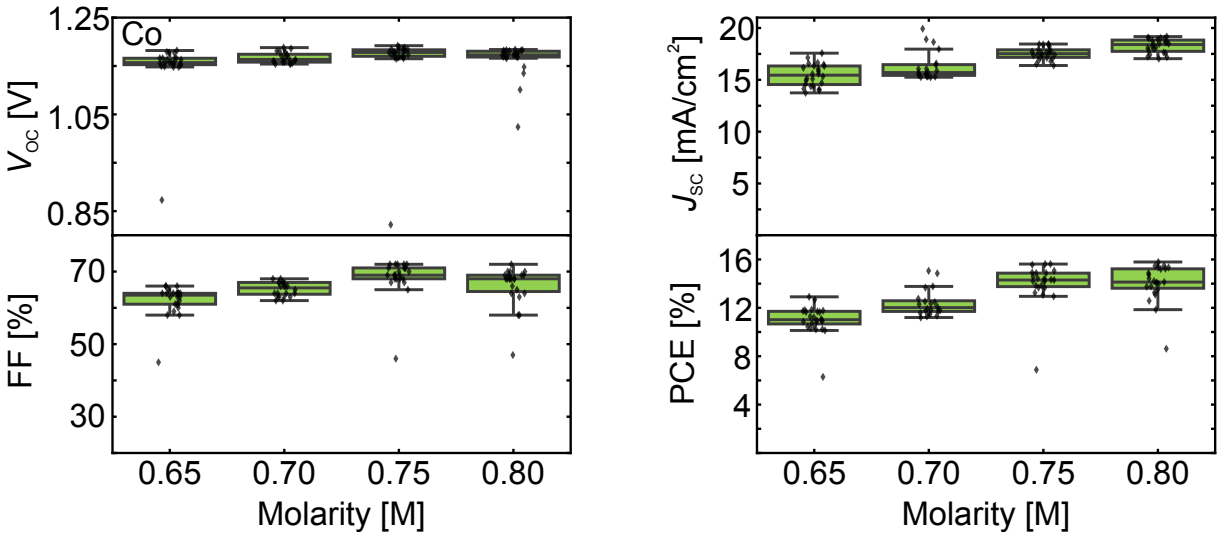

Figure A.3: Statistical distribution (in total 91 devices) of the open-circuit voltage (V_{OC}), fill factor (FF), short-circuit current density (J_{SC}) and power conversion efficiency (PCE) of semitransparent PSCs for stability measurements under ISOS-L1 test conditions for different molarities of the organic cation solution for co-deposition (Co) of the inorganic scaffold. PSC: Perovskite solar cell, ISOS: International Organization for Standardization

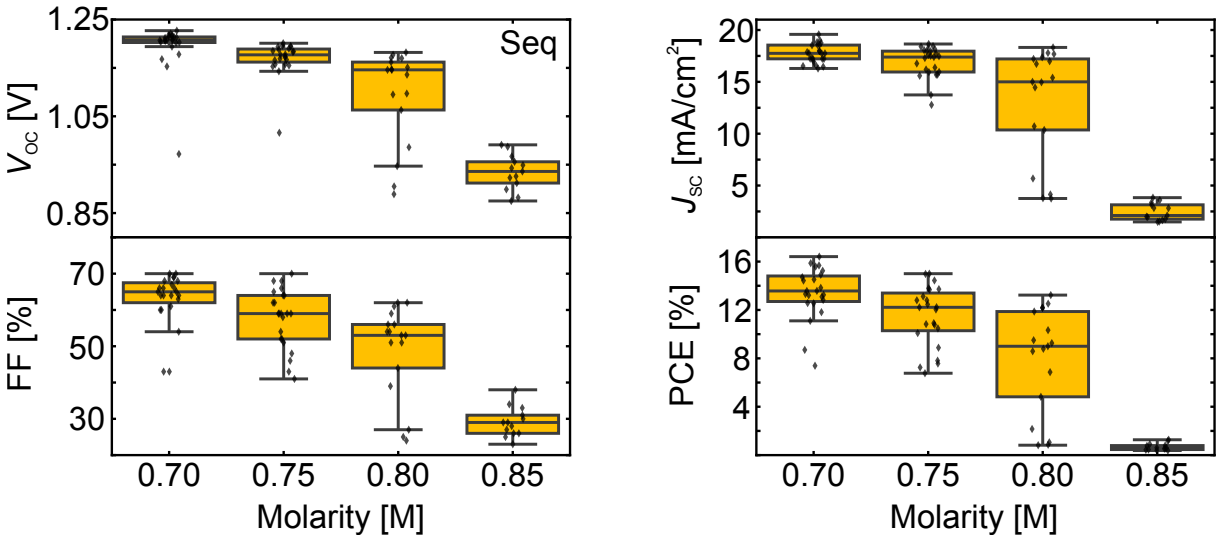

Figure A.4: Statistical distribution (in total 77 devices) of the open-circuit voltage (V_{OC}), fill factor (FF), short-circuit current density (J_{SC}) and power conversion efficiency (PCE) of semitransparent PSCs for stability measurements under ISOS-L1 test conditions for different molarities of the organic cation solution for sequential deposition (Seq) of the inorganic scaffold. PSC: Perovskite solar cell, ISOS: International Organization for Standardization

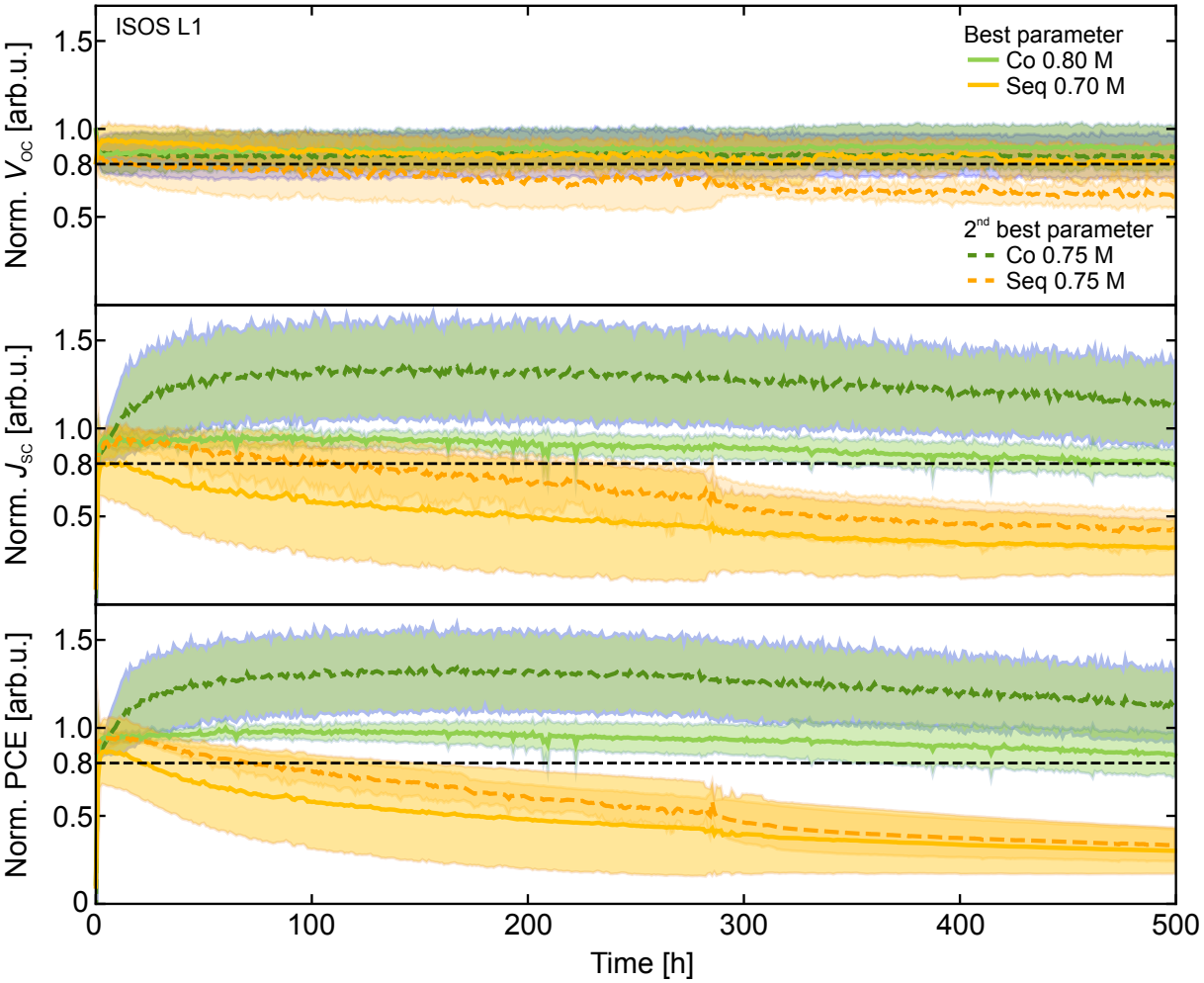

Figure A.5: Normalized V_{OC}, J_{SC} and PCE at the MPP tracking of semitransparent PSCs with co-deposition (Co) and sequential deposition (Seq) of the inorganic scaffold with optimal molarity (best parameter) and second-best parameter under ISOS-L1 test conditions (100 mW cm^{-2}, 25 °C, MPP tracking) for 500 h. MPP: Maximum power point, PSC: perovskite solar cell, ISOS: International Organization for Standardization

A.1.0.4 Detailed Analysis of Batch A

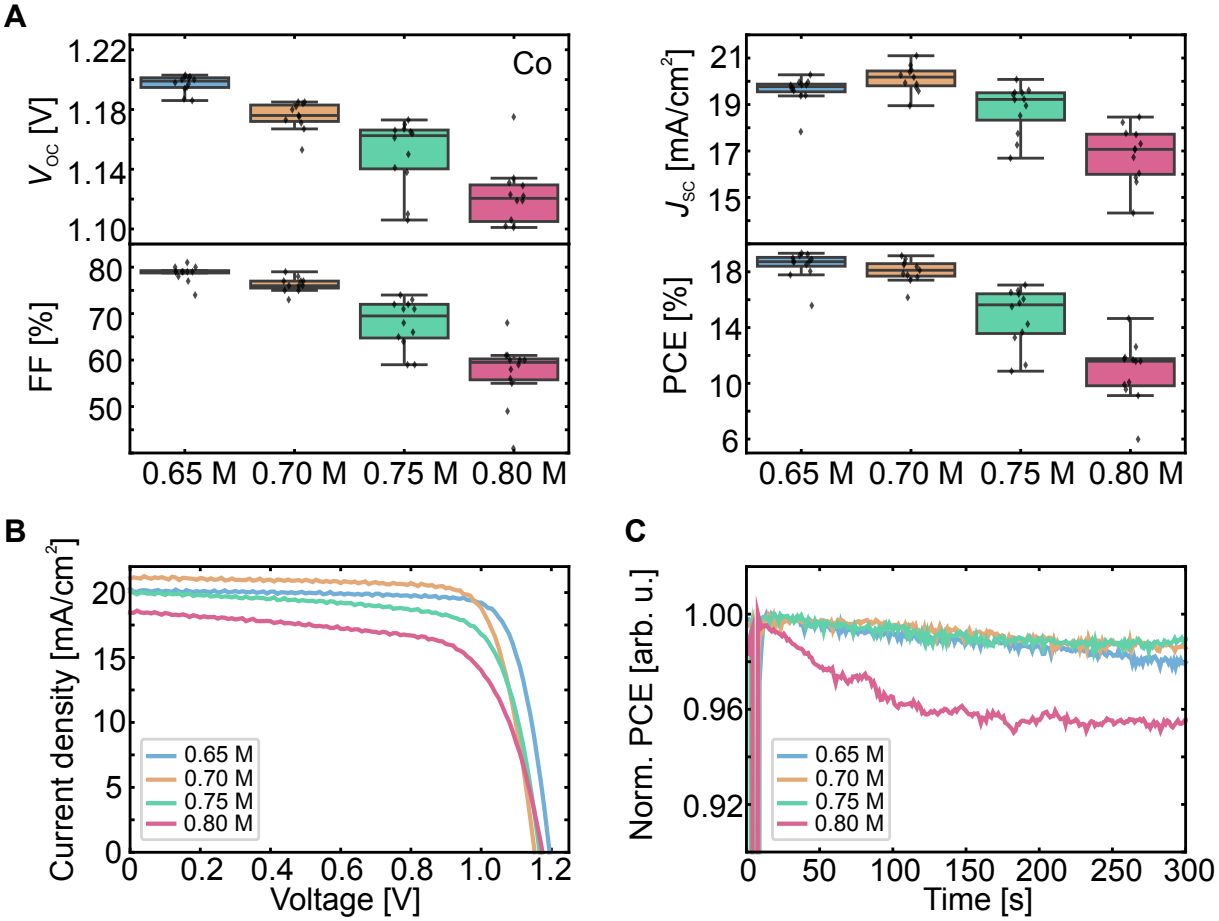

Figure A.6: **A** Statistical distribution (in total 47 devices) of the open-circuit voltage (V_{OC}), fill factor (FF), short-circuit current density (J_{SC}) and power conversion efficiency (PCE), **B** current density *versus* voltage (J–V) characteristics and **C** MPP tracking for different molarities of the organic cation solution for co-deposition (Co) of the inorganic scaffold. MPP: Maximum power point

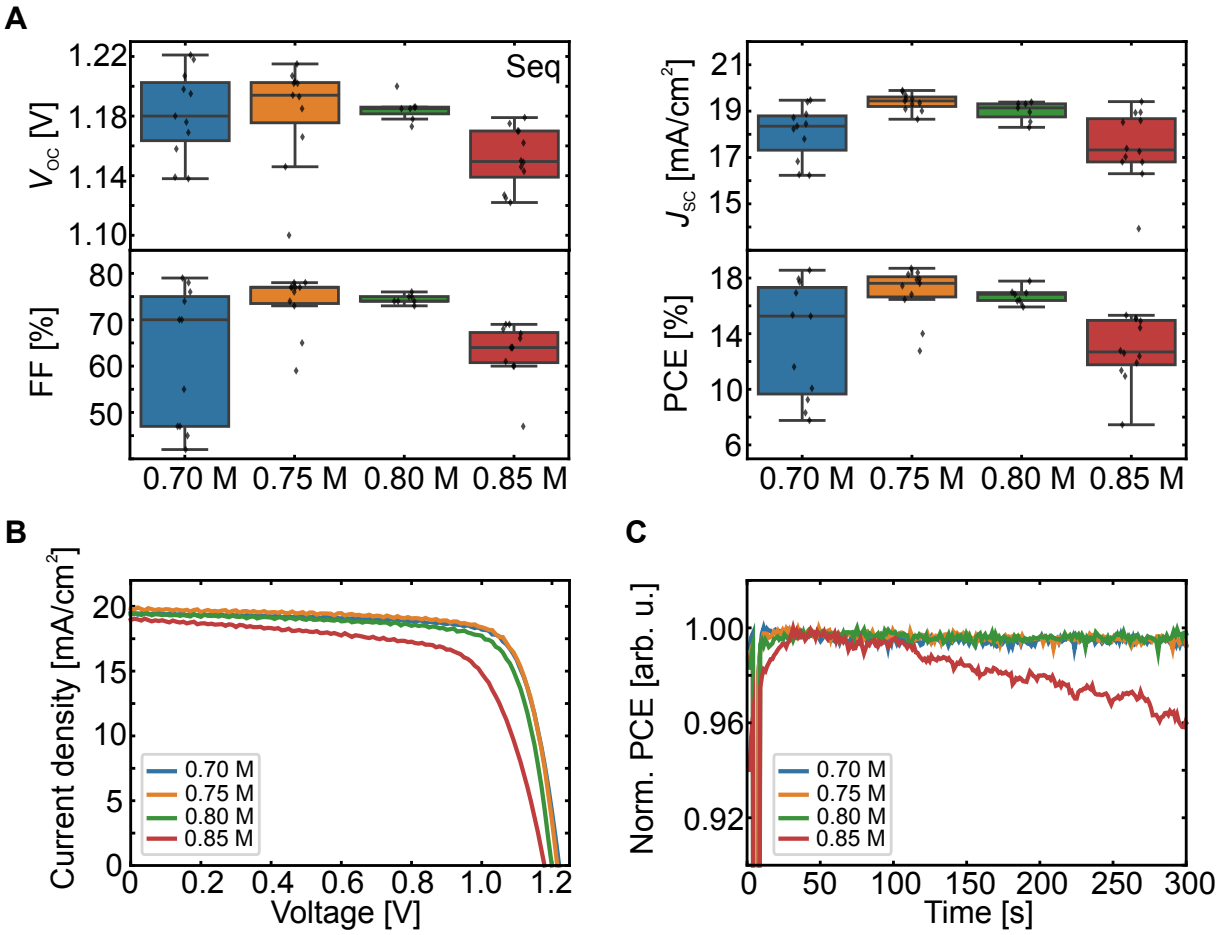

Figure A.7: **A** Statistical distribution (in total 41 devices) of the open-circuit voltage (V_{OC}), fill factor (FF), short-circuit current density (J_{SC}) and power conversion efficiency (PCE), **B** current density *versus* voltage (J–V) characteristics and **C** MPP tracking for different molarities of the organic cation solution for sequential deposition (Seq) of the inorganic scaffold. MPP: Maximum power point

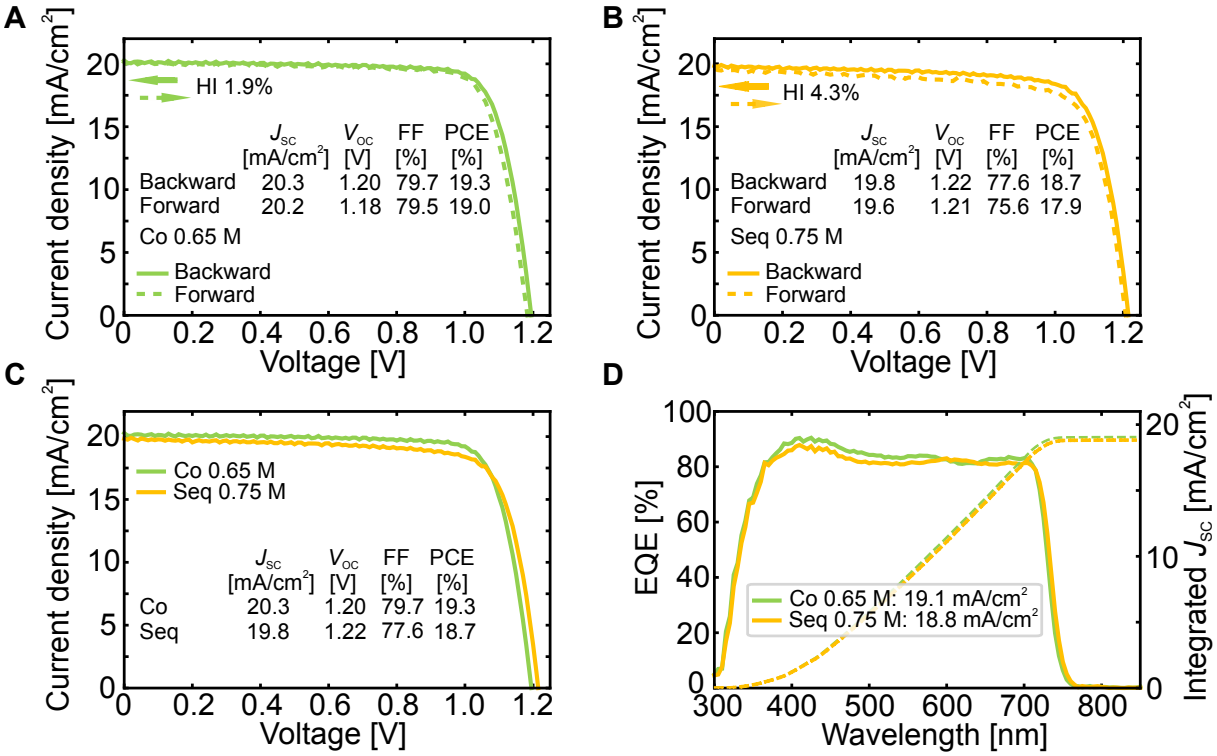

Figure A.8: Current density *versus* voltage (*J*–*V*) characteristics of the champion opaque PSCs with **A** co-deposition (Co) and **B** sequential deposition (Seq) of the inorganic scaffold with optimal molarity of the organic cation solution from Batch A. PSC: Perovskite solar cell, HI: hysteresis index.

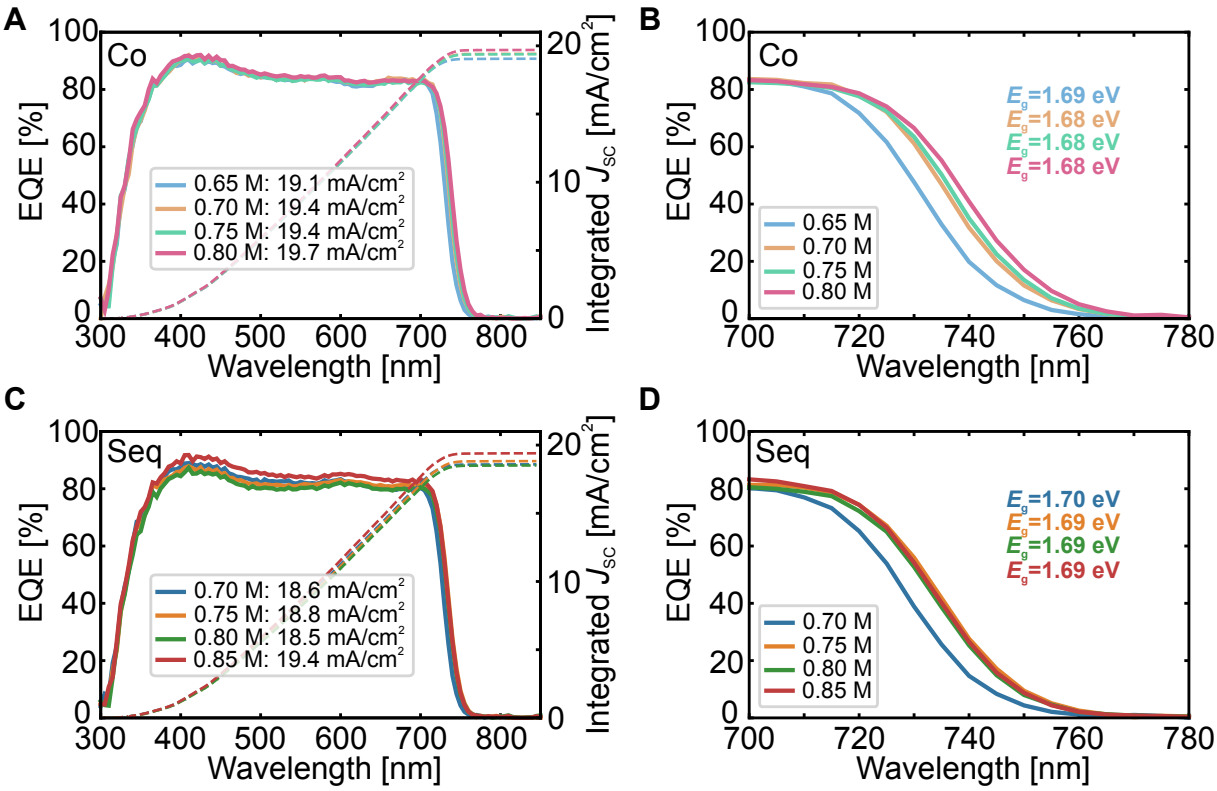

Figure A.9: EQE spectra for different molarities of the organic cation solution for **A** co-deposition (Co) and **C** sequential deposition (Seq) of the inorganic scaffold. Optical bandgap extracted from the inflection point of the EQE spectra for **B** co-deposition (Co) and **D** sequential deposition (Seq) of the inorganic scaffold. EQE: External quantum efficiency

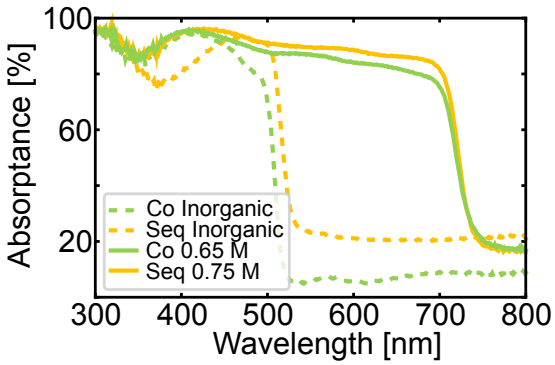

Figure A.10: Absorptance spectra for the inorganic scaffold as well as the perovskite films with optimal molarity of the organic cation solution fabricated with co-deposition (Co) and sequential deposition (Seq) of the inorganic scaffold from Batch A.

A.2 Resources, Funding, and Tools

All experimental work was performed within the laboratory infrastructure of the Light Technology Institute (LTI) at the Karlsruhe Institute of Technology (KIT), primarily provided by Prof. Dr. Ulrich W. Paetzold and Prof. Dr. Ulrich Lemmer. A detailed description of the experimental tools used for this work as well of the contributions of external collaborators can be found in **Chapter 3**. This PhD thesis and the associated research were only made possible by funding and support of various funding agencies listed in the following:

The work presented in this thesis was funded by the Initiating and Networking funding of the Helmholtz Association (Helmholtz young investigator grant of Ulrich W. Paetzold [VHNG-1148]), the Helmholtz Energy Materials Foundry, and the Helmholtz Association through program-oriented funding phase IV (Materials and Technologies for the Energy Transition, Topic 1: Photovoltaics and Wind Energy, Codes: 38.01.02, 38.01.03, 38.01.04), including the Solar Technology Acceleration Platform (Solar TAP). Additional support was provided by the Helmholtz European Partnering Program (TAPAS). Financial support was further provided by the German Federal Ministry for Economic Affairs and Climate Action (BMWK) through the projects 27Plus6 (03EE1056B) and SHAPE (03EE1123A, 03EE1123 A-E), as well as by the German Federal Ministry of Education and Research (BMBF) through the Zeitenwende Energy Security project and the national high-performance computing initiative. Additional funding was provided by the Ministry of Science and Culture in the State of Lower Saxony through the program "zukunft.niedersachsen" (project NextGenPV). Funding from the European Commission Horizon Europe research and innovation program under the NEXUS grant (101075330) is gratefully acknowledged. This work was partially funded by the European Union. Views and opinions expressed are however those of the author(s) only and do not necessarily reflect those of the European Union or RIA. Neither the European Union nor the granting authority can be held responsible for them. The NEXUS project has received funding from the European Union's Horizon Europe research and innovation program under grant agreement No. 101075330. Additional support was provided by the European Research Council under the European Union's Horizon 2020 research and innovation program (grant agreement No. 101042290 PATTERNCHEM). Parts of this work were carried out within the HyPer project, funded by the CETPartnership under the Joint Call 2023. The CETPartnership's research projects are co-funded by the European Commission (Grant Agreement No. 101069750) and the national funding organizations listed on the CETPartnership website. The BMWE funding for KIT is also listed under the funding code 03EE1222B. Support was provided by the Karlsruhe School of Optics & Photonics (KSOP) and the Ministry of Science, Research and Arts of Baden-Württemberg as part of the sustainability financing of the projects of the Excellence Initiative II. Parts of this work were carried out with the support of the Karlsruhe Nano Micro Facility (KNMF) (www.kit.edu/knmf), a Helmholtz Research Infrastructure at Karlsruhe Institute of Technology (KIT), including projects 2024-033-032255 and 2025-033-032285. Computing time was provided on the high-performance computer Noctua 2 under the project hpc-prf-patchem at the NHR Center PC2, funded by the Federal Ministry of Education and Research and the participating federal states on the basis of the resolutions of the GWK for national high-performance computing at universities

(www.nhr-verein.de/unsere-partner). This research used resources of the Advanced Light Source, which is a DOE Office of Science User Facility under contract No. DE-AC02-05CH11231. Open access funding was enabled and organized by Projekt DEAL.

Data evaluation was performed using OriginPro and Python. Molecular structures were drawn and modeled using ChemDraw, Chem3D, and Avogadro. The thesis was written in LaTeX using the Overleaf editor. Crystal structures were visualized using Mercury. AI-assisted technologies were used as writing aids to check spelling and suggest grammatical improvements. These tools were strictly used to improve readability and grammar and did not contribute to the creation of the scientific content. The author reviewed and edited all AI-based suggestions and takes full responsibility for the content of the work. The AI-based tools used include ChatGPT 5 and DeepL.

A.3 Author Contributions According to CRediT System

When publishing within collaborative research projects, *CRediT (Contributor Roles Taxonomy)* is a taxonomy that allows for a high-level description of 14 roles played by contributors in the research process. It informs about individual author contributions to the research project and reduces disagreements between collaboration partners.[269]

Table A.4: Overview of the categories used in this work to identify the contributions of different authors according to the contributor role taxonomy (CRediT) by Brand *et al.*[269]

Category	Definition
Conceptualization	Ideas; formulation or evolution of overarching research goals and aims
Methodology	Development or design of methodology; creation of models
Investigation	Conducting a research and investigation process, specifically performing the experiments, or data/evidence collection
Data Curation	Management activities to annotate (produce metadata), scrub data and maintain research data (including software code, where it is necessary for interpreting the data itself) for initial use and later reuse
Software	Programming, software development; designing computer programs; implementation of the computer code and supporting algorithms; testing of existing code components
Formal Analysis	Application of statistical, mathematical, computational, or other formal techniques to analyze or synthesize study data
Validation	Verification, whether as a part of the activity or separate, of the overall replication/reproducibility of results/experiments and other research outputs
Writing – Original Draft	Preparation, creation and/or presentation of the published work, specifically writing the initial draft (including substantive translation)
Writing – Review & Editing	Preparation, creation and/or presentation of the published work by those from the original research group, specifically critical review, commentary or revision – including pre- or post-publication stages
Visualization	Preparation, creation and/or presentation of the published work, specifically visualization/data presentation
Project Administration	Management and coordination responsibility for the research activity planning and execution
Funding Acquisition	Acquisition of the financial support for the project leading to this publication
Resources	Provision of study materials, reagents, materials, patients, laboratory samples, animals, instrumentation, computing resources, or other analysis tools
Supervision	Oversight and leadership responsibility for the research activity planning and execution, including mentorship external to the core team

A.3.1 Industrialization of Perovskite Solar Cell Fabrication: Strategies to achieve High-Throughput Vapor Deposition Processes

The research article "Industrialization of Perovskite Solar Cell Fabrication: Strategies to achieve High-Throughput Vapor Deposition Processes" was published in *EES Solar* (**2025**) by *Julian Petry (J.P.), Viktor Škorjanc (V.S.), Alexander Diercks (A.D.), Thomas Feeney (T.F.), Amedeo Morsa (A.M.), Sara Rose Kimmig (S.R.K.), Jens Baumann (J.B.), Frank Löffler (F.L.), Stefan Auschill (S.A.), Joshua Damm (J.D.), Daniel Baumann (D.B.), Felix Laufer (F.L.), Jona Kurpiers (J.K.), Michael Müller (M.M.), Lars Korte (L.K.), Steve Albrecht (S.A.), Marcel Roß (M.R.), Ulrich W. Paetzold (U.W.P.) and Paul Fassl (P.F.).*[36]

Table A.5: Author CRediT to "Industrialization of Perovskite Solar Cell Fabrication: Strategies to achieve High-Throughput Vapor Deposition Processes"

Category	Authors	Details
Conceptualization	**J.P.** (lead), A.D. J.B. F.L. U.W.P. P.F.	U.W.P. conceived the original idea which was further developed by J.P. A.D, F.L. and P.F. provided continuous feedback. J.B. provided technical insights of linear source arrangements.
Data curation	**J.P.** (lead)	
Software	**J.P.** J.D. D.B.	Software to calculate fabrication throughput was developed by J.P. with assistance of D.B. J.D. developed the GUI and improved the code.
Methodology	**J.P.** (lead), J.B., F.L., D.B.	-
Formal analysis	**J.P.** (lead)	-
Investigation	**J.P.** (lead), V.S., A.D., T.F., A.M. (KEMS), S.R.K. (ICP-OES), S.A. (sublimation experiments), J.K., M.R.	-
Validation	V.S., J.K., M.R.	V.S., J.K. and M.R. provided data of vapor flux distributions for validation.
Visualization	**J.P.** (lead), F.L.	-
Writing – original draft preparation	**J.P.** (lead)	-
Writing – review & editing	**J.P.** V.S. A.D. T.F. A.M. S.R.K. J.B. F.L. D.B. M.R. U.W.P. P.F.	All authors reviewed the manuscript.
Project administration	**J.P.** (lead), U.W.P.	-
Funding acquisition	J.K., L.K., S.A., U.W.P., P.F.	-
Supervision	M.M., L.K., S.A., M.R., U.W.P., P.F.	-

A.3.2 Particle Size Matters – Impact of Particle Size and Crucible Geometry on Sublimation Behavior of Formamidinium Iodide

The research article "Particle Size Matters – Impact of Particle Size and Crucible Geometry on Sublimation Behavior of Formamidinium Iodide" was published in *Adv. Mater. Technol.* (**2025**) by *Julian Petry* (J.P.), Alexander Diercks* (A.D.), Thomas Feeney (T.F.), Richard Thelen (R.T.), Paul Fassl (P.F.) and Ulrich W. Paetzold (U.W.P.).*
J.P. and A.D. contributed equally to this work.

Table A.6: Author CRediT to "Particle Size Matters – Impact of Particle Size and Crucible Geometry on Sublimation Behavior of Formamidinium Iodide"

Category	Authors	Details
Conceptualization	**J.P.** A.D.	J.P. conceived the original idea which was further developed with A.D
Data curation	**J.P.** A.D.	
Methodology	**J.P.** A.D. R.T.	R.T. assisted with white-light interferometry measurements
Formal analysis	**J.P.** A.D.	-
Investigation	**J.P.** A.D.	-
Visualization	**J.P.** A.D.	-
Writing – original draft preparation	**J.P.** A.D.	-
Writing – review & editing	**J.P.** A.D., T.F., R.T., P.F., U.W.P.	All authors reviewed the manuscript.
Project administration	U.W.P., P.F.	-
Funding acquisition	U.W.P., P.F.	-
Resources	R.T.	Access to the white-light interferometry measurement setup
Supervision	U.W.P., P.F.	-

A.3.3 Understanding and Exploiting Interfacial Interactions between Phosphonic Acid Functional Groups and Co-Evaporated Perovskites

The research article "Understanding and Exploiting Interfacial Interactions between Phosphonic Acid Functional Groups and Co-Evaporated Perovskites" was published in *Matter* (**2024**) by *Julian Petry (J.P.), Thomas Feeney (T.F.), Abderrezak Torche (A.T.), Dirk Hauschild (D.H.), Benjamin Hacene (B.H.), Constantin Wansorra (C.W.), Alexander Diercks (A.D.), Michelle Ernst (M.E.), Lothar Weinhardt (L.W.), Clemens Heske (C.H.), Ganna Gryn'ova (G.G.), Ulrich W. Paetzold (U.W.P.) and Paul Fassl (P.F.)*.
J.P. and T.F. contributed equally to this work.

Table A.7: Author CRediT to "Understanding and Exploiting Interfacial Interactions between Phosphonic Acid Functional Groups and Co-Evaporated Perovskites"

Category	Authors	Details
Conceptualization	**J.P.** T.F.	T.F. conceived the original idea which was further developed jointly with J.P
Data curation	**J.P.** T.F.	
Methodology	**J.P.** T.F., A.T., D.H., C.W., M.E.	J.P. and T.F. optimized the perovskite co-deposition process. A.T. and M.E. conducted all DFT calculations. D.H. and C.W. conducted all XES measurements
Formal analysis	**J.P.** T.F.	-
Investigation	**J.P.** (NMR and PSC fabrication) T.F. (PSC fabrication and all thin-film characterizations), A.T. (DFT), D.H. (XES), C.W. (XES), M.E. (DFT), A.D. (SEM), B.H. (TCSPC)	J.P. performed early stage PSC fabrication. All solar cells and their data of the original publication were fabricated and analyzed by T.F.
Visualization	**J.P.** T.F.	-
Writing – original draft preparation	**J.P.** T.F.	-
Writing – review & editing	**J.P.** T.F., A.T., D.H., B.H., C.W., A.D., M.E., L.W., C.H., G.G., U.W.P., P.F.	All authors reviewed the manuscript.
Project administration	L.W., C.H., G.G., U.W.P., P.F.	-
Funding acquisition	L.W., C.H., G.G., U.W.P., P.F.	-
Resources	D.H., C.W., L.W., C.H., G.G.	D.H., C.W., L.W. and C.H. provided access to the synchrotron beamline. G.G. provided infrastructure for DFT calculations
Supervision	L.W., C.H., G.G., U.W.P., P.F.	-

A.3.4 Benchmarking Inorganic Deposition Routes for Hybrid Two-Step Processed Perovskite Solar Cells: A Materials Perspective

The research article "Benchmarking Inorganic Deposition Routes for Hybrid Two-Step Processed Perovskite Solar Cells: A Materials Perspective" was published in *SolarRRL* (**2026**) by *Julian Petry (J.P.), Alexander Welle (A.W.), Tonghan Zhao (T.Z.), Alexander Diercks (A.D.), Raphael Pesch (R.P.), Moritz Krause (M.K.), Paul Fassl (P.F.) and Ulrich W. Paetzold (U.W.P.)*.
J.P. and R.P. contributed equally to this work.

Table A.8: Author CRediT to "Benchmarking Inorganic Deposition Routes for Hybrid Two-Step Processed Perovskite Solar Cells: A Materials Perspective"

Category	Authors	Details
Conceptualization	**J.P.** R.P., P.F., U.W.P.	-
Data curation	**J.P.** R.P., A.W., T.Z.	-
Formal analysis	**J.P.** R.P.	-
Investigation	**J.P.** R.P., A.W. (ToF-SIMS), T.Z. (GIWAXS), A.D. (SEM), R.P., M.K.	-
Visualization	**J.P.** R.P.	-
Writing – original draft preparation	**J.P.** R.P.	-
Writing – review & editing	**J.P.** R.P., A.W., T.Z., A.D., R.P., M.K., P.F., U.W.P	All authors reviewed the manuscript.
Project administration	**J.P.** R.P.	-
Funding acquisition	P.F., U.W.P.	-
Resources	P.F., U.W.P.	-
Supervision	P.F., U.W.P.	-

List of Figures

List of Tables

Bibliography

[1] IPCC. *Climate Change 2022: Mitigation of Climate Change. Contribution of Working Group III to the Sixth Assessment Report of the Intergovernmental Panel on Climate Change*. Ed. by P. Shukla et al. Cambridge, UK and New York, NY, USA: Cambridge University Press, 2022. doi: 10.1017/9781009157926. url: https://www.ipcc.ch/report/ar6/wg3/downloads/report/IPCC_AR6_WGIII_FullReport.pdf.

[2] Climate Watch / World Resources Institute. *Greenhouse Gas Emissions by Sector (1990–2022)*. 2022. url: https://www.climatewatchdata.org/ghg-emissions?breakBy=sector&end_year=2022&sectors=energy&start_year=1990 (accessed 2026-01-11).

[3] IPCC. "Summary for Policymakers". In: *Climate Change 2022: Mitigation of Climate Change. Contribution of Working Group III to the Sixth Assessment Report of the Intergovernmental Panel on Climate Change*. Ed. by P. Shukla et al. Cambridge, UK and New York, NY, USA: Cambridge University Press, 2022. doi: 10.1017/9781009157926.001. url: https://www.ipcc.ch/report/ar6/wg3/downloads/report/IPCC_AR6_WGIII_SummaryForPolicymakers.pdf.

[4] World Resources Institute. *4 Charts Explain Greenhouse Gas Emissions by Sector*. 2024. url: https://www.wri.org/insights/4-charts-explain-greenhouse-gas-emissions-countries-and-sectors (accessed 2026-01-11).

[5] L. Clarke et al. "Energy Systems". In: *Climate Change 2022: Mitigation of Climate Change. Contribution of Working Group III to the Sixth Assessment Report of the Intergovernmental Panel on Climate Change*. Ed. by P. Shukla et al. Cambridge, UK and New York, NY, USA: Cambridge University Press, 2022. Chap. 6. doi: 10.1017/9781009157926.008. url: https://www.ipcc.ch/report/ar6/wg3/downloads/report/IPCC_AR6_WGIII_Chapter06.pdf.

[6] International Renewable Energy Agency (IRENA). *Tripling renewable power and doubling energy efficiency by 2030*. 2025. url: https://www.irena.org/Digital-Report/Tripling-renewable-power-and-doubling-energy-efficiency-by-2030.

[7] International Energy Agency (IEA). *Energy security*. 2025. url: https://www.iea.org/topics/energy-security.

[8] International Energy Agency (IEA). *Strategies for affordable and fair clean energy transitions: Price shocks and affordability*. 2025. url: https://www.iea.org/reports/strategies-for-affordable-and-fair-clean-energy-transitions/price-shocks-and-affordability.

[9] European Stability Mechanism. *Renewable energy can fuel increased energy security*. 2024. url: https://www.esm.europa.eu/blog/renewable-energy-can-fuel-increased-energy-security.

[10] H. Ritchie et al. *CO_2 and Greenhouse Gas Emissions*. 2023. url: https://ourworldindata.org/co2-and-greenhouse-gas-emissions (accessed 2026-01-09).

[11] H. Ritchie. *What are the safest and cleanest sources of energy?* 2020. url: https://archive.ourworldindata.org/20251125-173858/safest-sources-of-energy.html (accessed 2026-01-09).

[12] International Energy Agency (IEA). *Global Energy Review 2025*. Paris, France: International Energy Agency, 2025. url: https://www.iea.org/reports/global-energy-review-2025 (accessed 2026-01-09).

[13] International Renewable Energy Agency (IRENA). *Renewable Power Generation Costs in 2024*. Abu Dhabi, United Arab Emirates: International Renewable Energy Agency, 2025. url: https://www.irena.org/-/media/Files/IRENA/Agency/Publication/2025/Jul/IRENA_TEC_RPGC_in_2024_2025.pdf.

[14] International Energy Agency (IEA). *Breakthrough Agenda Report 2025*. Paris, France: International Energy Agency, 2025. url: https://www.iea.org/reports/breakthrough-agenda-report-2025.

[15] H. Ritchie. *Solar photovoltaic module price*. 2025. url: https://ourworldindata.org/grapher/solar-pv-prices-vs-cumulative-capacity?country= (accessed 2026-01-09).

[16] International Renewable Energy Agency (IRENA). *Renewable Energy Statistics 2025*. Abu Dhabi, United Arab Emirates: International Renewable Energy Agency, 2025. url: https://www.irena.org/-/media/Files/IRENA/Agency/Publication/2025/Jul/IRENA_DAT_RE_Statistics_2025.pdf (accessed 2026-01-09).

[17] IEA Photovoltaic Power Systems Programme (IEA PVPS). *Snapshot of Global PV Markets 2025*. Paris, France: IEA Photovoltaic Power Systems Programme, 2025. url: https://iea-pvps.org/wp-content/uploads/2025/04/Snapshot-of-Global-PV-Markets_2025.pdf (accessed 2026-01-09).

[18] SolarPower Europe. *Global Market Outlook for Solar Power 2025*. Brussels, Belgium: SolarPower Europe, 2025. url: https://api.solarpowereurope.org/uploads/Global_Market_Outlook_2025_v1_aaebd9698b.pdf?updated_at=2025-05-05T08:46:30.243Z (accessed 2026-01-09).

[19] K. Alberi et al. "Historical and future learning for the new era of multi-terawatt photovoltaics". In: *Nat. Energy* 10 (2025), pp. 795–810. doi: 10.1038/s41560-025-01929-z.

[20] Fraunhofer Institute for Solar Energy Systems ISE and PSE Projects GmbH. *Photovoltaics Report 2025*. Freiburg, Germany: Fraunhofer Institute for Solar Energy Systems ISE, 2025. url: https://www.ise.fraunhofer.de/en/publications/studies/photovoltaics-report.html.

[21] C. Case et al. "Industrial Insights into Perovskite Photovoltaics". In: *ACS Energy Lett.* 4.11 (2019), pp. 2760–2762. doi: 10.1021/acsenergylett.9b02105.

[22] T. J. Jacobsson et al. “An open-access database and analysis tool for perovskite solar cells based on the FAIR data principles”. In: *Nat. Energy* 7.1 (2022), pp. 107–115. doi: 10.1038/s41560-021-00941-3.

[23] National Renewable Energy Laboratory (NREL). *Best Research-Cell Efficiencies*. 2025. url: https://www.nrel.gov/pv/cell-efficiency.html.

[24] T. G. Allen et al. “A Practical Efficiency Target for Perovskite/Silicon Tandem Solar Cells”. In: *ACS Energy Lett.* 10.1 (2025), pp. 238–245. doi: 10.1021/acsenergylett.4c02152.

[25] M. A. Green et al. “Solar Cell Efficiency Tables (Version 65)”. In: *Prog. Photovolt.: Res. Appl.* 33.1 (2025), pp. 3–15. doi: 10.1002/pip.3867.

[26] Longi. *34.85%! LONGi Breaks World Record for Crystalline Silicon-Perovskite Tandem Solar Cell Efficiency Again*. Web Page. 2025. url: https://www.longi.com/en/news/silicon-perovskite-tandem-solar-cells-new-world-efficiency/.

[27] S. Wang et al. “Flexible perovskite/silicon tandem solar cells with 33.6% efficiency”. In: *Nature* 649 (2026), 59–64. doi: 10.1038/s41586-025-09849-4.

[28] K. Artuk et al. “60 cm^2 perovskite/silicon tandem solar cells with an efficiency of 28.9% by homogeneous passivation”. In: *Nat. Commun.* 16 (2025), p. 63673. doi: 10.1038/s41467-025-63673-y.

[29] X. Y. Chin et al. “Interface passivation for 31.25%-efficient perovskite/silicon tandem solar cells”. In: *Science* 381.6653 (2023), pp. 59–63. doi: 10.1126/science.adg0091.

[30] L. Fang et al. “Interfacial design strategies for stable and high-performance perovskite/silicon tandem solar cells on industrial silicon cells”. In: *Nat. Commun.* 16 (2025), p. 8881. doi: 10.1038/s41467-025-64467-y.

[31] G. Yang et al. “Towards efficient, scalable and stable perovskite/silicon tandem solar cells”. In: *Nat. Photonics* 19 (2025). doi: 10.1038/s41566-025-01732-y.

[32] M. Dimitrievska et al. “Lessons from copper indium gallium sulfo-selenide solar cells for progressing perovskite photovoltaics”. In: *Nat. Energy* 11 (2026). doi: 10.1038/s41560-025-01936-0.

[33] A. N. Specified. *Oxford PV starts commercial distribution of perovskite solar modules*. pv magazine. Sept. 2024. url: https://www.pv-magazine.com/2024/09/05/oxford-pv-starts-commercial-distribution-of-perovskite-solar-modules/.

[34] Fraunhofer ISE. *Oxford PV and Fraunhofer ISE develop full-sized tandem PV module with record efficiency of 25 percent*. Fraunhofer Institute for Solar Energy Systems ISE. Sept. 2024. url: https://www.ise.fraunhofer.de/en/press-media/press-releases/2024/oxford-pv-and-fraunhofer-ise-develop-full-sized-tandem-pv-module-with-record-efficiency-of-25-percent.html.

[35] V. Shaw. *Trina Solar stellt Prototyp eines 841-Watt-Perowskit-Silizium-Tandemmoduls vor*. pv magazine. July 2025. url: https://www.pv-magazine.de/2025/06/19/trina-solar-stellt-prototyp-eines-841-watt-perowskit-silizium-tandemmoduls-vor/.

[36] J. Petry et al. "Industrialization of Perovskite Solar Cell Fabrication: Strategies to Achieve High-Throughput Vapor Deposition Processes". In: *EES Solar* 1 (2025), pp. 404–418. doi: 10.1039/D5EL00069F.

[37] Y. Vaynzof. "The Future of Perovskite Photovoltaics—Thermal Evaporation or Solution Processing?" In: *Adv Energy Mater* 10 (2020), p. 2003073. doi: 10.1002/aenm.202003073.

[38] T. Abzieher et al. "Vapor phase deposition of perovskite photovoltaics: short track to commercialization?" In: *Energy Environ. Sci.* 17.5 (2024), pp. 1645–1663. doi: 10.1039/d3ee03273f.

[39] D. B. Ritzer et al. "Upscaling of perovskite solar modules: The synergy of fully evaporated layer fabrication and all-laser-scribed interconnections". In: *Prog. Photovolt.: Res. Appl.* 30.4 (2021), pp. 360–373. doi: 10.1002/pip.3489.

[40] M. Roß et al. "Co-Evaporated Formamidinium Lead Iodide Based Perovskites with 1000 h Constant Stability for Fully Textured Monolithic Perovskite/Silicon Tandem Solar Cells". In: *Adv. Energy Mater.* 11.35 (2021). doi: 10.1002/aenm.202101460.

[41] T. Feeney et al. "High-Rate FA-Based Co-Evaporated Perovskites: Understanding Rate Limitations and Practical Considerations to Overcome Their Impact". In: *Adv. Funct. Mater.* n/a.n/a (2025), e17873. doi: 10.1002/adfm.202517873.

[42] A. Diercks et al. "Particle Size Matters – Impact of Particle Size and Crucible Geometry on Sublimation Behavior of Formamidinium Iodide". In: *Adv. Mater. Technol.* 1.3 (2025), e01549. doi: 10.1002/admt.202501549.

[43] M. A. A. Mahmoud et al. "Unveiling the complexity of co-evaporation of perovskite: Why co-evaporation might not be the optimal choice". In: *J. Mater. Chem. A* 13.48 (2025), pp. 42281–42288. doi: 10.1039/D5TA08316H.

[44] T. Abzieher et al. "From Groundwork to Efficient Solar Cells: On the Importance of the Substrate Material in Co-Evaporated Perovskite Solar Cells". In: *Adv. Funct. Mater.* 31.42 (2021), p. 2104482. doi: ARTN210448210.1002/adfm.202104482.

[45] P. Chen et al. "The Promise and Challenges of Inverted Perovskite Solar Cells". In: *Chem. Rev.* 124.19 (2024), pp. 10623–10700. doi: 10.1021/acs.chemrev.4c00073.

[46] Y. Liu et al. "Techno-economic challenges and opportunities behind the perovskite–silicon alliance". In: *Watt* 1.1 (2026), p. 1. doi: 10.1007/s44503-026-00001-5.

[47] M. Zhang et al. "Hole-selective Transparent In Situ Passivation Contacts for Efficient and Stable n–i–p Graded Perovskite/Silicon Tandem Solar Cells". In: *Adv. Mater.* 37.14 (2025), p. 2416530. doi: https://doi.org/10.1002/adma.202416530.

[48] Y. Wu et al. "Monolithic perovskite/silicon-homojunction tandem solar cell with over 22% efficiency". In: *Energy Environ. Sci.* 10.11 (2017), pp. 2472–2479. doi: 10.1039/C7EE02288C.

[49] A. J. Bett et al. “Two-terminal Perovskite silicon tandem solar cells with a high-Bandgap Perovskite absorber enabling voltages over 1.8 V”. In: *Prog. Photovolt.: Res. Appl.* 28.2 (2020), pp. 99–110. doi: https://doi.org/10.1002/pip.3208.

[50] T. Zhang et al. “Ion-modulated radical doping of spiro-OMeTAD for more efficient and stable perovskite solar cells”. In: *Science* 377.6605 (2022), pp. 495–501. doi: 10.1126/science.abo2757.

[51] R. Azmi et al. “Moisture-Resilient Perovskite Solar Cells for Enhanced Stability”. In: *Adv. Mater.* 36.12 (2024), p. 2211317. doi: https://doi.org/10.1002/adma.202211317.

[52] H. Zhu et al. “Long-term operating stability in perovskite photovoltaics”. In: *Nat. Rev. Mater.* 8.9 (2023), pp. 569–586. doi: 10.1038/s41578-023-00582-w.

[53] F. M. Rombach et al. “Lessons learned from spiro-OMeTAD and PTAA in perovskite solar cells”. In: *Energy Environ. Sci.* 14.10 (2021), pp. 5161–5190. doi: 10.1039/D1EE02095A.

[54] T. Hellmann et al. “The Electronic Structure of MAPI-Based Perovskite Solar Cells: Detailed Band Diagram Determination by Photoemission Spectroscopy Comparing Classical and Inverted Device Stacks”. In: *Adv. Energy Mater.* 10.42 (2020), p. 2002129. doi: https://doi.org/10.1002/aenm.202002129.

[55] C. Das et al. “Band Bending at Hole Transporting Layer-Perovskite Interfaces in n-i-p and in p-i-n Architecture”. In: *Solar RRL* 6.9 (2022), p. 2200348. doi: https://doi.org/10.1002/solr.202200348.

[56] D. Marongiu et al. “The role of excitons in 3D and 2D lead halide perovskites”. In: *J. Mater. Chem. C* 7.39 (2019), pp. 12006–12018. doi: 10.1039/C9TC04292J.

[57] K. Galkowski et al. “Determination of the exciton binding energy and effective masses for methylammonium and formamidinium lead tri-halide perovskite semiconductors”. In: *Energy Environ. Sci.* 9.3 (2016), pp. 962–970. doi: 10.1039/C5EE03435C.

[58] V. D’innocenzo et al. “Excitons *versus* free charges in organo-lead tri-halide perovskites”. In: *Nat. Commun.* 5.1 (2014), p. 3586. doi: 10.1038/ncomms4586.

[59] J. E. Lee et al. “Unraveling Loss Mechanisms Arising from Energy-Level Misalignment between Metal Halide Perovskites and Hole Transport Layers”. In: *Adv. Funct. Mater.* 34.30 (2024), p. 2401052. doi: 10.1002/adfm.202401052.

[60] U. Würfel et al. “Charge carrier separation in solar cells”. In: *IEEE Journal of Photovoltaics* 5.1 (2014), pp. 461–469. doi: 10.1109/JPHOTOV.2014.2363550.

[61] P. Würfel. “Frontmatter”. In: *Physics of Solar Cells*. John Wiley & Sons, Ltd, 2005. doi: 10.1002/9783527618545.fmatter. url: https://onlinelibrary.wiley.com/doi/abs/10.1002/9783527618545.fmatter.

[62] W. Shockley et al. “Detailed Balance Limit of Efficiency of pn Junction Solar Cells”. In: *J. Appl. Phys.* 32.3 (1961), pp. 510–519. doi: 10.1063/1.1736034.

[63] T. Tiedje et al. “Limiting Efficiency of Silicon Solar Cells”. In: *IEEE Trans. Electron Devices* 31.5 (1984). doi: 10.1109/T-ED.1984.21594.

[64] National Renewable Energy Laboratory (NREL). *Reference Air Mass 1.5 Spectra (Solar Spectral Irradiance)*. National Renewable Energy Laboratory, 2025. url: https://www.nrel.gov/grid/solar-resource/spectra-am1.5.

[65] R. Das Adhikari et al. “Decoding recombination dynamics in perovskite solar cells: an in-depth critical review”. In: *Chem. Soc. Rev.* 54 (8 2025), pp. 3962–4034. doi: 10.1039/D4CS01231C.

[66] C. S. J. Ponseca et al. “Mechanism of Charge Transfer and Recombination Dynamics in Organo Metal Halide Perovskites and Organic Electrodes, PCBM, and Spiro-OMeTAD: Role of Dark Carriers”. In: *Journal of the American Chemical Society* 137.51 (2015), pp. 16043–16048. doi: 10.1021/jacs.5b08770.

[67] I. Zarazua et al. “Surface Recombination and Collection Efficiency in Perovskite Solar Cells from Impedance Analysis”. In: *J. Phys. Chem. Lett.* 7.24 (2016), pp. 5105–5113. doi: 10.1021/acs.jpclett.6b02193.

[68] M. Saliba et al. “Perovskite Solar Cells: From the Atomic Level to Film Quality and Device Performance”. In: *Angew. Chem. Int. Ed.* 57.10 (2018), pp. 2554–2569. doi: https://doi.org/10.1002/anie.201703226.

[69] Y. Ko et al. “Recent Progress in Interconnection Layer for Hybrid Photovoltaic Tandems”. In: *Adv. Mater.* 32.51 (2020), p. 2002196. doi: 10.1002/adma.202002196.

[70] A. Kojima et al. “Organometal Halide Perovskites as Visible-Light Sensitizers for Photovoltaic Cells”. In: *J. Am. Chem. Soc.* 131.17 (2009), pp. 6050–6051. doi: 10.1021/ja809598r.

[71] G. Rose. *De novis quibusdam fossilibus quae in montibus Uraliis inveniuntur*. typis AG Schadii, 1839.

[72] V. M. Goldschmidt. “Die Gesetze der Krystallochemie”. In: *Naturwissenschaften* 14.21 (1926), pp. 477–485. doi: 10.1007/BF01507527.

[73] J.-W. Lee et al. “Rethinking the A cation in halide perovskites”. In: *Science* 375.6583 (2022), eabj1186. doi: 10.1126/science.abj1186.

[74] T. J. Jacobsson et al. “Goldschmidt’s Rules and Strontium Replacement in Lead Halogen Perovskite Solar Cells: Theory and Preliminary Experiments on $CH_3NH_3SrI_3$”. In: *J. Phys. Chem. C* 119.46 (2015), pp. 25673–25683. doi: 10.1021/acs.jpcc.5b06436.

[75] Z. Li et al. “Stabilizing Perovskite Structures by Tuning Tolerance Factor: Formation of Formamidinium and Cesium Lead Iodide Solid-State Alloys”. In: *Chemistry of Materials* 28.1 (2016), pp. 284–292. doi: 10.1021/acs.chemmater.5b04107.

[76] C. Otero-Martínez et al. “Fast A-site cation cross-exchange at room temperature: single-to double-and triple-cation halide perovskite nanocrystals”. In: *Angew. Chem. Int. Ed.* 61.34 (2022), e202205617. doi: 10.1002/anie.202205617.

[77] Z. Xiao et al. “Progress in Theoretical Study of Metal Halide Perovskite Solar Cell Materials”. In: *Adv. Energy Mater.* 7.22 (2017), p. 1701136. doi: 10.1002/aenm.201701136.

[78] Z. Ou et al. “Role of A-Site Cation Hydrogen Bonds in Hybrid Organic–Inorganic Perovskites: A Theoretical Insight”. In: *J. Phys. Chem. Lett.* 16.3 (2025), pp. 802–810. doi: 10.1021/acs.jpclett.4c03211.

[79] W. Li et al. “The role of ion migration, octahedral tilt, and the A-site cation on the instability of Cs1-xFAxPbI3”. In: *Nat. Commun.* 14.1 (2023), p. 8523. doi: 10.1038/s41467-023-44235-6.

[80] M. P. Hautzinger et al. “A-Site Cation Chemistry in Halide Perovskites”. In: *Chemistry of Materials* 36.21 (2024), pp. 10408–10420. doi: 10.1021/acs.chemmater.4c02043.

[81] Y. Liang et al. “Toward stabilization of formamidinium lead iodide perovskites by defect control and composition engineering”. In: *Nat. Commun.* 15.1 (2024), p. 1707. doi: 10.1038/s41467-024-46044-x.

[82] M. Saliba et al. “Cesium-containing triple cation perovskite solar cells: improved stability, reproducibility and high efficiency”. In: *Energy Environ. Sci.* 9.6 (2016), pp. 1989–1997. doi: 10.1039/C5EE03874J.

[83] W.-J. Yin et al. “Unique Properties of Halide Perovskites as Possible Origins of the Superior Solar Cell Performance”. In: *Adv. Mater.* 26.27 (2014), pp. 4653–4658. doi: 10.1002/adma.201306281.

[84] S. De Wolf et al. “Organometallic Halide Perovskites: Sharp Optical Absorption Edge and Its Relation to Photovoltaic Performance”. In: *J. Phys. Chem. Lett.* 5.6 (2014), pp. 1035–1039. doi: 10.1021/jz500279b.

[85] J. Wu et al. “A Comparison of Charge Carrier Dynamics in Organic and Perovskite Solar Cells”. In: *Adv. Mater.* 34.2 (2022), p. 2101833. doi: 10.1002/adma.202101833.

[86] J. Lim et al. “Long-range charge carrier mobility in metal halide perovskite thin-films and single crystals *via* transient photo-conductivity”. In: *Nat. Commun.* 13.1 (2022), p. 4201. doi: 10.1038/s41467-022-31569-w.

[87] M. V. Kovalenko et al. “Properties and potential optoelectronic applications of lead halide perovskite nanocrystals”. In: *Science* 358.6364 (2017), pp. 745–750. doi: 10.1126/science.aam709.

[88] W.-J. Yin et al. “Unique properties of halide perovskites as possible origins of the superior solar cell performance”. In: *Adv. Mater.* 26.27 (2014), pp. 4653–4658. doi: 10.1002/adma.201306281.

[89] R. E. Brandt et al. “Identifying defect-tolerant semiconductors with high minority-carrier lifetimes: beyond hybrid lead halide perovskites”. In: *MRS Commun.* 5.2 (2015), pp. 265–275. doi: 10.1557/mrc.2015.26.

[90] W. Gao et al. “Quasiparticle band gap of organic-inorganic hybrid perovskites: Crystal structure, spin-orbit coupling, and self-energy effects”. In: *Phys. Rev. B* 93.8 (2016), p. 085202. doi: 10.1103/PhysRevB.93.085202.

[91] L. M. Herz. “Charge-carrier mobilities in metal halide perovskites: fundamental mechanisms and limits”. In: *ACS Energy Lett.* 2.7 (2017), pp. 1539–1548. doi: 10.1021/acsenergylett.7b00276.

[92] D.-A. Park et al. “Perovskite-Inspired Materials (PIMs): Exploring Their Potential for Photovoltaic Applications”. In: *SusMat* 5.3 (2025), e70018. doi: 10.1002/sus2.70018.

[93] L. Schmidt-Mende et al. “Roadmap on organic–inorganic hybrid perovskite semiconductors and devices”. In: *APL Mater.* 9.10 (Oct. 2021), p. 109202. doi: 10.1063/5.0047616.

[94] J. Endres et al. “Valence and Conduction Band Densities of States of Metal Halide Perovskites: A Combined Experimental–Theoretical Study”. In: *J. Phys. Chem. Lett.* 7.14 (2016), pp. 2722–2729. doi: 10.1021/acs.jpclett.6b00946.

[95] H. Brune. “Epitaxial Growth of Thin Films”. In: *Surface and Interface Science: Solid-Solid Interfaces and Thin Films*. Ed. by K. Wandelt. 1st ed. Weinheim, Germany: Wiley-VCH, 2014. Chap. 20, pp. 421–491. doi: 10.1002/9783527680566.ch20.

[96] P. Du et al. “Thermal Evaporation for Halide Perovskite Optoelectronics: Fundamentals, Progress, and Outlook”. In: *Adv. Opt. Mater.* 10.4 (2022), p. 2101770. doi: 10.1002/adom.202101770.

[97] M. Kroll et al. “Insights into the evaporation behaviour of FAI: material degradation and consequences for perovskite solar cells”. In: *Sustain. Energy Fuels* 6 (2022), pp. 3230–3239. doi: 10.1039/D2SE00373B.

[98] G. Sauerbrey. “Verwendung von Schwingquarzen zur Wägung dünner Schichten und zur Mikrowägung”. In: *Zeitschrift für physik* 155.2 (1959), pp. 206–222. doi: 10.1007/BF01337937.

[99] J. Borchert et al. “Impurity Tracking Enables Enhanced Control and Reproducibility of Hybrid Perovskite Vapor Deposition”. In: *ACS Appl Mater Interfaces* 11 (2019), pp. 28851–28857. doi: 10.1021/acsami.9b07619.

[100] I. Levchuk et al. “Deciphering the Role of Impurities in Methylammonium Iodide and Their Impact on the Performance of Perovskite Solar Cells”. In: *Adv. Mater. Interfaces* 3.22 (2016), p. 1600593. doi: 10.1002/admi.201600593.

[101] K. P. S. Zanoni et al. “Photovoltaic Devices Using Sublimed Methylammonium Lead Iodide Perovskites: Long-Term Reproducible Processing”. In: *Sol. RRL* 7.7 (2023), p. 2201073. doi: 10.1002/solr.202201073.

[102] B. S. Kim et al. “Deposition Kinetics and Compositional Control of Vacuum-Processed $CH_3NH_3PbI_3$ Perovskite”. In: *J Phys Chem Lett* 11.16 (2020), pp. 6852–6859. doi: 10.1021/acs.jpclett.0c01995.

[103] T. Feeney et al. “Understanding and exploiting interfacial interactions between phosphonic acid functional groups and co-evaporated perovskites”. In: *Matter* 7 (2024), pp. 2066–2090. doi: 10.1016/j.matt.2024.02.004.

[104] J. Zhao et al. “Charge Carrier Dynamics in Co-evaporated $MAPbI_3$ with a Gradient in Composition”. In: *ACS Appl. Energy Mater.* 5.6 (2022), pp. 7049–7055. doi: 10.1021/acsaem.2c00664.

[105] J. Li et al. “Co-Evaporated $MAPbI_3$ with Graded Fermi Levels Enables Highly Performing, Scalable, and Flexible p-i-n Perovskite Solar Cells”. In: *Adv. Funct. Mater.* 31.42 (2021), p. 2103252. doi: 10.1002/adfm.202103252.

[106] A. Diercks et al. “Sequential Evaporation of Inverted $FAPbI_3$ Perovskite Solar Cells - Impact of Substrate on Crystallization and Film Formation”. In: *ACS Energy Lett* (2025), pp. 1165–1173. doi: 10.1021/acsenergylett.4c03315.

[107] J. Petry et al. “Benchmarking Inorganic Deposition Routes for Hybrid Two-Step Processed Perovskite Solar Cells: A Materials Perspective”. In: *Sol. RRL* 10.4 (2026), e202500698. doi: https://doi.org/10.1002/solr.202500698.

[108] R. Pappenberger et al. “Versatile Two-Step Process for Perovskite-Based Tandem Photovoltaics”. In: *Sol. RRL* 9.13 (2025). doi: 10.1002/solr.202500193.

[109] O. Er-raji et al. “Toward efficient and industrially compatible fully textured perovskite silicon tandem solar cells: Controlled process parameters for reliable perovskite formation”. In: *Prog. Photovolt.: Res. Appl.* 33.1 (2023), pp. 86–99. doi: 10.1002/pip.3770.

[110] M. A. A. Mahmoud et al. “Tuning Perovskite Crystal Growth Dynamics Using Additives on Textured Silicon Substrates”. In: *Sol. RRL* 8.24 (2024), p. 2400471. doi: 10.1002/solr.202400471.

[111] O. Er-raji et al. “Tailoring perovskite crystallization and interfacial passivation in efficient, fully textured perovskite silicon tandem solar cells”. In: *Joule* 8.10 (2024), pp. 2811–2833. doi: 10.1016/j.joule.2024.06.018.

[112] R. Pesch et al. “Hybrid Two-Step Inkjet-Printed Perovskite Solar Cells”. In: *Sol. RRL* 8.13 (2024), p. 2400165. doi: 10.1002/solr.202400165.

[113] V. Cimrová et al. “Formamidinium Lead Iodide Perovskite Thin Films Formed by Two-Step Sequential Method: Solvent–Morphology Relationship”. In: *Materials* 16.3 (2023), p. 1049. doi: 10.3390/ma16031049.

[114] T. Xu et al. “Stable alpha-$FAPbI_3$ via porous PbI_2 for efficient perovskite solar cells”. In: *J. Chem. Phys.* 157.19 (Nov. 2022), p. 194704. doi: 10.1063/5.0122201.

[115] L. Onsager. “THEORIES AND PROBLEMS OF LIQUID DIFFUSION”. In: *Ann. N. Y. Acad. Sci.* 46.5 (1945), pp. 241–265. doi: 10.1111/j.1749-6632.1945.tb36170.x.

[116] E. B. Watson et al. “Diffusion in solid-Earth systems”. In: *Earth Planet. Sci. Lett.* 253.3 (2007), pp. 307–327. doi: 10.1016/j.epsl.2006.11.015.

[117] O. Er-raji et al. “Insights into Perovskite Film Formation Using the Hybrid Evaporation/Spin-Coating Route: An $InSitu$ XRD Study”. In: *ACS Appl. Energy Mater.* 6.11 (2023), pp. 6183–6193. doi: 10.1021/acsaem.3c00698.

[118] P. Ahlawat et al. “A combined molecular dynamics and experimental study of two-step process enabling low-temperature formation of phase-pure $FAPbI_3$”. In: *Sci. Adv.* 7.17 (2021), eabe3326. doi: 10.1126/sciadv.abe3326.

[119] Y. Xu et al. “The Effect of Humidity upon the Crystallization Process of Two-Step Spin-Coated Organic–Inorganic Perovskites”. In: *ChemPhysChem* 17.1 (2016), pp. 112–118. doi: 10.1002/cphc.201500844.

[120] J. Li et al. “Luminescent Intermediates and Humidity-Dependent Room-Temperature Conversion of the $MAPbI_3$ Perovskite Precursor”. In: *ACS Omega* 3.10 (2018), pp. 14494–14502. doi: 10.1021/acsomega.8b01799.

[121] R. A. Nambiar et al. “Interdiffusion control in sequentially evaporated organic–inorganic perovskite solar cells”. In: *EES Sol.* 1.2 (2025), pp. 129–138. doi: 10.1039/D5EL00017C.

[122] A. Farag et al. “Evaporated Self-Assembled Monolayer Hole Transport Layers: Lossless Interfaces in p-i-n Perovskite Solar Cells”. In: *Adv. Energy Mater.* 13.8 (2023), p. 2203982. doi: 10.1002/aenm.202203982.

[123] K. B. Lohmann et al. “Solvent-Free Method for Defect Reduction and Improved Performance of p-i-n Vapor-Deposited Perovskite Solar Cells”. In: *ACS Energy Lett* 7 (2022), pp. 1903–1911. doi: 10.1021/acsenergylett.2c00865.

[124] Y. Li et al. “Wide Bandgap Interface Layer Induced Stabilized Perovskite/Silicon Tandem Solar Cells with Stability over Ten Thousand Hours”. In: *Adv. Energy Mater.* 11.48 (2021), p. 2102046. doi: 10.1002/aenm.202102046.

[125] L. Krückemeier et al. “How to Report Record Open-Circuit Voltages in Lead-Halide Perovskite Solar Cells”. In: *Adv. Energy Mater.* 10.1 (2020), p. 1902573. doi: 10.1002/aenm.201902573.

[126] J. C. Fischer et al. “GIWAXS Characterization of Metal-Organic Framework Thin Films and Heterostructures: Quantifying Structure and Orientation”. In: *Adv. Mater. Interfaces* 10.11 (2023). doi: 10.1002/admi.202202259.

[127] Z. Jiang. “GIXSGUI: a MATLAB toolbox for grazing-incidence X-ray scattering data visualization and reduction, and indexing of buried three-dimensional periodic nanostructured films”. In: *J. Appl. Crystallogr.* 48.3 (2015), pp. 917–926. doi: 10.1107/s1600576715004434.

[128] L. Bischof et al. “Quantification of thermodynamic properties for vaporisation reactions above solid Ga and In by Knudsen Effusion Mass Spectrometry”. In: *Calphad* 80 (2023), p. 102507. doi: 10.1016/j.calphad.2022.102507.

[129] J. Drowart et al. “Investigation of Inorganic Systems at High Temperature by Mass Spectrometry”. In: *Angew. Chem. Int. Edit.* 6.7 (1967), pp. 581–596. doi: 10.1002/anie.196705811.

[130] D. Kobertz et al. “Vaporization and caloric studies on lead titanate”. In: *Calphad* 46 (2014), pp. 62–79. doi: 10.1016/j.calphad.2014.02.001.

[131] G. R. Fulmer et al. “NMR Chemical Shifts of Trace Impurities: Common Laboratory Solvents, Organics, and Gases in Deuterated Solvents Relevant to the Organometallic Chemist”. In: *Organometallics* 29.9 (2010), pp. 2176–2179. doi: 10.1021/om100106e.

[132] P. Giannozzi et al. “QUANTUM ESPRESSO: a modular and open-source software project for quantumsimulations of materials”. In: *J. Phys.: Condens. Matter* 21.39 (2009), p. 395502. doi: 10.1088/0953-8984/21/39/395502.

[133] S. Grimme et al. “A consistent and accurate ab initio parametrization of density functional dispersion correction (DFT-D) for the 94 elements H-Pu”. In: *The Journal of chemical physics* 132.15 (2010). doi: 10.1063/1.3382344.

[134] T. Chen et al. “Entropy-driven structural transition and kinetic trapping in formamidinium lead iodide perovskite”. In: *Sci. Adv.* 2.10 (2016), e1601650. doi: 10.1126/sciadv.1601650.

[135] M Blum et al. “Solid and liquid spectroscopic analysis (SALSA)–a soft x-ray spectroscopy endstation with a novel flow-through liquid cell”. In: *Rev. Sci. Instrum.* 80.12 (2009). doi: 10.1063/1.3257926.

[136] O. Fuchs et al. “High-resolution, high-transmission soft x-ray spectrometer for the study of biological samples”. In: *Rev. Sci. Instrum.* 80.6 (2009). doi: 10.1063/1.3133704.

[137] L. Weinhardt et al. “Sulfate speciation analysis using soft X-ray emission spectroscopy”. In: *Anal. Chem.* 93.23 (2021), pp. 8300–8308. doi: 10.1021/acs.analchem.1c01187.

[138] A. Diercks et al. “Particle Size Matters – Impact of Particle Size and Crucible Geometry on Sublimation Behavior of Formamidinium Iodide”. In: *Adv. Mater. Technol.* n/a.n/a (2025), e01549. doi: 10.1002/admt.202501549.

[139] E. Aydin et al. “Pathways toward commercial perovskite/silicon tandem photovoltaics”. In: *Science* 383.6679 (2024), eadh3849. doi: 10.1126/science.adh3849.

[140] F. E. Subhan et al. “Optical optimization of double-side-textured monolithic perovskite–silicon tandem solar cells for improved light management”. In: *RSC Adv.* 10, (2020), pp. 26631–26638. doi: 10.1039/d0ra04634e.

[141] M. De Bastiani et al. “Efficient bifacial monolithic perovskite/silicon tandem solar cells via bandgap engineering”. In: *Nat. Energy* 6, (2021), pp. 167–175. doi: 10.1038/s41560-020-00756-8.

[142] F. Gota et al. “Energy yield modelling of textured perovskite/silicon tandem photovoltaics with thick perovskite top cells”. In: *Opt. Express* 30, (2022), p. 14172. doi: 10.1364/oe.447069.

[143] W. Qarony et al. “Influence of Perovskite Interface Morphology on the Photon Management in Perovskite/Silicon Tandem Solar Cells”. In: *ACS Appl. Mater. Interfaces* 12, (2020), pp. 15080–15086. doi: 10.1021/acsami.9b21985.

[144] A. S. Subbiah et al. “High-Performance Perovskite Single-Junction and Textured Perovskite/Silicon Tandem Solar Cells via Slot-Die-Coating”. In: *ACS Energy Lett.* 5, (2020), pp. 3034–3040. doi: 10.1021/acsenergylett.0c01297.

[145] F. H. Isikgor et al. “Concurrent cationic and anionic perovskite defect passivation enables 27.4% perovskite/silicon tandems with suppression of halide segregation”. In: *Joule* 5, (2021), pp. 1566–1586. doi: 10.1016/j.joule.2021.05.013.

[146] F. Sahli et al. “Fully textured monolithic perovskite/silicon tandem solar cells with 25.2% power conversion efficiency”. In: *Nat. Mater.* 17.9 (2018), pp. 820–826. doi: 10.1038/s41563-018-0115-4.

[147] M. Jošt et al. “21.6%-Efficient Monolithic Perovskite/Cu(In,Ga)Se2 Tandem Solar Cells with Thin Conformal Hole Transport Layers for Integration on Rough Bottom Cell Surfaces”. In: *ACS Energy Lett.* 4.2 (2019), pp. 583–590. doi: 10.1021/acsenergylett.9b00135.

[148] A. Farag et al. “Mitigation of Open-Circuit Voltage Losses in Perovskite Solar Cells Processed over Micrometer-Sized-Textured Si Substrates”. In: *Adv. Funct. Mater.* 33.3 (2023), p. 2210758. doi: 10.1002/adfm.202210758.

[149] F. U. Kosasih et al. “Thermal evaporation and hybrid deposition of perovskite solar cells and mini-modules”. In: *Joule* 6 (2022), pp. 2692–2734. doi: 10.1016/j.joule.2022.11.004.

[150] A. Paliwal et al. “Fully vacuum-deposited perovskite solar cells in substrate configuration”. In: *Matter* 6.10 (2023), pp. 3499–3508. doi: 10.1016/j.matt.2023.07.011.

[151] L. Gil-Escrig et al. “Fully Vacuum-Processed Perovskite Solar Cells on Pyramidal Microtextures”. In: *Sol. RRL* 5 (2021). doi: 10.1002/solr.202000553.

[152] H. Li et al. “Sequential Vacuum-Evaporated Perovskite Solar Cells with More than 24% Efficiency”. In: *Sci Adv* 8 (28 2022). doi: 10.1126/sciadv.abo7422.

[153] N. Li et al. “Optimal perovskite vapor partitioning on textured silicon for high-stability tandem solar cells”. In: *Science* 390.6779 (2025), eadz3698. doi: 10.1126/science.adz3698.

[154] V. Škorjanc et al. “CsCl seed layer homogenizes co-evaporated perovskite growth for high-efficiency fully textured perovskite-silicon tandem solar cells”. In: *arXiv* (2025). doi: 10.48550/arXiv.2511.23004.

[155] Y. Liu et al. “Cost effectivities analysis of perovskite solar cells: will it outperform crystalline silicon ones?” In: *Nano-Micro Lett.* 17.1 (2025), p. 219. doi: 10.1007/s40820-025-01744-x.

[156] N. Bhati et al. “Techno-economic analysis framework for perovskite solar module production at various manufacturing capacities”. In: *Renewable Energy* 256 (2026), p. 123752. doi: https://doi.org/10.1016/j.renene.2025.123752.

[157] M. Piot et al. “Fast Coevaporation of 1 mum Thick Perovskite Solar Cells”. In: *ACS Energy Lett.* 8.11 (2023), pp. 4711–4713. doi: 10.1021/acsenergylett.3c01724.

[158] H. A. Dewi et al. “Accelerated MAPbI Co-evaporation: Productivity Gains without Compromising Performance”. In: *ACS Energy Lett.* 9.9 (2024), pp. 4319–4322. doi: 10.1021/acsenergylett.4c01597.

[159] M. Jung et al. “Perovskite precursor solution chemistry: from fundamentals to photovoltaic applications”. In: *Chem Soc Rev* 48.7 (2019), pp. 2011–2038. doi: 10.1039/c8cs00656c.

[160] M. Roß et al. “Revealing the Role of Methylammonium Iodide Purity on the Vapor-Phase Deposition Process of Perovskites”. In: *Sol. RRL* 6.10 (2022), p. 2200500. doi: 10.1002/solr.202200500.

[161] M. J. Baekbo et al. “Deposition of methylammonium iodide *via* evaporation - combined kinetic and mass spectrometric study”. In: *RSC Adv.* 8.52 (2018), pp. 29899–29908. doi: 10.1039/c8ra04851g.

[162] A. Latini et al. “A study on the nature of the thermal decomposition of methylammonium lead iodide perovskite, $CH_3NH_3PbI_3$: an attempt to rationalise contradictory experimental results”. In: *Sustain. Energy Fuels* 1.6 (2017), pp. 1351–1357. doi: 10.1039/c7se00114b.

[163] B. Conings et al. “Intrinsic thermal instability of methylammonium lead trihalide perovskite”. In: *Adv. Energy Mater.* 5.15 (2015), p. 1500477. doi: 10.1002/aenm.201500477.

[164] M. Wang et al. “Stable and Efficient Methylammonium-, Cesium-, and Bromide-Free Perovskite Solar Cells by In-Situ Interlayer Formation”. In: *Adv. Funct. Mater.* 31.7 (2020), p. 2007520. doi: 10.1002/adfm.202007520.

[165] B. Conings et al. “Intrinsic Thermal Instability of Methylammonium Lead Trihalide Perovskite”. In: *Adv Energy Mater* 5 (2015). doi: 10.1002/aenm.201500477.

[166] W. T. M. Van Gompel et al. “Degradation of the Formamidinium Cation and the Quantification of the Formamidinium–Methylammonium Ratio in Lead Iodide Hybrid Perovskites by Nuclear Magnetic Resonance Spectroscopy”. In: *J. Phys. Chem. C* 122.8 (2018), pp. 4117–4124. doi: 10.1021/acs.jpcc.7b09805.

[167] M. J. Radke et al. “Monte Carlo simulation of a Knudsen effusion mass spectrometer sampling system”. In: *Rapid Commun. Mass Spectrom.* 31.12 (2017), pp. 1041–1046. doi: 10.1002/rcm.7873.

[168] R. A. Kerner et al. “Analytical Evaluation of Lead Iodide Precursor Impurities Affecting Halide Perovskite Device Performance”. In: *ACS Appl. Energy Mater.* 6.1 (2022), pp. 295–301. doi: 10.1021/acsaem.2c02842.

[169] H. Li et al. “Sequential vacuum-evaporated perovskite solar cells with more than 24% efficiency”. In: *Sci. Adv.* 8.28 (2022), eabo7422. doi: 10.1126/sciadv.abo7422.

[170] M. Piot et al. “Vacuum Deposition of Triple-Halide Wide-Bandgap Perovskites Enabled by Sublimation of Mixed Organic-Halide Pellets”. In: *ACS Mater. Lett.* 7.11 (2025), pp. 3692–3698. doi: 10.1021/acsmaterialslett.5c01161.

[171] D. P. McMeekin et al. “A mixed-cation lead mixed-halide perovskite absorber for tandem solar cells”. In: *Science* 351.6269 (2016), pp. 151–5. doi: 10.1126/science.aad5845.

[172] O. A. Syzgantseva et al. “Stabilization of the Perovskite Phase of Formamidinium Lead Triiodide by Methylammonium, Cs, and/or Rb Doping”. In: *J. Phys. Chem. Lett.* 8.6 (2017), pp. 1191–1196. doi: 10.1021/acs.jpclett.6b03014.

[173] M. Saliba et al. “Cesium-containing triple cation perovskite solar cells: improved stability, reproducibility and high efficiency”. In: *Energy Environ. Sci.* 9.6 (2016), pp. 1989–1997. doi: 10.1039/c5ee03874j.

[174] R. Pesch et al. “Efficient Perovskite/Silicon Tandem Solar Cells Using Hybrid Two-Step Inkjet Printing with Edge Isolation Precision”. In: *Small Sci.* (2025), e202500362. doi: 10.1002/smsc.202500362.

[175] W. Haynes. *CRC Handbook of Chemistry and Physics*. CRC Press, 2016. doi: 10.1201/9781315380476.

[176] C. W. Bale et al. “FactSage thermochemical software and databases, 2010–2016”. In: *Calphad* 54 (2016), pp. 35–53. doi: 10.1016/j.calphad.2016.05.002.

[177] M. M. Tavakoli et al. “Multilayer evaporation of MAFAPbI$_{3-x}$Cl$_x$ for the fabrication of efficient and large-scale device perovskite solar cells”. In: *J Phys D Appl Phys* 52 (2019), p. 034005. doi: 10.1088/1361-6463/aaebf1.

[178] H. Li et al. “Molten Salt Strategy for Reproducible Evaporation of Efficient Perovskite Solar Cells”. In: *Adv Funct Mater* 33 (2023), p. 2211232. doi: 10.1002/adfm.202211232.

[179] J. S. Zhao et al. “Charge Carrier Dynamics in Co-evaporated MAPbI with a Gradient in Composition”. In: *ACS Appl. Energy Mater.* 5.6 (2022), pp. 7049–7055. doi: 10.1021/acsaem.2c00664.

[180] X. Luo et al. “Efficient Perovskite/Silicon Tandem Solar Cells on Industrially Compatible Textured Silicon”. In: *Adv. Mater.* 35.9 (2023), p. 2207883. doi: 10.1002/adma.202207883.

[181] A. Z. Afshord et al. “Efficient and Stable Inverted Wide-Bandgap Perovskite Solar Cells and Modules Enabled by Hybrid Evaporation-Solution Method”. In: *Adv. Funct. Mater.* 33.31 (2023), p. 2301695. doi: 10.1002/adfm.202301695.

[182] M. Roß et al. “Co-Evaporated p-i-n Perovskite Solar Cells beyond 20% Efficiency: Impact of Substrate Temperature and Hole-Transport Layer”. In: *ACS Appl Mater Interfaces* 12 (2020), pp. 39261–39272. doi: 10.1021/acsami.0c10898.

[183] J. Zhou et al. “Highly efficient and stable perovskite solar cells *via* a multifunctional hole transporting material”. In: *Joule* 8 (2024), pp. 1691–1706. doi: 10.1016/j.joule.2024.02.019.

[184] InfoLink Consulting. *Rectangular module: Trends and prospects*. 2024. url: https://www.infolink-group.com/energy-article/solar-topic-trends-prospects-for-rectangular-module.

[185] Z. Wu et al. “Scalable Two-Step Production of High-Efficiency Perovskite Solar Cells and Modules”. In: *Sol. RRL* 7.1 (2023), p. 2200571. doi: 10.1002/solr.202200571.

[186] J. Liu et al. “Perovskite/silicon tandem solar cells with bilayer interface passivation”. In: *Nature* 635.8039 (2024), pp. 596–603. doi: 10.1038/s41586-024-07997-7.

[187] O. Er-raji et al. “Coating dynamics in two-step hybrid evaporated/blade-coated perovskites for scalable fully-textured perovskite/silicon tandem solar cells”. In: *EES Sol.* 1.3 (2025), pp. 419–430. doi: 10.1039/D5EL00073D.

[188] N. Rodkey et al. “Incremental Feeding of Perovskite Powders: Angstrom-Precision Growth for Single-Source Solar Cell Fabrication”. In: *Adv Eng Mater* 26 (2024). doi: 10.1002/adem.202400636.

[189] E. Pérez-Gutiérrez et al. “Control of the Morphology and Crystallinity of a PbI_2 Layer for Large-Area Perovskite Films Prepared by Close Space Sublimation”. In: *ACS Appl. Energy Mater.* 1.8 (2018), pp. 3843–3849. doi: 10.1021/acsaem.8b00610.

[190] Q. Guo et al. “The growth of a $CH_3NH_3PbI_3$ thin film using simplified close space sublimation for efficient and large dimensional perovskite solar cells”. In: *Energy Environ. Sci.* 9.4 (2016), pp. 1486–1494. doi: 10.1039/c5ee03620h.

[191] G. J. Zhang et al. “Ultrafast Growth of High-Quality CsFAPb(Br I) Thin Films Achieved Using Super-Close-Space Sublimation”. In: *ACS Appl. Energy Mater.* 5.5 (2022), pp. 5797–5803. doi: 10.1021/acsaem.2c00132.

[192] C. Y. Duan et al. “Oriented Growth for Efficient and Scalable Perovskite Solar Cells by Vapor-Solid Reaction”. In: *Adv. Funct. Mater.* 34.21 (2024), p. 2313435. doi: 10.1002/adfm.202313435.

[193] T. Abzieher et al. “Continuous flash sublimation of inorganic halide perovskites: overcoming rate and continuity limitations of vapor deposition”. In: *J. Mater. Chem. A* 12.14 (2024), pp. 8405–8419. doi: 10.1039/d3ta05881f.

[194] C. Camus et al. *Going beyond Alchemy: In-situ Analysis of Perovskite Growth by Optical Reflectance*. Conference Paper. 2020. doi: 10.1109/PVSC45281.2020.9300415.

[195] N. Rezaei-Hartmann et al. *Unveiling the Chemistry: A Dive into Wet Chemical Perovskite Thin Film Creation Revealed by Spectral in-situ Reflectance*. Conference Paper. 2024. doi: 10.1109/PVSC57443.2024.10749151.

[196] V. Held et al. “Evolution of Defects, Morphology, and Strain during FAMAPbI(3) Perovskite Vacuum Deposition: Insights from $InSitu$ Photoluminescence and X-ray Scattering”. In: *ACS Appl. Mater. Interfaces* 16.27 (2024), pp. 35723–35731. doi: 10.1021/acsami.4c04095.

[197] V. Held et al. “Evolution of Structure and Optoelectronic Properties during Halide Perovskite Vapor Deposition”. In: *J Phys Chem Lett* 13 (2022), pp. 11905–11912. doi: 10.1021/acs.jpclett.2c03422.

[198] B. Hacene et al. “Intensity Dependent Photoluminescence Imaging for In-Line Quality Control of Perovskite Thin Film Processing”. In: *Adv. Mater. Technol.* 9.11 (2023), p. 2301279. doi: 10.1002/admt.202301279.

[199] F. Laufer et al. “Process Insights into Perovskite Thin-Film Photovoltaics from Machine Learning with $InSitu$ Luminescence Data”. In: *Sol. RRL* 7.7 (2023), p. 2201114. doi: 10.1002/solr.202201114.

[200] R. E. Kumar et al. “Opportunities for machine learning to accelerate halide-perovskite commercialization and scale-up”. In: *Matter* 5.5 (2022), pp. 1353–1366. doi: 10.1016/j.matt.2022.04.016.

[201] K. L. Heinze et al. “Structural Evolution of Sequentially Evaporated (Cs,FA)Pb(I,Br) Perovskite Thin Films $via\ InSitu$ X-Ray Diffraction”. In: *Phys. Status Solidi A* 221.3 (2024), p. 2300690. doi: 10.1002/pssa.202300690.

[202] P. Pistor et al. “Monitoring the Phase Formation of Coevaporated Lead Halide Perovskite Thin Films by $InSitu$ X-ray Diffraction”. In: *J. Phys. Chem. Lett.* 5.19 (2014), pp. 3308–12. doi: 10.1021/jz5017312.

[203] M. Hull et al. “Prospective techno-economic analysis of 4T and 2T perovskite on silicon tandem photovoltaic modules at GW-scale production”. In: *Sol. RRL* 7.23 (2023), p. 2300503. doi: 10.1002/solr.202300503.

[204] L. Mao et al. “Fully Textured, Production-Line Compatible Monolithic Perovskite/Silicon Tandem Solar Cells Approaching 29% Efficiency”. In: *Adv. Mater.* 34.40 (2022), p. 2206193. doi: 10.1002/adma.202206193.

[205] J. Vollbrecht et al. “Less is more: Enabling Solvent-Free Fabrication of Perovskite Solar Cells via Thermal Evaporation of Ultrathin Self-Assembled Monolayers”. In: *Sol. RRL* 9.17 (2025), p. 2500429. doi: 10.1002/solr.202500429.

[206] O. Er-raji et al. “Coating dynamics in two-step hybrid evaporated/blade-coated perovskites for scalable fully-textured perovskite/silicon tandem solar cells”. In: *EES Sol.* 1.3 (2025), pp. 419–430. doi: 10.1039/D5EL00073D.

[207] Z. Zhang et al. “Progress on Inkjet Printing Technique for Perovskite Films and Their Optoelectronic and Optical Applications”. In: *ACS Photonics* 10.10 (2023), pp. 3435–3450. doi: 10.1021/acsphotonics.3c00897.

[208] K. Geistert et al. “Controlling Thin Film Morphology Formation during Gas Quenching of Slot-Die Coated Perovskite Solar Modules”. In: *ACS Appl. Mater. Interfaces* 15.45 (2023), pp. 52519–52529. doi: 10.1021/acsami.3c11923.

[209] C. Teixeira et al. “Fabrication of low-cost and flexible perovskite solar cells by slot-die coating for indoor applications”. In: *Mater. Adv.* 4.17 (2023), pp. 3863–3873. doi: 10.1039/D3MA00285C.

[210] K. Geistert et al. “Spatially Regulated Gas Flow Control for Batch-Drying of Large Area Slot-Die-Coated Perovskite Thin Films”. In: *Adv. Energy Mater.* 15.30 (2025), p. 2500923. doi: 10.1002/aenm.202500923.

[211] J. Ihrenberger et al. “Solution-Free Growth of CsPbBr3 Perovskite Films Using a Fast and Scalable Close Space Sublimation Method”. In: *Cryst. Growth Des.* 24.13 (2024), pp. 5542–5548. doi: 10.1021/acs.cgd.4c00249.

[212] N. Rodkey et al. “Close-Space Sublimation as a Scalable Method for Perovskite Solar Cells”. In: *ACS Energy Lett.* 9.3 (2024), pp. 927–933. doi: 10.1021/acsenergylett.3c02794.

[213] I. Gomar-Fernández et al. “Large-area close-space sublimation enables the fabrication of efficient and stable perovskite solar cells”. In: *EES Sol.* 1.6 (2025), pp. 1126–1134. doi: 10.1039/D5EL00145E.

[214] A. G. Kuba et al. “Bandgap Tunable Two-Step Vapor-Deposited Perovskite Absorbers for Perovskite-Silicon Tandem Solar Cells”. In: *ACS Energy Lett.* 0.0 (2026). doi: 10.1021/acsenergylett.6c00156.

[215] M. A. Scarpulla et al. “CdTe-based thin film photovoltaics: Recent advances, current challenges and future prospects”. In: *Sol. Energy Mater. Sol. Cells* 255 (2023), p. 112289. doi: https://doi.org/10.1016/j.solmat.2023.112289.

[216] Z. Xing et al. “Atomic layer deposition of metal oxides in perovskite solar cells: present and future”. In: *Small Methods* 4.12 (2020), p. 2000588. doi: 10.1002/smtd.202000588.

[217] L. Hoffmann et al. “Spatial Atmospheric Pressure Atomic Layer Deposition of Tin Oxide as an Impermeable Electron Extraction Layer for Perovskite Solar Cells with Enhanced Thermal Stability”. In: *ACS Appl. Mater. Interfaces* 10.6 (2018), pp. 6006–6013. doi: 10.1021/acsami.7b17701.

[218] A.-F. Castro-Méndez et al. “Tailoring Interface Energies *via* Phosphonic Acids to Grow and Stabilize Cubic $FAPbI_3$ Deposited by Thermal Evaporation”. In: *J. Am. Chem. Soc.* 146.27 (2024), pp. 18459–18469. doi: 10.1021/jacs.4c03911.

[219] A. Al-Ashouri et al. “Conformal monolayer contacts with lossless interfaces for perovskite single junction and monolithic tandem solar cells”. In: *Energy Environ. Sci.* 12.11 (2019), pp. 3356–3369. doi: 10.1039/C9EE02268F.

[220] A. Al-Ashouri et al. “Monolithic perovskite/silicon tandem solar cell with >29% efficiency by enhanced hole extraction”. In: *Science* 370.6522 (2020), pp. 1300–1309. doi: 10.1126/science.abd4016.

[221] S. A. Paniagua et al. “Phosphonic Acids for Interfacial Engineering of Transparent Conductive Oxides”. In: *Chem. Rev.* 116.12 (2016), pp. 7117–7158. doi: 10.1021/acs.chemrev.6b00061.

[222] Y. Gao et al. “Rethinking the Role of Excess/Residual Lead Iodide in Perovskite Solar Cells”. In: *Adv. Funct. Mater.* 33.26 (2023), p. 2215171. doi: 10.1002/adfm.202215171.

[223] R. Singh et al. “Danger in the Dark: Stability of Perovskite Solar Cells with Varied Stoichiometries and Morphologies Stressed at Various Conditions”. In: *ACS Appl. Mater. Interfaces* 16.21 (2024), pp. 27450–27462. doi: 10.1021/acsami.4c04350.

[224] T. J. Jacobsson et al. “Unreacted PbI_2 as a Double-Edged Sword for Enhancing the Performance of Perovskite Solar Cells”. In: *J. Am. Chem. Soc.* 138.32 (2016), pp. 10331–10343. doi: 10.1021/jacs.6b06320.

[225] F. Ren et al. “Impacts of PbI_2 on high-efficiency perovskite solar cells: exploring intercalation orientations and defects”. In: *J. Mater. Chem. C* 11.39 (2023), pp. 13281–13289. doi: 10.1039/D3TC02770H.

[226] C. Kamal et al. “Coupling Methylammonium and Formamidinium Cations with Halide Anions: Hybrid Orbitals, Hydrogen Bonding, and the Role of Dynamics”. In: *J. Phys. Chem. C* 125.46 (2021), pp. 25917–25926. doi: 10.1021/acs.jpcc.1c08932.

[227] Y. Fu et al. “Stabilization of the metastable lead iodide perovskite phase *via* surface functionalization”. In: *Nano Lett.* 17.7 (2017), pp. 4405–4414. doi: 10.1021/acs.nanolett.7b01500.

[228] D. H. Fabini et al. “Reentrant structural and optical properties and large positive thermal expansion in perovskite formamidinium lead iodide”. In: *Angew. Chem.* 128.49 (2016), pp. 15618–15622. doi: 10.1002/anie.201609538.

[229] T. Chen et al. “Entropy-driven structural transition and kinetic trapping in formamidinium lead iodide perovskite”. In: *Sci. Adv.* 2.10 (2016), e1601650. doi: 10.1126/sciadv.1601650.

[230] Z. Zheng et al. “Development of formamidinium lead iodide-based perovskite solar cells: efficiency and stability”. In: *Chem. Sci.* 13.8 (2022), pp. 2167–2183. doi: 10.1039/D1SC04769H.

[231] A. Al-Ashouri et al. “Wettability Improvement of a Carbazole-Based Hole-Selective Monolayer for Reproducible Perovskite Solar Cells”. In: *ACS Energy Lett.* 8.2 (2023), pp. 898–900. doi: 10.1021/acsenergylett.2c02629.

[232] M. Krause. “Strategies to Increase Fabrication Throughput for Perovskite Absorbers Using Hybrid Deposition Methods”. Master’s thesis. Karlsruhe, Germany: Karlsruhe Institute of Technology, May 2025.

[233] Y. Hoppe. “Bandgap Engineering of Hybrid-Deposited Perovskite Thin Films towards Triple-Junction Applications”. Master’s thesis. Karlsruhe, Germany: Karlsruhe Institute of Technology, Aug. 2025.

[234] A. Mocanu. “Engineering Wide-Bandgape Perovskite Absorbers for Multi-Junction Solar Cells”. Master’s thesis. Karlsruhe, Germany: Karlsruhe Institute of Technology, Nov. 2025.

[235] L. Gil-Escrig et al. “Vacuum Deposited Triple-Cation Mixed-Halide Perovskite Solar Cells”. In: *Adv. Energy Mater.* 8.14 (2018). doi: 10.1002/aenm.201703506.

[236] T. Abzieher et al. “Efficient All-Evaporated pin-Perovskite Solar Cells: A Promising Approach Toward Industrial Large-Scale Fabrication”. In: *IEEE Journal of Photovoltaics* 9.5 (2019), pp. 1249–1257. doi: 10.1109/jphotov.2019.2920727.

[237] C. Momblona et al. “Efficient methylammonium lead iodide perovskite solar cells with active layers from 300 to 900 nm”. In: *APL Mater.* 2.8 (2014). doi: 10.1063/1.4890056.

[238] P. S. Schulze et al. “Perovskite hybrid evaporation/spin coating method: From band gap tuning to thin film deposition on textures”. In: *Thin Solid Films* 704 (2020), p. 137970. doi: 10.1016/j.tsf.2020.137970.

[239] L. Cojocaru et al. “Detailed Investigation of Evaporated Perovskite Absorbers with High Crystal Quality on Different Substrates”. In: *ACS Appl. Mater. Interfaces* 10.31 (2018), pp. 26293–26302. doi: 10.1021/acsami.8b07999.

[240] Z. Liu et al. “Strained heterojunction enables high-performance, fully textured perovskite/silicon tandem solar cells”. In: *Joule* 8.10 (2024), pp. 2834–2850. doi: 10.1016/j.joule.2024.06.015.

[241] E. C. Pettit et al. “Controlling Preferred Grain Orientation in Vapor-Deposited Metal-Halide Perovskite Thin Films”. In: *J. Phys. Chem. C* 129.23 (2025), pp. 10643–10651. doi: 10.1021/acs.jpcc.5c00165.

[242] Q. Luo et al. “Combined evaporation-solution methodology for high-efficiency perovskite solar cells with exceptional reproducibility”. In: *J. Mater. Chem. A* (2025). doi: 10.1039/d5ta03304g.

[243] P. Fassl et al. “Fractional deviations in precursor stoichiometry dictate the properties, performance and stability of perovskite photovoltaic devices”. In: *Energy Environ. Sci.* 11.12 (2018), pp. 3380–3391. doi: 10.1039/C8EE01136B.

[244] J. A. Steele et al. “How to GIWAXS: Grazing Incidence Wide Angle X-Ray Scattering Applied to Metal Halide Perovskite Thin Films”. In: *Adv. Energy Mater.* 13.27 (2023). doi: 10.1002/aenm.202300760.

[245] W. Lee et al. “Spin–orbit effects on the electronic and optical properties of lead iodide”. In: *Appl. Phys. Lett.* 122.21 (May 2023), p. 212110. doi: 10.1063/5.0146397.

[246] K. Meng et al. “$InSitu$ Observation of Crystallization Dynamics and Grain Orientation in Sequential Deposition of Metal Halide Perovskites”. In: *Adv. Funct. Mater.* 29.35 (2019). doi: 10.1002/adfm.201902319.

[247] T. M. Brenner et al. “Conversion of single crystalline PbI_2 to $CH_3NH_3PbI_3$: Structural relations and transformation dynamics”. In: *Chemistry of Materials* 28.18 (2016), pp. 6501–6510. doi: 10.1021/acs.chemmater.6b01747.

[248] S. Kumar et al. “Topotactic, vapor-phase, $InSitu$ monitored formation of ultrathin, phase-pure 2D-on-3D halide perovskite surfaces”. In: *ACS Appl. Mater. Interfaces* 15.19 (2023), pp. 23908–23921. doi: 10.1021/acsami.3c01881.

[249] F. Battran et al. “Investigation of Additive-Driven Film Formation and Performance in Hybrid Two-Step Perovskite Solar Cells”. In: *Sol. RRL* 9.23 (2025), e202500630. doi: 10.1002/solr.202500630.

[250] W. Soltanpoor et al. “Hybrid Vapor-Solution Sequentially Deposited Mixed-Halide Perovskite Solar Cells”. In: *ACS Appl. Energy Mater.* 3.9 (2020), pp. 8257–8265. doi: 10.1021/acsaem.0c00686.

[251] H. Hu et al. “Triple-junction perovskite–perovskite–silicon solar cells with power conversion efficiency of 24.4%”. In: *Energy Environ. Sci.* 17.8 (2024), pp. 2800–2814. doi: 10.1039/D3EE03687A.

[252] K. Artuk et al. “Triple-junction solar cells with improved carrier and photon management”. In: *Nature* (2026), pp. 1–3.

[253] R. Pappenberger et al. “Bandgap Engineering of Two-Step Processed Perovskite Top Cells for Perovskite-Based Tandem Photovoltaics”. In: *Adv. Funct. Mater.* 34.9 (2024), p. 2311424. doi: 10.1002/adfm.202311424.

[254] J. Chen et al. “Surface Molecular Engineering for Fully Textured Perovskite/Silicon Tandem Solar Cells”. In: *Angew. Chem. Int. Ed.* 63.36 (2024), e202407151. doi: 10.1002/anie.202407151.

[255] Y. Li et al. “CsCl induced efficient fully-textured perovskite/crystalline silicon tandem solar cell”. In: *Nano Energy* 122 (2024), p. 109285. doi: 10.1016/j.nanoen.2024.109285.

[256] C. Yang et al. “Achievements, challenges, and future prospects for industrialization of perovskite solar cells”. In: *Light Sci. Appl.* 13.1 (2024). doi: 10.1038/s41377-024-01461-x.

[257] X. Zheng et al. “Solvent engineering for scalable fabrication of perovskite/silicon tandem solar cells in air”. In: *Nat. Commun.* 15.1 (2024). doi: 10.1038/s41467-024-49351-5.

[258] A. A. Said et al. “Sublimed C_{60} for efficient and repeatable perovskite-based solar cells”. In: *Nat. Commun.* 15.1 (2024), p. 708. doi: 10.1038/s41467-024-44974-0.

[259] Z. Xiong et al. “Constructing tin oxides Interfacial Layer with Gradient Compositions for Efficient Perovskite/Silicon Tandem Solar Cells with Efficiency Exceeding 28%”. In: *Small* 20.15 (2024), p. 2308024. doi: 10.1002/smll.202308024.

[260] T. Yang et al. “Efficient and Stable Perovskite/Silicon Tandem Solar Cells Modulated with Triple-Functional Passivator”. In: *Adv. Energy Mater.* 14.7 (2023), p. 2303149. doi: 10.1002/aenm.202303149.

[261] H. Luo et al. “Inorganic Framework Composition Engineering for Scalable Fabrication of Perovskite/Silicon Tandem Solar Cells”. In: *ACS Energy Lett.* 8.12 (2023), pp. 4993–5002. doi: 10.1021/acsenergylett.3c02002.

[262] Y. Sun et al. “Ionic Liquid Modified Polymer Intermediate Layer for Improved Charge Extraction toward Efficient and Stable Perovskite/Silicon Tandem Solar Cells”. In: *Small* 20.21 (2024), p. 2308553. doi: 10.1002/smll.202308553.

[263] F. Zhang et al. “Buried-Interface Engineering of Conformal 2D/3D Perovskite Heterojunction for Efficient Perovskite/Silicon Tandem Solar Cells on Industrially Textured Silicon”. In: *Adv. Mater.* 35.42 (2023), p. 2303139. doi: 10.1002/adma.202303139.

[264] L. Tan et al. “Combined Vacuum Evaporation and Solution Process for High-Efficiency Large-Area Perovskite Solar Cells with Exceptional Reproducibility”. In: *Adv. Mater.* 35.13 (2023), p. 2205027. doi: 10.1002/adma.202205027.

[265] J. Fang et al. “Anion exchange promoting non-impurities enables conformable and efficient inverted perovskite solar cells”. In: *Energy Environ. Sci.* 17.20 (2024), pp. 7829–7837. doi: 10.1039/D4EE02718C.

[266] M. R. Golobostanfard et al. “Bifacial perovskite/silicon heterojunction tandem solar cells based on $FAPbI_3$-based perovskite via hybrid evaporation-spin coating”. In: *Nano Energy* 131 (2024), p. 110269. doi: 10.1016/j.nanoen.2024.110269.

[267] J. Wang et al. “Streamlined Phase Transition and Reaction Compensation in Hybrid Evaporation-Solution Deposited Inverted Perovskite Solar Cells”. In: *Adv. Energy Mater.* 15.15 (2025), p. 2404954. doi: 10.1002/aenm.202404954.

[268] Y.-D. Wang et al. “Regulating wide-bandgap perovskite face-on stacking in hybrid-deposited perovskite/organic tandem solar cells”. In: *Nat. Commun.* 16.1 (2025), p. 6142. doi: 10.1038/s41467-025-61404-x.

[269] A. Brand et al. “Beyond authorship: attribution, contribution, collaboration, and credit”. In: *Learned Publ.* 28.2 (2015), pp. 151–155. doi: 10.1087/20150211.

List of Publications and Conference Contributions

Patents

- **Julian Petry** (50 %), Daniel Baumann (15 %), Nils W. Rosemann (10 %), Paul Fassl (10 %), Ulrich W. Paetzold (15 %), "Solarzelle enthaltend eine Adamantan- und/oder eine Diadamantan- basierte Passivierungsschicht"

Journal Articles

Peer-Reviewed Publications (First Author)

- **Julian Petry***, Thomas Feeney*, Abderrezak Torche, Dirk Hauschild, Benjamin Hacene, Constantin Wansorra, Alexander Diercks, Michelle Ernst, Lothar Weinhardt, Clemens Heske, Ganna Gryn'ova, Ulrich W. Paetzold and Paul Fassl, "Understanding and Exploiting Interfacial Interactions between Phosphonic Acid Functional Groups and Co-Evaporated Perovskites", In: *Matter*, **2024**, Vol. 7, Issue 6, p. 2066-2090, DOI: `https://doi.org/10.1016/j.matt.2024.02.004`

- **Julian Petry**, Viktor Škorjanc, Alexander Diercks, Thomas Feeney, Amedeo Morsa, Sara Rose Kimmig, Jens Baumann, Frank Löffler, Stefan Auschill, Joshua Damm, Daniel Baumann, Felix Laufer, Jona Kurpiers, Michael Müller, Lars Korte, Steve Albrecht, Marcel Roß, Ulrich W. Paetzold and Paul Fassl, "Industrialization of Perovskite Solar Cell Fabrication: Strategies to achieve High-Throughput Vapor Deposition Processes", In: *EES Solar*, **2025**, Issue 1, p. 404 - 418, DOI: `https://doi.org/10.1039/D5EL00069F`
  Highlighted in EES Solar 2025 HOT Articles, EES Solar most popular 2025 articles and EES Family journals: showcase collection.

- **Julian Petry***, Alexander Diercks*, Thomas Feeney, Richard Thelen, Paul Fassl and Ulrich W. Paetzold, "Particle Size Matters – Impact of Particle Size and Crucible Geometry on Sublimation Behavior of Formamidinium Iodide", In: *Adv. Mater. Technol.*, **2025**, e01549, DOI: `https://doi.org/10.1002/admt.202501549`

- **Julian Petry***, Ronja Pappenberger*, Alexander Welle, Tonghan Zhao, Alexander Diercks, Raphael Pesch, Paul Fassl and Ulrich W. Paetzold, "Benchmarking Inorganic Deposition Routes for Hybrid Two-Step Processed Perovskite Solar Cells: A Materials Perspective", In: *Solar RRL*, **2026**, e202500698, DOI: `https://doi.org/10.1002/solr.202500698`

- **Julian Petry**, Lingyi Fang, Dirk Hauschild, Hendrik Leutz, Daniel Baumann, Ting Pan, Yijin Wang, Hang Hu, Benjamin Hacene, Theresa Küchle, Joshua Esteves, Julian Petermann, Constantin Wansorra, Lothar Weinhardt, Paul Fassl, Renjun Guo, Nils W. Rosemann and Ulrich W. Paetzold, "Diamondoid Isolator as Bandgap Universal Surface Passivation for Perovskite Photovoltaics", In preparation

* these authors contributed equally to the respective work.

Peer-Reviewed Publications (Co-Author)

- Alexander Diercks, **Julian Petry**, Thomas Feeney, Roja Singh, Tonghan Zhao, Hang Hu, Yang Li, Ulrich W. Paetzold and Paul Fassl, "Sequential Evaporation of Inverted $\mathrm{FAPbI_3}$ Perovskite Solar Cells – Impact of Substrate on Crystallization and Film Formation", In: *ACS Energy Letters*, **2025** 10, 1165-1173, DOI: `https://doi.org/10.1021/acsenergylett.4c03315`
- Raphael Pesch, Alexander Diercks, **Julian Petry**, Alexander Welle, Ronja Pappenberger, Fabian Schackmar, Helge Eggers, Johannes Sutter, Ulrich Lemmer and Ulrich W. Paetzold, "Hybrid Two-Step Inkjet-Printed Perovskite Solar Cells", In: *Solar RRL*, **2024** 8 (13), 2400165, DOI: `https://doi.org/10.1002/solr.202400165`
- Raphael Pesch, **Julian Petry**, Julian Petermann, Ronja Pappenberger, Theresa Kuechle, Johannes Schenck, Lena P. Rothbauer, Lingyi Fang, Xuzheng Liu, Saeid Rafizadeh, Bahram A. Nejand, Johannes Sutter, Ulrich Lemmer and Ulrich W. Paetzold, "Efficient Perovskite/Silicon Tandem Solar Cells Using Hybrid Two-Step Inkjet Printing with Edge Isolation Precision", In: *Small Science*, **2025**, 2500362, DOI: `https://doi.org/10.1002/smsc.202500362`
- Ronja Pappenberger, Alexander Diercks, **Julian Petry**, Somayeh Moghadamzadeh, Paul Fassl and Ulrich W. Paetzold, "Bandgap Engineering of Two-Step Processed Perovskite Top Cells for Perovskite-Based Tandem Photovoltaics", In: *Advanced Functional Materials*, **2024** 34 (9), 2311424, DOI: `https://doi.org/10.1002/adfm.202311424`
- Kevin Synnatschke, Martin Jonak, Alexander Storm, Sourav Laha, Janis Köster, **Julian Petry**, Steffen Ott, Beata Szydłowska, Georg S. Duesberg, Ute Kaiser, Rüdiger Klingeler, Bettina V. Lotsch and Claudia Backes, "Sonication-assisted liquid exfoliation and size-dependent properties of magnetic two-dimensional $\alpha - \mathrm{RuCl_3}$", In: *Journal of Physics D: Applied Physics*, **2023** 56 (27), 274001, DOI: `https://doi.org/10.1088/1361-6463/accc3e`
- Dennis Popp, Sven M Elbert, Chantal Barwig, **Julian Petry**, Frank Rominger and Michael Mastalerz, "Palladium-Catalyzed Cyclization of a Pyryne Precursor to Higher Pyrenylenes", In: *Angewandte Chemie International Edition*, **2023** 62 (19), e202219277, DOI: `https://doi.org/10.1002/anie.202219277`

- Tobias Wesp, Tim Bruckhoff, **Julian Petry**, Hubert Wadepohl and Lutz H. Gade, "Towards Nitrogen-Rich N-Heteropolycycles: Synthesis of Octaazaperopyrenes (OAPP)", In: *Chemistry–A European Journal*, **2022** 28 (17), e202200129, DOI: `https://doi.org/10.1002/chem.202200129`
- Thomas Feeney, Aleksandra Miaskiewicz, **Julian Petry**, Felix Laufer, Roja Singh, Stefanie Severin, Viktor Škorjanc, Alexander Diercks, Suresh Maniyarasu, Lars Korte, Steve Albrecht, Ulrich W. Paetzold, Marcel Roß and Paul Fassl, "High-Rate FA-Based Co-Evaporated Perovskites: Understanding Rate Limitations and Practical Considerations to Overcome Their Impact", In: *Advanced Functional Materials*, **2025** e17873, DOI: `https://doi.org/10.1002/adfm.202517873`
- Ronja Pappenberger, Roja Singh, Alexander Diercks, Tonghan Zhao, Raphael Pesch, **Julian Petry**, Daniel Baumann, Xuzheng Liu and Ulrich W. Paetzold, "Versatile Two-Step Process for Perovskite-Based Tandem Photovoltaics", In: *Solar RRL*, **2025** Volume 9 Issue 13, p. 202500193, DOI: `https://doi.org/10.1002/solr.202500193`

Conference Contributions

Conference Proceedings

- Alexander Diercks, **Julian Petry**, Thomas Feeney, Ulrich W. Paetzold, Paul Fassl, "Particle Size Matters-Impact of Particle Size and Crucible Geometry on Sublimation Behavior of Formamidinium Iodide", In: *Proceedings of MATSUS Fall 2025 Conference*, **2025**, València, Spain, URL: `https://www.nanoge.org/proceedings/MATSUSFall25/6862b602f6178838ecc947bf`
- **Julian Petry**, Viktor Škorjanc, Alexander Diercks, Thomas Feeney, Amedeo Morsa, Sara R. Kimmig, Jens Baumann, Stefan Auschill, Josua Damm, Jona Kurpiers, Michael Müller, Lars Korte, Steve Albrecht, Marcel Roß, Ulrich W. Paetzold, Paul Fassl, "Industrialization of Perovskite Solar Cell Fabrication: Strategies towards High-Throughput PVD Processes", In: *2025 IEEE 53rd Photovoltaic Specialists Conference (PVSC)*, **2025**, Montreal, Canada, DOI: `https://doi.org/10.1109/PVSC59419.2025.11132872`
- Thomas Feeney, Aleksandra Miaskiewicz, **Julian Petry**, Felix Laufer, Roja Singh, Stefanie Severin, Viktor Škorjanc, Alexander Diercks, Suresh Maniyarasu, Lars Korte, Steve Albrecht, Ulrich W. Paetzold, Marcel Roß, Paul Fassl, "Deposition rate limitations for FA-based co-evaporated perovskites and how to overcome them", In: *Proceedings of International Conference on Perovskite Thin Film Photovoltaics and Perovskite Photonics and Optoelectronics (NIPHO25)*, **2025**, Cagliari, Italy (Sardinia), URL: `https://www.nanoge.org/proceedings/NIPHO25/67f93770969d0f32d487dbb1`

Oral and Poster Contributions (First Author Only)

- **Poster - Perowskit Workshop Baden-Württemberg 2023**
  Julian Petry, Thomas Feeney, Abderrezak Torche, Dirk Hauschild, Alexander Diercks, Constantin Wansorra, Lothar Weinhardt, Michelle Ernst, Despina Savvidou, Clemens Heske, Ganna Gryn'ova, Ulrich W. Paetzold and Paul Fassl, "How Substrate Surface Passivation Dictates Preferential Growth of Thermally Co-Evaporated Perovskite Thin Films", Perowskit Workshop Baden-Württemberg, Stuttgart, Germany
- **Poster - PSCO Conference 2023**
  Julian Petry, Thomas Feeney, Abderrezak Torche, Dirk Hauschild, Alexander Diercks, Constantin Wansorra, Lothar Weinhardt, Michelle Ernst, Despina Savvidou, Clemens Heske, Ganna Gryn'ova, Ulrich W. Paetzold and Paul Fassl, "How Substrate Surface Passivation Dictates Preferential Growth of Thermally Co-Evaporated Perovskite Thin Films", PSCO, Oxford, United Kingdom
- **Poster - Tandem PV Workshop 2024**
  Julian Petry, Thomas Feeney, Abderrezak Torche, Dirk Hauschild, Benjamin Hacene, Constantin Wansorra, Alexander Diercks, Michelle Ernst, Lothar Weinhardt, Clemens Heske, Ganna Gryn'ova, Ulrich W. Paetzold and Paul Fassl, "Evaporated Self-Assembled Monolayer HTLs: Implications for Perovskite Film Growth", Tandem PV Workshop, Amsterdam, The Netherlands
- **Talk - IEEE-53 2025**
  Julian Petry, Viktor Škorjanc, Alexander Diercks, Thomas Feeney, Amedeo Morsa, Sara Rose Kimmig, Jens Baumann, Stefan Auschill, Joshua Damm, Daniel Baumann, Felix Laufer, Jona Kurpiers, Michael Müller, Lars Korte, Steve Albrecht, Marcel Roß, Ulrich W. Paetzold and Paul Fassl, "Industrialization of Perovskite Solar Cell Fabrication: Strategies towards High-Throughput PVD Processes", IEEE-53 Conference, Montreal, Canada
- **Talk - EUPVSEC-42 2025**
  Julian Petry, Viktor Škorjanc, Alexander Diercks, Thomas Feeney, Amedeo Morsa, Sara Rose Kimmig, Jens Baumann, Stefan Auschill, Joshua Damm, Daniel Baumann, Felix Laufer, Jona Kurpiers, Michael Müller, Lars Korte, Steve Albrecht, Marcel Roß, Ulrich W. Paetzold and Paul Fassl, "Industrialization of Perovskite Solar Cell Fabrication: Strategies towards High-Throughput PVD Processes", EUPVSEC-42, Bilbao, Spain

Supervised Student Projects

- Joshua A. Esteves: Inorganic Chemistry Research Internship (AC-F) "Metallorganische Passivierung von Perowskit Solarzellen", in cooperation with University of Heidelberg, conducted at KIT at the Light Technology Insitute (LTI), **2024**, Examiner: Ulrich W. Paetzold and Gerald Linti, Supervisors: Ulrich W. Paetzold and Julian Petry.

- Joshua A. Esteves: Physical Chemistry Research Internship (PC-F) "Herstellung und Implementierung von neuartigen selbst-organisierenden Einzelschichten für die Anwendung in Perowskit Solarzellen", in cooperation with University of Heidelberg, experimental work was conducted at KIT at the Light Technology Insitute (LTI) and at the University of Heidelberg at the Organic Chemical Insitute (OCI), **2024**, Examiner: Ulrich W. Paetzold and Reiner Dahint, Supervisors: Ulrich W. Paetzold, Pascal Merten and Julian Petry.
- Joshua A. Esteves: Masters Thesis "Implementierung von neuartigen selbst organisierenden Einzelschichten für die Anwendung in Perowskit Solarzellen", in cooperation with University of Heidelberg at the Physical Chemistry Institute (PCI), the experimental work was conducted at KIT at the Light Technology Insitute (LTI), **2025**, Examiners: Ulrich W. Paetzold and Felix Deschler, Supervisors: Ulrich W. Paetzold, Felix Deschler and Julian Petry.
- Moritz Krause: Masters Thesis "Strategies to Increase Production Throughput for Perovskite Absorbers Using Hybrid Deposition Methods", conducted at KIT at the Light Technology Insitute (LTI), **2025**, Examiner: Ulrich W. Paetzold, Supervisors: Ulrich W. Paetzold, Alexander Diercks and Julian Petry.
- Yan Hoppe: Masters Thesis: "Bandgap Engineering of Hybrid-Deposited Perovskite Thin Films towards Triple-Junction Applications", conducted at KIT at the Light Technology Insitute (LTI), **2025**, Examiner: Ulrich W. Paetzold, Supervisors: Ulrich W. Paetzold, Joshua Damm and Julian Petry.
- Alex Mocanu: Masters Thesis: "Bandgap Engineering of Hybrid-Deposited Perovskite Thin Films towards Triple-Junction Applications", conducted at KIT at the Light Technology Insitute (LTI), **2025**, Examiner: Ulrich W. Paetzold, Supervisors: Ulrich W. Paetzold, and Julian Petry.

Acknowledgments

I would like to express my sincere gratitude to Ulrich Paetzold for giving me the opportunity to pursue my doctoral studies in his research group. I am thankful for his continuous support, guidance, and the many insightful discussions throughout this journey. I especially appreciate the trust he placed in me to carry out independent research projects, as well as the opportunities to attend numerous conferences and project meetings.

My sincere thanks go to Ulrich Lemmer for his continuous support during my time at LTI, and for the trust he placed in me by appointing me as the (unofficial) senior chemist of the institute.

I thank Steve Albrecht for kindly taking on the role of second reviewer.

I am grateful to the TSPPS subgroup members Paul Fassl, Alexander Diercks, Thomas Feeney, and Joshua Damm for their valuable discussions and support. I greatly appreciated the opportunity to contribute to various project meetings and conferences, and to connect with many researchers across the European perovskite community.

I would also like to thank the KIT–Heidelberg chemistry subgroup members Pascal Merten and Joshua Esteves for their contributions to material synthesis and the exploration of new chemical designs.

I am deeply thankful to all members of the Perovskite Taskforce: Ronja Pappenberger, Alexander Diercks, Daniel Baumann, Theresa Küchle, Felix Laufer, Roja Singh, Mohammad Gholipoor, Xuzheng Liu, Julian Petermann, Benjamin Hacene, Joshua Esteves, Joshua Damm, Thomas Feeney, Kristina Geistert, Fabian Schackmar, Bahram Abdollahi, Hang Hu, Ting Pan, Lingyi Fang, Yijin Wei, Helge Eggers, David Ritzer, Ahmed Farag, Marco Ruiz Preciado, Yang Li, Raphael Pesch, and Tonghan Zhao. It was a pleasure working with such a talented and collaborative team. You made my time at LTI truly enjoyable.

I would like to acknowledge the students I had the pleasure of supervising: Joshua Esteves, Yan Hoppe, Alex Mocanu, and Moritz Krause. It was a rewarding experience to guide you through your theses and projects.

I am grateful for the many fruitful collaborations that contributed to this work. I thank Abderrezak Torche, Michelle Ernst, and Ganna Gryn'ova for DFT simulations; Dirk Hauschild, Constantin Wansorra, Lothar Weinhardt, and Clemens Heske for synchrotron-based spectroscopy, with special thanks to Dirk Hauschild for both scientific and non-scientific discussions during beam time. I also thank Viktor Škorjanc, Jona Kurpiers, Lars Korte, Steve Albrecht, and Marcel Roß for discussions on vapor deposition; Jens Baumann, Frank Löffler, and René Köhler for insights into scaling laboratory research to industrial applications; Stefan Auschill for conducting sublimation experiments; Amedeo Morsa and Michael Müller for their support with KEMS measurements; Sara Rose Kimmig for ICP-OES measurements; Richard Thelen for surface analysis support; Tonghan Zhao for GIWAXS measurements; Alexander Welle for ToF-SIMS

measurements; Nils Rosemann for assistance with TCSPC measurements and (unofficial) mentorship; and Andreas Rapp, Despina Savvidou, and Tanja Ohmer-Scherrer for NMR measurements. I am deeply appreciative of all these contributions. The discussions and technical expertise significantly shaped this thesis.

I would also like to sincerely thank Nicole Klöfer, Jurana Hetterich, Reza Akbarzadeh Naseri, Christian Kayser, Julian Schickle, Hans Vögele, and Mario Sütsch for their invaluable administrative and technical support at LTI over the past years.

Finally, I thank Felix Laufer, Julie Roger, Ronja Pappenberger, Daniel Baumann, Joshua Damm, Paul Fassl, and Ulrich Paetzold for proofreading and providing valuable feedback on this thesis.